

LA-ICP-MS zircon geochronology of granulite xenoliths from the Geronimo Volcanic Field, SE  
Arizona: implications for crustal evolution since 2.4 Ga

by

Mikaela Elaine Rader

B.S., Kansas State University, 2018

A THESIS

submitted in partial fulfillment of the requirements for the degree

MASTER OF SCIENCE

Department of Geology  
College of Arts and Sciences

KANSAS STATE UNIVERSITY  
Manhattan, Kansas

2021

Approved by:

Major Professor  
Dr. Pamela Kempton

# **Copyright**

© Mikaela Rader 2021.

## Abstract

Lower crustal granulite xenoliths entrained in alkaline basalts from the Geronimo Volcanic Field (GVF), SE Arizona, provide constraints on composition, structure, and age of the lower crust in the southern Basin and Range. The GVF is located in the Mazatzal Province, accreted to the southern margin of Laurentia at ~1.69-1.65 Ga. Previous work conducted in this area provided information on the petrology, geochemistry and geothermometry for the xenolith suite, but age constraints of the xenoliths were limited to Nd model ages, making it difficult to place the evolution of the lower crust in the broader context of the geologic history of the region. This project uses zircon U-Pb geochronology and Hf-isotope analysis to determine the age of formation of GVF lower crust, as well as provide evidence for subsequent tectonic events that impacted its composition. Samples for this suite range in composition from mafic meta-cumulates (plg + cpx ± opx ± ol ± sp) to metadiorites and quartzofeldspathic lithologies (plg + kspar + cpx + ox ± qtz ± opx). GVF xenoliths analyzed for U-Pb geochronology present three distinct zircon age populations at ~1.63-1.65 Ga, ~1.48-1.42 Ga, and ~76-2 Ma, with the majority of young ages concentrated between 35-25 Ma. Zircon U-Pb ages for quartzofeldspathic lithologies present evidence of an event at ~1.65 Ga, suggesting an age of formation consistent with the age of the Mazatzal terrane. However, one quartzofeldspathic zircon core was dated at 2.38 Ga, suggesting the presence of an older component during formation of the Mazatzal crust, possibly originating as cratonic Laurentian sediment. Two quartzofeldspathic xenoliths (MR-GN21-39 and MR-GN21-53) contain zircon cores with discordant U-Pb ages that trend toward ~1.48-1.42 Ga, suggesting modification of the Mazatzal terrane beginning at ~1.48 Ga, the onset of the Picuris Orogeny and widespread 1.48-1.35 Ga plutonism in the southwestern US. These same quartzofeldspathic

samples present young ages ranging from ~50-15 Ma, suggesting later alteration of the Proterozoic terrane by Tertiary magmatism associated with Farallon slab subduction. Metadiorites, which were previously inferred to be ~ 1.4 Ga on the basis of whole rock Nd model ages, yielded zircon U-Pb ages ranging from ~76 to 2 Ma, suggesting an origin through thermal resetting of zircons in older Paleoproterozoic crust or addition of new juvenile melts that assimilated Paleoproterozoic crust during magmatic underplating in the Cenozoic. Zircon Hf isotope data from both quartzofeldspathic and metadiorite lithologies are consistent with mantle separation at 2.4 Ga, following an intermediate ( $^{176}\text{Lu}/^{177}\text{Hf} = 0.018$ ) crustal isotope evolution path. The existence of positive  $\epsilon\text{Hf}(t)$  values in Mesoproterozoic zircon cores of some quartzofeldspathic xenoliths suggest reworking of this older Paleoproterozoic crust sometime between the time of Mazatzal formation and the 1.4 Ga Picuris orogeny and/or the widespread A-type granite event that also occurred across Laurentia at about this time. Eocene to Oligocene age zircons have  $\epsilon\text{Hf}(t)$  values that range from -17 to 0, suggesting significant lower crustal modification during Farallon slab subduction.

# Table of Contents

List of Figures .....	vii
List of Tables .....	ix
Chapter 1 - Introduction.....	1
1.1. Previous Research.....	3
Chapter 2 - Scope and Structure of Thesis.....	6
2.1. The Scope of this Thesis .....	6
2.2. Thesis Outline .....	6
Chapter 3 - Manuscript .....	7
Abstract.....	7
3.1. Introduction.....	8
3.2. Geronimo Volcanic Field.....	18
3.2.1. The Xenolith Suite and Sample Selection .....	19
3.3. Analytical Methods.....	21
3.3.1. Petrography .....	21
3.3.2. Whole Rock Geochemistry .....	21
3.3.3. Mineral separation .....	22
3.3.4. Cathodoluminescence Imaging .....	23
3.3.5. Zircon U-Pb LA ICP-MS.....	23
3.3.6. Hf LA ICP-MS.....	26
3.3.7. Microprobe and Geothermometry.....	26
3.4 Results.....	29
3.4.1. Petrography and Geothermometry .....	29
3.4.2. Whole Rock Geochemistry .....	35
3.4.3. Zircon Cathodoluminescence.....	48
3.4.4. U-Pb Geochronology .....	62
3.4.5. Zircon Trace Element Analyses .....	73
3.4.6. Zircon Hf Isotopes .....	80
3.5. Discussion.....	83
3.5.1. Lower Crustal Temperatures.....	83

3.5.2. Lower Crustal Composition in SE Arizona .....	86
3.5.3. Geologic History of SE Arizona as Evidenced by U-Pb and Hf Geochronology.....	95
3.6. Conclusions.....	104
Chapter 4 - Further Research .....	105
References.....	106
Appendix A - Mineral Abbreviations .....	112
Appendix B - Petrographic Descriptions .....	113
Appendix C - Whole Rock Geochemistry .....	149
Appendix D - Geothermometry .....	154
Appendix E - Cathodoluminescence Imaging .....	155
Appendix F - U-Pb LA-ICP-MS Laser Methods and Geochronology Data.....	169
Appendix G - Hf Isotope Data .....	170

## List of Figures

Figure 1.1. Geronimo Volcanic Field, SE Arizona.....	2
Figure 1.2. $^{143}\text{Nd}/^{144}\text{Nd}$ vs. $^{87}\text{Sr}/^{86}\text{Sr}$ .....	4
Figure 3.1. Proterozoic accretion of Laurentia. ....	10
Figure 3.2. Paths of Shatsky & Hess conjugate plateaux. ....	12
Figure 3.3. $^{143}\text{Nd}/^{144}\text{Nd}$ vs. $^{87}\text{Sr}/^{86}\text{Sr}$ .....	14
Figure 3.4. Model presented by Axen et al. (2018). ....	16
Figure 3.5. The Geronimo Volcanic Field locality.....	18
Figure 3.6. Oblique view of the San Bernardino Valley.....	20
Figure 3.7. Equations 37, used in two-pyroxene geothermometry (Putirka, 2008).....	28
Figure 3.8. Equations 27b, used in two-feldspar geothermometry (Putirka, 2008).....	28
Figure 3.9. Whole rock Mg# vs. $\text{SiO}_2/\text{Al}_2\text{O}_3$ . ....	37
Figure 3.10. REE plots for whole rock trace element analyses, normalized to Primitive Mantle (Sun and McDonough, 1989).....	42
Figure 3.11. Spider diagrams for whole rock trace element analyses, normalized to Primitive Mantle (Sun and McDonough, 1989). ....	46
Figure 3.12. Spider diagrams for whole rock trace element analyses averaged for each lithology, normalized to Primitive Mantle (Sun and McDonough, 1989). ....	47
Figure 3.13. CL images of representative zircon from MR-GN21-39. ....	50
Figure 3.14. CL images of representative zircon from MR-GN21-53. ....	52
Figure 3.15. CL images of representative zircon from pk-G-GN22-5. ....	53
Figure 3.16. CL images of representative zircon from MR-GN21-34. ....	55
Figure 3.17. CL images of representative zircon from MR-GN22-27. ....	57
Figure 3.18. CL images of representative zircon from MR-GN22-35. ....	59
Figure 3.19. CL images of representative zircon from pk-G-GN22-3. ....	61
Figure 3.20. U-Pb zircon geochronology results for quartzofeldspathic granulites pk-G-GN22-5 and pk-G-GN22-10. ....	64
Figure 3.21. U-Pb zircon geochronology results for quartzofeldspathic granulite MR-GN21-39. .....	66

Figure 3.22. U-Pb zircon geochronology results for quartzofeldspathic granulite MR-GN21-53. .....	68
Figure 3.23. U-Pb zircon geochronology results for metadiorite xenolith pk-G-GN22-3.....	69
Figure 3.24. U-Pb zircon geochronology results for metadiorite xenoliths MR-GN21-34, MR- GN22-27, and MR-GN22-35.....	72
Figure 3.25. Trace elements for zircon analyzed by LA-ICP-MS simultaneously with U-Pb. ....	76
Figure 3.26. Ti in zircon temperature vs. Age (Ma). .....	80
Figure 3.27. Hf isotope analysis for three metadiorites and two quartzofeldspathic samples.....	81
Figure 3.28. Hf isotope analyses, with crustal evolution lines from 1.65 Ga. Expanded to veiw the last 80 m.y. ....	82
Figure 3.29. Geothermometry Data with 30°C/km against Plank and Forsythe (2016) Conductive Geotherms .....	85
Figure 3.30. Whole rock Mg# vs. SiO <sub>2</sub> /Al <sub>2</sub> O <sub>3</sub> .....	87
Figure 3.31. Spider diagrams for whole rock trace element analyses normalized to middle and lower crust.....	93
Figure 3.32. Spider diagram for whole rock trace element analyses of quartzofeldspathic granulites normalized to upper crust. ....	94
Figure 3.33. Hf isotope analyses, with crustal evolution lines from 2.4 Ga. ....	97
Figure 3.34. Hf isotope analyses, with crustal evolution lines from 2.4 Ga. Expanded to veiw the last 80 m.y. ....	98
Figure 3.35. Hf isotope model. ....	101
Figure 3.36. Additional Hf isotope model .....	103

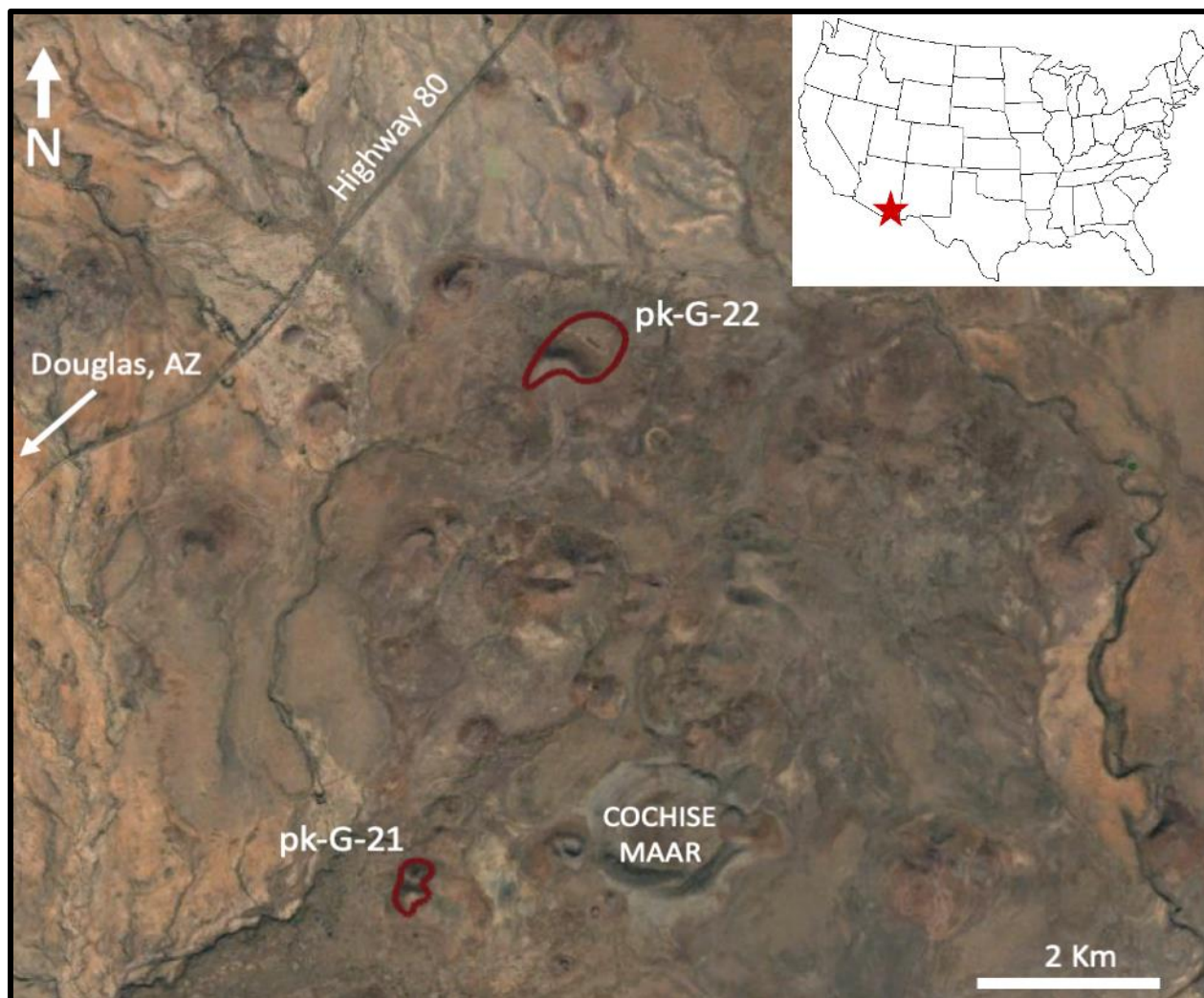
## List of Tables

Table 3.1. Reference standards and methods.....	25
Table 3.2. Summary of all samples and analyses completed and used in this study.....	30
Table 3.3. Summary of petrography for new samples.....	31
Table 3.4. Summary of geothermometry calculations.....	35
Table 3.5. Whole rock major and trace elements.....	39
Table 3.6. Summary of geochronology, including date ranges, age peaks, and Discordia model ages.....	62

## **Chapter 1 - Introduction**

Knowledge of the lower crust contributes significantly to our understanding of tectonic evolution and growth of continents (Whitmeyer and Karlstrom, 2007), but the lower crust is a relatively inaccessible part of the Earth. Seismic reflection surveys and exposed crustal terranes can give clues to the structure and composition of the lower crust (Rudnick & Gao, 2014); but seismic data can only record the structure today and exposed crustal terranes are, by definition, no longer in situ. As a result, we have little access to information about in situ lower crustal composition, age, and development. Xenoliths brought to the surface by basaltic magma are a key source of this information (Kay & Kay, 1981).

Much of the previous research on the lower crust of the western U.S.A. has focused on xenoliths from Archean cratonic regions, such as the Wyoming craton (e.g. Bolhar et al., 2007) or areas around the Colorado Plateau (e.g. Crowley et al, 2006)—the latter with particular interest in understanding its sustained uplift (Butcher et al., 2017; Chapman et al., 2020). Less attention has been given to the lower crust of the southern Basin and Range province, which represents its own unique geologic history. Therefore, this study examines lower crustal xenoliths entrained in Quaternary-age alkaline basalts from the Geronimo Volcanic Field (GVF) of southeast Arizona, southern Basin and Range (Fig. 1.1), using geochronology and geochemistry to better understand the age and origin of the lower crust in this region. With this knowledge we can better “ground truth” the timing of and drivers for tectonic events that shaped western North America.



**Figure 1.1. Geronimo Volcanic Field, SE Arizona.**

Geronimo Volcanic Field, SE Arizona, highlighting two key sample localities, cinder cones pk-G-22 and pk-G-21, outlined in red; image modified from Google Earth, 2019. Inset shows sample location within the southwestern US.

## 1.1. Previous Research

Kempton et al. (1990) report a detailed analysis of the petrology and geochemistry of the granulite xenoliths from the GVF. These authors describe the rocks as ranging in composition from mafic meta-cumulates (plg + cpx ± opx ± ol ± sp) to metadiorites and quartzofeldspathic lithologies (plg + kspar + cpx + ox ± qtz ± opx) (mineral abbreviations found in Appendix A). The study includes petrographic descriptions, bulk rock major and trace elemental geochemistry, H- and O-isotope data, two-pyroxene geothermometry, and whole rock radiogenic isotopic analyses of Sr, Nd, and Pb.

Nd model ages for the xenolith suite range from 2.2 Ga to essentially age of eruption, with metadiorites clustering between 1.4 – 1.1 Ga, and the one quartzofeldspathic granulite analyzed representing the upper limit at 2.2 Ga. Granulite xenoliths have higher  $^{87}\text{Sr}/^{86}\text{Sr}$  and lower  $^{143}\text{Nd}/^{144}\text{Nd}$  than the host basalts, with quartzofeldspathic xenoliths recording the highest Sr-isotope and lowest Nd-isotope values ( $^{87}\text{Sr}/^{86}\text{Sr} = 0.81853$  and  $^{143}\text{Nd}/^{144}\text{Nd} = 0.51199$ ). Mafic meta-cumulates form an array between metadiorites and host basalts, suggesting that GVF basalts interacted with the old lower crustal metadiorites before erupting at the surface (Fig. 1.2). From these data, Kempton et al. (1990) proposed that the mafic metacumulate xenoliths record underplating of the lower crust by young (e.g. <9Ma) mafic GVF basalts that intruded and interacted with the Proterozoic (e.g. ca. 1.4 Ga) metadiorite crust.

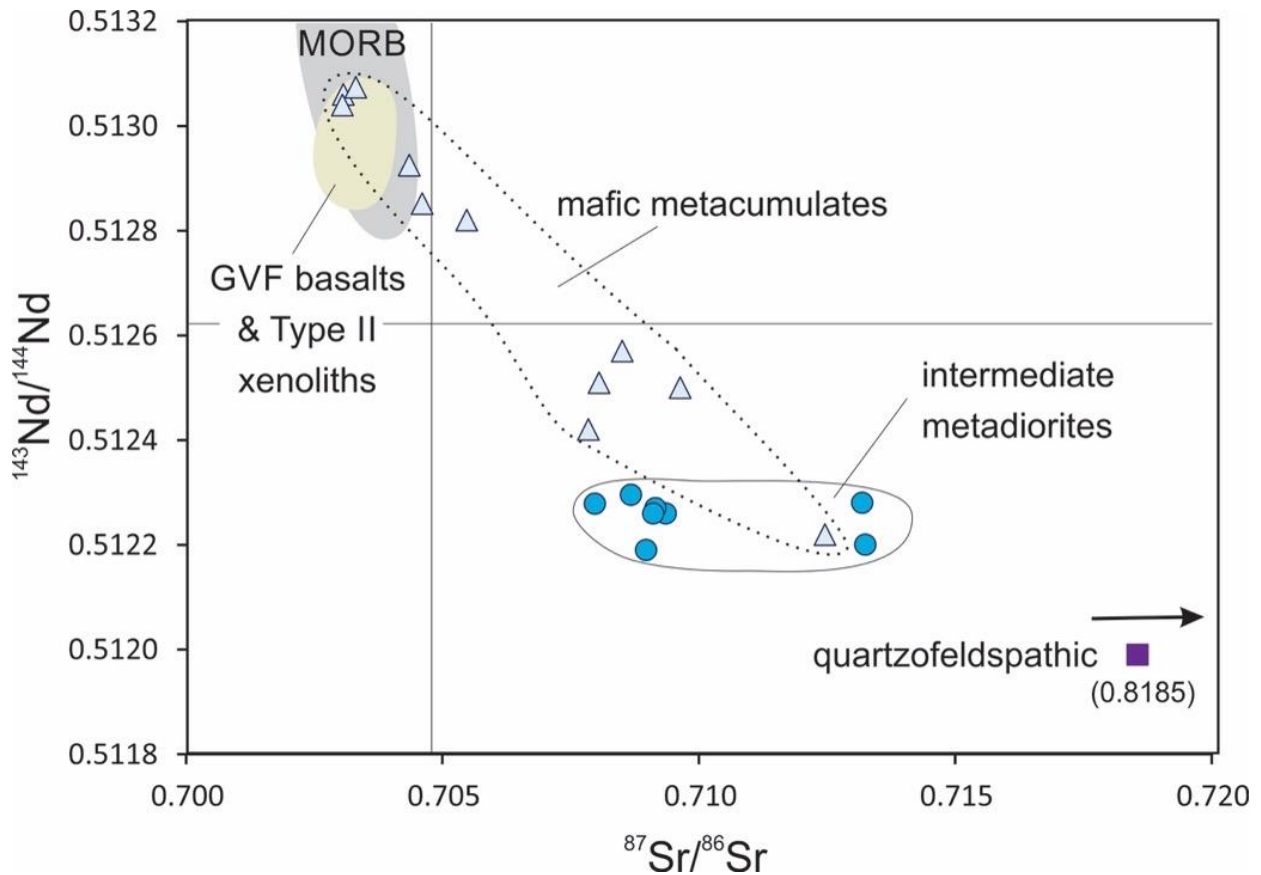


**Figure 1.2.**  $^{143}\text{Nd}/^{144}\text{Nd}$  vs.  $^{87}\text{Sr}/^{86}\text{Sr}$ .

Metadiorites have higher Sr-isotope and lower Nd-isotope ratios than host basalts.

Metacumulates form an array between GVF host basalt and metadiorites. The quartzofeldspathic sample has higher Sr-isotope and lower Nd-isotope ratios than other GVF granulites; modified from (Kempton et al., 1990).

In an effort to better constrain the geologic evolution of the GVF lower crust, Rader et al. (2017) assessed the previously studied samples for the presence of zircon suitable for U-Pb geochronological analysis. Zircon was not found in thin sections of mafic metacumulate lithologies, but quartzofeldspathic granulites and metadiorites were found to contain zircon suitable for study. Three samples were selected and analyzed by LA ICP-MS at the University of Kansas, producing the first robust age constraints on the in situ lower crust in this region (Rader et al., 2017). Two quartzofeldspathic xenoliths (pk-G-GN22-5, pk-G-GN22-10) yielded concordant ages at 1.64 Ga, consistent with the age of the Mazatzal terrane in which the GVF occurs. One zircon core from pk-G-GN22-5 was dated at 2.4 Ga, consistent with the 2.2 Ga Nd model ages for this sample (Kempton et al., 1990), which suggests the Mazatzal terrane may not be limited to juvenile arc crust as previously assumed (Whitmeyer and Karlstrom, 2007). Two metadiorites yielded much younger ages of 76 to 1.7 Ma, suggesting delamination and replacement of Paleoproterozoic crust in a multi-stage process that broadly corresponds to the time when slab rollback was underway beneath western North America (Rader et al., 2019). These conclusions contrast with the geologic history proposed by Kempton et al. (1990), prompting the more detailed geochronological study reported in this thesis.

## **Chapter 2 - Scope and Structure of Thesis**

### **2.1. The Scope of this Thesis**

This study presents new in situ U-Pb zircon geochronology, zircon Hf isotope data and zircon trace element compositions, as well as new whole rock major and trace element geochemistry for granulite xenoliths from the GVF. The aim is to develop a better understanding of the origin and evolution of the lower crust of the southern Basin and Range by defining the timing of geologic events affecting its development. Zircon Hf-isotope ratios and trace element data, whole rock geochemistry, and two-pyroxene and two-feldspar geothermometry establish parameters for lower crustal formation by pinpointing zircon origin, i.e. whether they represent the product of reworked pre-existing Proterozoic crust or crystallization from juvenile, mantle-derived melt additions. This research creates a new narrative for lower crustal evolution of the region, providing new constraints on the nature and composition of the Proterozoic Mazatzal terrane and its later modification by Cenozoic events.

### **2.2. Thesis Outline**

The main body of this thesis is presented as a journal-style manuscript in Chapter 3. Due to this format, some aspects of this introduction are repeated in section 3.1. Chapter 4 summarizes the key findings from this project and offers suggestions for future research. Appendices follow, containing mineral abbreviations used throughout this thesis (Appendix A), detailed petrographic descriptions of samples (Appendix B), whole rock geochemistry (Appendix C), geothermometry data (Appendix D), CL images (Appendix E), U-Pb Geochronology (Appendix F), and Hf-isotope analyses (Appendix G).

## Chapter 3 - Manuscript

### Abstract

Lower crustal granulite xenoliths entrained in alkaline basalts from the Geronimo Volcanic Field (GVF), SE Arizona, provide constraints on composition, structure, and age of the lower crust in the southern Basin and Range. The GVF is located in the Mazatzal Province, accreted to the southern margin of Laurentia at ~1.69-1.65 Ga. Previous work conducted in this area provided information on the petrology, geochemistry and geothermometry for the xenolith suite, but age constraints were limited to whole rock Nd model ages, making it difficult to place the evolution of the lower crust in the broader context of the geologic history of the region. This project uses zircon U-Pb geochronology and Hf-isotope analysis to determine the age of formation of GVF lower crust, as well as provide evidence for subsequent tectonic events that impacted its composition. Samples for this suite range in composition from mafic meta-cumulates (plg + cpx ± opx ± ol ± sp) to metadiorites and quartzofeldspathic lithologies (plg + kspar + cpx + ox ± qtz ± opx). GVF xenoliths analyzed for U-Pb geochronology present three distinct zircon age populations at ~1.63-1.65 Ga, ~1.48-1.42 Ga, and ~76-2 Ma, with the majority of young ages concentrated between 35-25 Ma. Zircon U-Pb ages for quartzofeldspathic lithologies present evidence of an event at ~1.65 Ga, suggesting an age of formation consistent with the age of the Mazatzal terrane. However, one quartzofeldspathic zircon core was dated at 2.38 Ga, suggesting the presence of an older component during formation of the Mazatzal crust, possibly originating as cratonic Laurentian sediment. Two quartzofeldspathic xenoliths (MR-GN21-39 and MR-GN21-53) contain zircon cores with discordant U-Pb ages that trend toward ~1.48-1.42 Ga, suggesting modification of the Mazatzal terrain beginning at ~1.48 Ga, at the onset of the Picuris orogeny and 1.48-1.35 Ga, dominantly A-type granite magmatism in the southwestern US. These same quartzofeldspathic

samples present young ages ranging from ~50-15 Ma, suggesting later alteration of the Proterozoic terrane by Cenozoic magmatism associated with Farallon slab subduction. Metadiorites, which were previously inferred to have formed at ~ 1.4 Ga on the basis of whole rock Nd model ages, yield zircon U-Pb ages ranging from ~76 to 2 Ma, suggesting an origin through thermal resetting of zircons in older Paleoproterozoic crust or addition of new juvenile melts that assimilated Paleoproterozoic crust during magmatic underplating in the Cenozoic. Zircon Hf isotope data from both quartzofeldspathic and metadioritic lithologies suggest possible separation from the mantle at 2.4 Ga, extrapolated from an intermediate ( $^{176}\text{Lu}/^{177}\text{Hf} = 0.018$ ) crustal evolution path. The existence of positive  $\epsilon\text{Hf}(t)$  values in Mesoproterozoic cores of some quartzofeldspathic xenoliths suggests reworking of this older Paleoproterozoic crust sometime between the time of Mazatzal terrane formation and the 1.4 Ga Picuris Orogeny and/or the widespread A-type granite event that also occurred across the Laurentian margin. Mid-Cenozoic age zircons have  $\epsilon\text{Hf}(t)$  values that range from -17 to 0, suggesting significant lower crustal modification during interaction with melts related to Farallon slab subduction.

### **3.1. Introduction**

Knowledge of the lower crust contributes significantly to our understanding of tectonic evolution and growth of continents (Whitmeyer and Karlstrom, 2007), but the lower crust is a relatively inaccessible part of the Earth. Seismic reflection surveys and exposed crustal terranes can give clues to the structure and composition of the lower crust (Rudnick & Gao, 2014); but seismic data can only record the structure today and exposed crustal terranes are, by definition, no longer in situ. As a result, we have little access to information about in situ lower crustal composition, age, and development. Xenoliths brought to the surface by basaltic magma are a key source of this information (Kay & Kay, 1981).

Much of the previous research on the lower crust of the western U.S.A. has focused on xenoliths from Archean cratons, such as the Wyoming craton (e.g. Bolhar et al., 2007) or areas around the Colorado Plateau (e.g. Crowley et al., 2006)—the latter with particular interest in understanding its sustained uplift (Butcher et al., 2017; Chapman et al., 2020). Less attention has been given to the lower crust of the southern Basin and Range province, which represents its own unique geologic history. Therefore, this study examines lower crustal xenoliths entrained in Quaternary-age alkaline basalts from the Geronimo Volcanic Field (GVF) of southeast Arizona, southern Basin and Range, using geochronology and geochemistry to better understand the age and origin of the lower crust in this region.

The GVF is located within the Cochise block of the Mazatzal terrane, which was accreted to North America between 1.69-1.65 Ga (Fig. 3.1; Whitmeyer and Karlstrom, 2007). It has been interpreted as a juvenile arc terrane (Whitmeyer and Karlstrom, 2007). From 1.48-1.35 Ga, this region was intruded by A-Type granites (e.g. Whitmeyer and Karlstrom, 2007). Post-terrane accretion along the southern margin of Laurentia lasted from ~1.4 to 0.4 Ga, although tectonic activity in the region was limited, being focused primarily along the eastern margin of Laurentia. In the mid- to late-Paleozoic, terrane accretion and minor orogenic events resumed on the western margin of North America (e.g. Speed and Sleep, 1982).

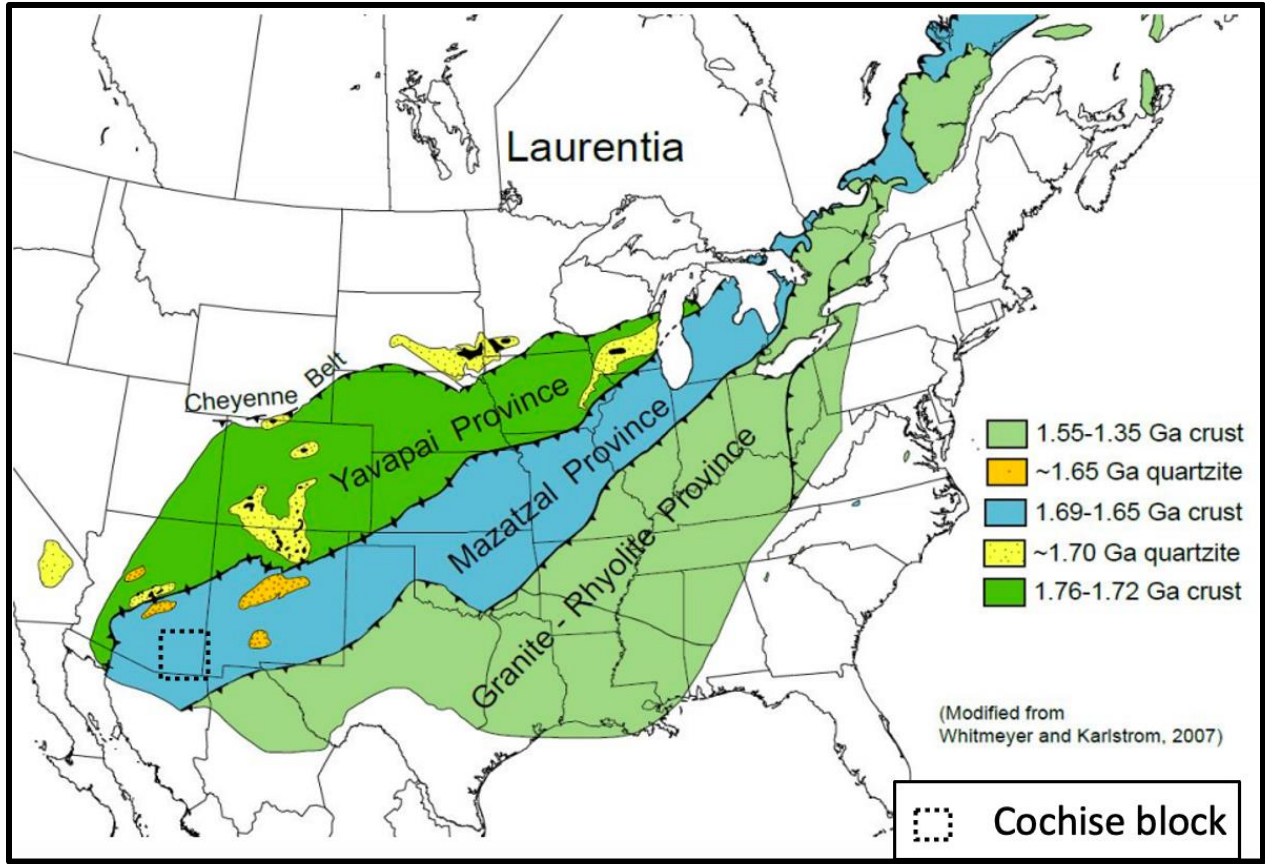


**Figure 3.1. Proterozoic accretion of Laurentia.**

Simplified figure from Whitmeyer and Karlstrom (2007) of Proterozoic accretion of Laurentia.

The GVF is located in the Cochise block (outline in yellow) of the Mazatzal Province.

At approximately 100 Ma, subduction of the Farallon plate began beneath western North America, with slab shallowing and flat slab subduction ensuing by 80-90 Ma. One model for flat slab subduction suggests that slab shallowing occurred as a combination of increased convergence rates and a change in plate motion (e.g. Bird, 1998). The second widely accepted model for flat slab subduction suggests that two large, buoyant oceanic plateaux intersected the southern portion of North America between ~90 Ma and 70 Ma (Liu et al. 2010). The first of the two plateaux, the Shatsky rise oceanic plateau correlative, subducted beneath southern California at ~90 Ma (Liu et al., 2010; Sun et al., 2017). The second oceanic plateau, the Hess rise correlative, intersected northern Mexico about 20 m.y. later (Liu et al., 2010). It has been suggested by a number of researchers (Dickinson, 1997; Saleeby, 2003; Liu et al., 2010; Sun et al., 2017) that the buoyancy of the partially subducted oceanic plateaux led to flat slab subduction, initiation of a break in the slab, and ultimately creation of a slab window beneath the southern Basin and Range.

The GVF is located at the intersection of the predicted subduction paths for these two plateaux (Fig. 3.2; Liu et al., 2010). Flat slab subduction ensued from ~70-40 Ma, resulting in uplift of the Laramide orogeny (Liu and Currie, 2016). Around 40 Ma, the subducting plate steepened and started to rollback, leading to the mid-Tertiary ignimbrite flare-up (Humphreys et al. 2003; Best et al, 2013). Rhyolite magmatism was active in the nearby Chiricahua mountains from ~34-23 Ma (du Bray et al., 2004). Geronimo volcanism began ~9-8 Ma, as a result of local Basin and Range extension and crustal thinning (Kempton et al., 1987; 1990).

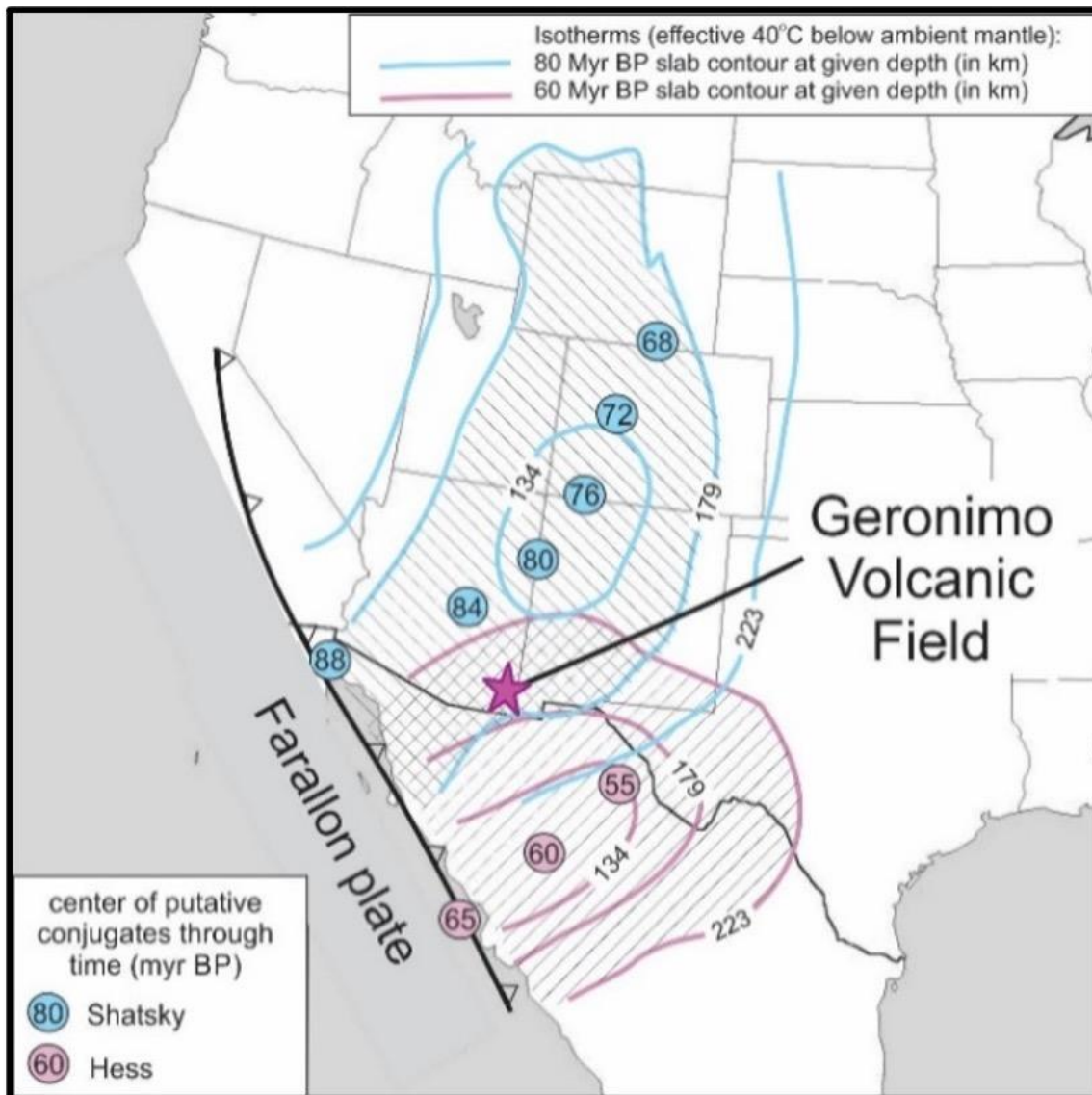


**Figure 3.2. Paths of Shatsky & Hess conjugate plateaux.**

Location of GVF between the predicted positions of Shatsky & Hess conjugate plateaux; modified from Liu et al. (2010).

To place the lower crust into the tectonic history of the Basin and Range province and the GVF in particular, Kempton et al. (1990) studied the granulite xenoliths entrained in the GVF alkali basalts. They describe the majority of the rocks as ranging in composition from mafic metacumulates (plg + cpx ± opx ± ol ± sp) to metadiorites and quartzofeldspathic lithologies (plg + kspar + cpx + ox ± qtz ± opx). Nd model ages for the suite range from 2.2 Ga to essentially age of eruption, with metadiorites clustering between 1.4 – 1.1 Ga, and the one quartzofeldspathic granulite analyzed representing the upper limit at 2.2 Ga. The granulite xenoliths have higher  $^{87}\text{Sr}/^{86}\text{Sr}$  and lower  $^{143}\text{Nd}/^{144}\text{Nd}$  than the host basalts, with quartzofeldspathic xenoliths recording the highest Sr-isotope and lowest Nd-isotope values ( $^{87}\text{Sr}/^{86}\text{Sr} = 0.81853$  and  $^{143}\text{Nd}/^{144}\text{Nd} = 0.51199$ ). Mafic metacumulates form an array between metadiorites and host basalts, suggesting that GVF basalts interacted with the older lower crustal metadiorites before erupting at the surface (Fig. 3.3). From these data, Kempton et al. (1990) proposed that the mafic metacumulate xenoliths record underplating of the lower crust by young (e.g. <9Ma) mafic GVF basalts that intruded and interacted with the older (e.g., ca. 1.4 Ga) metadiorite crust.

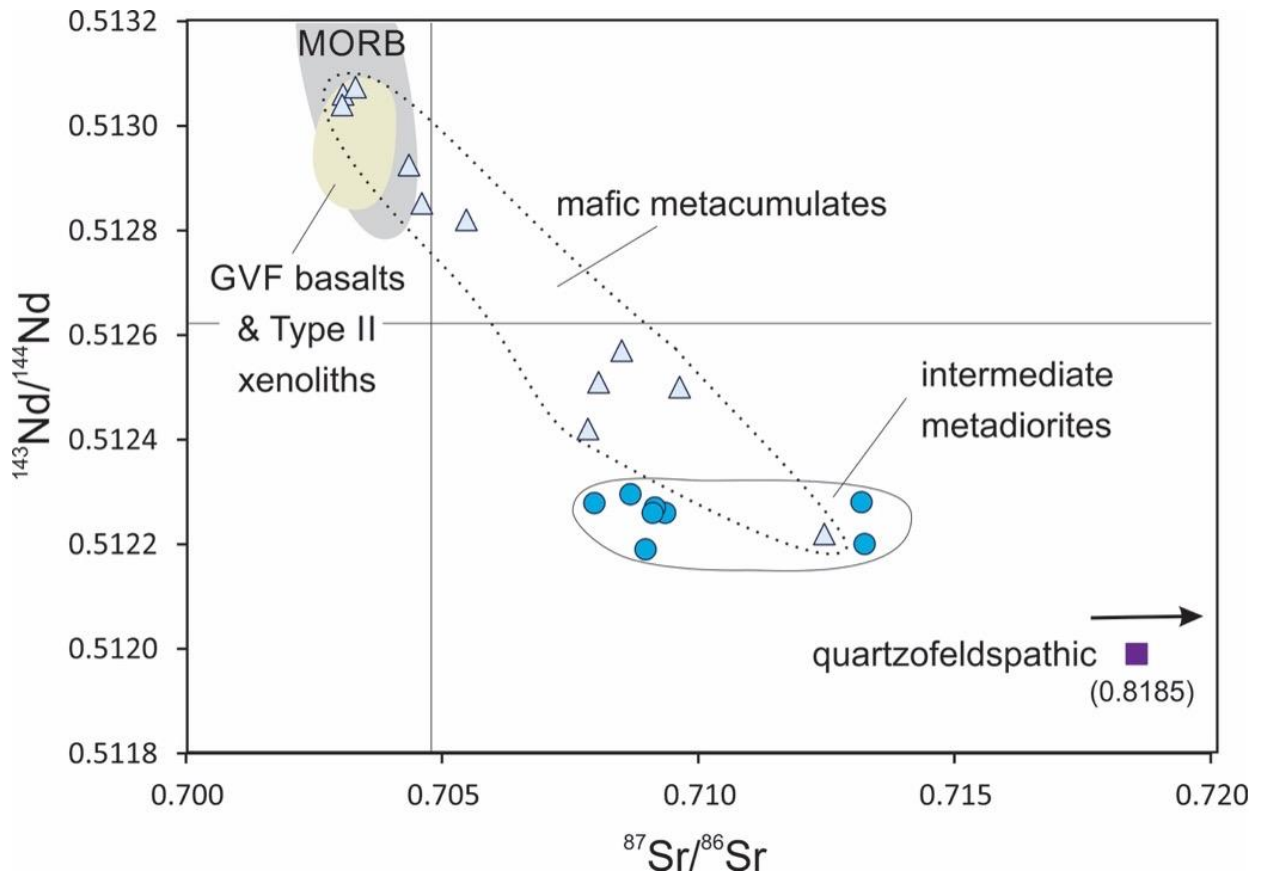


**Figure 3.3.**  $^{143}\text{Nd}/^{144}\text{Nd}$  vs.  $^{87}\text{Sr}/^{86}\text{Sr}$ .

Metadiorites have higher Sr-isotope and lower Nd-isotope ratios than host basalts.

Metacumulates form an array between GVF host basalt and metadiorites. The quartzofeldspathic sample has higher Sr-isotope and lower Nd-isotope ratios than other GVF granulites; modified from (Kempton et al., 1990).

Rader et al. (2017) analyzed zircons from three samples studied by Kempton et al. (1990), producing the first robust age constraints on the in situ lower crust in this region. Two quartzofeldspathic xenoliths yielded concordant ages at 1.64 Ga, consistent with the age of the Mazatzal terrane in which the GVF occurs. One zircon core from this sample was dated at 2.4 Ga, which suggests the Mazatzal terrane may not be limited to juvenile arc crust as previously assumed (Whitmeyer and Karlstrom, 2007). Two metadiorites yielded much younger ages of 76 to 1.7 Ma, suggesting delamination and replacement of Paleoproterozoic crust in a multi-stage process that broadly corresponds to the time when slab rollback was underway beneath western North America (Rader et al., 2019).

These conclusions contrast with the geologic history proposed by Kempton et al. (1990). They also contrast with the post-Laramide history proposed for the lower crust of the Colorado Plateau Transition Zone (CPTZ) less than 400 km to the north (Fig. 3.4; Axen et al., 2018; Chapman et al., 2019). These authors have proposed that the root of the Cordilleran arc was translated eastward from beneath the southern California batholith during Laramide flat-slab subduction and is currently attached to the lithosphere beneath the Colorado Plateau. These very different tectonic scenarios demonstrate the need for better knowledge of the in situ lower crust and greater understanding of the role the lower crust has played in the tectonic evolution of western North America.

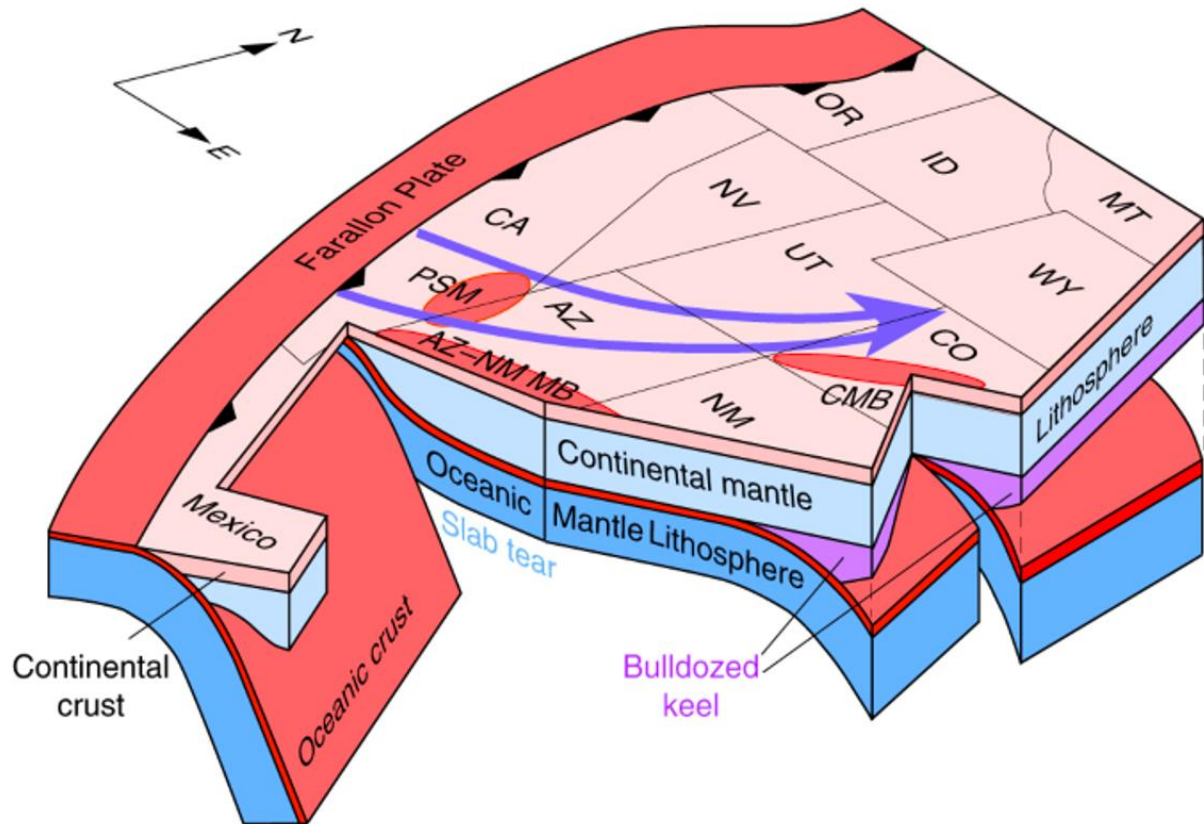


**Figure 3.4. Model presented by Axen et al. (2018).**

Model presented by Axen et al. (2018), shows the bulldozed lithospheric root of the California batholith that was translated eastward by flat slab subduction. This model suggests that a slab tear accounts for the differing lower crustal histories between the Colorado Plateau and regions further south. Blue arrow is the proposed path of the Shatsky oceanic plateau correlative.

Therefore, this study presents new U-Pb zircon geochronology, zircon Hf isotope data and zircon trace element compositions, as well as new whole rock major and trace element geochemistry for granulite xenoliths from the GVF. The aim is to develop a better understanding of the origin and evolution of the lower crust of the southern Basin and Range by defining the timing of tectonic events affecting its development; in particular, we address the following questions:

- (1) Is the Mazatzal Province wholly juvenile in origin, or does it include a component of older reworked crust (Whitmeyer and Karlstrom, 2007; Holland et al. 2020), and how does this modify our understanding of Proterozoic terrane accretion to Laurentia?
- (2) Can we refine the post-Laramide xenolith ages and distinguish discrete events in the evolution of Basin & Range lower crust? If so, can we better constrain the timing of and effects from Farallon slab subduction and rollback?
- (3) What are the processes that have given rise to the different lower crustal histories of the Colorado Plateau Transition Zone (central Arizona) relative to that of the Basin & Range in southeastern Arizona.

The new geochemistry and geochronology data establish parameters for lower crustal formation by pinpointing zircon origin, i.e. whether they represent the product of reworked pre-existing crust or crystallization from juvenile mantle-derived melt additions. This research creates a new narrative for lower crustal evolution of the region, providing new constraints on the origin of the Proterozoic Mazatzal terrane as well as the Cenozoic tectonic evolution of western North America.

### 3.2. Geronimo Volcanic Field

The Geronimo Volcanic Field (GVF) is situated in southeastern Arizona, in the San Bernardino Valley (Fig. 3.5). As part of the southern Basin and Range, the San Bernardino Valley is an extensional basin, bounded on both sides by N-NE oriented normal faults and a series of mountain ranges (the Chiricahua, Pedregosa, and Perilla Mountains to the west, and the Peloncilla Mountains to the east). Cenozoic volcanic rocks in this region include Plio-Pleistocene alkali basaltic cinder cones, lavas, and air fall tuff deposits from the GVF (Fig. 3.6). Normal faulting within the region has resulted in older (9-3 Ma) basalts being exposed on the uplifted flanks of the valley. Xenoliths and xenocrysts are entrained in GVF basalts of all ages, although lower crustal and mantle xenoliths are most prevalent in the areas immediately surrounding the <2 Ma cinder cones and maars erupted on the valley floor (Kempton et al., 1987, 1990).

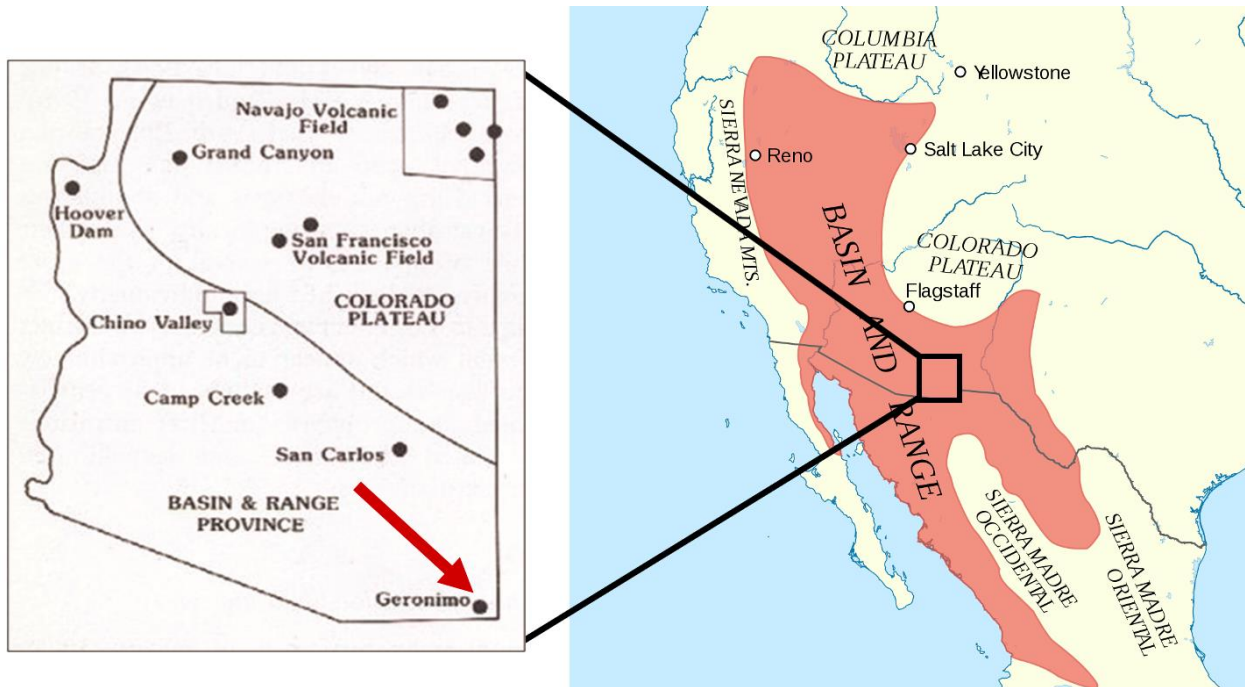
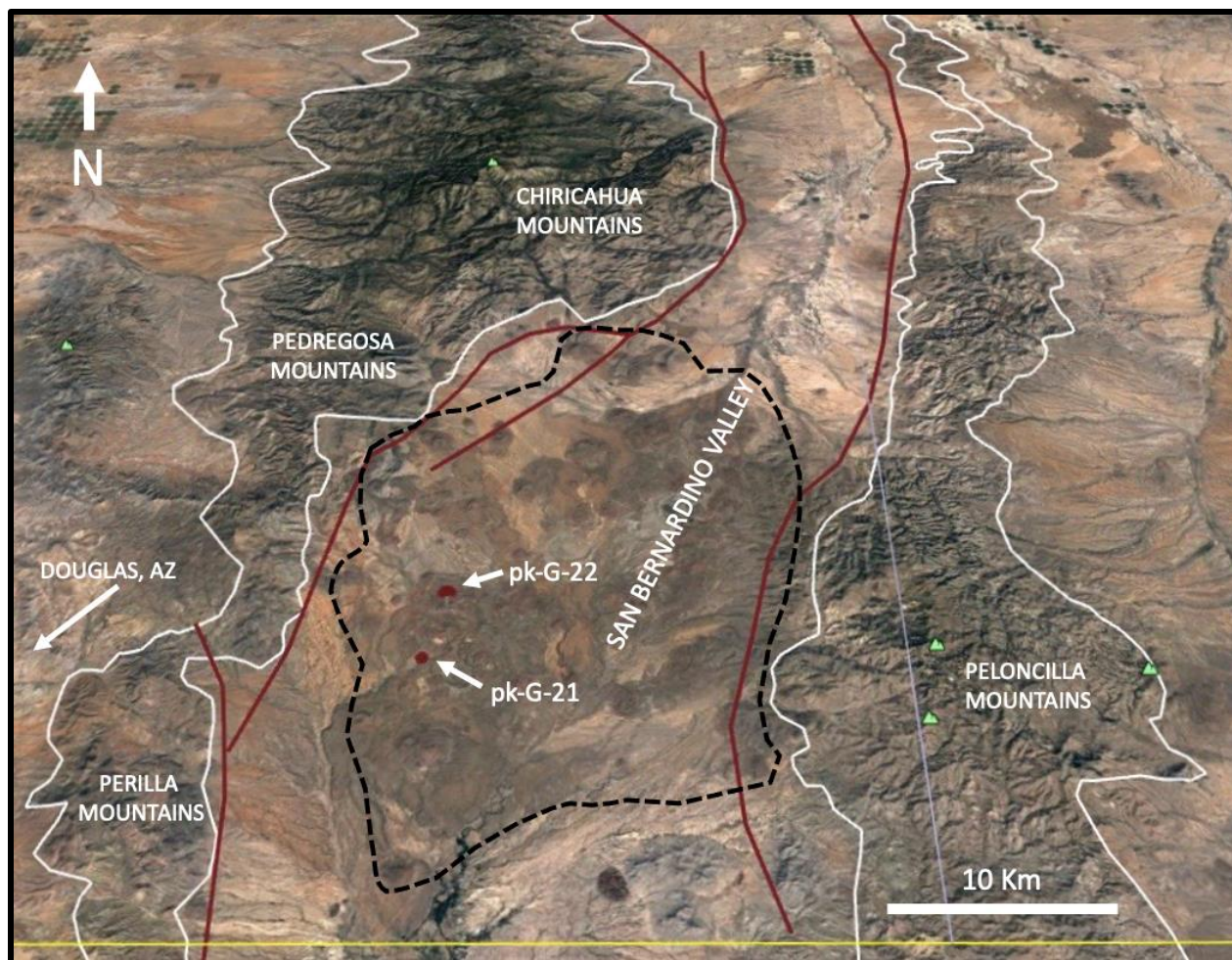


Figure 3.5. The Geronimo Volcanic Field locality.

The Geronimo Volcanic Field is located in southeastern Arizona, in the southern Basin and Range. Modified from Menzies et al. (1985) and Dickenson (2002).

### **3.2.1. The Xenolith Suite and Sample Selection**

The pilot geochronology project reported by Rader et al. (2017) used samples collected by P. Kempton as part of her PhD thesis, but prior research depleted much of the original material, which limited the scope of further study. Therefore, additional fieldwork was undertaken in June 2019 to collect new material for analysis. This yielded an extensive collection consisting of over 100 new samples. Xenoliths were collected from alkali basaltic cinder cones and air fall tuff deposits that crop out near localities pk-G-21 and pk-G-22 (Fig. 3.6), which are described in Kempton (1984) and Kempton et al. (1987). Samples for this project come from both the original and new collections. For clarity, sample names from the original sample set are prefixed with pk-G plus a sample identifier (e.g. pk-G-GN22-5), where GN refers to granulite xenoliths, 22 is the locality number (i.e. pk-G-22) and 5 is the sample number. Samples from the new collection follow a similar convention but are prefaced by MR, e.g. MR-GN22-35, where GN again refers to granulite xenolith, 22 is the locality number and 35 is the sample number.



**Figure 3.6. Oblique view of the San Bernardino Valley.**

The San Bernardino Valley is bounded on both sides by a series of mountain ranges. The Chiricahua, Pedregosa, and Perilla Mountains are outlined in white to the west, and the Peloncilla Mountains are visible to the east. N-NE normal faults are represented by red lines. Normal faults modified from Thorman and Drewes (1978); image modified from Google Earth (2019).

### **3.3. Analytical Methods**

#### **3.3.1. Petrography**

From a collection of ~100 granulite xenoliths, 36 samples were selected for petrographic analysis that represent the range of lithologies present in the GVF. Selected samples were cut into thin section billets at KSU using a diamond-tipped saw blade and shipped to Spectrum Petrographics for thin-section preparation. Petrographic analysis, using a Leica DM750P petrographic microscope, produced detailed descriptions of mineral relationships and textural features, including presence of zircon for U-Pb geochronology (see Appendix B for descriptions).

#### **3.3.2. Whole Rock Geochemistry**

Based on mineral composition and degree of alteration, sixteen samples were selected for whole rock major and trace element analysis. Samples were broken into smaller pieces using a RockLabs Hydraulic Press with tungsten splitting jaws. Weathering rinds were removed using a diamond-tipped saw blade. Cut surfaces were ground to remove saw marks, using 60-grit sandpaper on a grinding wheel. Samples were cleaned in deionized water, scrubbed using a toothbrush, and allowed to dry overnight. Once dry, samples were crushed into pea-sized pieces using the crushing plates on a RockLabs Hydraulic Press. Approximately 150-200 grams of each sample were shipped to Hamilton Analytical Laboratory for powdering using an alumina ring mill and whole rock analysis by XRF and LA-ICP-MS. Additionally, 14 sample powders from the original collection (Kempton et al., 1990) were reanalyzed by LA-ICP-MS, with two of these also being analyzed by XRF.

XRF analysis was completed using a Thermo ARL Perform'x, using 45 kV accelerating voltage at 45 mA. For most samples, 3.5 gm of sample were used to create 29 mm diameter disks. Each disk was analyzed for ~2 hours to measure 44 elements (majors and traces). At least one

internal standard was run with each sample batch, and at least one duplicate for every batch to ensure sample homogeneity and reproducibility of data. Ignition loss was measured for all samples by heating overnight in a silica crucible at 900°C (Johnson et al., 1999).

Samples for LA-ICP-MS analysis were ablated using a Photon Machines Analyte 193 (G1) ablation station (UV excimer laser, 193nm, with laminar flow frame cell), with a laser spot size of 150  $\mu\text{m}^2$  and 7 Hz repetition rate. Ablated material was carried to the ICP-MS using He gas, tied in with Ar make-up gas in a mixing volume (20ml), before entering the plasma torch. The ICP-MS is run in “peak-hopping, time-resolved mode” for 54 major and trace element analyses, with dwell times of 10 ms per mass (Conrey et al., 2019).

### **3.3.3. Mineral separation**

Zircons from eight samples (MR-GN21-34, MR-GN21-39, MR-GN21-53, MR-GN21-59, MR-GN22-27, MR-GN22-35, pk-G-GN22-3, and pk-G-GN22-5) were prepared for geochronology at the University of Kansas. Large hand samples were broken into smaller pieces using a hydraulic press. Crushed sample portions for whole rock geochemistry and geochronology were prepared separately from adjacent chunks of the same rock. Samples were crushed to create pea-sized fragments using a chipmunk jaw crusher. Pea-sized pieces were broken down further using a disk mill until the majority of the sample was <1 mm. Samples were then handwashed with tap water in a large plastic pitcher. Sediment was agitated and overturned by hand and allowed to settle for 30 seconds before decanting. Washing continued until the water was clear after resting 30 seconds. Handwashed sample was dried in an oven at ~60°C until dry. Each sample was sieved using 500-micron mesh. Approximately 250 grams of the <500-micron portion of each sample underwent density separation using methylene iodide (MeI) (s.g. 3.3 g/cm<sup>3</sup>). Magnetic minerals were then removed from the MeI heavies by first using a hand magnet then with a Frantz Magnetic

separator at 0.1, 0.3, 0.5, 0.7, and 1.0 Amps at 10° sideways and 10° forward tilt. Representative splits of the non-magnetic fraction from the 1.0-amp Frantz separation were produced using a microsplits. Intact zircon crystals were picked for optical clarity and lack of inclusions using a Leica binocular stereomicroscope. Approximately 150 zircons were chosen for each sample, with half being mounted on double-sided tape and the other half set into epoxy. Epoxy mounts were ground and polished to about 40-50% width to expose the interior of each grain.

### **3.3.4. Cathodoluminescence Imaging**

Polished epoxy mounts were imaged at the University of Nevada, Reno, using a JSM-7100FT FESEM equipped with a Deben panchromatic cathodoluminescence (CL) detector. CL images were analyzed to pinpoint the internal structures of zircon for U-Pb and Hf LA-ICP-MS (see Appendix E). Approximately 5-6 different internal zones were identified for each sample (see section 3.4.3), with spots placed in an attempt to target each identified zone at least 6 times for both U-Pb only analysis and U-Pb + trace analysis (explained further in LA-ICP-MS section below).

### **3.3.5. Zircon U-Pb LA ICP-MS**

U-Pb zircon geochronology and trace element analysis of seven samples (MR-GN21-34, MR-GN21-39, MR-GN21-53, MR-GN22-27, MR-GN22-35, pk-G-GN22-3, and pk-G-GN22-5) was conducted at the University of Kansas using a Thermo Scientific ELEMENT 2 high resolution sector-field ICP-MS coupled with a Teledyne/Photon Machines ANALYTE.G2 excimer laser with 193nm wavelength and 5ns pulse length. For epoxy mounts, CL images were used to place analyses to target core and rim structures. Approximately half the zircons for each sample were analyzed only for U-Pb ratios. The other half were analyzed for both U-Pb and trace elements within the same session. Samples from preliminary work (pk-G-GN22-3 and pk-G-GN22-5) were

analyzed by U-Pb analysis only. After 3 preablation pulses to clean the surface, zircon were analyzed using a 20  $\mu\text{m}$  spot with a laser fluency of 2.0 J/cm<sup>2</sup>, with 250 pulses at 10 Hz laser repetition rate, resulting in pits of  $\sim 15$   $\mu\text{m}$  depth. Due to the presence of thin outer rims, zircons for each sample were also analyzed in tape mounts to create an age profile of the outer most 15  $\mu\text{m}$ . For tape mounts (MR-GN21-34, MR-GN21-39, MR-GN21-53, MR-GN21-59, MR-GN22-27, MR-GN22-35, pk-G-GN22-3 and pk-G-GN22-5), the laser was centered on each zircon grain and focused at the surface. Zircons were analyzed using a 25  $\mu\text{m}$  spot. Ablated material was carried to the ICP-MS using He gas with a flow rate of 1.1 l/min, tied in with Ar gas with a flow rate of 1.1 l/min, before entering the plasma torch. Analysis was completed in ten sessions. Methods and run parameters for all sessions can be found in the Appendix F. Elemental fractionation, down-hole fractionation and calibration drift were corrected by bracketing measurements of unknowns with GJ1 zircon reference material (Jackson et al., 2004) and data reduction using the VisualAge data reduction scheme (Petrus and Kamber, 2012) for the IOLITE software package (Paton et al., 2010, 2011). Three secondary reference standards were used: Plešovice (PL) (Sláma et al., 2008), Fish Canyon Tuff (FCT) (e.g. Wotzlaw et al., 2013), and Duluth Gabbro (FCSZ) (Paces and Miller, 1993). Reference standards produced Concordia ages within 1-2% uncertainty of chemical abrasion thermal ionization mass spectrometry (CA-TIMS) analyses. Concordia ages for each reference standard from each session is listed below (Table 3.1).

Session	Date	Unknowns	Analysis	Method	GJ	PL	FCT	FCSZ
1	9/16/17	pk-G-GN22-3, pk-G-GN22-5, pk-G-GN22-10	Tape mount UPb (22-3, 22-5), Thin section 22-10	zirconcount PbnoU235_ June15	600.8 ± 1.2 (n=43; MSWD=1.1)	332.2 ± 0.93 (n=22; MSWD=0.58)	28.10 ± 0.20 (n=21; MSWD=1.1)	–
2	2/19/19	pk-G-GN22-3, pk-G-GN22-5	UPb	zirconcount PbnoU235_ June15	601.0 ± 0.9 (n=52; MSWD=0.92)	337.3 ± 0.86 (n=24; MSWD=1.1)	28.30 ± 0.26 (n=21; MSWD=2.9)	1106 ± 3 (n=20; MSWD=1.2)
3	2/21/19	pk-G-GN22-3	Tape mount UPb	zirconYoung_ Mar15	601.1 ± 0.9 (n=38; MSWD=0.87)	335.1 ± 0.83 (n=20; MSWD=0.64)	28.29 ± 0.20 (n=18; MSWD=1.6)	–
4	10/19/20	MR-GN21-34, MR-GN21-53	UPb	zirconcount PbnoU235_ June15	601.3 ± 0.9 (n=29; MSWD=0.70)	339.7 ± 1.2 (n=16; MSWD=1.3)	28.39 ± 0.32 (n=14; MSWD=1.5)	1113 ± 12 (n=17; MSWD=5.6)
5	10/19/20	MR-GN21-34, MR-GN21-53	UPb and Trc	UPbTraces_ Oct20	600.8 ± 2.1 (n=29; MSWD=0.98)	339.8 ± 1.8 (n=20; MSWD=1.2)	26.83 ± 2.53 (n=18; MSWD=8.8)	1121 ± 6 (n=20; MSWD=0.67)
6	11/3/20	MR-GN21-39	UPb	zirconcount PbnoU235_ June15	600.9 ± 1.0 (n=22; MSWD=0.96)	342.7 ± 2.1 (n=9; MSWD=1.8)	28.5 ± 0.5 (n=6; MSWD=1.9)	1120 ± 11 (n=12; MSWD=4.2)
7	11/6/20	MR-GN22-27, GN22-5	UPb	zirconcount PbnoU235_ June15	600.8 ± 0.8 (n=31; MSWD= 0.76)	343.5 ± 1.5 (n=14; MSWD=1.6)	28.8 ± 0.6 (n=10; MSWD=3.6)	1118 ± 7 (n=15; MSWD=2.5)
8	11/9/20	MR-GN22-35	UPb	zirconYoung_ Oct20	600.8 ± 1 (n=28; MSWD= 0.83)	339.5 ± 1.2 (n=15; MSWD=1.1)	28.1 ± 0.3 (n=13; MSWD=2)	1100 ± 3 (n=16; MSWD=0.59)
9	11/17/20	MR-GN21-34, MR-GN21-39, MR-GN21-53, MR-GN22-27, MR-GN22-35	Tape mount UPb	zirconYoung_ Oct20	600.8 ± 0.8 (n=45; MSWD=0.84)	338.8 ± 0.89 (n=16; MSWD=0.88)	28.0 ± 0.3 (n=15; MSWD=2.5)	1112 ± 3 (n=20; MSWD=1.1)
10	11/23/20	MR-GN21-39, MR-GN22-27, MR-GN22-35	UPb and Trc	zirconUPb_ Traces_ Nov20b	600.8 ± 1.7 (n=42; MSWD=1.1)	342.2 ± 1.6 (n=20; MSWD=1.1)	28.7 ± 0.6 (n=16; MSWD=2.1)	1100 ± 8 (n=19; MSWD=1.6)

**Table 3.1. Reference standards and methods.**

GJ reference material, and secondary reference standard Concordia ages for each ablation session. UPb analysis refer to U-Pb geochronology in epoxy mounts. UPb and Trace refers to simultaneous U-Pb geochronology and trace element analyses in epoxy mounts. Tape mount UPb refers to U-Pb geochronology only on tape mounted zircon. GJ1 (GJ), Plešovice (PL), Fish Canyon Tuff (FCT), and Duluth Gabbro (FCSZ). Red values indicate MSWD > 3.

### **3.3.6. Hf LA ICP-MS**

Hf isotope analyses of five samples (MR-GN21-34, MR-GN21-39, MR-GN21-53, MR-GN22-27, MR-GN22-35) were performed at the University of Florida using a Nu-Plasma 3D multi-collector inductively coupled plasma mass spectrometer (MC-ICP-MS) equipped with a NWR213 laser ablation system (<http://www.nwrlasers.com>). Laser ablation (LA) sites for Hf analyses were selected to be close to and within the same zones as the U-Pb analyses. During the Hf analyses, the sample was ablated in a He atmosphere (around 0.4 l/min flow) and the dry aerosol carried by the He gas was mixed with Ar gas (around 1 l/min) before introduction to the plasma. Both He and Ar gas flows were adjusted daily for maximum instrument performance. On-peak background measurements were performed for 20 seconds before each analysis with the laser off. Following blank measurement, each sample was ablated for 200 pulses at 5 Hz, 5% power, and 35 microns spot size. Isotopic measurements were made simultaneously in static mode on Faraday detectors. The analyses were performed with on-line Lu and Yb isobaric interference corrections, using  $^{176}\text{Lu}/^{175}\text{Lu} = 0.02653$  and  $^{176}\text{Yb}/^{172}\text{Yb} = 0.5870$ , following the method described in Mueller et al. (2008). Because of the low abundances of Yb, all isotopic ratios, including Lu and Yb, were corrected for mass bias using  $^{178}\text{Hf}/^{177}\text{Hf} = 1.46718$ . Average (n=20)  $^{176}\text{Hf}/^{177}\text{Hf} = 0.28217$  ( $\pm 0.00005$ , 2s.e.) for the FC-1 zircon standard ablated together with the unknown zircons is indistinguishable from solution and long-term LA analyses of this standard (Mueller et al., 2008).

### **3.3.7. Microprobe and Geothermometry**

Five samples selected for geochronology (MR-GN21-34, MR-GN21-39, MR-GN21-53, MR-GN22-27, MR-GN22-35) were also analyzed by electron microprobe (EMP) in the Department of Geological Sciences at the University of Colorado Boulder to calculate equilibrium temperatures and infer pre-entrainment residence depths (data presented in Appendix E). Thin

sections were coated with carbon and analyzed using a JEOL JXA-8230 equipped with LaB6 electron gun. Feldspars and pyroxenes were selected from backscatter electron images and confirmed quantitatively by energy dispersive x-ray spectroscopy before EMP analysis. Highly fractured grains and inclusions were avoided. Transects of 6-8 points were taken for each grain to determine compositional heterogeneity. Quantitative spot analyses of pyroxene and feldspar grains were conducted with an accelerating voltage of 15 keV, a 20nA beam current, and a 2  $\mu$ m beam diameter. Peak counting was 20 seconds for all elements. Standards consisted of Albite Amelia for Na  $k_{\alpha}$ , Cr-Diopside for Ca  $k_{\alpha}$ , Cr  $k_{\alpha}$ , Mg  $k_{\alpha}$ , Orthoclase for K  $k_{\alpha}$ , Pentlandite for Ni  $k_{\alpha}$ , Labradorite for Si  $k_{\alpha}$ , Al  $k_{\alpha}$ , Rhodonite for Mn  $k_{\alpha}$ , Rutile for Ti  $k_{\alpha}$ , and Johnstown Hypersthene for Fe  $k_{\alpha}$  from the CM Taylor Company and Astimex Standards Ltd. Peak intensity data were corrected for Time Dependent Intensity (TDI) loss (or gain) using a self-calibrated correction for Si  $k_{\alpha}$ , Fe  $k_{\alpha}$ , Ca  $k_{\alpha}$ , Cr  $k_{\alpha}$ , Na  $k_{\alpha}$ . The off-peak counting time was 20 seconds for all elements. The off-peak correction method was linear for all elements determined by wavelength dispersive spectroscopy. Unknown and standard peak intensities were corrected for detector deadtime. Oxygen was calculated by cation stoichiometry and included in the matrix correction. The matrix correction method was ZAF and the mass absorption coefficients dataset was FFAST Chantler (2005). The ZAF algorithm utilized was Armstrong (1988).

Pyroxenes (orthopyroxene and clinopyroxene) and feldspar (plagioclase and alkali feldspar) were analyzed from three samples (MR-GN21-34, MR-GN22-27, MR-GN22-35) in preparation for two-pyroxene and two-feldspar geothermometry. The remaining two samples (MR-GN21-39, MR-GN21-53) were analyzed for two-feldspar geothermometry only, due to the absence of two pyroxenes. Two samples (MR-GN21-34, MR-GN21-53) contained either perthite or antiperthite, and both plagioclase and potassium feldspar were analyzed.

Equilibrium temperatures were then calculated using methods developed by Putirka (2008). Areas with significant grain boundary melting were avoided. Therefore, crystals analyzed showed very little evidence for compositional heterogeneities, and transect data were averaged for each analyzed grain. For two-pyroxene geothermometry, since Mg#s for these samples were below 0.75, Equation 37 was used to calculate equilibration temperatures (Putirka, 2008; Fig. 3.7). Pre-entrapment residence depths were calculated assuming a geothermal gradient of 30 °C/km for the Basin and Range (Padovani and Carter, 1977). Pressures were calculated from depth, assuming 0.3 kbar/km. For two-feldspar geothermometry, alkali feldspar and plagioclase compositions were used in equation 27b to calculate equilibration temperatures (Putirka, 2008; Fig. 3.8). Since pressures could not be determined directly for these samples, they were inferred from two-pyroxene geothermometry.

$$\frac{10^4}{T(^{\circ}\text{C})} = 13.4 - 3.4 \ln \left( \frac{X_{EnFs}^{cpx}}{X_{EnFs}^{opx}} \right) + 5.59 \ln (X_{Mg}^{cpx}) - 8.8 (Mg\#^{cpx}) \\ + 23.85 (X_{Mn}^{opx}) + 6.48 (X_{FmAl_2SiO_6}^{opx}) - 2.38 (X_{Di}^{cpx}) - 0.044P(\text{kbar})$$

**Figure 3.7. Equations 37, used in two-pyroxene geothermometry (Putirka, 2008).**

$$T(^{\circ}\text{C}) = \frac{-442 - 3.72P(\text{kbar})}{-0.11 + 0.11 \ln \left( \frac{X_{Ab}^{afs}}{X_{Ab}^{pl}} \right) - 3.27 (X_{An}^{afs}) + 0.098 \ln (X_{An}^{afs}) + 0.52 (X_{An}^{plag} X_{Ab}^{pl})}$$

**Figure 3.8. Equations 27b, used in two-feldspar geothermometry (Putirka, 2008).**

## **3.4 Results**

### **3.4.1. Petrography and Geothermometry**

The sixteen samples analyzed in this study can be classified into five groups based on petrographic and geochemical data. The relationship of these groups to those originally identified by Kempton et al. (1990) is shown in Table 3.2. Detailed petrographic descriptions of individual samples can be found in Appendix B, but a brief overview of the major characteristics of each group is given in the text below. Petrography of individual samples is summarized in Table 3.3. Modal abundances are estimated. Samples range in size from ~9-40 cm, fine- to coarse-grained, with granuloblastic textures for all but the quartzofelspathic granulites, which are porphyroblastic.

Lithology	Sample Name	Analyses Discussed in this Thesis	Other Relevant Analyses	Nd-Model Ages (DM)
One-Pyroxene Metacumulates	MR-GN21-33	Petrography, whole rock XRF and LA-ICP-MS		
	MR-GN21-37	Petrography, whole rock XRF and LA-ICP-MS		
	MR-GN21-62	Petrography, whole rock XRF and LA-ICP-MS		
	pk-G-GN21-1	Petrography, whole rock XRF and LA-ICP-MS, Nd isotope analysis	$\delta^{18}\text{O}$ , Sr-Nd-Pb	1232 Ma
	pk-G-GN21-6	Petrography, whole rock XRF and LA-ICP-MS, Nd isotope analysis	$\delta^{18}\text{O}$ , Sr-Nd-Pb	1765 Ma
	pk-G-GN21-8	Petrography, whole rock XRF and LA-ICP-MS	$\delta^{18}\text{O}$	
	pk-G-GN21-9	Petrography, whole rock XRF and LA-ICP-MS, Nd isotope analysis	$\delta^{18}\text{O}$ , Sr-Nd-Pb	537 Ma
Olivine Meta-Gabbronorites	MR-GN21-9	Petrography, whole rock XRF and LA-ICP-MS		
	MR-GN21-56	Petrography, whole rock XRF and LA-ICP-MS		
Two-pyroxene Metacumulates	MR-GN21-7	Petrography, whole rock XRF and LA-ICP-MS		
	MR-GN21-59	Petrography, whole rock XRF and LA-ICP-MS, U-Pb geochronology of 1 zircon		
	pk-G-GN21-3	Petrography, whole rock XRF and LA-ICP-MS	$\delta^{18}\text{O}$	
	pk-G-GN21-4	Petrography, whole rock XRF and LA-ICP-MS, Nd isotope analysis	$\delta^{18}\text{O}$ , Sr-Nd-Pb	1078 Ma
	pk-G-GN21-5	Petrography, whole rock XRF and LA-ICP-MS, Nd isotope analysis	$\delta^{18}\text{O}$ , Sr-Nd-Pb	849 Ma
Metadiorite + Biotite	MR-GN22-25	Petrography, whole rock XRF and LA-ICP-MS		
	MR-GN22-36	Petrography, whole rock XRF and LA-ICP-MS		
Metadiorites	MR-GN21-34	Petrography, whole rock XRF and LA-ICP-MS, U-Pb geochronology and trace element analyses, and Hf-isotope analyses		
	MR-GN21-35	Petrography, whole rock XRF and LA-ICP-MS		
	MR-GN22-27	Petrography, whole rock XRF and LA-ICP-MS, U-Pb geochronology and trace element analyses, and Hf-isotope analyses		
	MR-GN22-35	Petrography, whole rock XRF and LA-ICP-MS, U-Pb geochronology and trace element analyses, and Hf-isotope analyses		
	pk-G-GN21-2	Petrography, whole rock XRF and LA-ICP-MS, Nd isotope analysis	$\delta^{18}\text{O}$ , Sr-Nd-Pb	1430 Ma
	pk-G-GN21-10	Petrography, whole rock XRF and LA-ICP-MS, Nd isotope analysis	$\delta^{18}\text{O}$ , Sr-Nd-Pb	1368 Ma
	pk-G-GN22-2	Petrography, whole rock XRF and LA-ICP-MS, Nd isotope analysis	$\delta^{18}\text{O}$ , Sr-Nd-Pb	1230 Ma
	pk-G-GN22-3	Petrography, whole rock XRF and LA-ICP-MS, U-Pb geochronology, and Nd isotope analysis	$\delta^{18}\text{O}$ , Sr-Nd-Pb	1173 Ma
Quartzofeldspathic	MR-GN21-16	Petrography, whole rock XRF and LA-ICP-MS		
	MR-GN21-39	Petrography, whole rock XRF and LA-ICP-MS, U-Pb geochronology and trace element analyses, and Hf-isotope analyses		
	MR-GN21-53	Petrography, whole rock XRF and LA-ICP-MS, U-Pb geochronology and trace element analyses, and Hf-isotope analyses		
	pk-G-GN22-5	Petrography, whole rock XRF and LA-ICP-MS, U-Pb geochronology, and Nd isotope analysis	$\delta^{18}\text{O}$ , Sr-Nd-Pb	2174 Ma

**Table 3.2. Summary of all samples and analyses completed and used in this study.**

MR-GN samples represent the new sample base, while pk-G-GN samples were part of the original sample suite analyzed by Kempton et al., 1990.

Modal Proportions as %													
Sample	Plg	Kspar	Qtz	Cpx	Opx	Ox	Sp	OI	Zircon	Apatite	Bt	Melt	Partial Melting
<b>One-Pyroxene Metacumulate</b>													
MR-GN21-33	80			20		x			no	no		~35%	patches of dark cryptocrystalline quench and secondary microcrystalline, euhedral, tabular plagioclase and opaques
MR-GN21-37	50			43		x	trace	7 secondary	no	no		~35%	patches of glass and secondary fine grained euhedral, tabular to acicular plagioclase, skeletal olivine (7%), and opaques
MR-GN21-62	40			60		x		secondary	no	trace		~25%	patches of dark mesostasis and secondary anhedral olivine, and opaques. Olivine rims are significantly altered, with a dark brown fuzzy cryptocrystalline quench
<b>Olivine Meta-Gabbronorite</b>													
MR-GN21-9	60			20	10	x		10	no	no		<10%	melting restricted to glass along grain boundaries and minimal involvement of primary pyroxenes and olivine
MR-GN21-56	50			25	10?	x	trace	15 +secondary	no	no		>50%	patches of glass and secondary euhedral, tabular plagioclase, skeletal olivine, and opaques
<b>Two-Pyroxene Metacumulate</b>													
MR-GN21-7	15			30	55	x	trace		no	no		~15%	patches of glass and secondary acicular plagioclase, cryptocrystalline quench, oxides, and a reddish-brown to honey colored mystery mineral with 60/120° cross hatching pattern
MR-GN21-59	80			15	5	x		secondary	no	no		~25%	patches of dark mesostasis and secondary euhedral iddingsitized olivine, fine to medium grain, euhedral, tabular plagioclase, and opaques
<b>Metadiorite + Biotite</b>													
MR-GN22-25	55	10		20	10	x			trace	trace	5	~10%	patches of brown cryptocrystalline quench and secondary opaques found near biotite, likely a result of dehydration melting
MR-GN22-36	40	20		20	15	x			no	no	5	~40%	patches of brown cryptocrystalline quench, secondary acicular pyroxenes, and opaques found near biotite. Biotite records partial breakdown reaction to opaques + melt/fluids.
<b>Metadiorite</b>													
MR-GN21-34	40	25	10	10	10	x			trace	trace		~15%	with melting restricted to brown glass along grain boundaries and secondary opaques, minimal involvement of primary pyroxenes/feldspars
MR-GN21-35	50	20	5	15	10	x			trace	trace		~20%	melting restricted to brown glass along grain boundaries and secondary opaques, minimal involvement of primary pyroxenes/feldspars
MR-GN22-27	50	15	10	15	10	x			trace	trace		~50%	patches of dark cryptocrystalline quench and secondary acicular pyroxene, fine grained, euhedral, tabular plagioclase, and opaques
MR-GN22-35	70	5		15	10	x			trace	trace		<10%	melting restricted to glass and cryptocrystalline quench along grain boundaries and minimal involvement of primary pyroxenes/feldspars
<b>Quartzofeldspathic Granulites</b>													
MR-GN21-16	20	50	30		<1	x			trace	no		<10%	melting restricted to glass or cryptocrystalline quench products common along grain boundaries.
MR-GN21-39	30	25	40		<2	x			trace	no		<10%	melting restricted to brown and colorless glass along grain boundaries and opaques, minimal involvement of primary pyroxenes/feldspars
MR-GN21-53	35	25	35		5	x			trace	trace		<10%	melting restricted to brown and colorless glass along grain boundaries and opaques, minimal involvement of primary pyroxenes/feldspars

**Table 3.3. Summary of petrography for new samples.**

Petrography for pk-G samples provided in Kempton et al. (1990). Partial melting refers to a mix of glass and cryptocrystalline matrix/quench, as described in the last column.

**One-pyroxene metacumulates** (MR-GN21-33, MR-GN21-37, MR-GN21-62) contain plagioclase + clinopyroxene ± secondary olivine + opaques + spinel ± apatite. Plagioclase and clinopyroxene are present in approximately equal proportions but modal proportions range from 40-80% plagioclase to 20-60% cpx, with minor amounts of opaque minerals, aluminous spinel, and apatite. Partial melting affects 25-35% of the samples and consists of patches of brown glass, dark mesostasis/cryptocrystalline quench material and secondary crystal growth of plagioclase, olivine, and opaque minerals, in some samples. Secondary crystal growth ranges from euhedral to skeletal crystals within the patches of brown glass and dark mesostasis to zoning adjacent to melt patches, reaction rims, and spongy textures in the primary mineral phases. These rocks are moderately to strongly foliated, with pyroxenes and opaques defining the foliation. Primary textures indicate metamorphic equilibration.

**Olivine meta-gabbronorites** (MR-GN21-9, MR-GN21-56) contain plagioclase + clinopyroxene + orthopyroxene + primary olivine + opaques ± spinel. Plagioclase is dominant (>50%), followed by clinopyroxene (20-25%), olivine (10-15%), and orthopyroxene (10%). Clinopyroxene is found throughout, but orthopyroxene is limited to one part or layer of the rock. Orthopyroxene is enclosed in necklaces of secondary olivine. Primary olivine is anhedral and highly iddingsitized. Opaques are present in trace amounts. Partial melting is minimal (<10%) to extensive (>50%), with patches of glass along grain boundaries. Where melting is more extensive, melt has crystallized to form secondary euhedral, tabular plagioclase, skeletal olivine, and opaques. Primary mineral phases exhibit zoning adjacent to melt patches and spongy textures. The rocks are nonfoliated to weakly foliated. Pyroxenes and opaques help to define foliation, where present. Primary minerals have 120-degree triple junctions, indicating metamorphic equilibration.

**Two-pyroxene metacumulates** (MR-GN21-7, MR-GN21-59) contain plagioclase + clinopyroxene + orthopyroxene ± secondary olivine + opaques ± spinel. Model proportions of plagioclase and pyroxene vary widely from 80/20% plag/pyx to 15/75% plag/pyx. Pyroxenes also vary in relationship to one another, with the plagioclase-rich sample having greater amounts of clinopyroxene and the plagioclase-poor sample having greater amounts of orthopyroxene. Opaques are present in trace amounts. Both rocks have undergone a small degree of partial melting (15-25%) with patches of dark mesostasis, cryptocrystalline quench material and secondary plagioclase, opaques, and olivine in one sample. Primary mineral phases exhibit zoning adjacent to melt patches, reaction rims, and spongy textures. These rocks lack foliation.

**Metadiorites** (MR-GN21-34, MR-GN21-35, MR-GN22-27, MR-GN22-35, w/biotite MR-GN22-25, MR-GN22-36) contain plagioclase + clinopyroxene + orthopyroxene + K-feldspar ± quartz + opaques ± biotite ± zircon ± apatite. Plagioclase is the predominant phase (>40%), with K-feldspar, orthopyroxene, and clinopyroxene present in relatively equal proportions. Quartz is present in three of the six metadiorites. Opaques, apatite, and zircon are present in trace amounts, with the exception of MR-GN22-36, which lacks zircon and apatite. Biotite is present in two samples, with varying degrees of alteration and partial dehydration melting. Partial melting affects all samples to some degree, with patches of dark cryptocrystalline quench material ± secondary acicular pyroxene; fine grained, euhedral, tabular plagioclase; and/or opaques. Primary mineral phases exhibit spongy textures and/or zoning adjacent to melt patches. Partial melting in MR-GN22-35 is minor and restricted to glass and cryptocrystalline quench along grain boundaries and minimal involvement of primary pyroxenes/feldspars.

**Quartzofeldspathic granulites** (MR-GN21-16, MR-GN21-39, MR-GN21-53) contain plagioclase + K-feldspar + quartz + orthopyroxene + opaques + zircon ± apatite. Plagioclase, K-

feldspar, and quartz make up the majority of these rocks, with minor amounts of orthopyroxene, opaques, and trace zircon. Feldspars are dominant, while quartz represents 30-40% of the samples. Textures indicate metamorphic equilibration. Partial melting is minor, with melting restricted to brown and colorless glass along grain boundaries and opaques, minimal involvement of primary pyroxenes/feldspars. Primary pyroxenes and feldspars exhibit reaction rims adjacent the brown glass. Samples are weakly to strongly foliated, with pyroxenes and opaques helping to define a foliation.

Due to the absence of garnet in GVF xenoliths, equilibration pressures could not be directly estimated. Instead, two-feldspar and two-pyroxene geothermometry methods were used to calculate temperatures of equilibration with pressures estimated by referring to the proposed geothermal gradient for the region. Where available, two-pyroxene methods are preferred, because temperature calculations were made independent of pressure. Calculated equilibration temperatures range from ~830-987°C (Table 3.4). Assuming a geothermal gradient of 30°C/km for the Basin and Range (Padovani and Carter, 1977), pre-entrainment residence depths are ~28-33 km, which corresponds with the base of the seismically determined lower crust in this region (Klemperer et al., 1986).

Geothermometry 2-Pyroxene Methods (Putirka, 2008)				
Sample	Rock Type	Temperature (°C)	Pressure (kbar)	Depth (km)
MR-GN21-34	Metadiorite	914.3	9.1	30.5
MR-GN22-27	Metadiorite	907.7	9.1	30.3
MR-GN22-35	Metadiorite	976.1	9.8	32.5
<i>pk-G-GN21-2</i>	<i>Metadiorite</i>	<i>857.9</i>	<i>8.6</i>	<i>28.6</i>
<i>pk-G-GN22-1</i>	<i>Metadiorite</i>	<i>968.8</i>	<i>9.7</i>	<i>32.3</i>
<i>pk-G-GN22-7</i>	<i>Metadiorite</i>	<i>962.2</i>	<i>9.6</i>	<i>32.1</i>
<i>pk-G-GN11-1</i>	<i>2-Pyx meta-cumulate</i>	<i>959.1</i>	<i>9.6</i>	<i>32.0</i>
<i>pk-G-GN21-4</i>	<i>2-Pyx meta-cumulate</i>	<i>987.4</i>	<i>9.9</i>	<i>32.9</i>

Geothermometry 2-Feldspar Methods (Putirka, 2008)				
Sample	Rock Type	Temperature (°C)	Pressure (kbar)	Depth (km)
MR-GN21-34	Metadiorite	830.7-843.4	8.3	27.7-28.1
MR-GN22-27	Metadiorite	893.7	8.9	29.8
MR-GN22-35	Metadiorite	898.2	9.0	29.9
MR-GN21-39	Quartzofeldspathic	889.0	8.9	29.6
MR-GN21-53	Quartzofeldspathic	901.9-918.7	9.0	30.1-30.6

**Table 3.4. Summary of geothermometry calculations.**

Normal font are new analyses collected in this study. Italic font are analyses completed by Kempton et al. 1990, recalculated using methods from Putirka, 2008.

### 3.4.2. Whole Rock Geochemistry

Major and trace element compositions for the sixteen newly collected GVF granulites are reported in Table 3.5. Compositions range from mafic to felsic (42-75 wt% SiO<sub>2</sub>, Mg-values of 23-76), with the most evolved compositions represented by four quartzofeldspathic granulites. Quartzofeldspathic granulite and most metadiorite xenoliths are quartz normative (Normative data in Appendix C). Metadiorite-type xenoliths containing biotite are hypersthene and olivine normative, having lower SiO<sub>2</sub> and higher MgO and Fe<sub>2</sub>O<sub>3</sub>. The most mafic lithologies are among the one pyroxene metacumulates.

The major element compositions, and variations among the lithologic groups, can be summarized in a plot of Mg# vs  $\text{SiO}_2/\text{Al}_2\text{O}_3$  (Fig. 3.9). The GVF samples are shown relative to the global compositional groups for lower crustal granulites identified empirically by Kempton and Harmon (1992). These authors identified three distinct mafic groups, an intermediate group and a silicic (i.e. felsic) group. The GVF quartzofelspathic xenoliths overlap the silicic group, having the highest wt%  $\text{SiO}_2$  concentrations and lowest Mg#s within the suite. Metadiorites are intermediate in composition, having  $\text{SiO}_2/\text{Al}_2\text{O}_3$  ratios that overlap those of representative basaltic magmas, but lower Mg#s. Of all the granulite xenolith groups from GVF, the metadiorites show the least compositional variation in major element composition, with most clustering on the Mg# vs  $\text{SiO}_2/\text{Al}_2\text{O}_3$  diagram near the top of the intermediate granulite compositional field. The exception is one biotite-bearing metadiorite, which has a higher Mg# compared to the other anhydrous metadiorites and plots within the primitive basalt field. One- and two-pyroxene metacumulates and metagabbro xenoliths have varied major element compositions that spread across the three mafic granulite groups identified by Kempton and Harmon (1992), indicating accumulation of pyroxene and plagioclase, consistent with the cumulate nature of these lithologies.

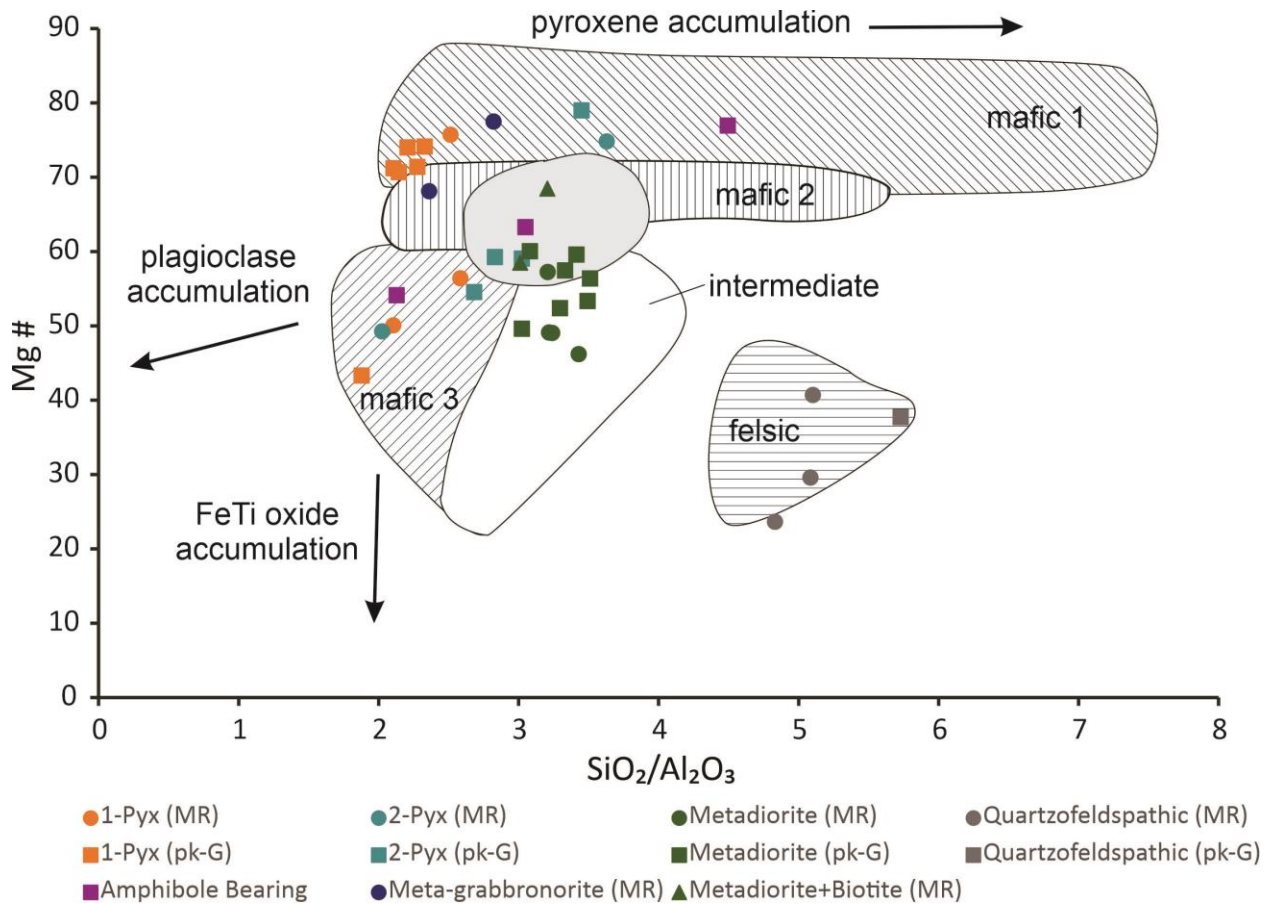


**Figure 3.9. Whole rock Mg# vs. SiO<sub>2</sub>/Al<sub>2</sub>O<sub>3</sub>.**

Plotted data are anhydrous. Data for both new (MR-GN) and old (pk-G) data sets are plotted.

Fields were defined by Kempton and Harmon (1992). Amphibole bearing samples were part of the original sample set (Kempton et al., 1990).

Sample ID	MR-GN21-33	MR-GN21-37	MR-GN21-62	MR-GN21-9	MR-GN21-56	MR-GN21-7	MR-GN21-59	MR-GN22-25	MR-GN22-36
Rock Type	One-pyx metacumulate			Meta-Gabbonorite		Two-pyx metacumulate		Metadiorite + biotite	
<b>Major Elements (wt%)</b>									
SiO <sub>2</sub>	53.08	49.40	42.30	50.22	51.02	47.52	51.16	54.39	52.41
TiO <sub>2</sub>	0.39	0.64	1.89	0.45	0.48	0.35	0.98	0.92	0.63
Al <sub>2</sub> O <sub>3</sub>	25.24	19.67	16.37	17.81	21.62	13.09	25.27	18.06	16.35
FeO*	2.75	4.86	9.73	5.85	5.46	11.74	3.95	7.08	7.65
MnO	0.04	0.10	0.14	0.12	0.09	0.18	0.03	0.12	0.14
MgO	1.32	7.24	6.01	9.61	5.57	16.63	1.83	4.76	7.92
CaO	10.72	14.41	19.92	11.72	10.62	7.61	11.38	7.96	10.47
Na <sub>2</sub> O	4.76	2.65	1.24	2.72	3.73	1.38	4.29	4.36	2.98
K <sub>2</sub> O	0.46	0.12	0.08	0.17	0.48	0.18	0.31	1.28	0.79
P <sub>2</sub> O <sub>5</sub>	0.11	0.09	0.68	0.12	0.20	0.09	0.04	0.24	0.10
Total	98.87	99.18	98.37	98.79	99.27	98.77	99.24	99.17	99.42
LOI	0.76	0.48	0.67	0.86	0.59	0.26	0.29	0.28	0.02
Mg#	50.10	75.75	56.43	77.50	68.15	74.82	49.28	58.51	68.47
<b>REE and Trace Elements (ppm)</b>									
Rb	2.0	0.4	0.6	0.7	2.4	1.0	0.6	6.7	3.8
Sr	1366	882	766	470	1456	471	1322	627	873
Y	5	11	24	9	7	7	2	21	17
Zr	16	21	96	13	40	21	3	85	68
V	43	178	182	148	88	70	112	153	151
Ni	16	53	52	242	82	347	22	52	152
Cr	8	104	24	100	22	25	11	73	149
Nb	1.3	0.2	1.9	0.9	7.8	0.6	0.7	6.3	2.5
Ga	20.0	16.0	17.6	12.3	14.5	12.4	19.9	20.5	16.9
Cu	20	5	35	42	29	21	18	9	17
Zn	63	81	73	41	79	128	59	83	74
Co	--	--	--	--	--	--	--	--	--
Ba	369	102	129	117	327	131	203	516	341
U	0.0	0.0	0.1	0.0	0.1	0.1	0.0	0.1	0.2
Th	0.2	0.0	0.2	0.1	0.5	0.2	0.0	0.1	0.5
Sc	6.2	28.6	21.3	26.5	12.8	15.7	6.6	17.8	27.0
Pb	3.1	0.3	0.9	0.9	0.9	1.4	0.8	7.9	3.8
Hf	0.48	0.92	2.89	0.49	1.05	0.62	0.13	2.26	2.15
Ta	0.15	0.07	0.41	0.28	0.46	0.25	0.10	0.59	0.37
Cs	0.02	0.01	0.01	0.01	0.01	0.02	0.01	0.04	0.05
La	6.05	2.11	14.77	3.58	11.54	3.54	1.07	19.16	11.22
Ce	10.18	5.30	40.14	5.89	19.24	7.73	1.79	40.21	25.87
Pr	1.11	0.90	6.08	0.87	2.12	1.16	0.24	5.02	3.65
Nd	4.59	5.19	28.71	4.30	8.52	5.42	1.23	20.94	16.67
Sm	1.01	1.77	6.43	1.24	1.72	1.40	0.32	4.60	3.91
Eu	0.87	0.80	1.83	0.67	1.06	0.55	0.46	1.34	1.10
Gd	0.92	2.18	5.81	1.61	1.67	1.46	0.39	4.10	3.76
Tb	0.16	0.36	0.86	0.27	0.26	0.23	0.06	0.63	0.56
Dy	0.92	2.11	4.64	1.65	1.49	1.38	0.32	3.77	3.21
Ho	0.18	0.39	0.87	0.33	0.28	0.28	0.06	0.74	0.65
Er	0.51	1.10	2.32	0.91	0.77	0.79	0.18	2.05	1.73
Tm	0.07	0.14	0.33	0.12	0.10	0.11	0.02	0.32	0.24
Yb	0.44	0.85	1.95	0.76	0.65	0.74	0.14	2.00	1.60
Lu	0.07	0.12	0.28	0.11	0.09	0.12	0.02	0.31	0.24

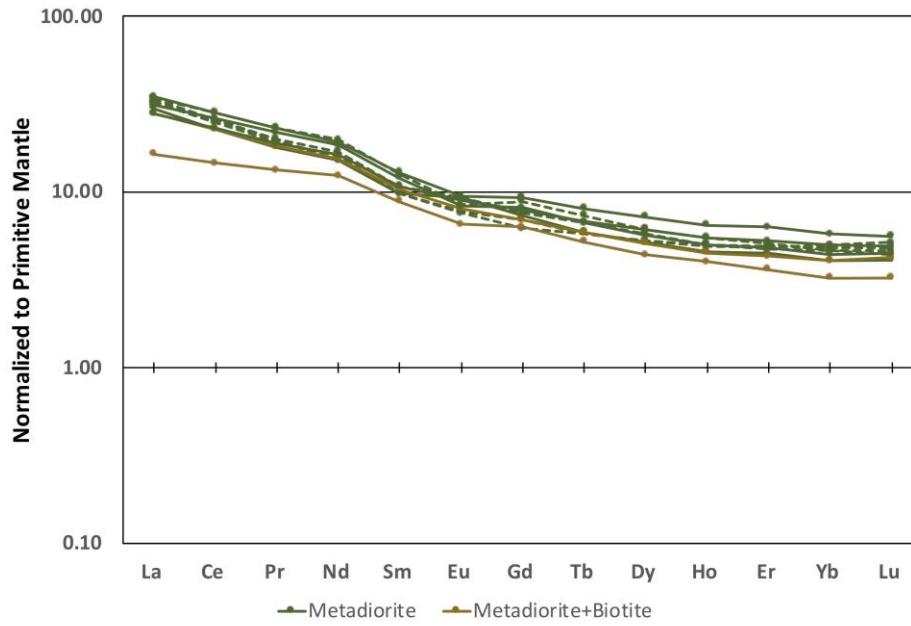
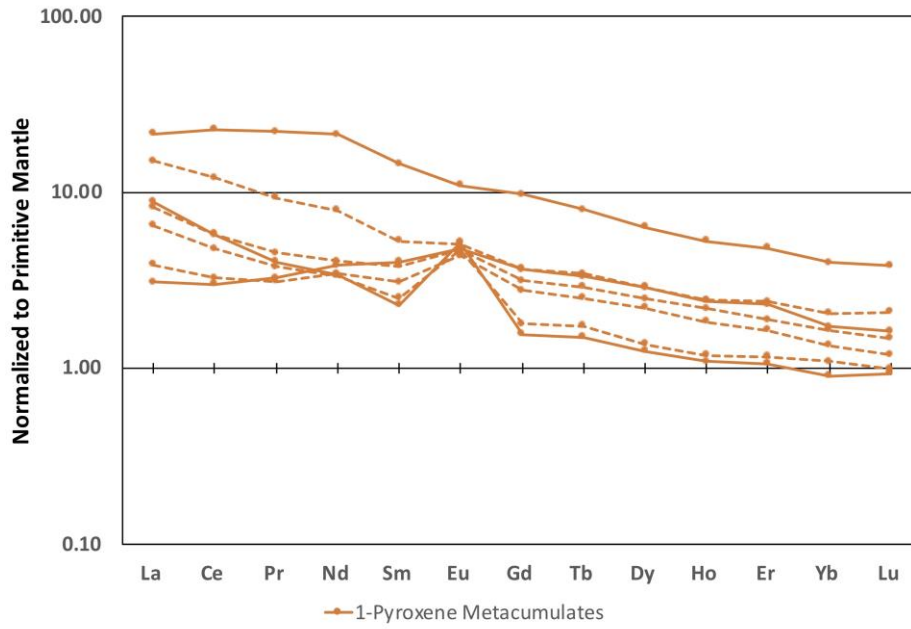
Sample ID	MR-GN21-34	MR-GN21-35	MR-GN22-27	MR-GN22-35	MR-GN21-16	MR-GN21-39	MR-GN21-53
Rock Type	Metadiorite				Quartzo-feldspathic		
<b>Major Elements (wt%)</b>							
SiO <sub>2</sub>	59.96	57.34	57.84	56.03	72.21	74.61	72.01
TiO <sub>2</sub>	0.85	0.96	0.91	0.91	0.08	0.06	0.32
Al <sub>2</sub> O <sub>3</sub>	17.49	17.83	17.86	17.47	14.95	14.68	14.12
FeO*	5.77	6.64	6.42	6.80	0.89	0.58	2.24
MnO	0.12	0.13	0.12	0.11	0.07	0.02	0.03
MgO	2.36	3.06	2.95	4.35	0.13	0.12	0.73
CaO	5.60	6.38	6.03	7.11	1.46	3.12	2.48
Na <sub>2</sub> O	3.78	3.90	3.77	3.93	3.96	4.65	3.43
K <sub>2</sub> O	2.49	1.95	2.00	2.03	4.26	1.05	3.30
P <sub>2</sub> O <sub>5</sub>	0.26	0.24	0.20	0.23	0.03	0.01	0.06
Total	98.67	98.43	98.09	98.98	98.05	98.88	98.73
LOI	0.53	0.63	0.96	0.41	1.10	0.51	0.50
Mg#	46.21	49.12	49.07	57.28	23.67	29.61	40.74
<b>REE and Trace Elements (ppm)</b>							
Rb	42.7	33.4	33.2	22.7	<i>106.1</i>	<i>16.0</i>	<i>54.0</i>
Sr	507	537	533	572	<i>182</i>	<i>436</i>	<i>406</i>
Y	22	30	25	23	<i>17</i>	<i>1</i>	<i>6</i>
Zr	171	177	197	156	<i>79</i>	<i>35</i>	<i>113</i>
V	117	156	124	147	<i>5</i>	<i>8</i>	<i>32</i>
Ni	7	10	10	46	<i>10</i>	<i>4</i>	<i>10</i>
Cr	4	3	5	95	<i>2</i>	<i>3</i>	<i>13</i>
Nb	7.7	9.6	8.5	7.0	<i>1.6</i>	<i>1.0</i>	<i>3.2</i>
Ga	18.8	20.1	19.1	22.4	<i>16.8</i>	<i>17.2</i>	<i>15.2</i>
Cu	7	6	12	7	<i>6</i>	<i>5</i>	<i>10</i>
Zn	114	121	80	91	<i>69</i>	<i>69</i>	<i>80</i>
Co	--	--	--	--	<i>--</i>	<i>--</i>	<i>--</i>
Ba	1204	713	916	636	<i>653</i>	<i>160</i>	<i>1074</i>
U	0.2	0.1	0.1	0.1	<i>0.3</i>	<i>0.2</i>	<i>0.1</i>
Th	0.6	0.2	0.1	0.1	<i>0.6</i>	<i>0.2</i>	<i>0.2</i>
Sc	12.5	17.4	14.6	16.8	<i>3.3</i>	<i>0.8</i>	<i>4.3</i>
Pb	11.7	10.7	10.3	9.6	<i>41.4</i>	<i>25.1</i>	<i>22.2</i>
Hf	4.07	4.57	4.86	4.01	<i>2.48</i>	<i>1.14</i>	<i>3.37</i>
Ta	0.51	0.65	0.53	0.55	<i>0.07</i>	<i>0.07</i>	<i>0.13</i>
Cs	0.09	0.03	0.02	0.02	<i>0.04</i>	<i>0.08</i>	<i>0.02</i>
La	20.39	23.92	19.08	21.41	<i>4.84</i>	<i>4.02</i>	<i>12.71</i>
Ce	40.39	49.75	40.66	46.10	<i>10.19</i>	<i>9.25</i>	<i>21.81</i>
Pr	4.94	6.30	5.16	5.98	<i>1.23</i>	<i>0.84</i>	<i>2.23</i>
Nd	20.43	25.92	21.99	24.89	<i>5.08</i>	<i>3.11</i>	<i>7.92</i>
Sm	4.37	5.71	4.77	5.35	<i>1.20</i>	<i>0.47</i>	<i>1.35</i>
Eu	1.56	1.57	1.50	1.39	<i>0.63</i>	<i>0.67</i>	<i>1.03</i>
Gd	4.35	5.55	4.68	4.85	<i>1.18</i>	<i>0.26</i>	<i>1.22</i>
Tb	0.64	0.87	0.73	0.71	<i>0.22</i>	<i>0.04</i>	<i>0.18</i>
Dy	3.78	5.31	4.53	4.20	<i>1.84</i>	<i>0.23</i>	<i>1.09</i>
Ho	0.75	1.06	0.90	0.82	<i>0.64</i>	<i>0.06</i>	<i>0.23</i>
Er	2.14	3.03	2.51	2.31	<i>2.96</i>	<i>0.21</i>	<i>0.67</i>
Tm	0.32	0.44	0.38	0.35	<i>0.59</i>	<i>0.04</i>	<i>0.09</i>
Yb	2.00	2.82	2.44	2.17	<i>4.79</i>	<i>0.33</i>	<i>0.58</i>
Lu	0.30	0.41	0.36	0.33	<i>0.90</i>	<i>0.06</i>	<i>0.10</i>

**Table 3.5. Whole rock major and trace elements.**

Whole rock major and trace elements. Non-italicized data was collected by XRF. Italicized data was collected via LA-ICP-MS.

Similar to the samples analyzed by Kempton et al. (1990), GVF granulites from this study are enriched in light rare earth elements (LREEs) compared to heavy rare earth elements (HREEs) (Fig. 3.10), with the exception of two quartzofeldspathic granulite samples (MR-GN21-16, MR-GN21-39) that show an unusual enrichment in the HREE relative to the MREE (Fig. 3.10d). Three of the four quartzofeldspathic xenoliths show a strong positive Eu anomaly, whereas pk-G-GN22-5 shows an equally strong negative Eu anomaly. The latter sample is also distinctive in its higher REE concentrations overall. In contrast, metadiorite xenoliths (Fig. 3.10a) have relatively smooth, uniform patterns, with one biotite-bearing metadiorite (MR-GN22-36) being slightly less LREE enriched relative to the rest. REE for metadiorites fall within a very narrow range compared to all other groups, but especially when compared with the wide range in the quartzofeldspathic granulites.

One- and two-pyroxene metacumulates and olivine meta-gabbroites (Figs. 3.10b and c) tend to have lower REE abundances compared to metadiorite samples, although most are enriched in LREE relative to HREE. The majority of these samples have positive Eu anomalies, with the exception of the most mafic granulites (i.e. lowest SiO<sub>2</sub> and lowest plagioclase/pyroxene ratios), suggesting that REE patterns are strongly affected by the relative proportions of plagioclase to clinopyroxene and orthopyroxene.

**a****Metadiorites & Metadiorite + Biotite****b****1-Pyroxene Metacumulates**

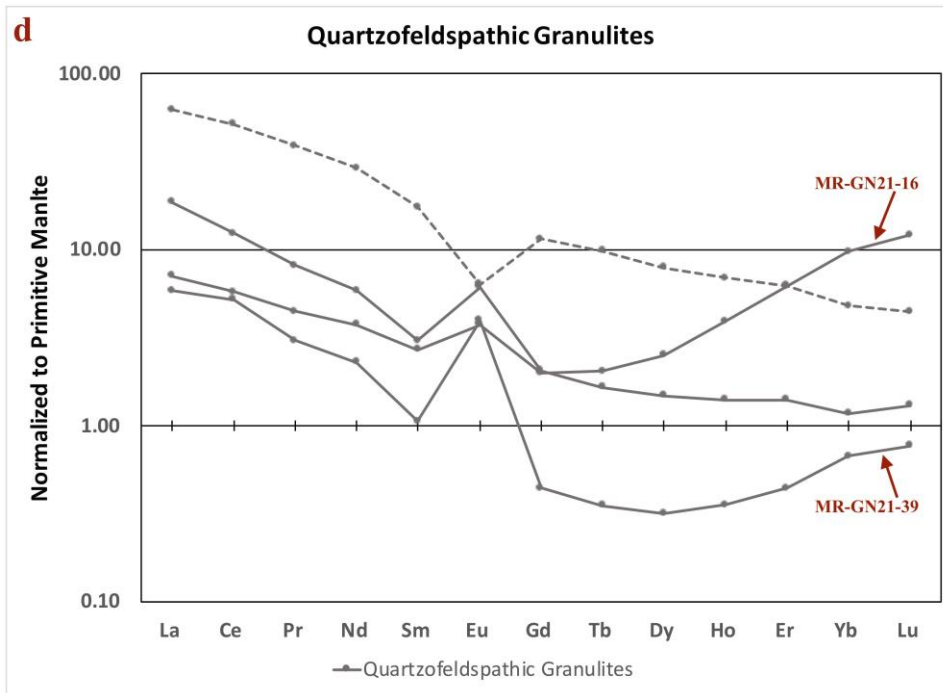
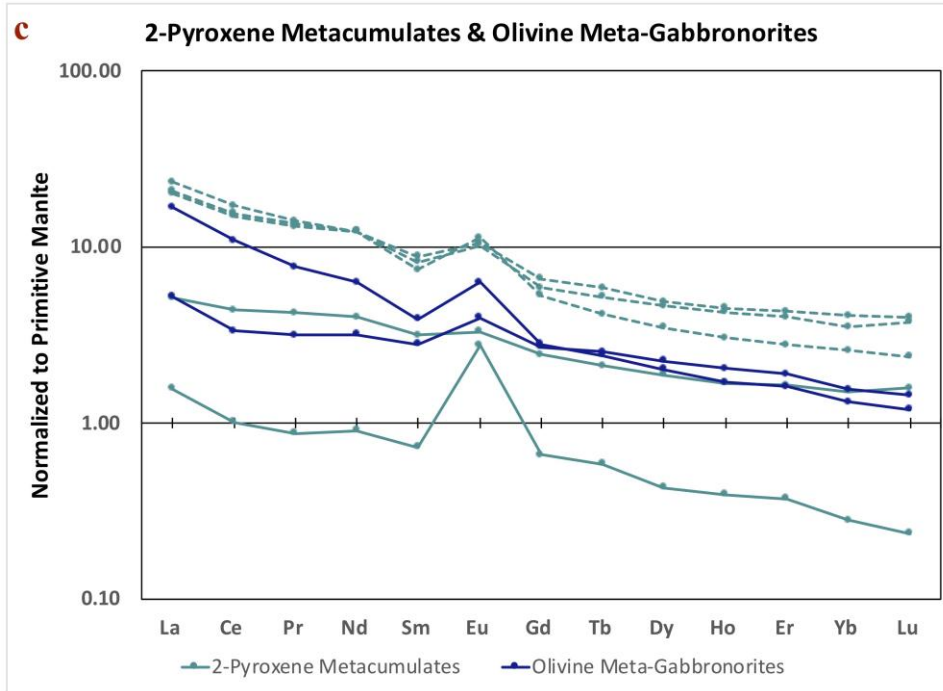
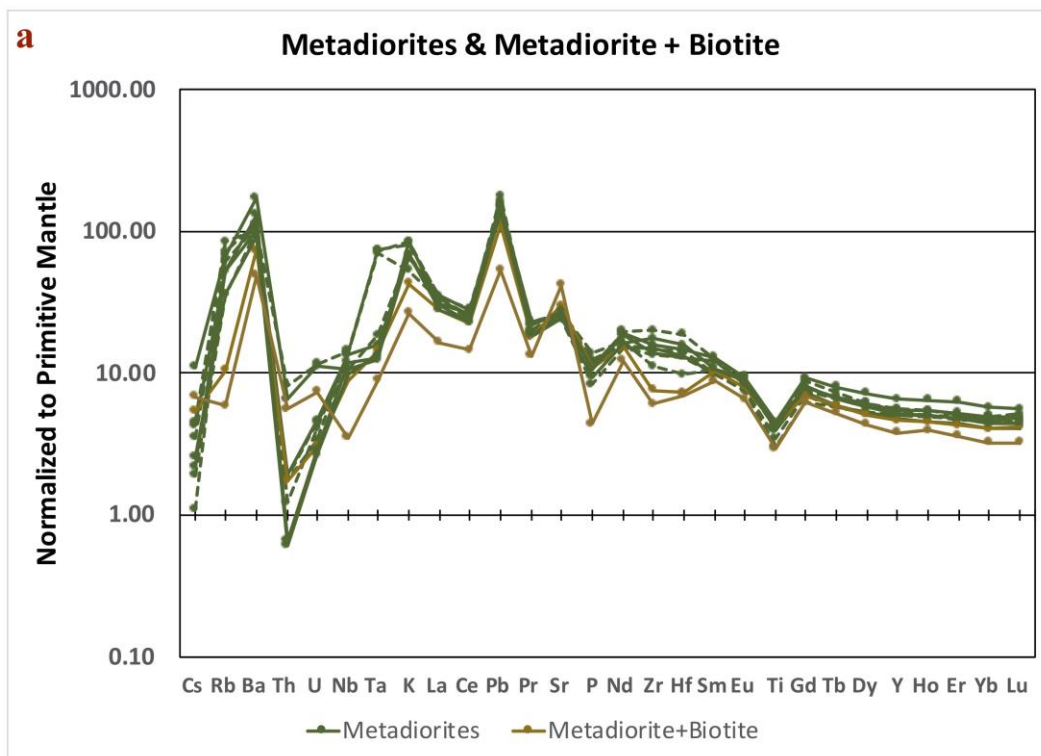


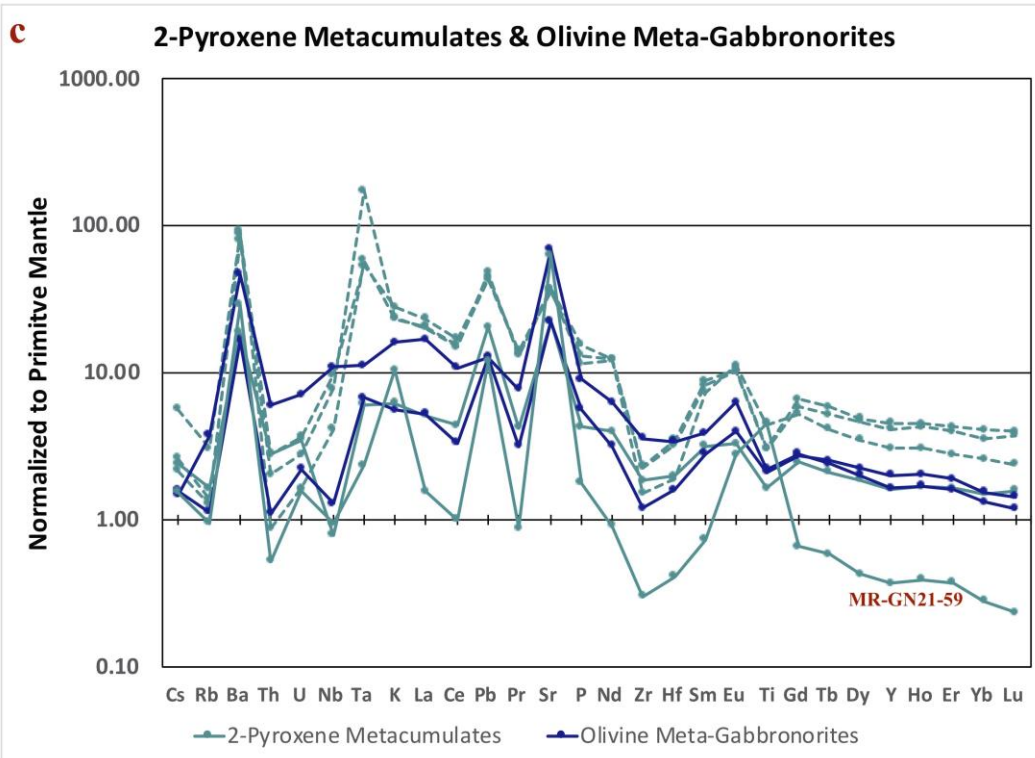
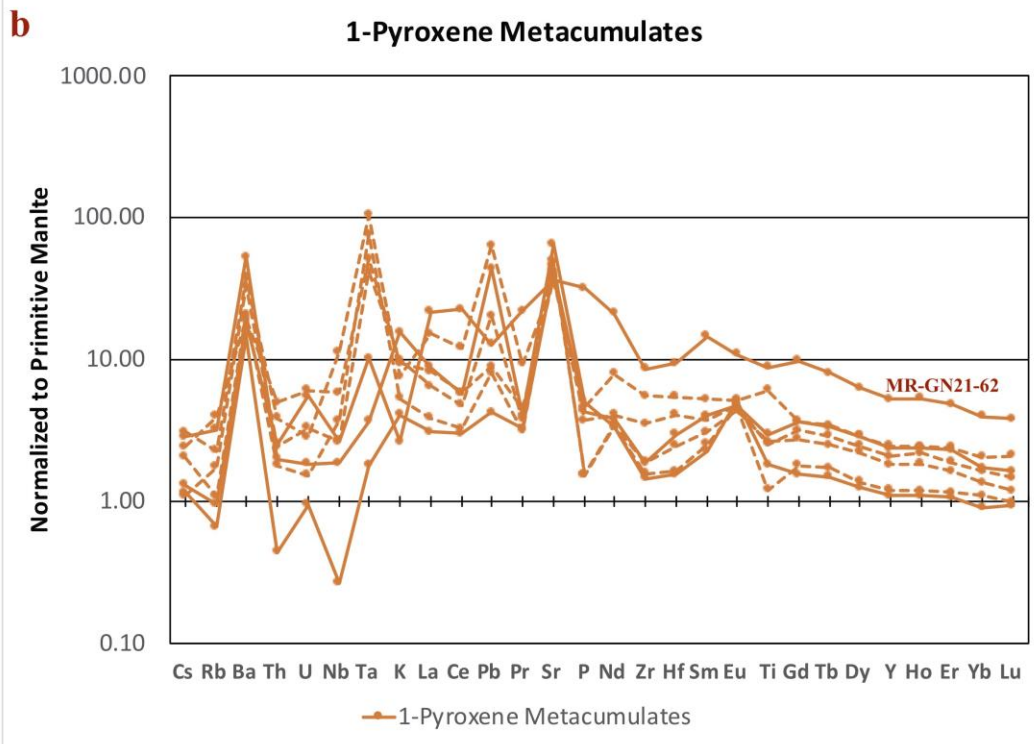
**Figure 3.10. REE plots for whole rock trace element analyses, normalized to Primitive Mantle (Sun and McDonough, 1989).**

Solid lines represent data for samples from the new collection; dashed lines are reanalyzed samples from the original collection. **a)** Metadiorites; **b)** One-pyroxene metacumulates; **c)** Two-pyroxene metacumulates and olivine meta-gabbronorites; **d)** Quartzofeldspathic granulites.

Expanded multi-element plots, normalized to primitive mantle, are presented for each lithology in Fig. 3.11. Elements are arranged in order of incompatibility, with the most incompatible elements on the left and the least incompatible elements on the right (Sun and McDonough, 1989). Most samples have large depletions in high field strength elements (HFSE), such as Ti, with strong enrichments in the large ion lithophile elements, such as Ba, Pb, and Sr. Metadiorites are enriched in the most incompatible elements compared to metacumulates (Fig. 3.12), with overall smoother and more consistent enrichment patterns across the group, with a relatively narrow range of concentrations (Fig. 3.11a). In addition to the trace element anomalies noted above, metadiorites have positive Rb, K, and negative P and Ti anomalies. Metadiorites with biotite are distinct, with unexpectedly lower K and Rb than biotite-free metadiorites. Metacumulates show far more compositional variability as a group, consistent with the variable modal mineral abundances (i.e. proportions of plagioclase to clinopyroxene and orthopyroxene) of the samples within this group (Fig. 3.11b and c). Metacumulates have overall lower trace element concentrations for most elements when compared with metadiorites, but with strong positive Ba, Sr anomalies, and depletions in HFSE like Ti, Zr, Nb, with the exception of one 2-pyx metacumulate (MR-GN21-59), which has a peculiar positive Ti anomaly. A similarly large positive K anomaly of this sample suggests it may contain a large amount of K-feldspar, suggesting a petrographic overestimation of plagioclase (Table 3.11c). Positive Sr anomalies in all the metacumulates suggest plagioclase accumulation. Reanalyzed metacumulates have an unusual peak at Ta, which may be an artifact of different sample preparation methods. These samples were powdered in tungsten carbide, rather than alumina. However, the peak is not uniformly observed, so the origin of this anomaly is uncertain. Similar to metadiorite lithologies, quartzofeldspathic

samples have positive Rb, K anomalies, and negative Cs and Th anomalies. Quartzofeldspathic xenoliths are distinctive for low Ti, P, Nb, Ta. Pk-G-GN22-5 contrasts with all xenoliths in its high U, Th and Cs, forming a group of its own. The other three quartzofeldspathic samples (MR-GN21-16, MR-GN21-39, and MR-GN21-53) form an additional group, with similar patterns from Cs to Gd. This group of quartzofeldspathic samples can be further differentiated by their REE patterns, where samples MR-GN21-16 and MR-GN21-39 have an unusual enrichment in HREE relative to the MREE, while MR-GN21-53 has a more typical, flat to negatively sloping, REE pattern (Fig. 3.11d).





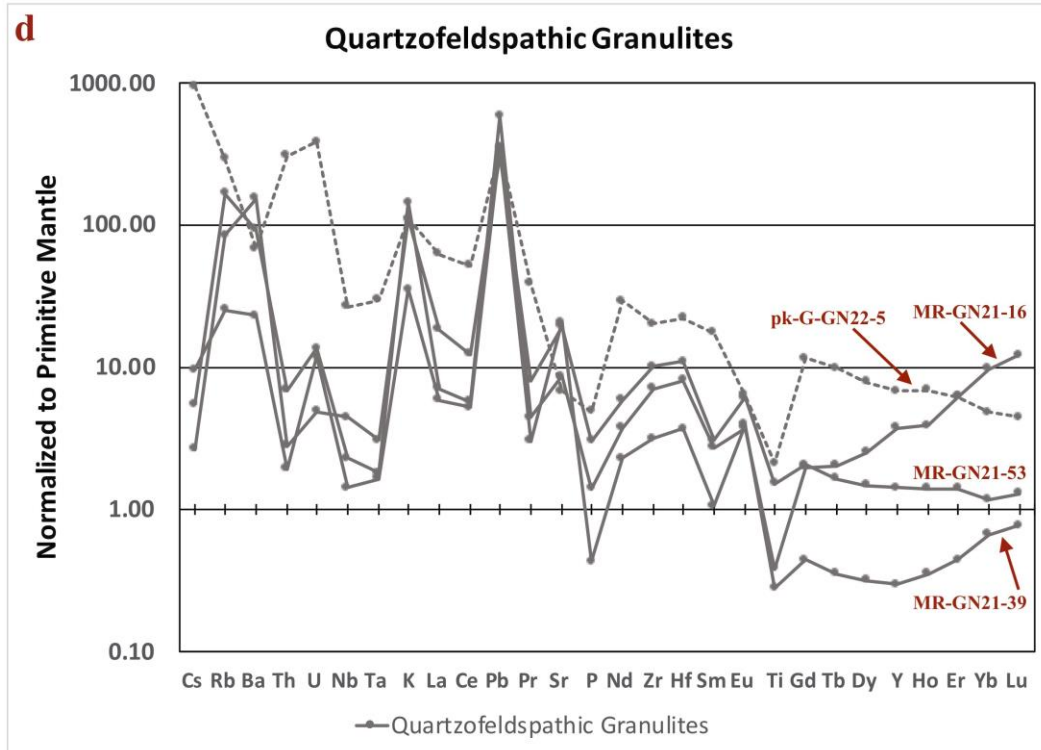


**Figure 3.11. Spider diagrams for whole rock trace element analyses, normalized to Primitive Mantle (Sun and McDonough, 1989).**

Decreasing incompatibility from left to right. Solid lines represent data for samples from the new collection; dashed lines are reanalyzed samples from the original collection. **a)** Metadiorites; **b)** One-pyroxene metacumulates; **c)** Two-pyroxene metacumulates and olivine meta-gabbro-norites; **d)** Quartzofeldspathic granulites.

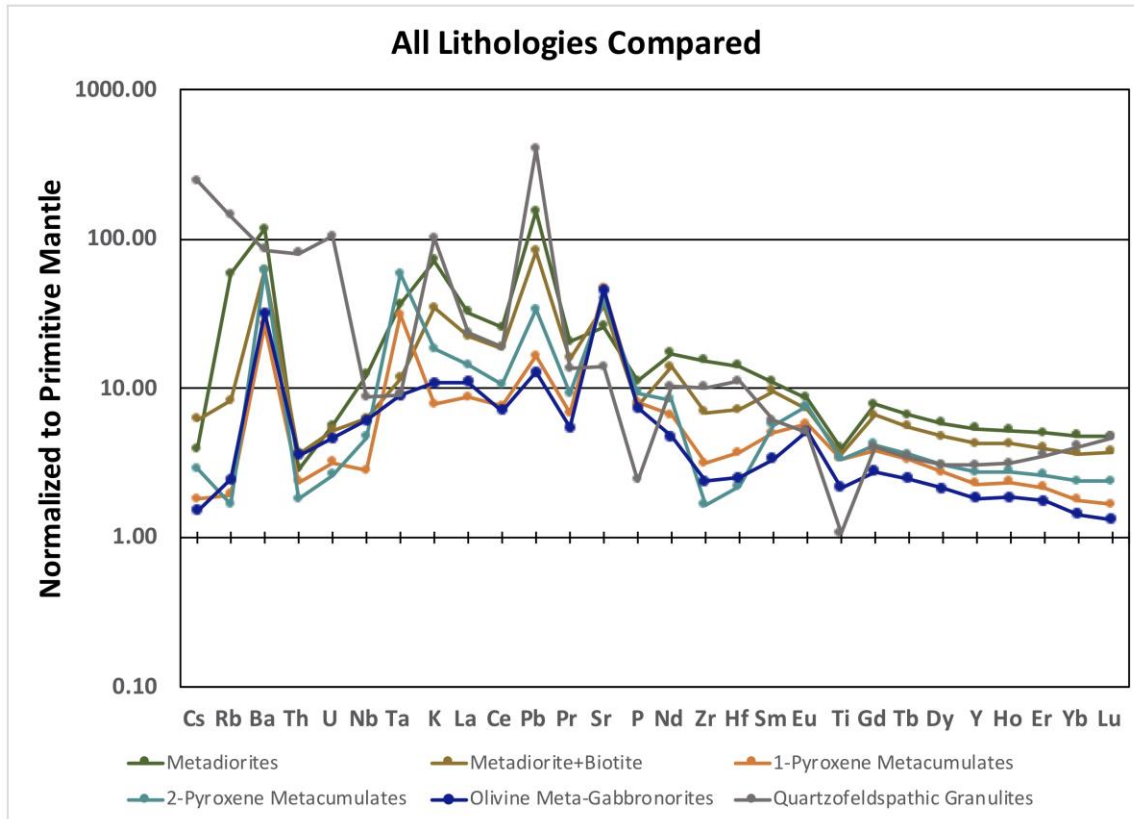


**Figure 3.12. Spider diagrams for whole rock trace element analyses averaged for each lithology, normalized to Primitive Mantle (Sun and McDonough, 1989).**

Compositions are averaged for each lithology for purposes of comparison between lithologies.

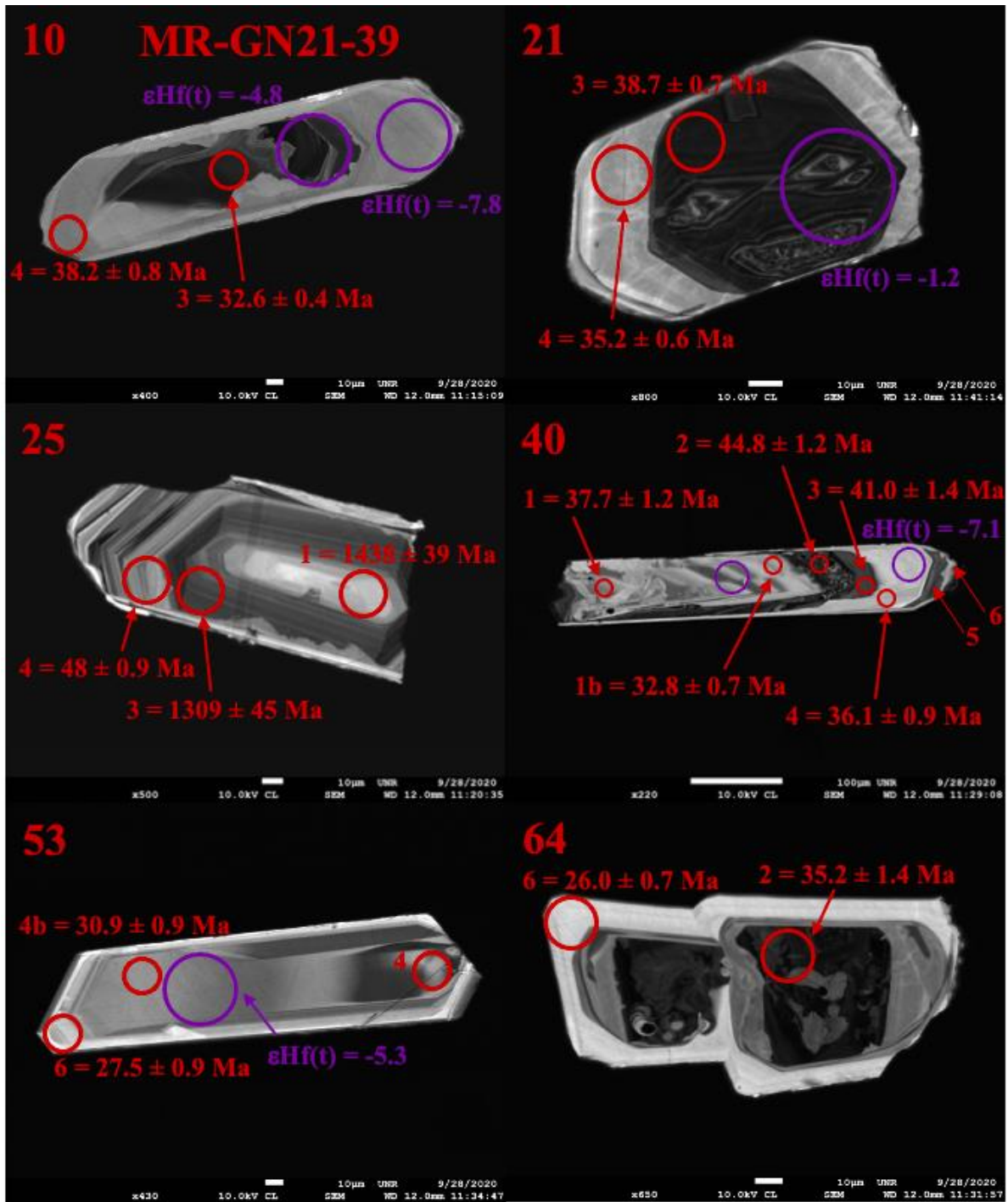
Decreasing incompatibility from left to right.

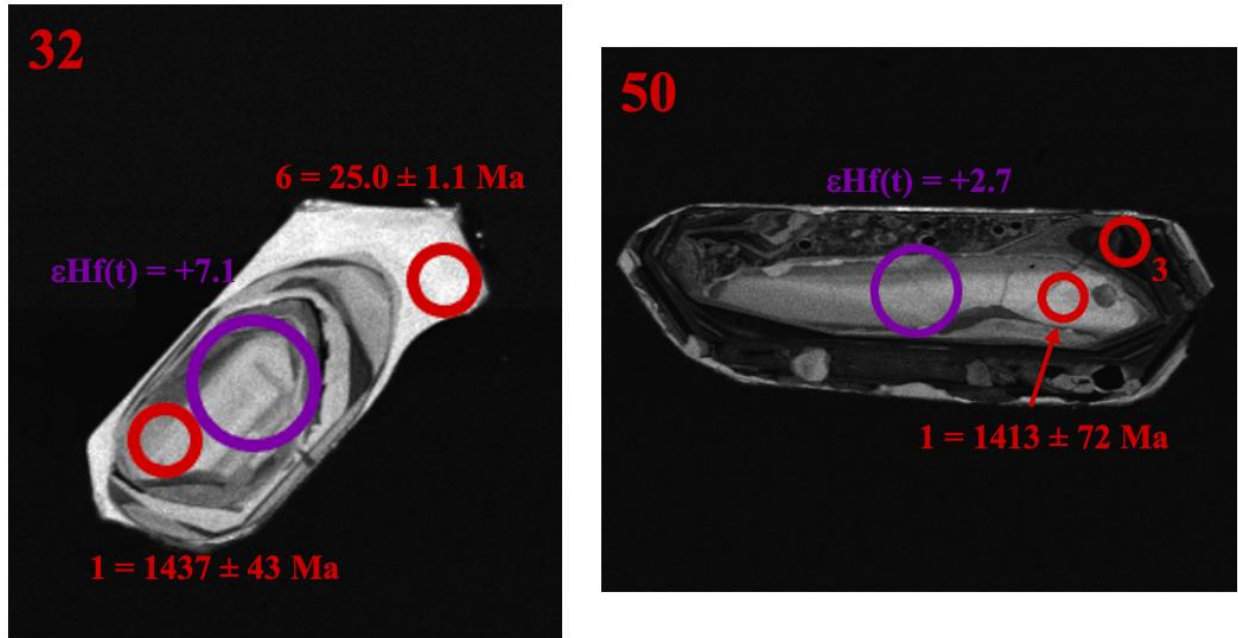
### 3.4.3. Zircon Cathodoluminescence

All zircons were imaged using cathodoluminescence (CL) (Appendix E); representative examples are presented in Figures 3.13 to 3.19.

#### **CL Images for zircons from quartzofeldspathic granulites**

**MR-GN21-39** has euhedral, doubly terminated prismatic zircon, ~50-200  $\mu\text{m}$  long. Six different growth zones were identified in zircons from this sample, representative grains are shown in Fig. 3.13. From innermost to outermost zone, zircon cores (zone 1) show light grey CL response with typical igneous oscillatory zonation, surrounded by a dark grey oscillatory overgrowth with metamict textures (zone 2). The remainder of the zones alternate between dark (zone 3 and 5) and light grey (zone 4) oscillatory zoning, with a very light grey, homogenous outer rim (zone 6), which overgrows truncations and embayments into other zones.

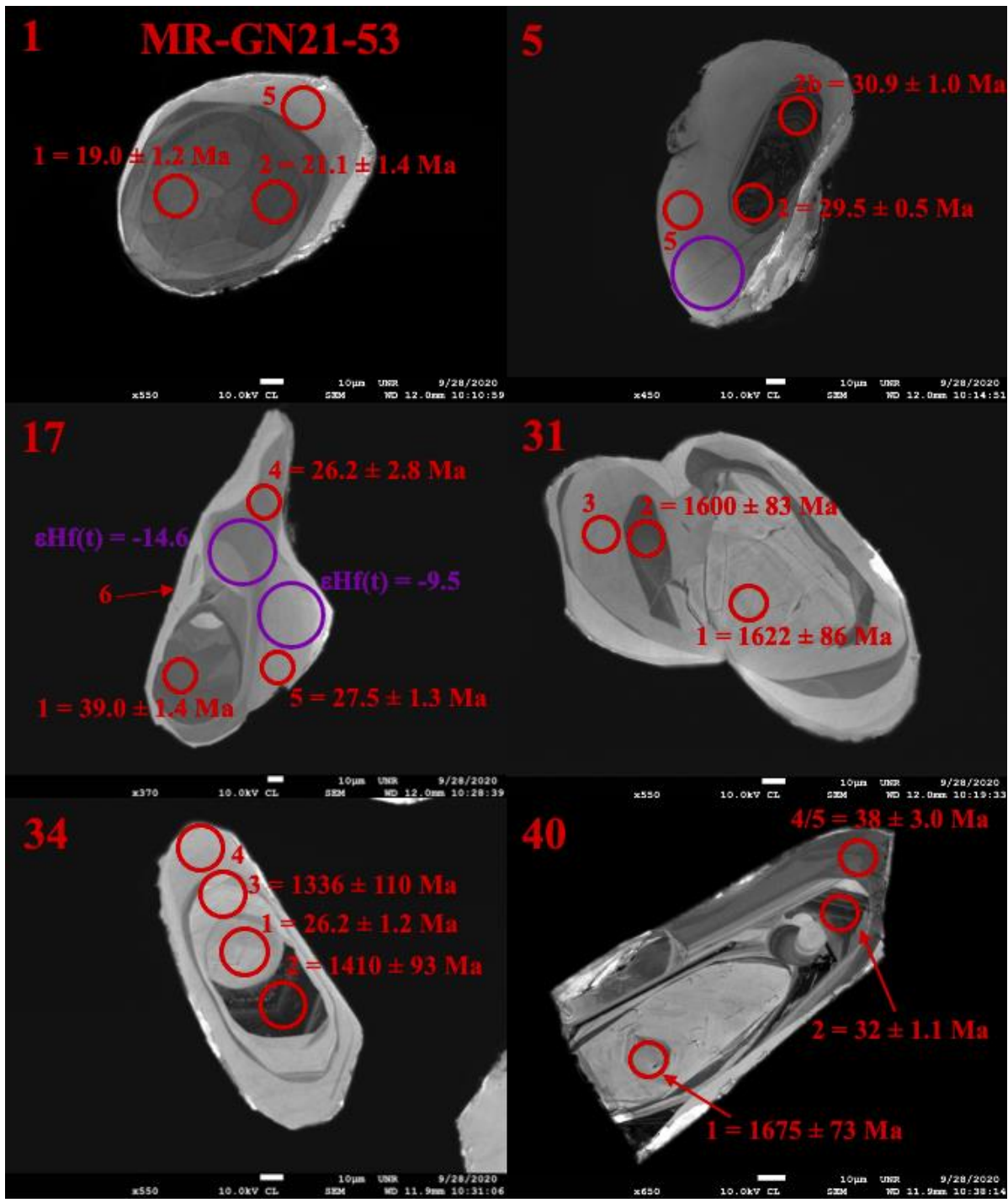




**Figure 3.13. CL images of representative zircon from MR-GN21-39.**

Large number in top left denote grain numbers. Red circles (20  $\mu\text{m}$ ) indicate spots for U-Pb analysis. Small numbers (1-6) that precede ages indicate the zone being analyzed. Purple spots (40  $\mu\text{m}$ ) indicate Hf-isotope analysis. Spots that lack ages or  $\epsilon\text{Hf}(t)$  values either had high errors or discordant data. The white bar at the bottom of each image is 10  $\mu\text{m}$  for scale. Long white bar on grain 40 is 100  $\mu\text{m}$ . The last two grains (32 and 50) are presented to show positive  $\epsilon\text{Hf}(t)$  values.

**MR-GN21-53** has subhedral to rounded zircon, ~50-150  $\mu\text{m}$  long. Six different growth zones were identified in zircons from this sample, representative grains are shown in Fig. 3.14. From innermost to outermost zone, zircon cores (zone 1) are dark to medium grey, rounded and sector zoned, surround by a dark igneous oscillatory zoned region with metamict textures (zone 2). Zircon cores are surrounded by a series of thick homogenous overgrowths in different shades of grey (zones 3-5), typical of metamorphic recrystallization and new crystal growth. Rims are very thin, light grey (zone 6).



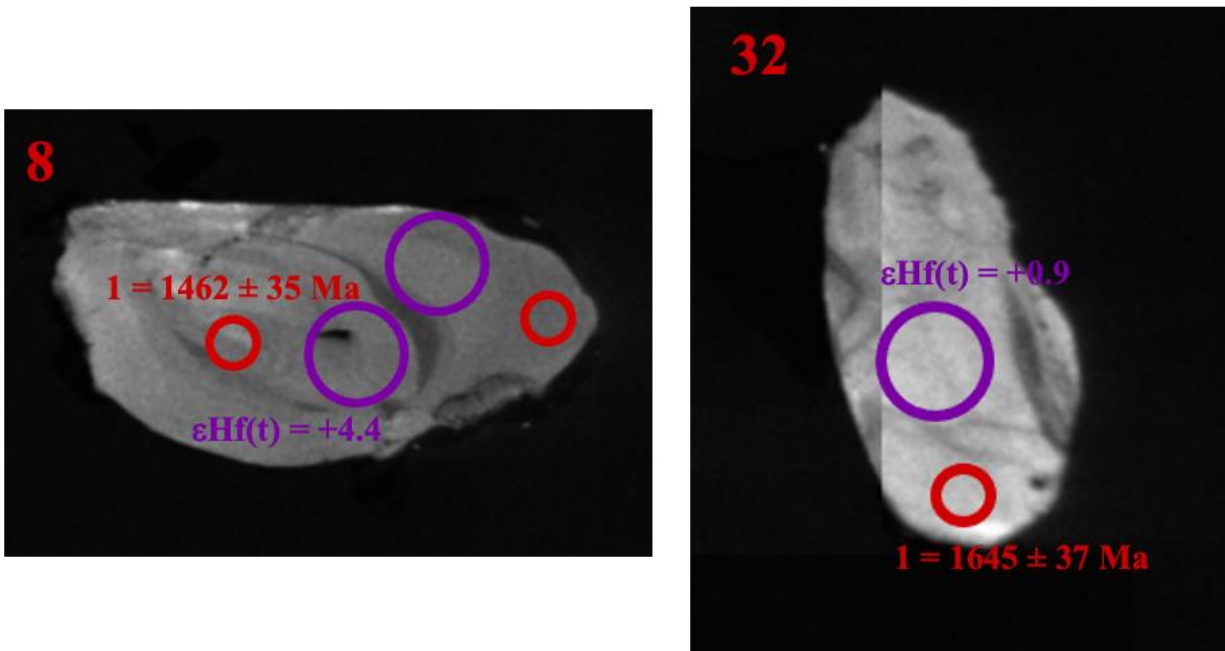


**Figure 3.14. CL images of representative zircon from MR-GN21-53.**

Large number in top left denote grain numbers. Red circles (20  $\mu\text{m}$ ) indicate spots for U-Pb analysis. Small numbers (1-6) that precede ages indicate the zone being analyzed. Purple spots (40  $\mu\text{m}$ ) indicate Hf-isotope analysis. Spots that lack ages or  $\epsilon\text{Hf}(t)$  values either had high errors or discordant data. The white bar at the bottom of each image is 10  $\mu\text{m}$  for scale. The last two grains (8 and 32) are presented to show positive  $\epsilon\text{Hf}(t)$  values.

**pk-G-GN22-5** has sub to anhedral zircon with some rounding,  $\sim 75\text{-}100\ \mu\text{m}$ . Five different growth zones were identified in zircons from this sample, representative grains are shown in Fig. 3.15. From innermost to outermost zone, zircon cores (zone 1) show medium grey CL response with typical igneous oscillatory zonation. Zone 1 is embayed by bright grey homogenous overgrowths (zone 2), surround by a medium to dark grey zone with ghost oscillatory zoning and smoky textures (zone 3). Zone 3 is overgrown by a thin homogenous bright zone (zone 4), and a thin dark outer rim (zone 5).

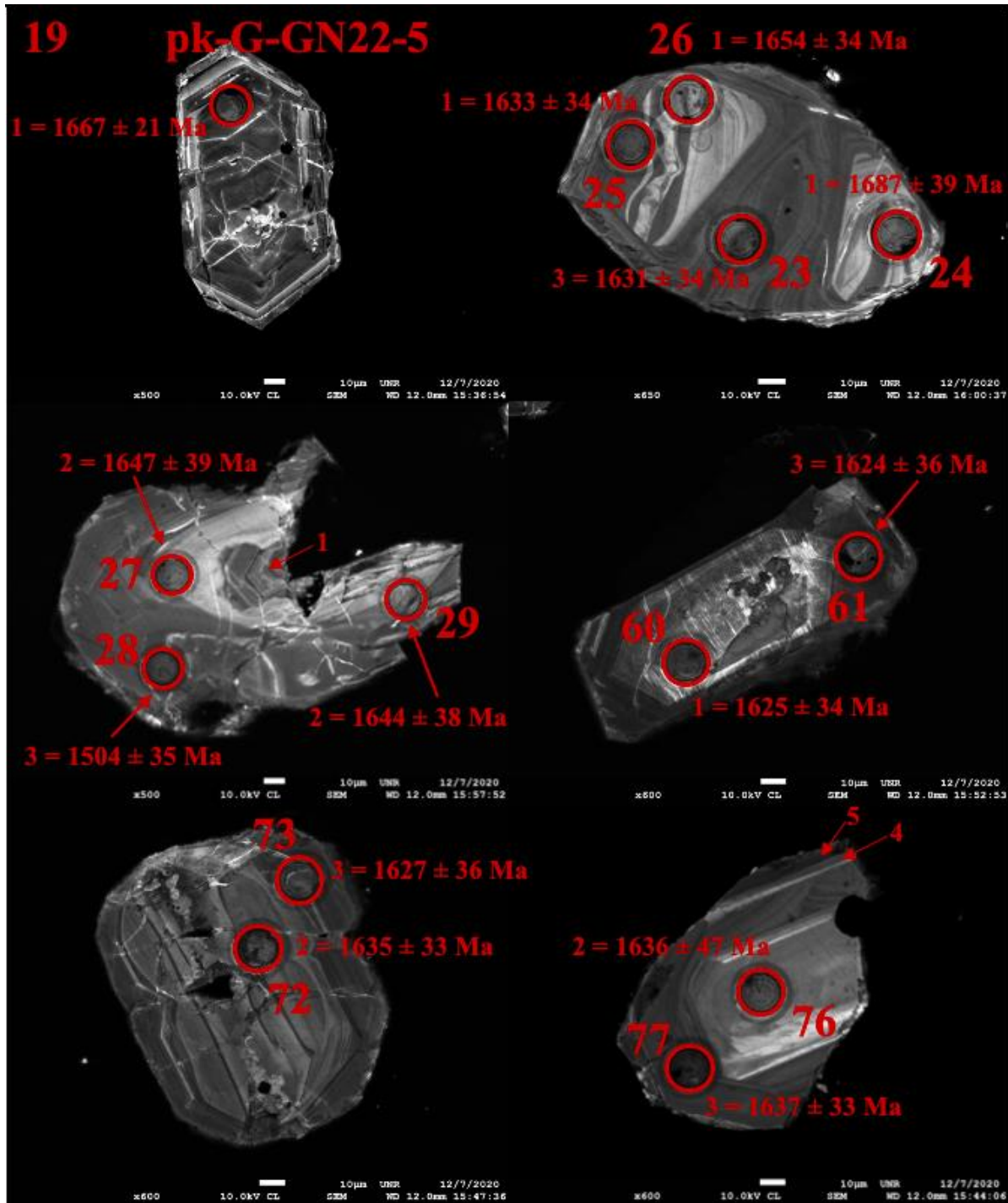


**Figure 3.15.** CL images of representative zircon from pk-G-GN22-5.

Large number denotes analysis number. Red circles (20  $\mu\text{m}$ ) indicate spots for U-Pb analysis. Small numbers (1-3) that precede ages indicate the zone being analyzed. The white bar at the bottom of each image is 10  $\mu\text{m}$  for scale.

### **CL Images for zircons from metadiorites**

**MR-GN21-34** has subhedral to rounded zircon, ~75-150  $\mu\text{m}$  long. Five different growth zones were identified in zircons from this sample, representative grains are shown in Fig. 3.16. From innermost to outermost zone, zircon cores (zone 1; visible in only ~10% of imaged zircons) have typical igneous oscillatory zonation with radiation damage and metamict textures visible in CL. The remaining 90% of cores are medium grey with a patchy or smoky texture indicating recrystallization (zone 2). Zircon cores are surrounded by a series of thick homogenous overgrowths in varying shades of grey (zone 3 and 4), typical of metamorphic recrystallization and new crystal growth. Zones 2 and 3 clearly truncate and embay earlier zones. Rims are light to medium grey with very faint oscillatory zonation (zone 5).

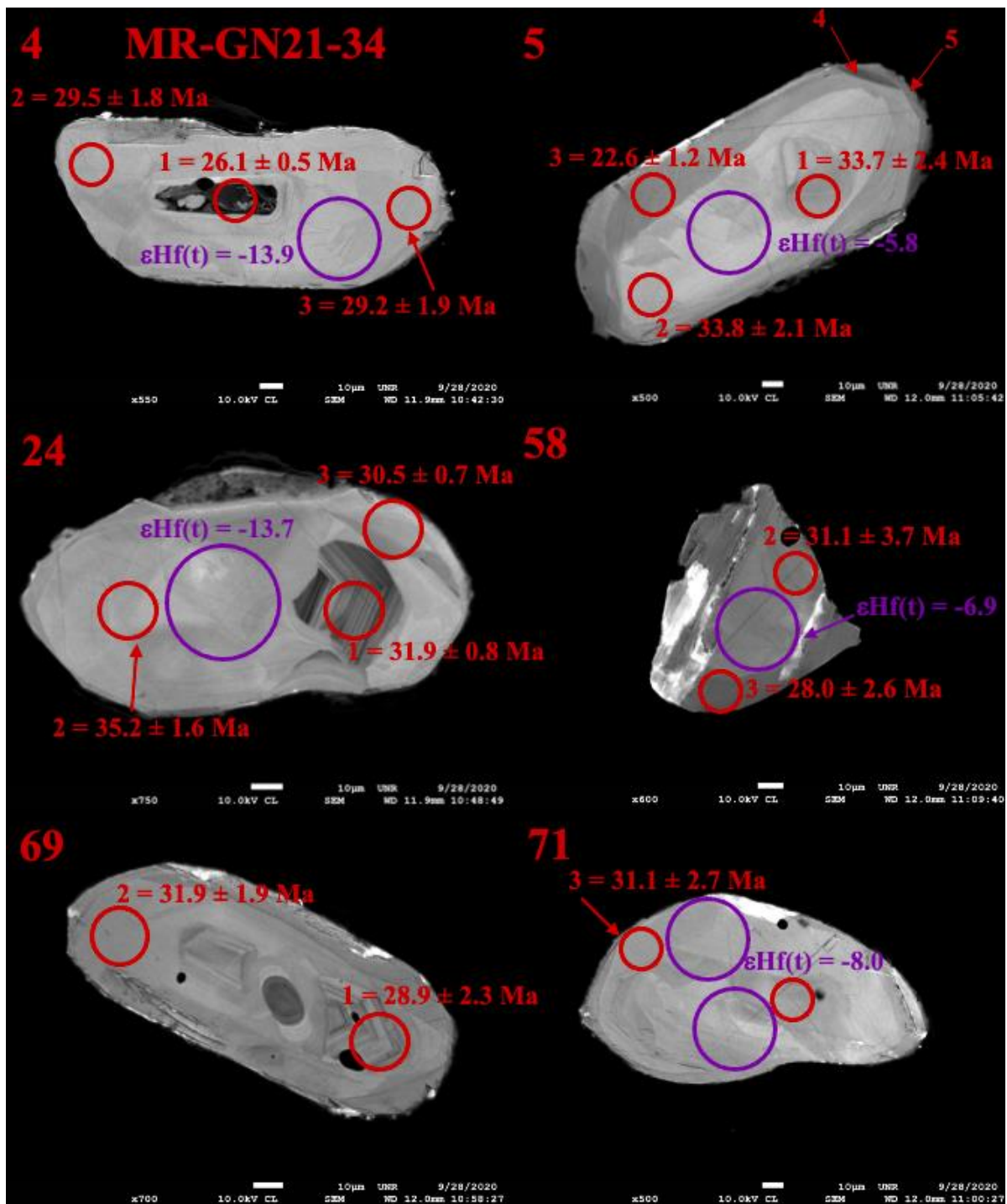


**Figure 3.16. CL images of representative zircon from MR-GN21-34.**

Large number in top left denote grain numbers. Red circles (20  $\mu\text{m}$ ) indicate spots for U-Pb analysis. Small numbers (1-5) that precede ages indicate the zone being analyzed. Purple spots (40  $\mu\text{m}$ ) indicate Hf-isotope analysis. Spots that lack ages or  $\epsilon_{\text{Hf}}(t)$  values either had high errors or discordant data. The white bar at the bottom of each image is 10  $\mu\text{m}$  for scale.

**MR-GN22-27** zircons are subhedral, elongate, with rounded ends, ~100-200  $\mu\text{m}$  long. Six different growth zones were identified in zircons from this sample, representative grains are shown in Fig. 3.17. From innermost to outermost zone, zircon cores (zone 1; visible in only ~10% of imaged zircon) have typical igneous oscillatory zonation with radiation damage and metamict textures. The remaining 90% of cores are light to medium grey with a patchy or smokey texture (zone 2). Zircon cores are surrounded by a thick light to medium grey zone (zone 3) with faint oscillatory zoning. Zone 3 is embayed and overgrown by a thin (max 5 $\mu\text{m}$ ) medium gray homogenous zone (zone 4), followed by an up to 40  $\mu\text{m}$  wide light grey homogenous zone (zone 5), and finally a thin very light grey outer rim (zone 6).

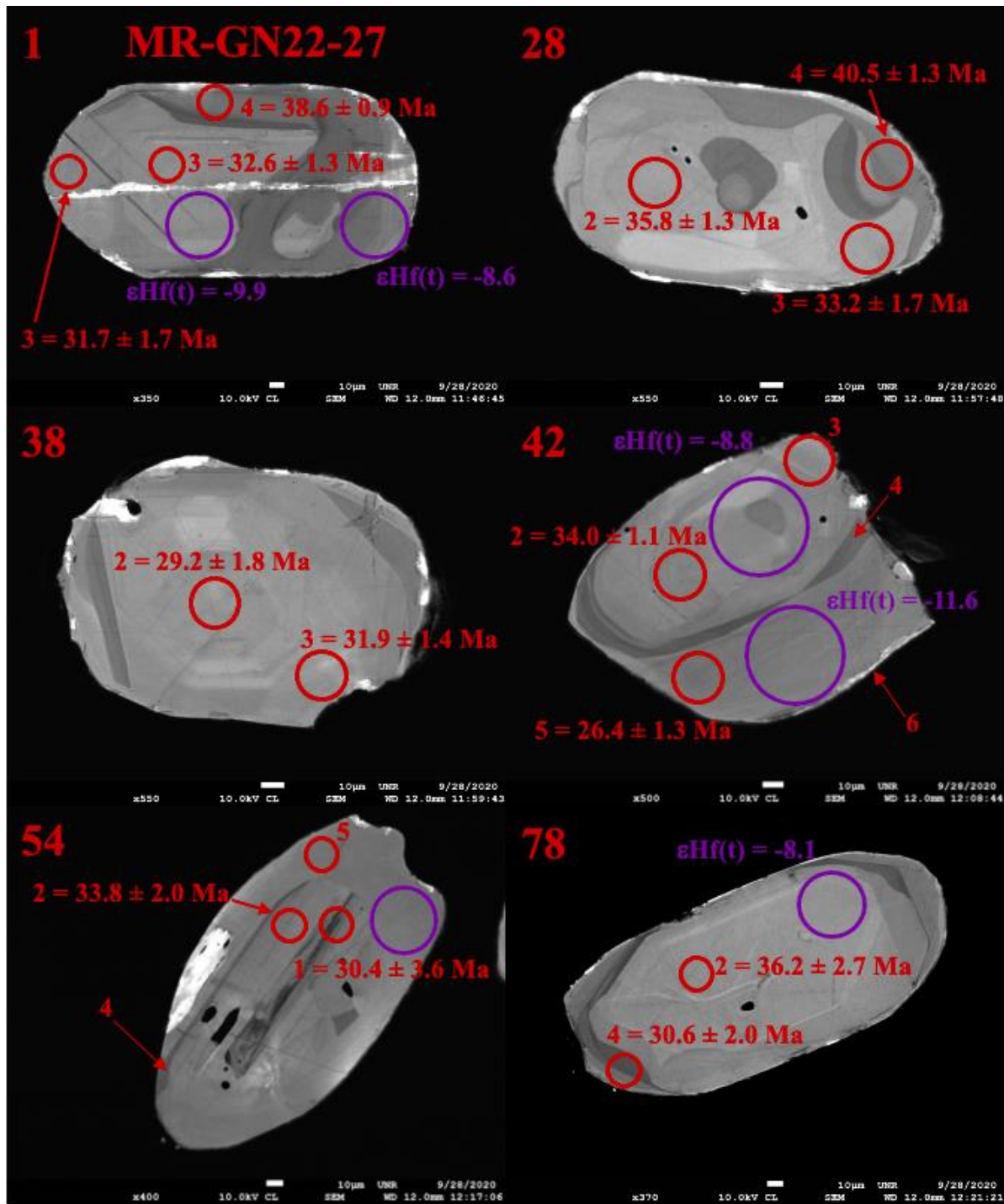


**Figure 3.17. CL images of representative zircon from MR-GN22-27.**

Large number in top left denote grain numbers. Red circles (20  $\mu\text{m}$ ) indicate spots for U-Pb analysis. Small numbers (1-5) that precede ages indicate the zone being analyzed. Purple spots (40  $\mu\text{m}$ ) indicate Hf-isotope analysis. Spots that lack ages or  $\epsilon_{\text{Hf}}(t)$  values either had high errors or discordant data. The white bar at the bottom of each image is 10  $\mu\text{m}$  for scale.

**MR-GN22-35** has subhedral, elongate zircon with rounded ends, 200-500  $\mu\text{m}$ . Five different growth zones were identified in zircons from this sample, representative grains are shown in Fig. 3.18. From innermost to outermost zone, zircon cores (zone 1) show light grey CL response with a patchy or smoky texture. Cores are embayed by a medium grey oscillatory and sector-zoned region (zone 2), followed by a medium to dark grey homogenous zone (zone 3) that embays zone 2. Zone 3 is also embayed by a thin medium to dark grey homogenous zone (zone 4). Upon further examination, it appears that zone 3 is gradational into zone 4, and that the two zones represent one process of dissolution precipitation during metamorphism. For further reference this zone will be referred to as zone 3/4. Zircon rims are thin, homogenous, light grey (zone 5).

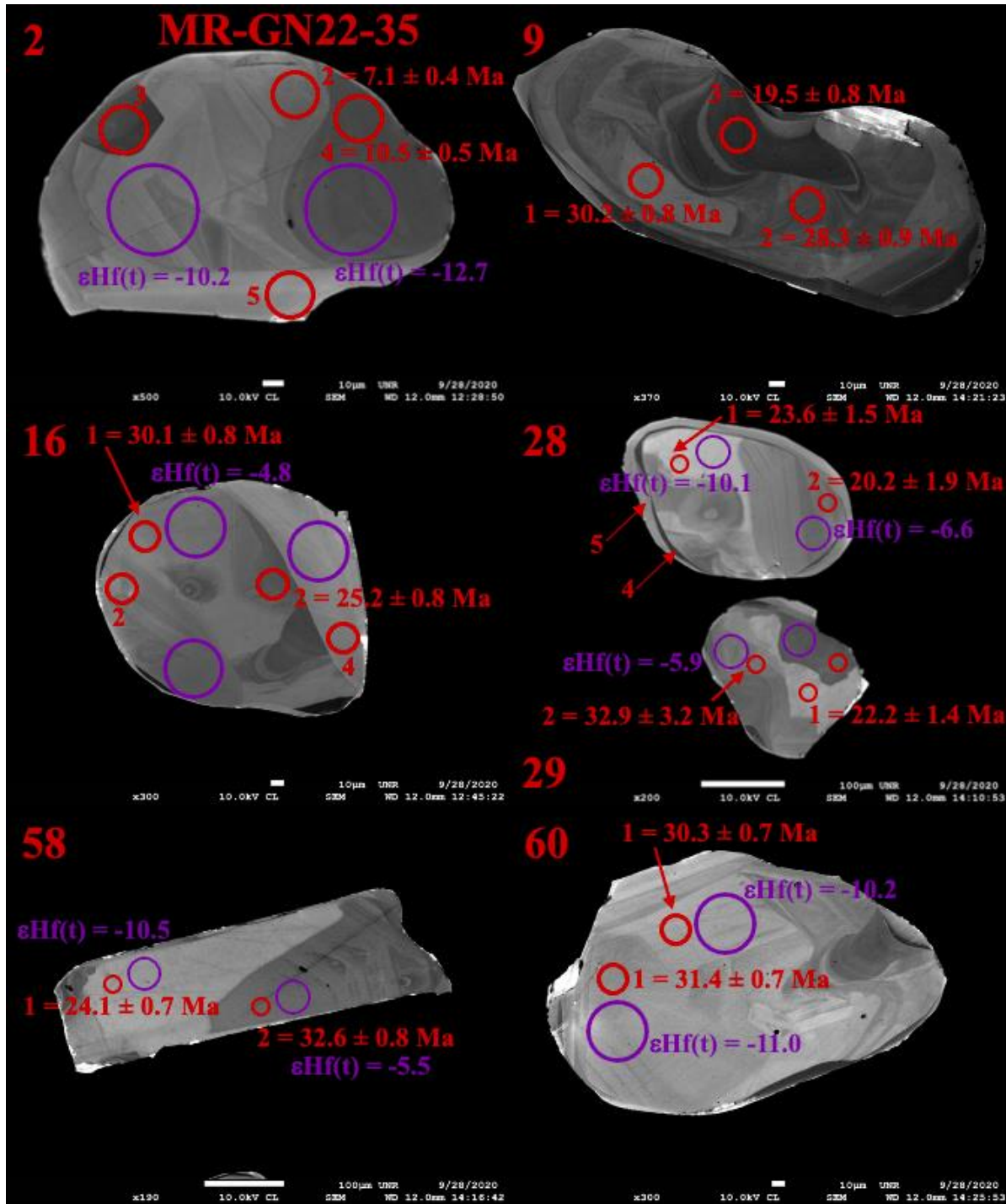


**Figure 3.18. CL images of representative zircon from MR-GN22-35.**

Large number in top left denote grain numbers. Red circles (20  $\mu\text{m}$ ) indicate spots for U-Pb analysis. Small numbers (1-5) that precede ages indicate the zone being analyzed. Purple spots (40  $\mu\text{m}$ ) indicate Hf-isotope analysis. Spots that lack ages or  $\epsilon\text{Hf}(t)$  values either had high errors

or discordant data. The white bar at the bottom of each image is 10  $\mu\text{m}$  for scale. Long white bar on grains 28/29 and 58 is 100  $\mu\text{m}$ .

**pk-G-GN22-3** has subhedral, rounded zircon, 100-200  $\mu\text{m}$ . Four different growth zones were identified in zircons from this sample, representative grains are shown in Fig. 3.19. From innermost to outermost zone, zircon cores (zone 1) show medium grey CL response with sector zoning. Cores are embayed by a dark grey homogenous zone (zone 2), with a medium grey thin, homogenous overgrowth (zone 3), and thin light grey rims (zone 4).

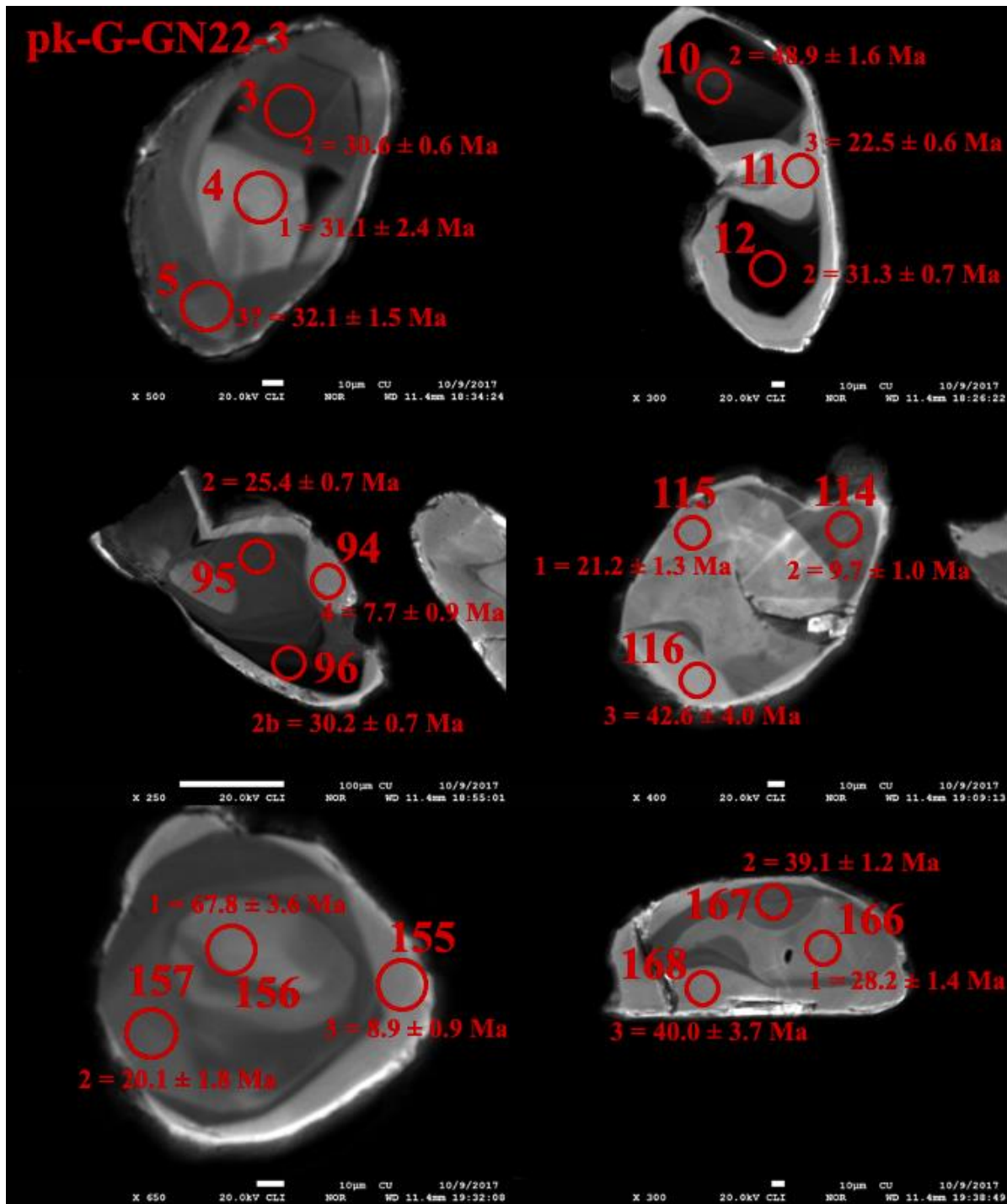


**Figure 3.19. CL images of representative zircon from pk-G-GN22-3.**

Large number denotes analysis number. Red circles indicate spots for U-Pb analysis. Small number (1-4) that precede ages indicate the zone being analyzed. The white bar at the bottom of each image is 10  $\mu\text{m}$  for scale. Long white bar on grain 94 is 100  $\mu\text{m}$ .

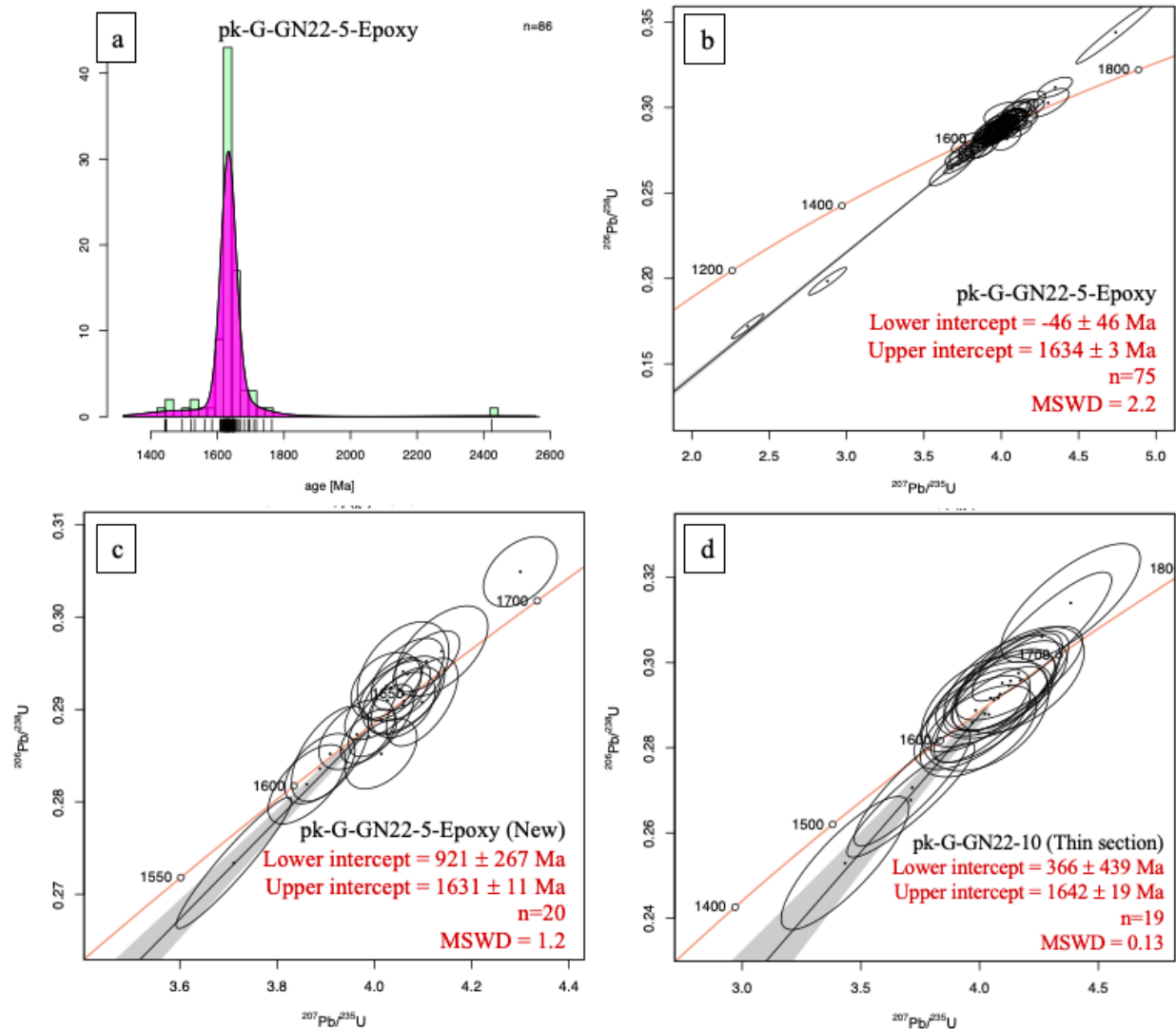
### 3.4.4. U-Pb Geochronology

U-Pb geochronology is summarized in Table 3.6; the complete U-Pb data set is available for all analyses in Appendix F, supplement file “MikaelaRader2021\_UPbGeochronology”. Kernel density (KDE) and Concordia plots are presented in Figures 3.20 to 3.24. KDE plots were created using concordant ages for  $^{206}\text{Pb}/^{238}\text{U}$  ages <100 Ma and  $^{207}\text{Pb}/^{206}\text{Pb}$  ages for ages >1000 Ma. Rules for data exclusion and uncertainty cutoffs are listed individually for each sample in the supplemental file.

Sample	$^{206}\text{Pb}/^{238}\text{U}$ age range (Ma)	$^{207}\text{Pb}/^{206}\text{Pb}$ date range (Ma)	Age peaks (interpreted from KDE plots)	Discordia model ages (Ma)
<b>Quartzfeldspathic</b>				
pk-G-GN22-5		1585 ± 37 - 2434 ± 29	~1630-1640 Ma	1634 ± 3 & 1631 ± 11
pk-G-GN22-10		1602 ± 47 - 1666 ± 46		1642 ± 19
MR-GN21-39	20.4 ± 0.8 - 50.7 ± 0.9		~35 Ma	1419 ± 85 & 1454 ± 25
MR-GN21-53	12.1 ± 0.3 - 54.5 ± 4.6		20-30 Ma	1482 ± 17 & 1631 ± 29
<b>Metadiorite</b>				
pk-g-GN22-3	1.7 ± 0.3 - 73.6 ± 4.4		8-9 Ma & 25-36 Ma	
MR-GN21-34	21.1 ± 1.2 - 43.7 ± 3.3		25-35 Ma	
MR-GN22-27	20.8 ± 1.5 - 49.3 ± 3.5		32 Ma	
MR-GN22-35	6.3 ± 0.4 - 57.6 ± 2.0		25-30 Ma	
<b>Two-pyroxene Metacumulate</b>				
MR-GN21-59		1799 ± 22		

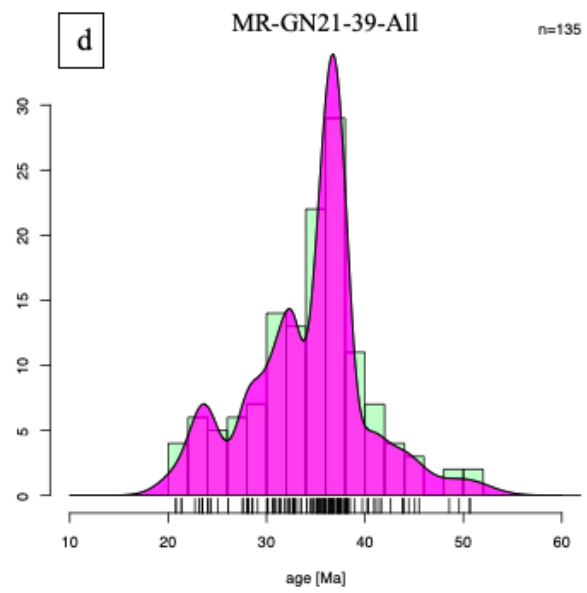
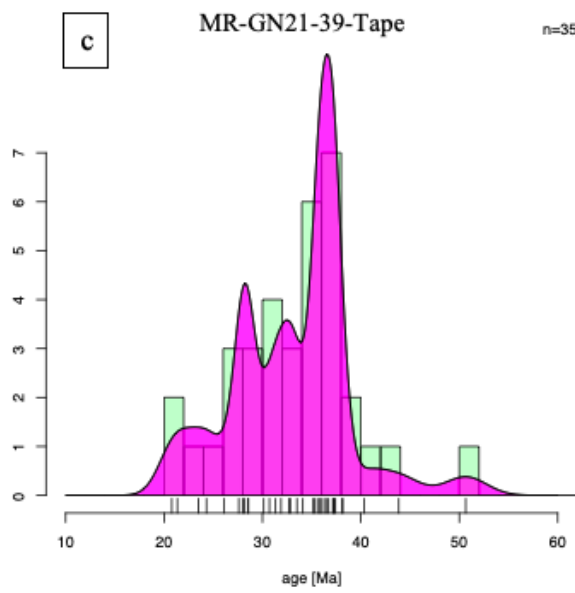
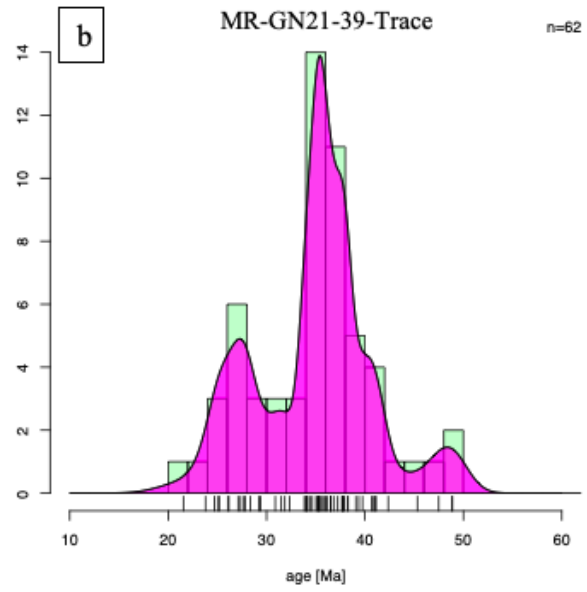
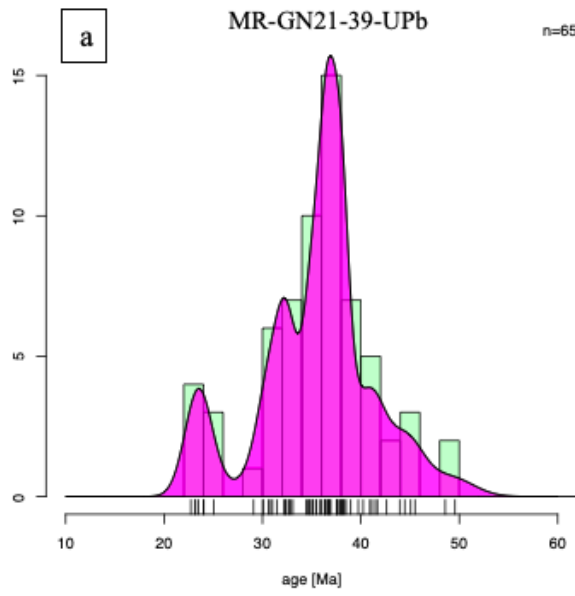
**Table 3.6. Summary of geochronology, including date ranges, age peaks, and Discordia model ages.**

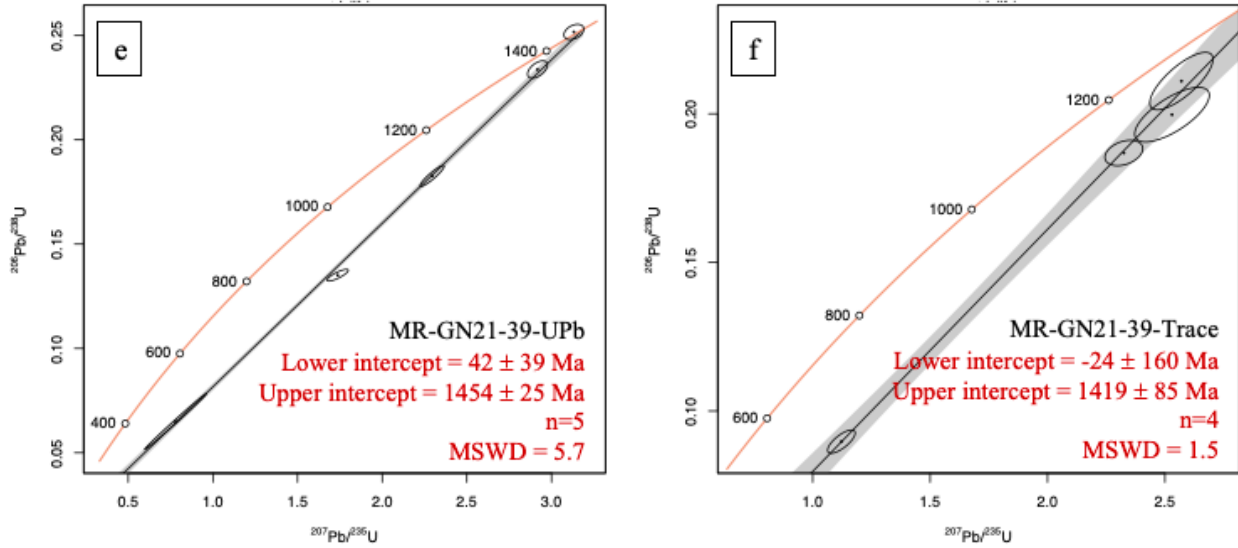
Zircons from quartzofeldspathic xenoliths have three distinct age populations ca. 1.63-1.64 Ga, 1.4-1.5 Ga, and 40-25 Ma (Appendix F). Samples pk-G-GN22-5 and pk-G-GN22-10 have discordant ages with upper intercepts at ca.  $1.63 \pm 0.005$  Ga (n=86) and  $1.64 \pm 0.019$  (n=20), respectively, and one old core dated at  $2.43 \pm 0.029$  Ga for pk-G-GN22-5 (Fig. 3.20a). Zircon from samples MR-GN21-39 and MR-GN21-53 have U-Pb ages ranging from ~51-21 Ma (n=149) and ~55-12 Ma (n=118) respectively, with little differentiation in age ranges between tape and polished epoxy mounts, indicating that we did not miss a significant younger age population of thin rims in polished mounts. Zircon age peaks occur between 40-25 Ma, with the highest number of ages at ~35 Ma for MR-GN21-39 and at ~25 Ma for MR-GN21-53 (Fig. 3.21-3.22). The polished grains in the epoxy mounts reveal cores with discordant ages trending to ~1.5-1.4 Ga and ~1.63 Ga, similar to ages recorded for pk-G-GN22-5 and pk-G-GN22-10.



**Figure 3.20. U-Pb zircon geochronology results for quartzofeldspathic granulites pk-G-GN22-5 and pk-G-GN22-10.**

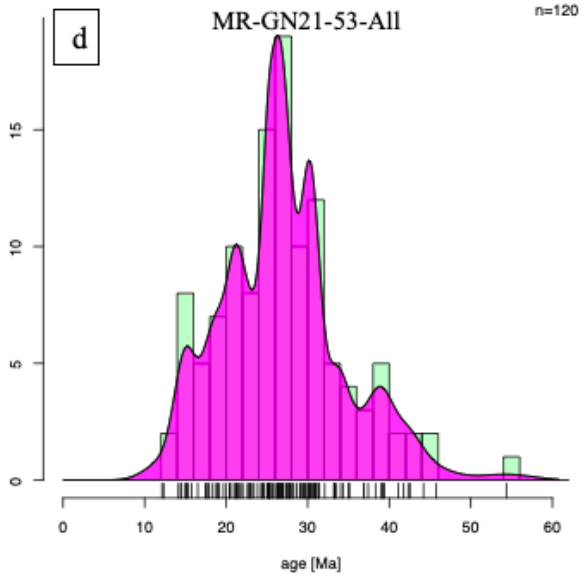
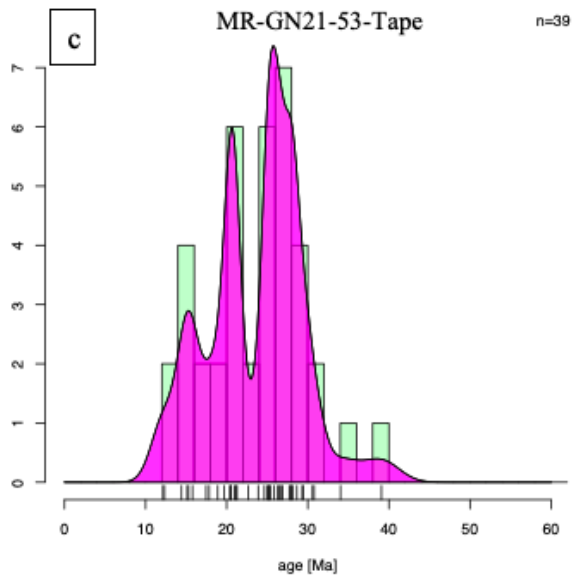
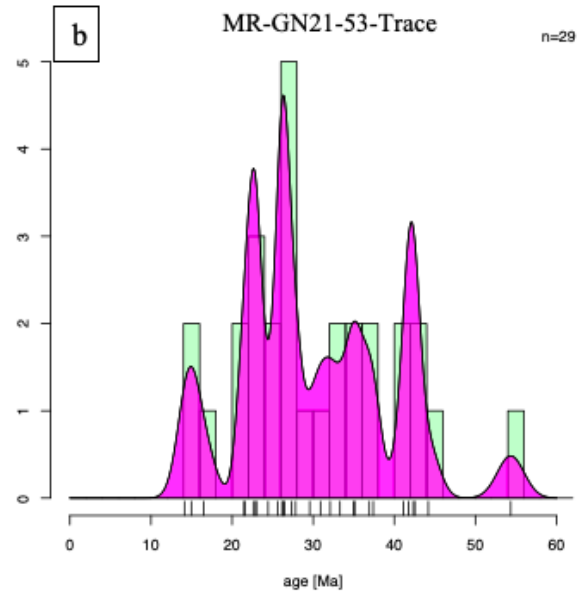
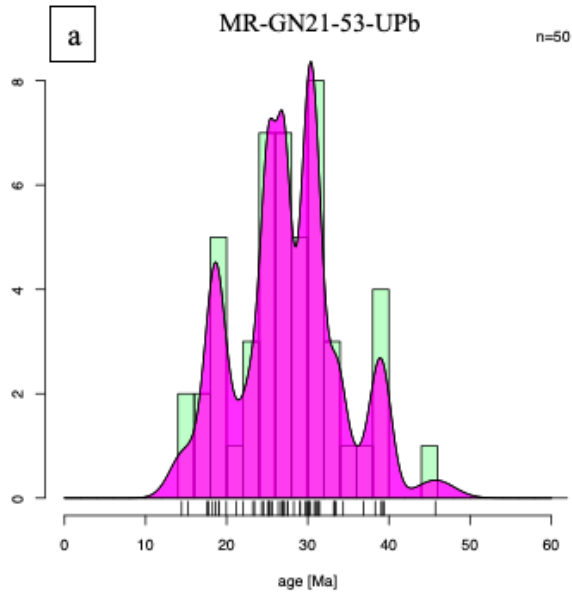
**a)** Kernel density plot of  $^{207}\text{Pb}/^{206}\text{Pb}$  ages for pk-G-GN22-5 epoxy mount U-Pb analysis (Table 3.1, session 2); **b)** Concordia plot of pk-G-GN22-5 epoxy mount U-Pb analysis (session 2); **c)** Concordia plot of pk-G-GN22-5, new analyses (session 7); **d)** Concordia plot for U-Pb analysis of pk-G-GN22-10 in thin section (session 1).

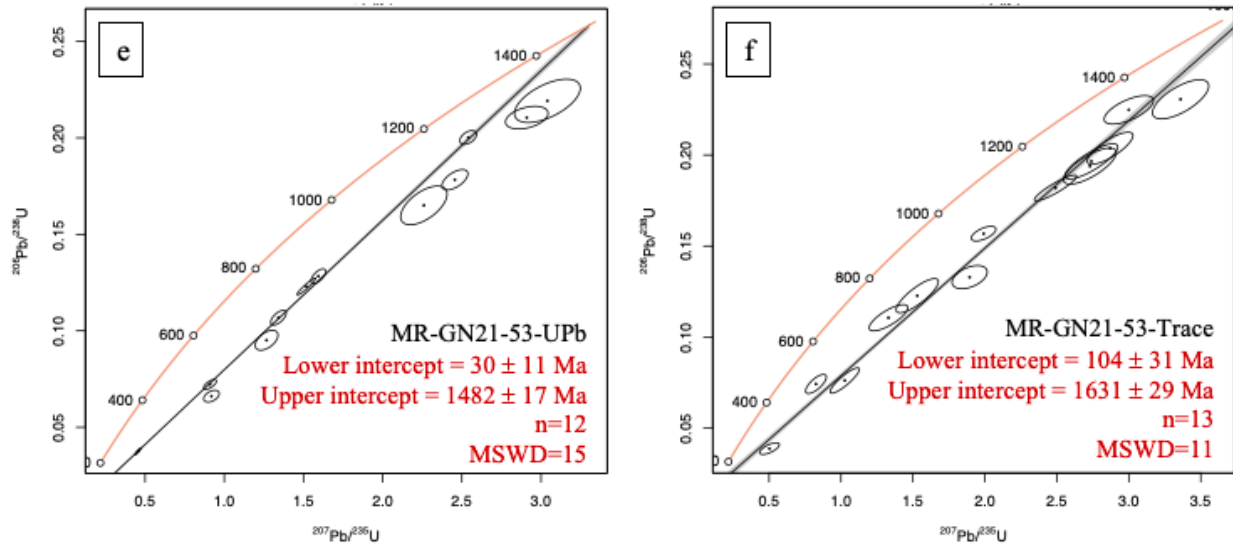




**Figure 3.21. U-Pb zircon geochronology results for quartzofeldspathic granulite MR-GN21-39.**

**a-d**) Kernel density and **e-f**) Concordia plots for MR-GN21-39; **a & e**) “UPb” analysis refer to U-Pb geochronology in epoxy mounts (Table 3.1, session 6). **b & f**) “Trace” refers to simultaneous U-Pb geochronology and trace element analyses in epoxy mounts (session 10). Note higher uncertainty. **c**) “Tape” refers to U-Pb geochronology only on tape mounted zircon (session 9). **d**) KDE of all analyses combined.

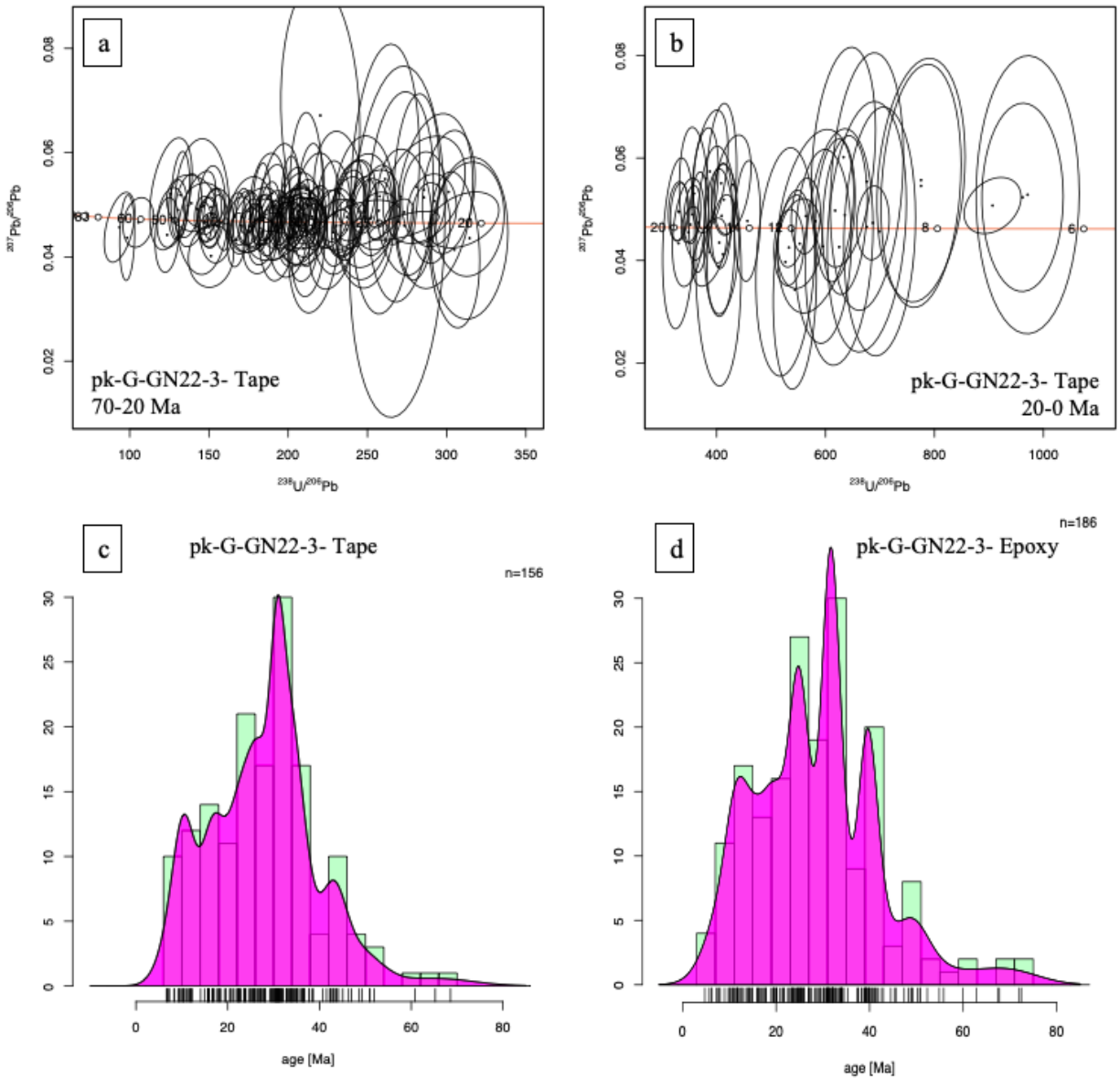




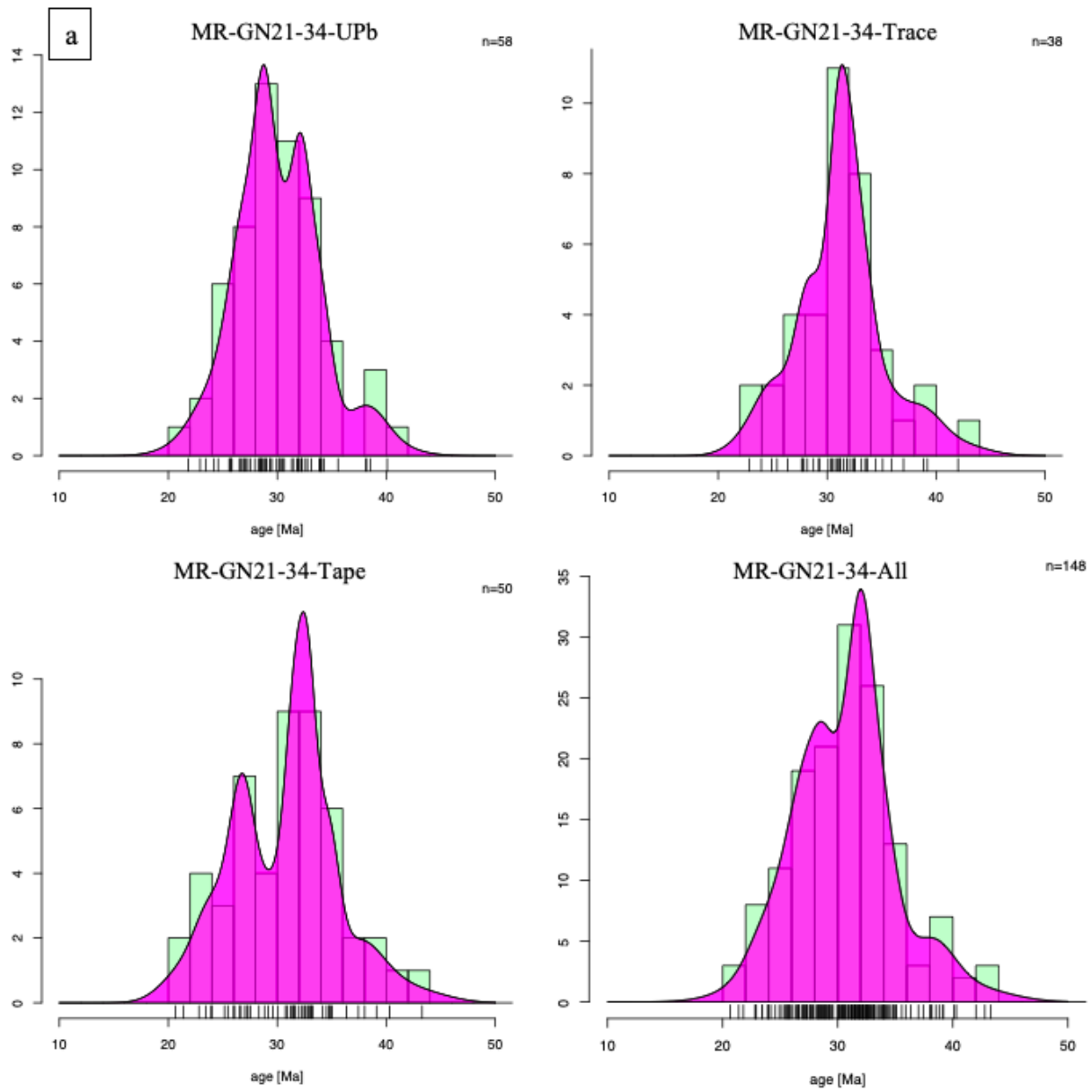
**Figure 3.22. U-Pb zircon geochronology results for quartzofeldspathic granulite MR-GN21-53.**

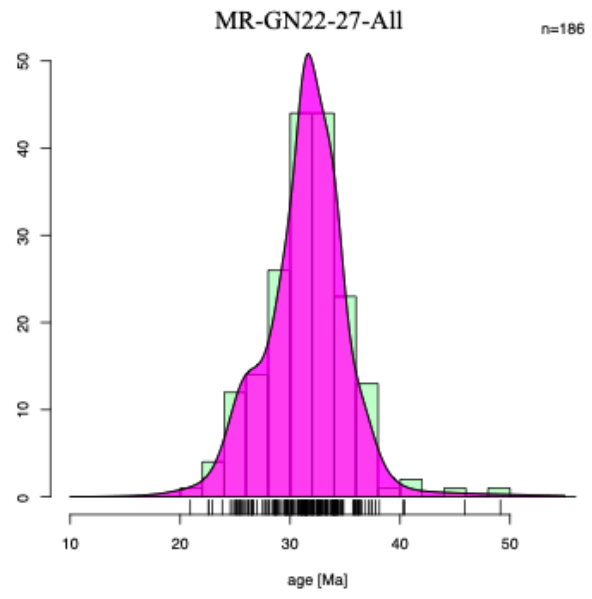
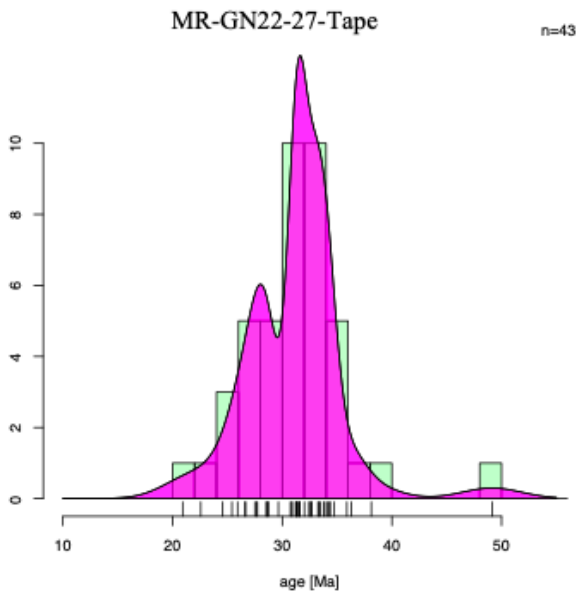
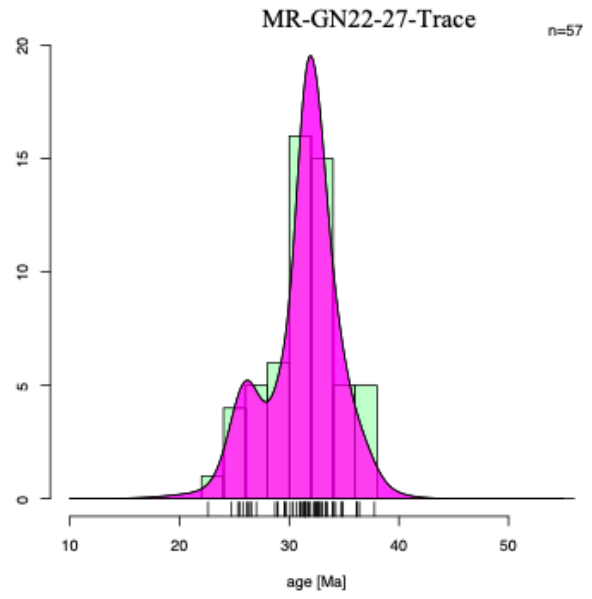
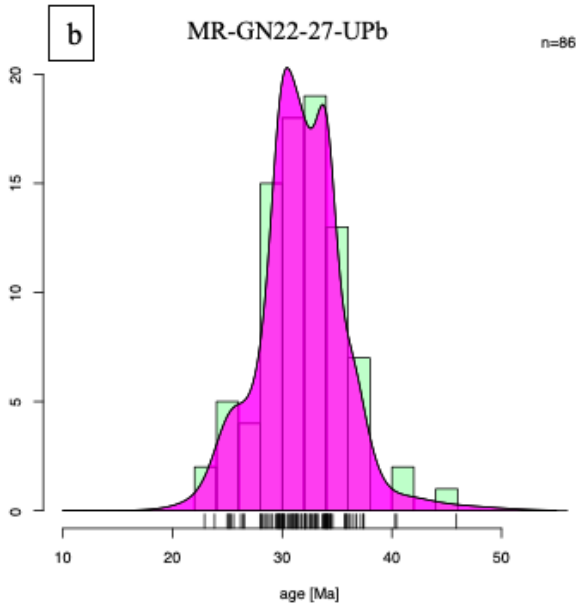
**a-d)** Kernel density and **e-f)** Concordia plots for MR-GN21-53; **a & e)** “UPb” analysis refer to U-Pb geochronology in epoxy mounts (Table 3.1, session 4). **b & f)** “Trace” refers to simultaneous U-Pb geochronology and trace element analyses in epoxy mounts (session 5). Note higher uncertainty. **c)** “Tape” refers to U-Pb geochronology only on tape mounted zircon (session 9). **d)** KDE of all analyses combined.

Zircons from four metadiorite xenoliths yield only young ages ranging from ~76-2 Ma. Sample **pk-G-GN22-3** covers the full range of young ages, with an age peak at ~35-25 Ma and a large shoulder extending to 8 Ma (Fig. 3.23). Samples from the new collection (**MR-GN21-34**, **MR-GN22-27**, **MR-GN22-35**) yield a narrower range of ages from 58-6 Ma. Age peaks occur between 35-24 Ma, with the greatest concentration of ages at 32 Ma (Fig. 3.24a-c). Unlike the zircons from the quartzofeldspathic xenoliths, no obvious age structure is preserved in the different zones for metadiorite zircons, with all zones covering the large range of ages.



**Figure 3.23. U-Pb zircon geochronology results for metadiorite xenolith pk-G-GN22-3.** **a-b)** Concordia plots and **c-d)** Kernel density of pk-G-GN22-3. **a)** Concordia ages from 80-20 Ma. **b)** Concordia ages from 20-0 Ma. **a-c)** “Tape” refers to U-Pb geochronology only on tape mounted zircon (Table 3.1, session 3). **d)** “Epoxy” analysis refers to U-Pb geochronology in epoxy mounts (session 2).





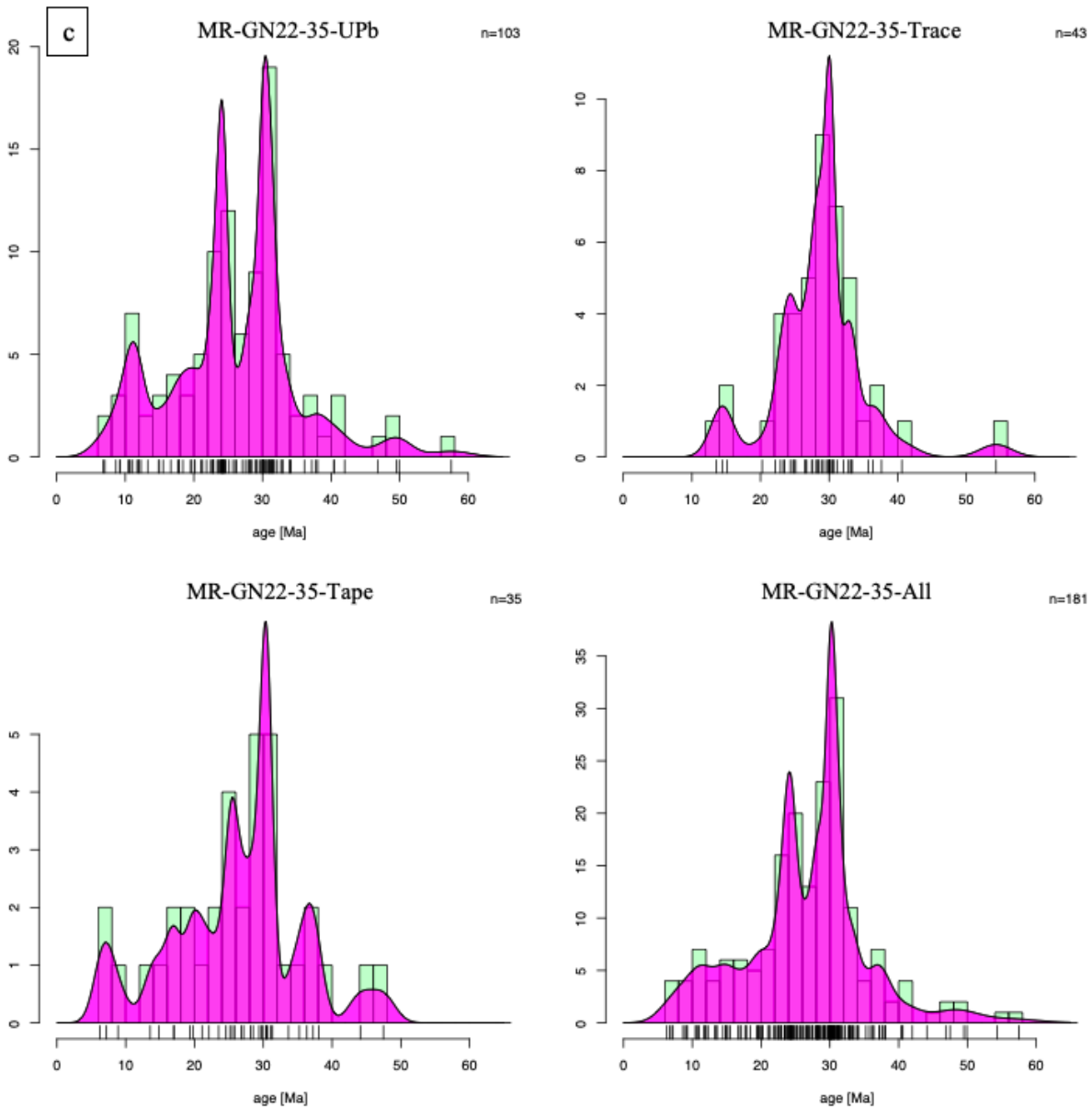


**Figure 3.24. U-Pb zircon geochronology results for metadiorite xenoliths MR-GN21-34, MR-GN22-27, and MR-GN22-35.**

Kernel density plots for **a)** MR-GN21-34, **b)** MR-GN22-27, and **c)** MR-GN22-35. Top left KDE is U-Pb only analyses (Table 3.1, sessions 4, 7, and 8 respectively), top right KDE are analyses with simultaneous U-Pb and trace elements (sessions 5 and 10), bottom left KDE is for U-Pb analyses of tape mounted zircon (session 9), and bottom right KDE is for all analyses combined. All KDE plots show peaks from ~35-24 Ma with the most prominent peaks at ~32-30 Ma. Tape mounts did not reveal a significantly younger population.

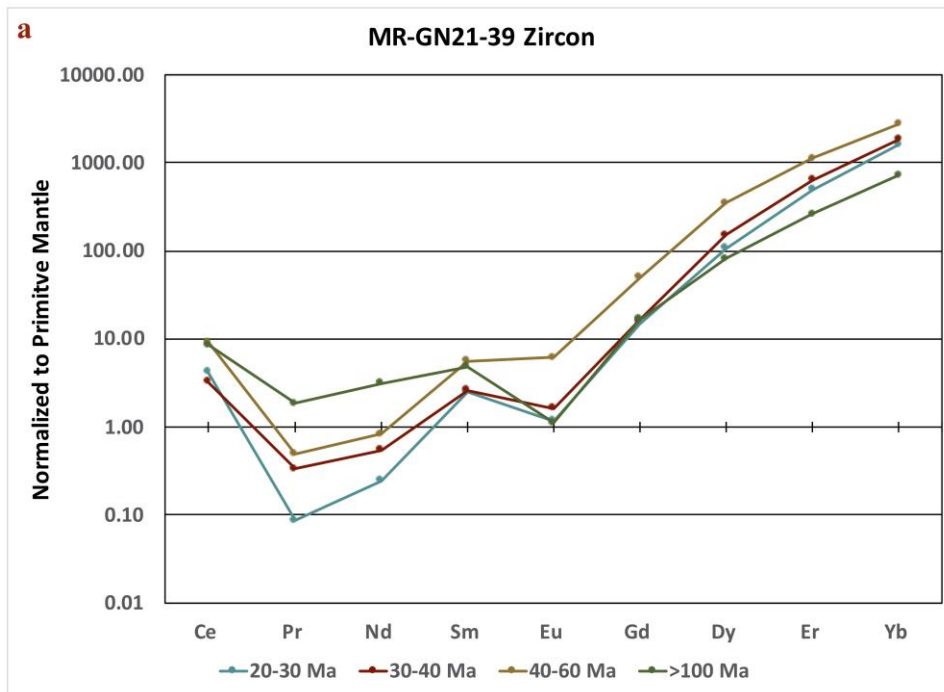
**Only one** zircon was extracted from a mafic metacumulate xenolith, i.e. two-pyroxene granulite **MR-GN21-59**. Analysis of this single zircon yielded a discordant (15.7% ; Discordance defined as  $[1 - ({}^{207}\text{Pb}/{}^{206}\text{Pb}_{\text{age}}) / ({}^{207}\text{Pb}/{}^{235}\text{U}_{\text{age}})] * 100$ )  ${}^{207}\text{Pb}/{}^{206}\text{Pb}$  age of  $1799 \pm 22$  Ma. While a Discordia age cannot be calculated from one sample analysis, this age is consistent with incorporation of Proterozoic zircon into the mafic metacumulate protolith.

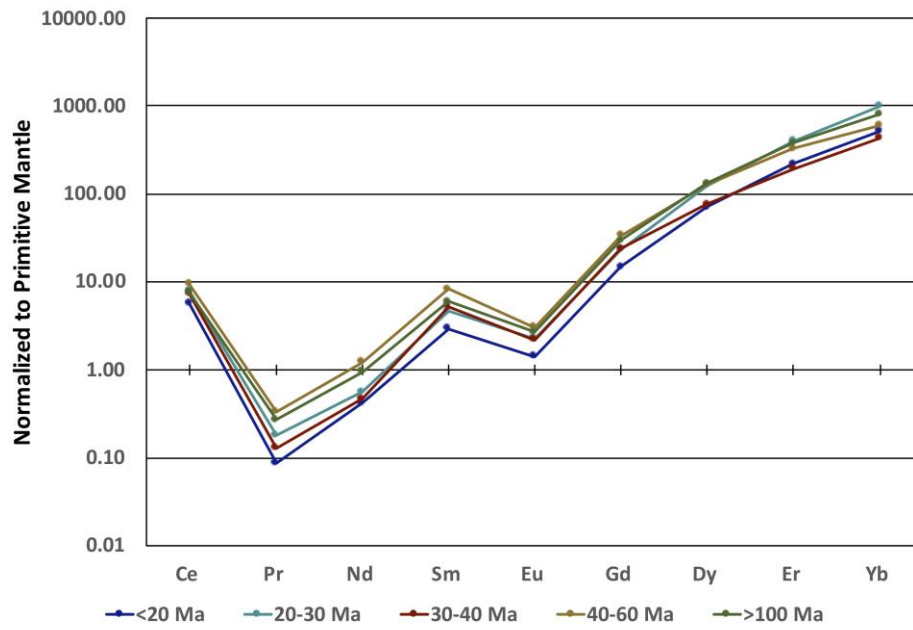
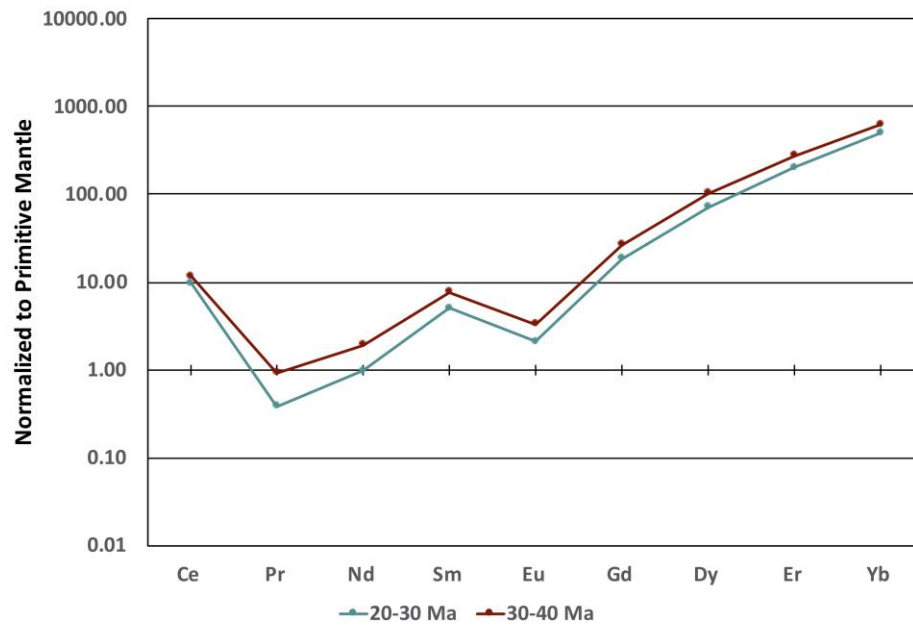
### **3.4.5. Zircon Trace Element Analyses**

Rare earth elements have been averaged for each age group for each zircon and normalized to primitive mantle values. Age groups (<20 Ma, 20-30 Ma, 30-40 Ma, 40-60 Ma, and >100 Ma) were chosen based on major age peaks on KDE plots. All zircon zones show enrichment in HREEs compared to LREEs, with a positive Ce and negative Eu anomalies, typical of zircons in granulite xenoliths worldwide (Thomas et al., 2002; Sláma et al., 2007; Koreshkova et al., 2017; Thakuridin et al., 2019; Turlin et al., 2019) (Fig. 3.25).

Ti-in-zircon temperatures were calculated according to Watson et al. (2006). Zircon from quartzofeldspathic xenolith MR-GN21-53 (Fig. 3.26 c, d) record a narrower range overall with zircon from 55-15 Ma falling within a 50°C temperature window from 750-800°C. Zircons greater than 1 Ga cover a wider temperature range from 750-850°C. In contrast, quartzofeldspathic xenolith MR-GN21-39 (Fig. 3.26 a, b) shows the greatest temperature range for zircons with ages between 50-32 Ma, with high- (>800°C) and ultrahigh-temperature (900-1100°C) zircon crystallization recorded for several grains (Harley et al. 2007). Zircons less than 32 Ma and greater than 1 Ga fall within narrower temperature ranges from 700-750°C and 750-800°C, respectively. Zircons of all ages from metadiorite xenoliths MR-GN21-34 and MR-GN22-27 exhibit narrow temperature ranges of 750-800 °C (with the exception of a few outliers; Fig. 3.26 e, f). Zircons from metadiorite MR-GN22-35 cover a narrow range at slightly higher temperatures than other

metadiorites of 800-850 °C (Fig. 3.26g). All three metadiorites appear to have small temperature peaks for zircons with ages of ~30 Ma. Nearly all calculated Ti-in-zircon temperatures are lower than two-feldspar and two-pyroxene temperatures from the same rocks, suggesting that the Ti-in-zircon temperatures do not record the peak metamorphic temperatures and do not represent ambient temperatures in the crust from which the xenoliths were entrained. Instead, the Ti-in-zircon temperatures are inherited from an earlier cooling event, presumably after formation of the Mazatzal lower crust (Ferry and Watson, 2007).



**b****MR-GN21-53 Zircon****c****MR-GN21-34 Zircon**

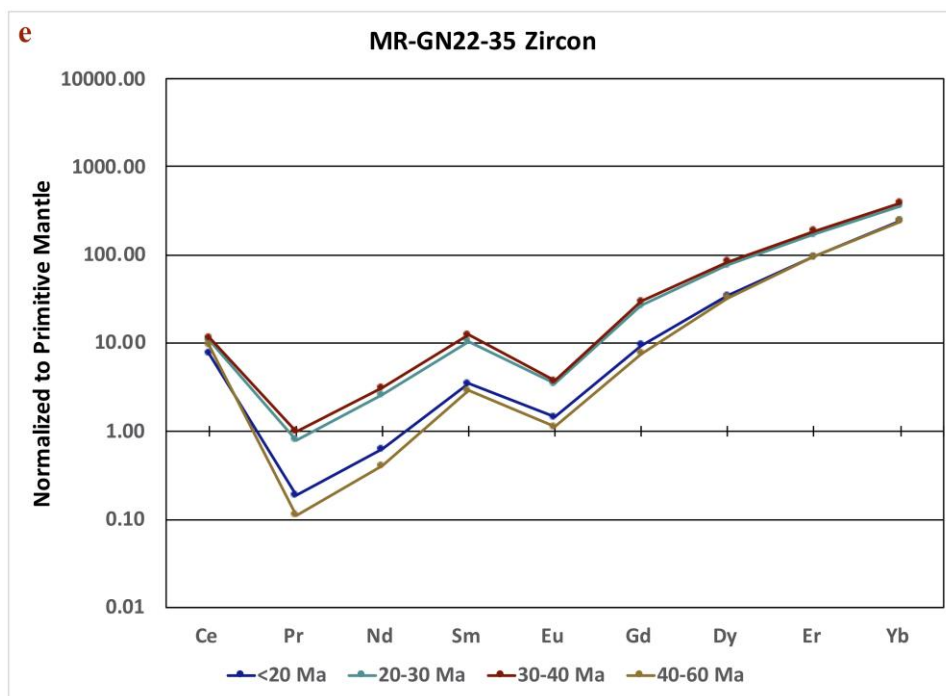
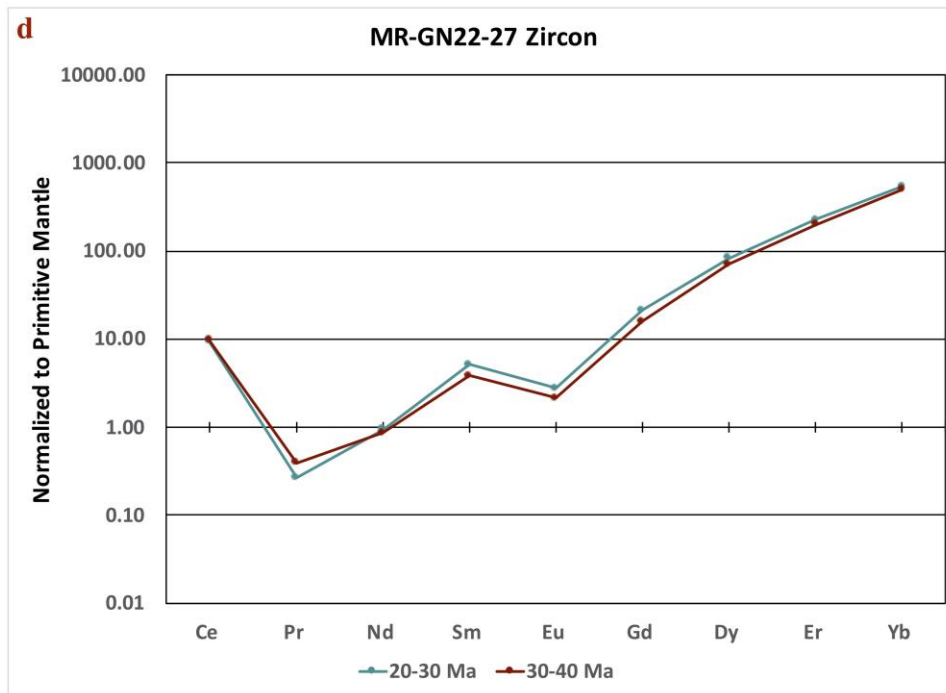
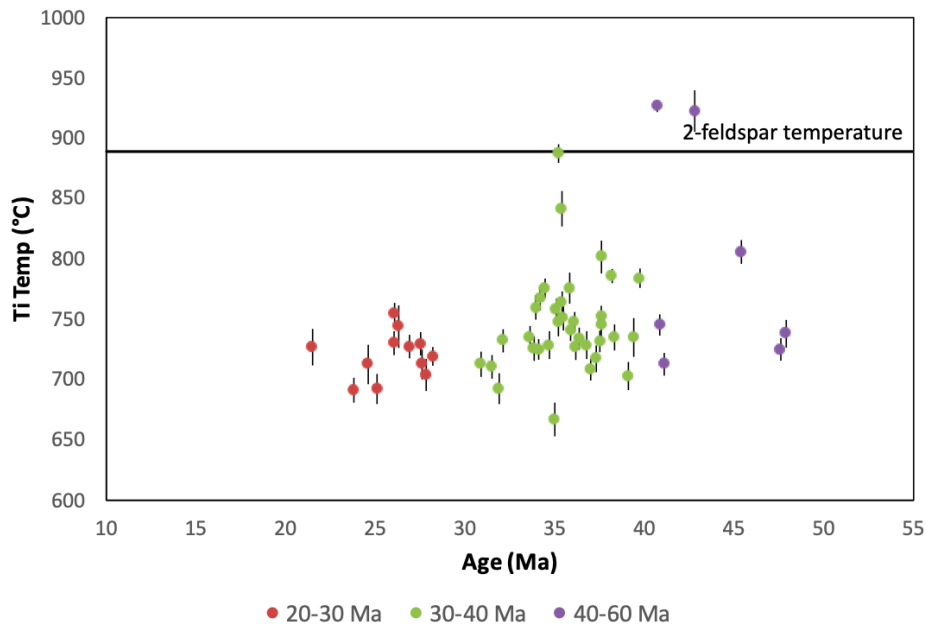


**Figure 3.25. Trace elements for zircon analyzed by LA-ICP-MS simultaneously with U-Pb.** Trace elements for each age group are averaged and plotted. Age groups were selected based off peaks on KDE plots. **a-b)** Quartzofeldspathic granulites; **c-e)** Metadiorite xenoliths.

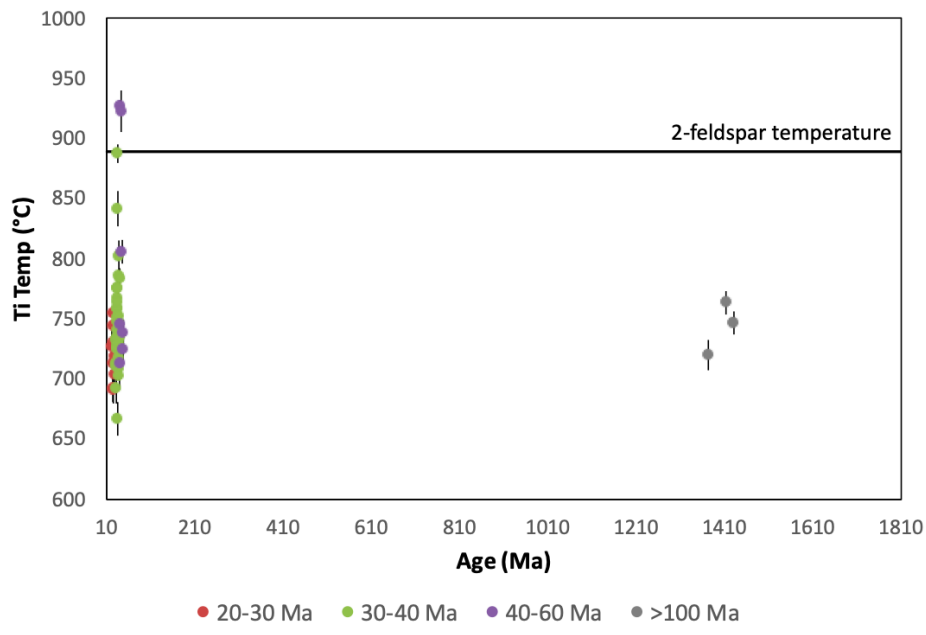
**a**

**Ti in Zircon Temperatures- MR-GN21-39**



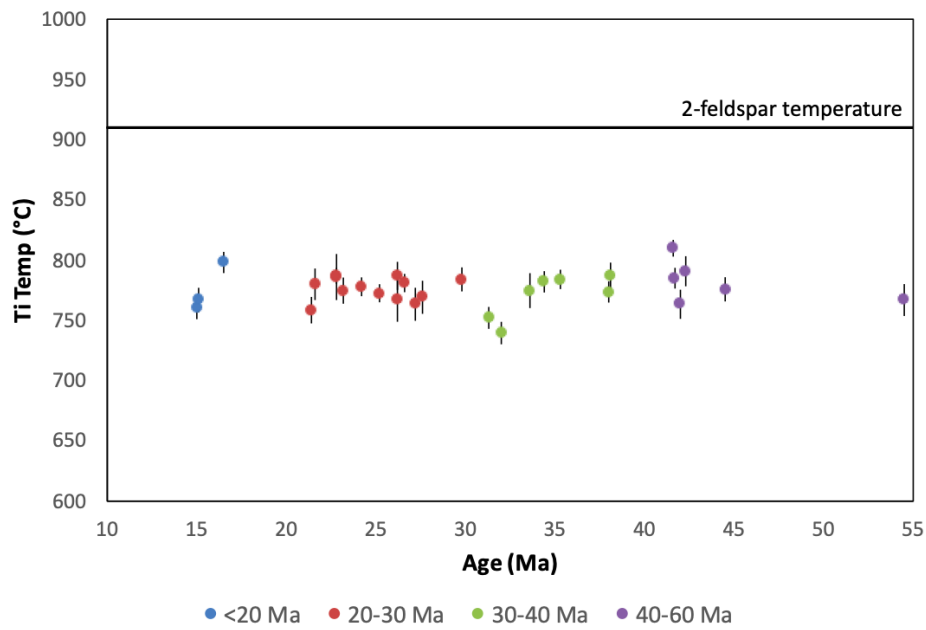
**b**

**Ti in Zircon Temperatures- MR-GN21-39**



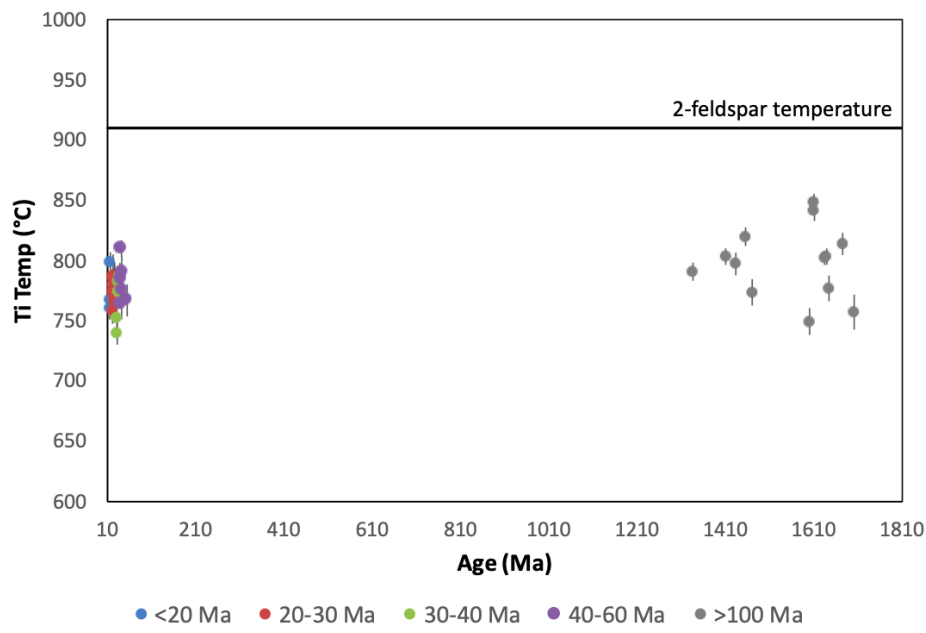
c

### Ti in Zircon Temperatures- MR-GN21-53



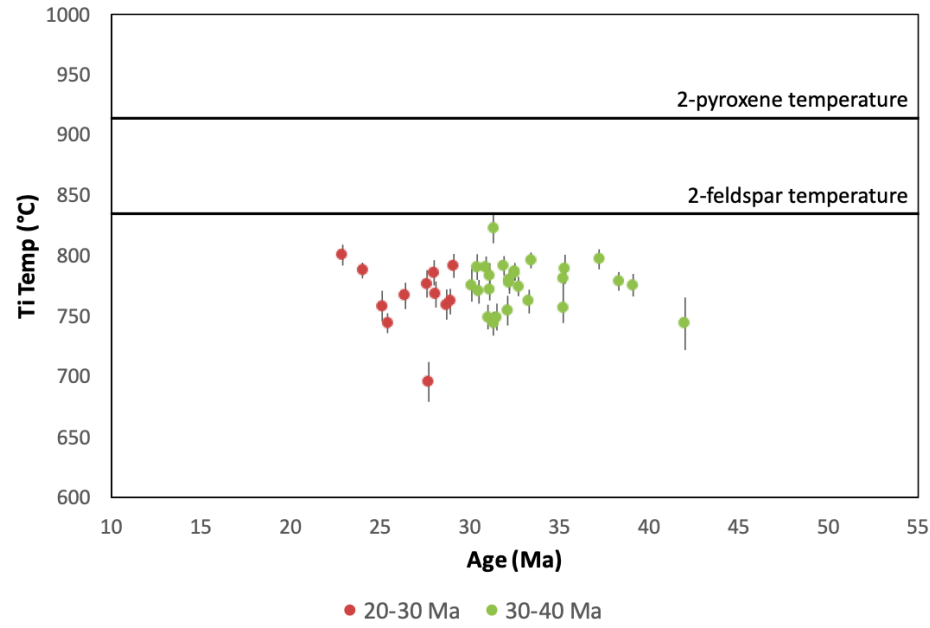
d

### Ti in Zircon Temperatures- MR-GN21-53



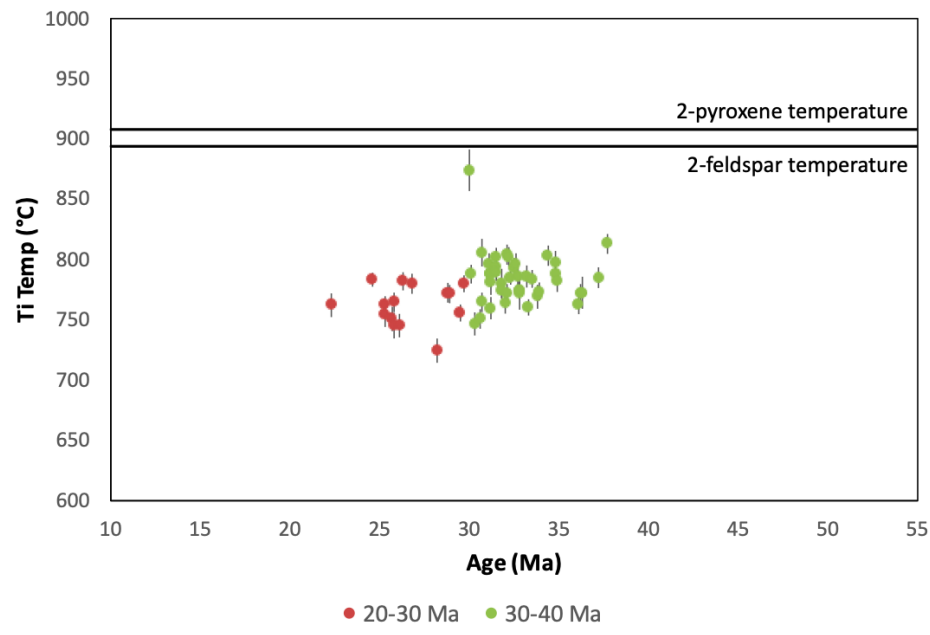
e

### Ti in Zircon Temperatures- MR-GN21-34



f

### Ti in Zircon Temperatures- MR-GN22-27



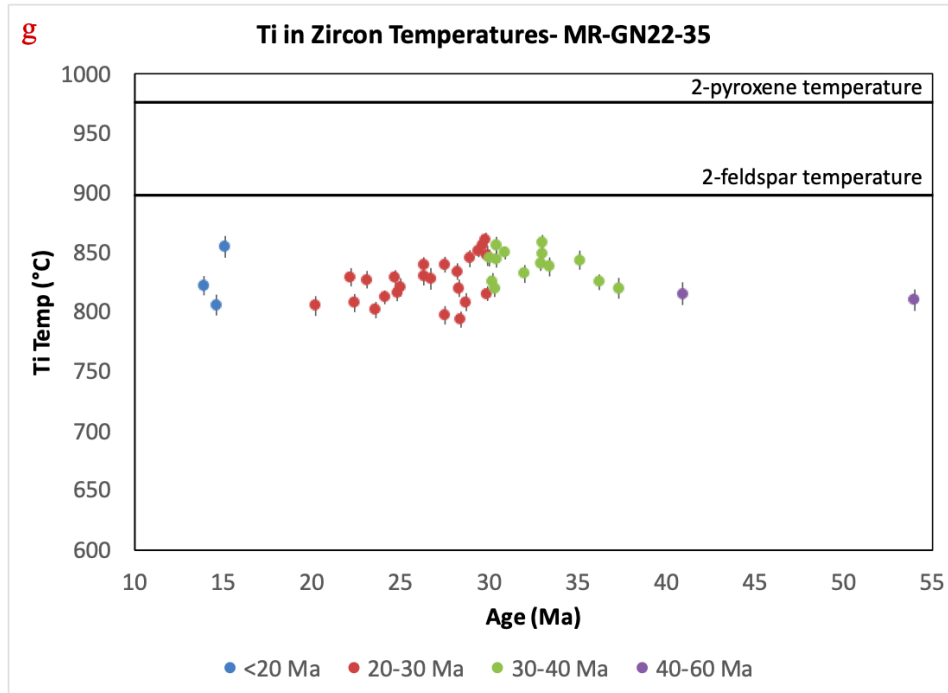


**Figure 3.26. Ti in zircon temperature vs. Age (Ma).**

**a-d)** Quartzofeldspathic granulites; **a & c)** presents zircon ages 10-55 Ma for the two quartzofeldspathic xenoliths, while **b & d)** present the whole zircon age range for these samples; **e-g)** Metadiorite xenoliths. Whole rock 2-pyroxene and 2-feldspar temperatures indicated where available.

### 3.4.6. Zircon Hf Isotopes

Zircon from quartzofeldspathic and metadiorite xenoliths with mid-Cenozoic ages exhibit a wide range of  $\epsilon\text{Hf}(t)$  values ranging from -17 to 0. In contrast, zircon cores from quartzofeldspathic granulites MR-GN21-39 and MR-GN21-53, which yielded Mesoproterozoic ages, have positive  $\epsilon\text{Hf}(t)$  values. Other than these old cores,  $\epsilon\text{Hf}(t)$  values for core and rim structures are indistinguishable, forming an array of negative to neutral values, with significant overlap among the samples (Fig. 3.27 & Fig. 3.28). Assuming separation from depleted mantle at the time of Mazatzal terrane formation (i.e. ~1.65 Ga), isotopic evolution lines have been plotted for average continental crust ( $^{176}\text{Lu}/^{177}\text{Hf} = 0.010\text{-}0.015$ ) and more mafic lithologies ( $^{176}\text{Lu}/^{177}\text{Hf}$

= 0.018, 0.022) (Spencer et al., 2020). Although such evolution lines encompass ~75% of the data, even the evolution line for the most mafic crustal composition (highest Lu/Hf) is unable to account for the least negative  $\epsilon\text{Hf}$  values, i.e. those above a  $\epsilon\text{Hf}(t)$  value of  $-5$ . Conversely, even the evolution curve for the most felsic crustal composition (i.e.  $^{176}\text{Lu}/^{177}\text{Hf} = 0.01$ ) is unable to account for the compositions of 3 of the 4 older cores.

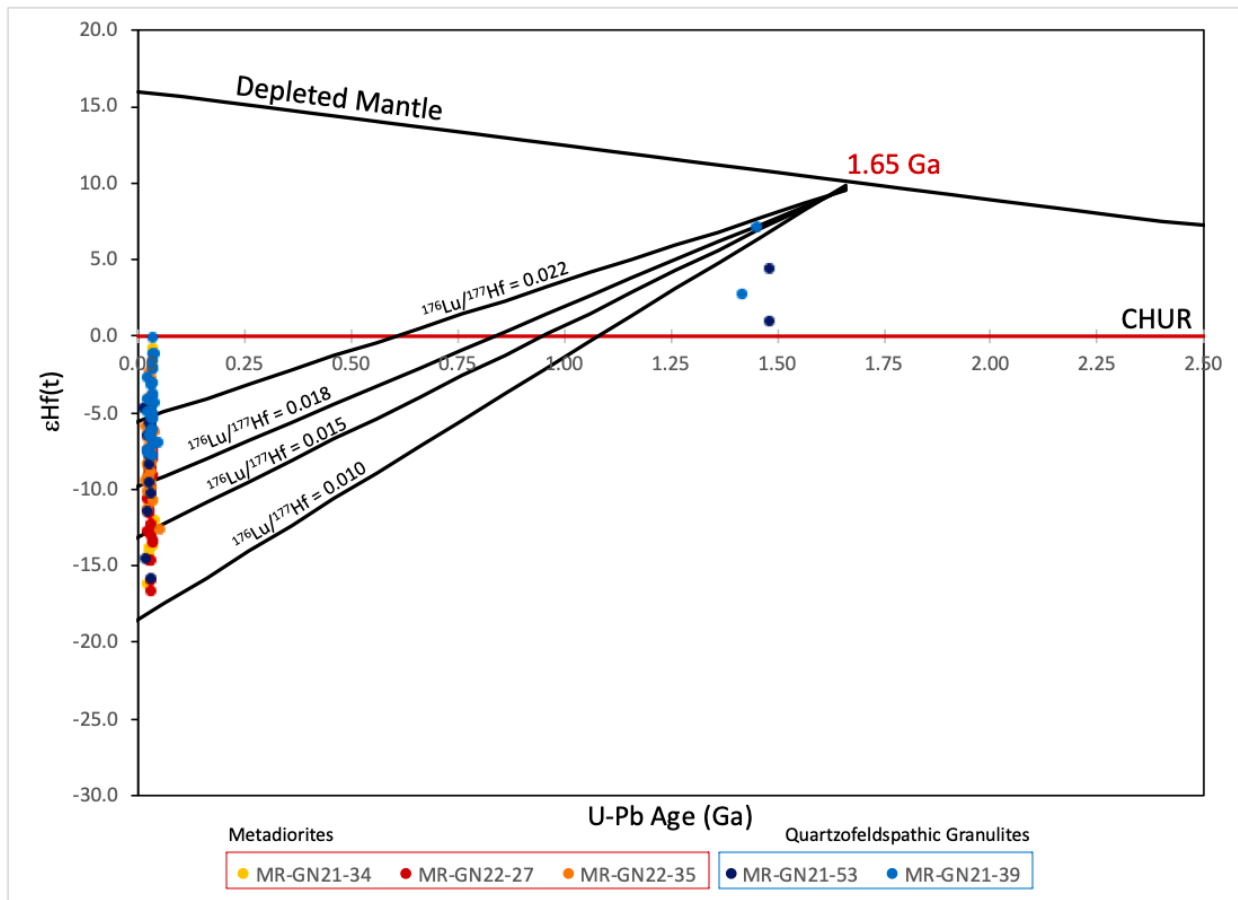


**Figure 3.27. Hf isotope analysis for three metadiorites and two quartzofeldspathic samples.** Crustal evolution lines plotted from Mazatzal formation at ~1.65 Ga. Isotopic evolution lines have been plotted for average continental crust ( $^{176}\text{Lu}/^{177}\text{Hf} = 0.010, 0.015$ ) and more mafic lithologies ( $^{176}\text{Lu}/^{177}\text{Hf} = 0.018, 0.022$ ).

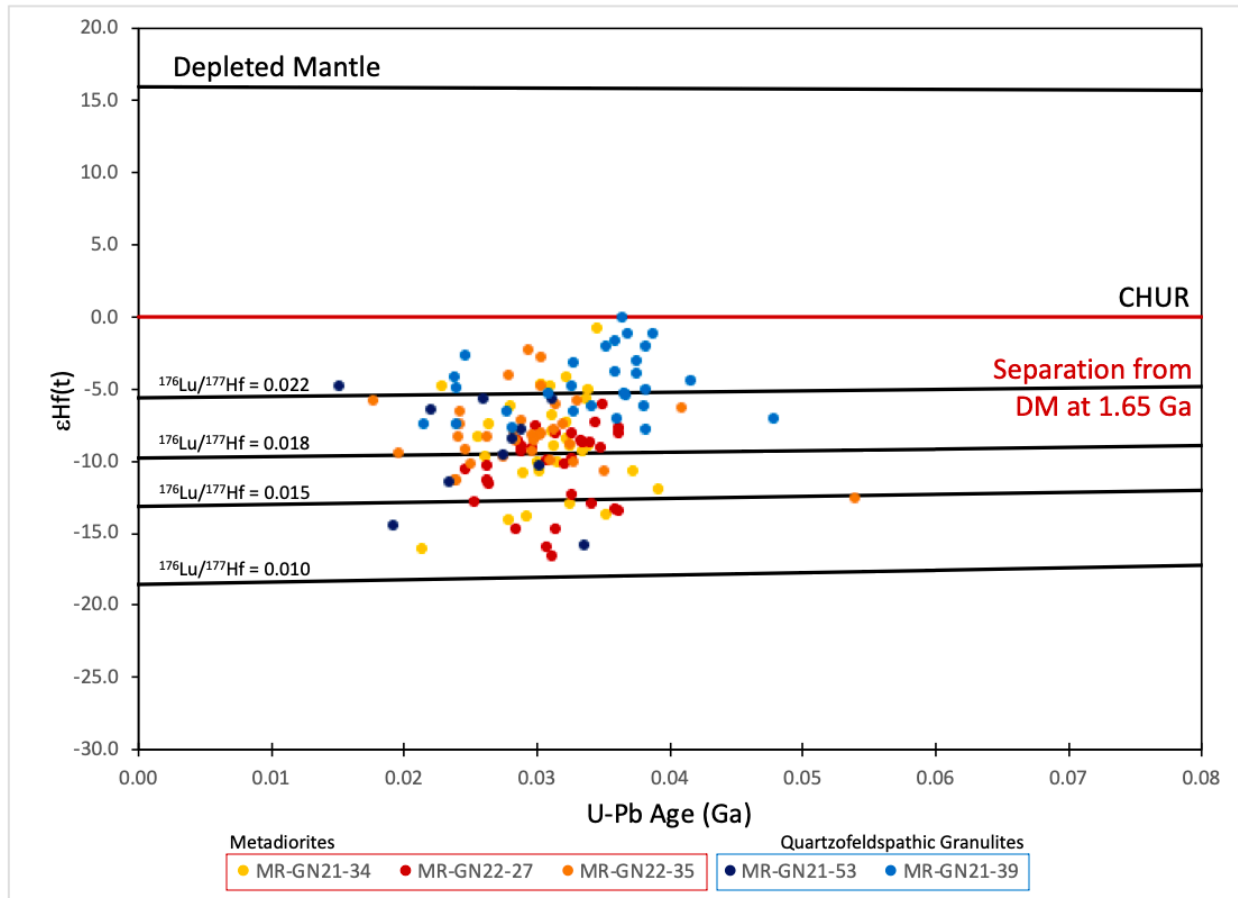


**Figure 3.28. Hf isotope analyses, with crustal evolution lines from 1.65 Ga. Expanded to view the last 80 m.y.**

## 3.5. Discussion

### 3.5.1. Lower Crustal Temperatures

An important first-order question for the GVF granulite xenoliths is to determine whether they are derived from the lower crust or some other crustal horizon. Calculated equilibration temperatures range from ~830-987°C (Table 3.4). Given the absence of garnet, pressures of equilibration, i.e. depth, have been assumed using an estimated geotherm. Padovani and Carter (1977) proposed a geothermal gradient of 30°C/km for the Basin and Range, which equates to pre-entrapment residence depths for the granulites of ~28-33 km (Fig. 3.29). This depth range corresponds with the base of the seismically determined lower crust in the northern Basin and Range (Klemperer et al., 1986). Similar seismic studies have not been performed across SE Arizona, so we can only infer a similar crustal structure to that reported by Klemperer et al. (1986). Plank and Forsythe (2016) proposed a thicker average crustal thickness of ca. 36 km, but they also proposed a lower geothermal gradient (18-29°C/km) for most areas across the western U.S. (Fig. 3.29). Extrapolation to these geothermal estimates would place the GVF granulites at greater depths of origin, e.g. ca. 40-45 km (Fig. 3.29), i.e. within the lithospheric mantle. This indicates that either these geotherms are too low or the position of the crust-mantle boundary in SE Arizona is deeper than that elsewhere across the western U.S.

The temperatures calculated for the GVF granulites are also much higher than others proposed for lower crustal temperatures. For example, Proterozoic lower crust in the Baltic shield ranges from 500-700°C (Artemieva, 2003). However, other tectonically active regions, such as the Pannonian Basin and Pali Aike show temperatures ranging from 930-970°C and 850-910°C, respectively (Kempton et al., 1997; Selverstone, 1982).

In this context, it is significant that the calculated equilibration temperatures for the GVF granulites (Table 3.4) overlap those calculated by two-pyroxene geothermometry for Type II ultramafic xenoliths (901-1084°C) from the same locality (Kempton, 1984) (Fig. 3.28). Type II xenoliths (i.e. cpx + olivine-rich rocks) are interpreted as ultramafic cumulates from basaltic magmatism; as such, they may be related to the same processes that formed the mafic metacumulate lower crustal rocks. These two-pyroxene temperatures for Type II xenoliths, however, are calculated from clinopyroxene – orthopyroxene exsolution pairs, i.e. they are cooling/re-equilibration temperatures. New equilibration temperatures for these and other Type II xenoliths that lack pyroxene exsolution have been calculated on the basis of Al-in-olivine (Coogan et al., 2016). These temperatures of equilibration are higher on average, ranging from 990° to 1230°C (Zweifelhofer et al., 2018). Thus, these elevated temperatures suggest that the lower crust in this region was still undergoing metamorphism at the time of xenolith entrainment and GVF eruptions. This recent metamorphism is reflected in some of the zircon CL images with recrystallization and dissolution precipitation, as well as in zircon U-Pb geochronology discussed below. Moreover, the geothermometry data suggest that if the accreted Mazatzal terrane ever had a thick crustal root, that material has been lost; either delaminated or tectonically scraped off during Farallon flat slab subduction.

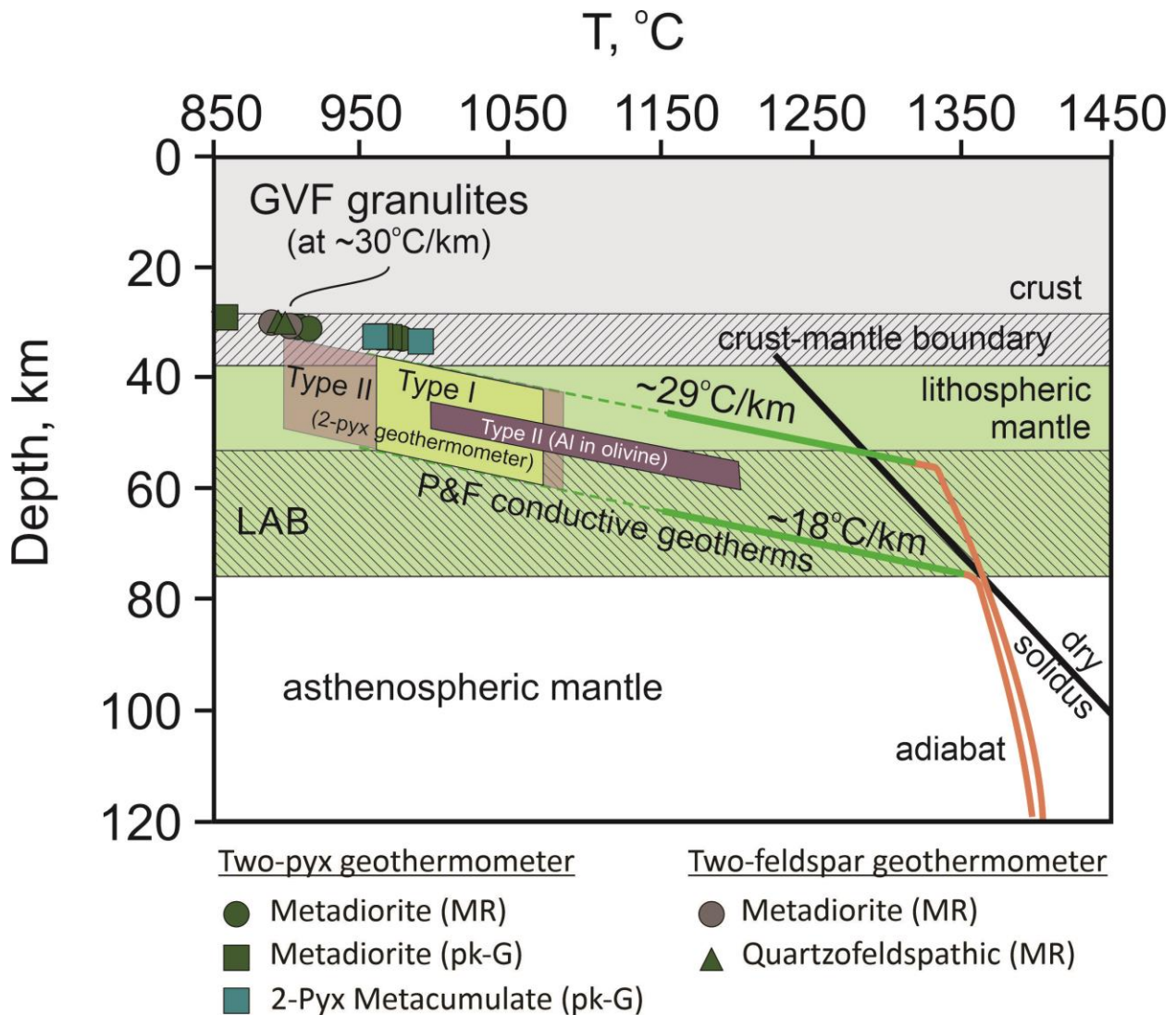


**Figure 3.29. Geothermometry Data with 30°C/km against Plank and Forsythe (2016) Conductive Geotherms**

GVF granulites plotted with a 30°C/km geotherm. Geothermal gradients (18-29°C/km) proposed by Plank and Forsythe plotted in green. The brown parallelogram represents 2-pyx thermometry for Type II pyroxenites; the green parallelogram is for Type I lherzolites; the darker brown bar shows the range of temperatures calculated for the Al in olivine thermometer. Because of the nature of the two geothermometers used, there is no overlap in the samples that were used for two-pyroxene and Al-in olivine T calculations for the Type II xenoliths. These higher temperatures, though, suggest they've recorded the higher magmatic textures for these cumulate xenoliths.

### 3.5.2. Lower Crustal Composition in SE Arizona

In light of the geothermometry discussed in Section 3.5.1, it is worth comparing the compositions of the GVF granulite xenoliths with estimated average crustal compositions (e.g., Rudnick and Gao, 2014). Fig. 3.30 shows that most metacumulate xenoliths have either lower  $\text{SiO}_2/\text{Al}_2\text{O}_3$  or higher Mg#s or both, relative to proposed average lower crust. Metadiorites have similar  $\text{SiO}_2/\text{Al}_2\text{O}_3$  but are more evolved than the proposed average lower crust, having lower Mg#s (i.e. <60). In contrast, the Mg# of average middle crust plots within the range of metadiorites, but its proposed composition is more evolved in terms of  $\text{SiO}_2/\text{Al}_2\text{O}_3$ . The quartzofeldspathic xenoliths have higher  $\text{SiO}_2/\text{Al}_2\text{O}_3$  than either middle or upper crust, although they have similar Mg numbers to the latter. In summary, there is not a clear relationship between the average crustal major element compositions and the GVF granulite xenoliths.

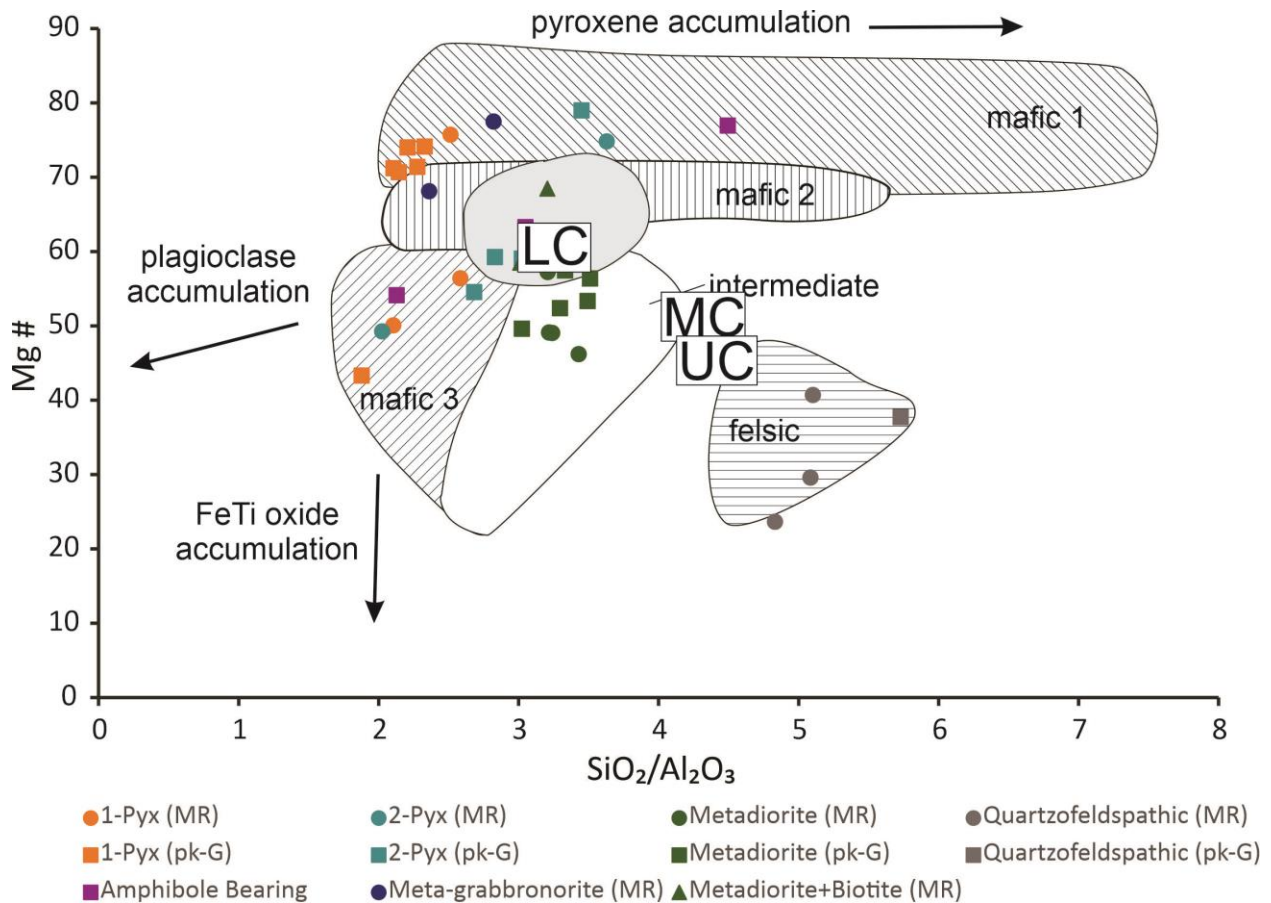


**Figure 3.30. Whole rock Mg# vs. SiO<sub>2</sub>/Al<sub>2</sub>O<sub>3</sub>.**

Plotted data are anhydrous. Data for both new (MR-GN) and old (pk-G) data sets are plotted. Fields were defined by Kempton and Harmon (1992). Amphibole bearing samples were part of the original sample set (Kempton et al., 1990). Average compositions for upper (UC), middle (MC) and lower crust (LC) have been added (Rudnick and Gao, 2014).

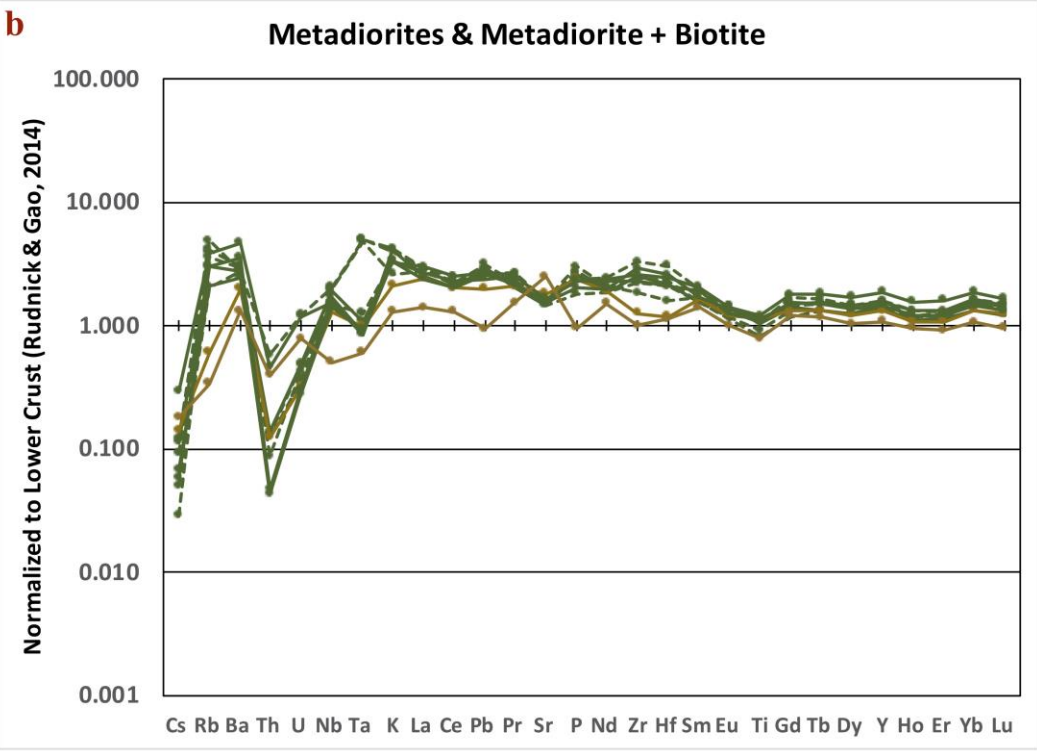
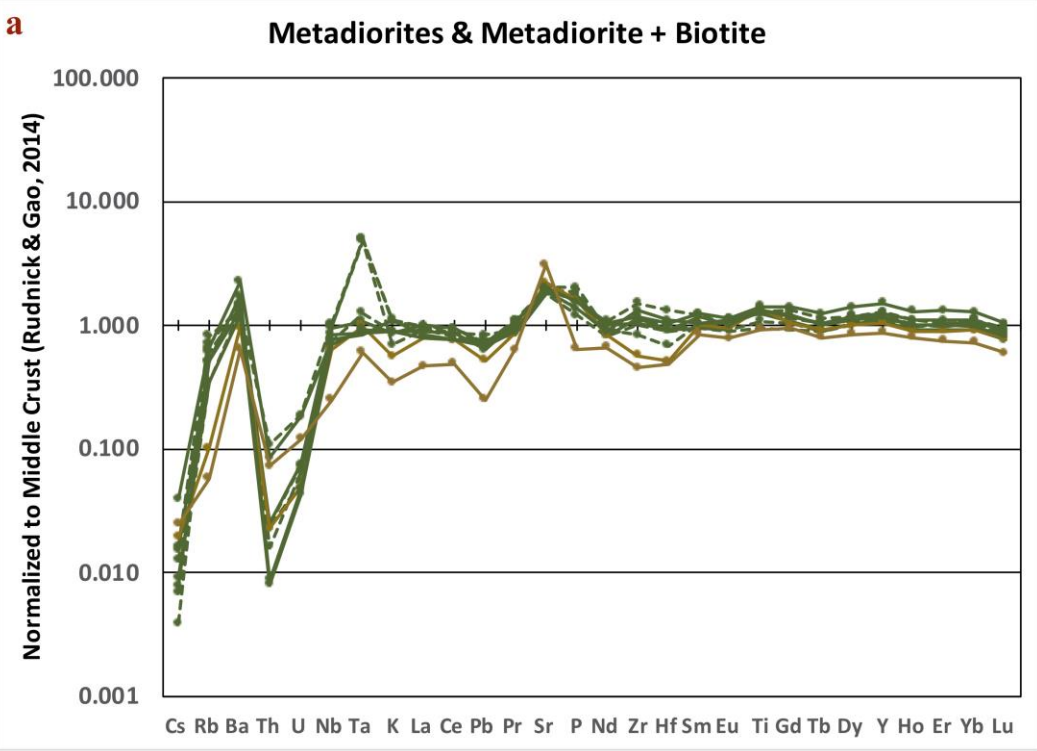
Figure 3.31 compares the GVF xenolith data to average lower (Fig. 3.31 b,d,f,h) and middle (Fig. 3.31 a,c,e,g) crustal trace element compositions proposed by Rudnick and Gao (2014). Not surprisingly, metacumulate xenoliths deviate significantly from average lower and middle crust, with both lower overall trace element contents (i.e. normalized values <1) for most, but also significant relative depletions in Cs, Pb, and Th, and strong positive enrichments in Rb and Sr. Although the similarity is poor for both lower and middle crustal averages, there is a slightly better

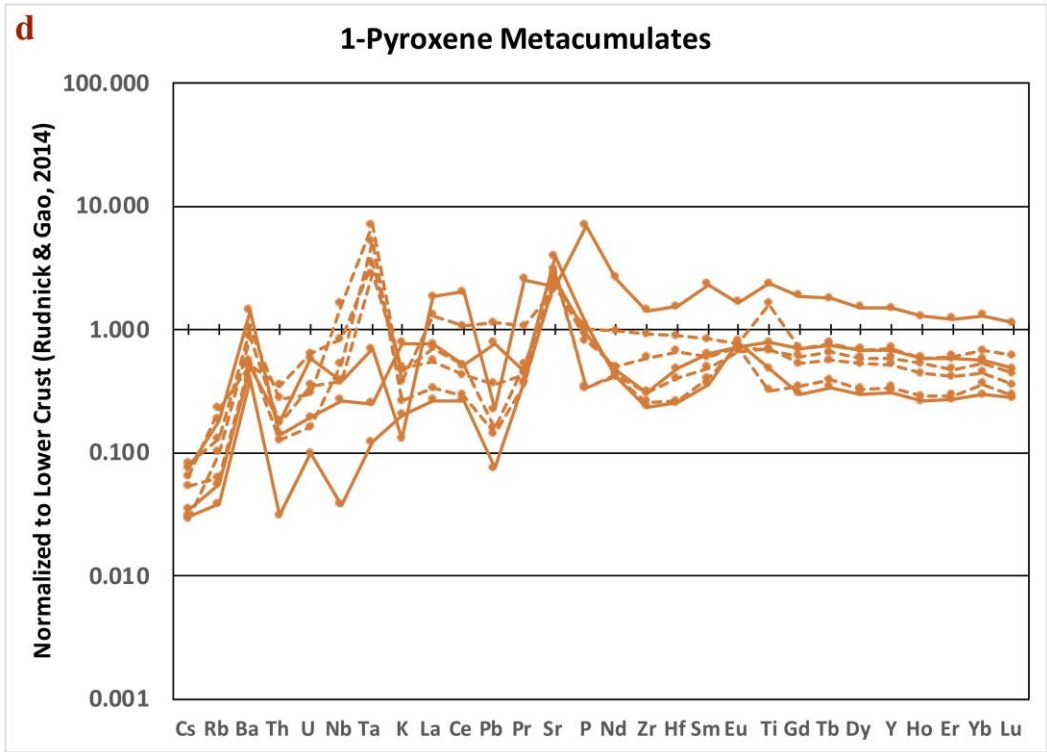
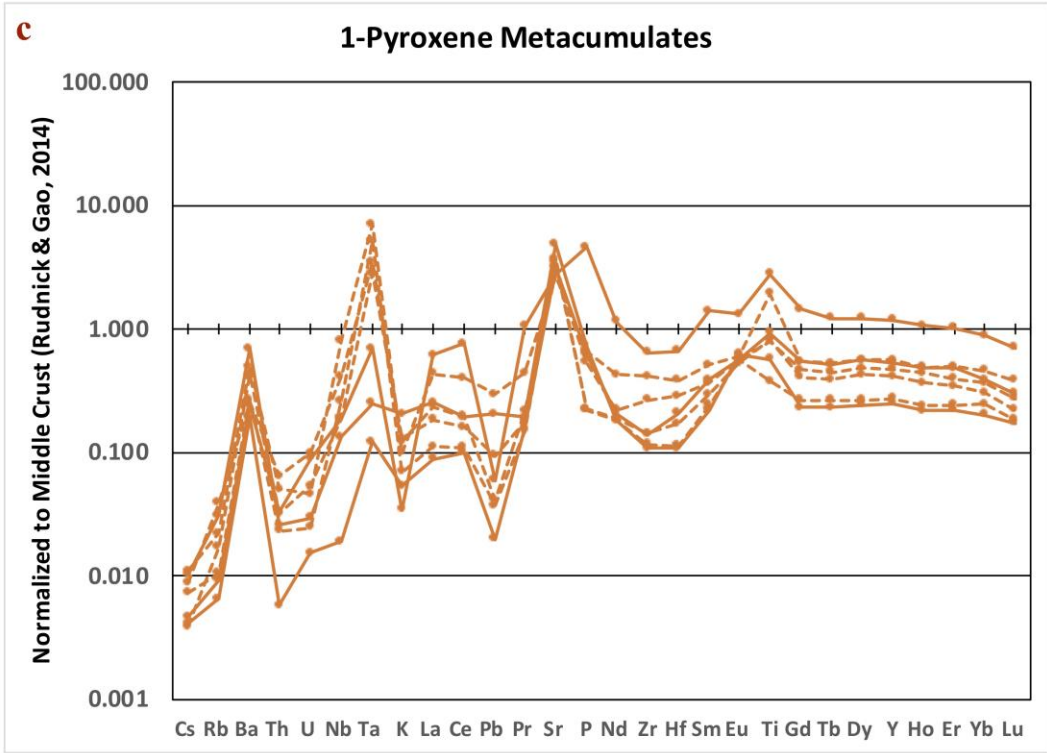
match between metacumulate samples and the average lower crust (Figs. 3.31 d and f) than with middle crust (Figs. 3.31 c and e).

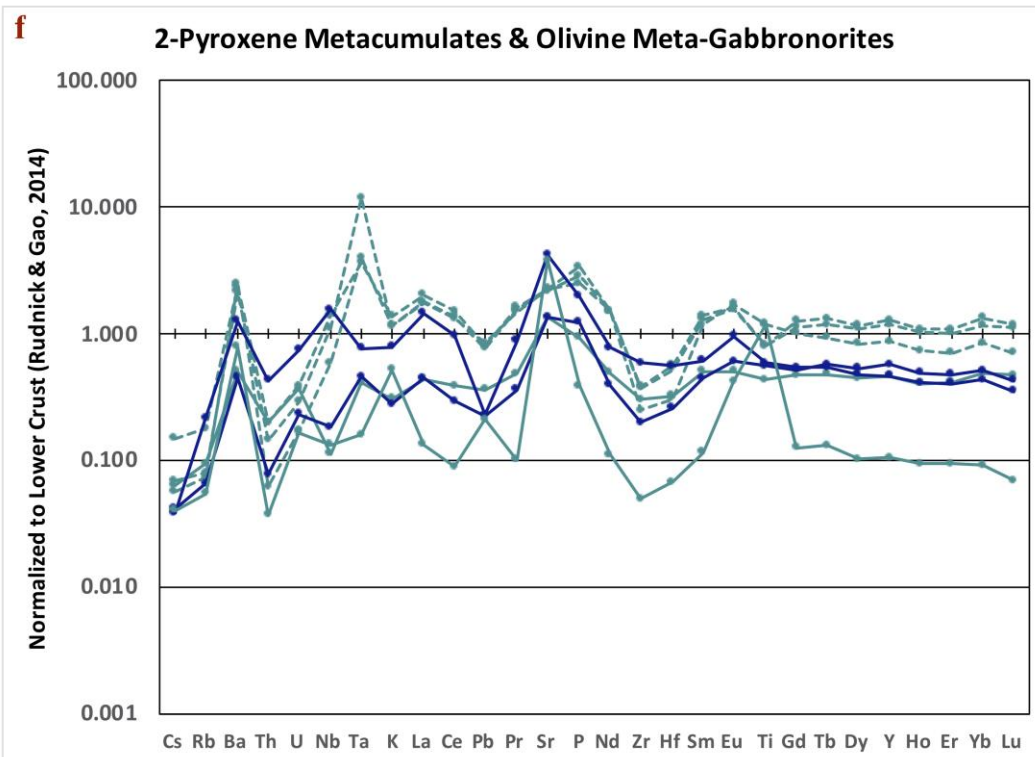
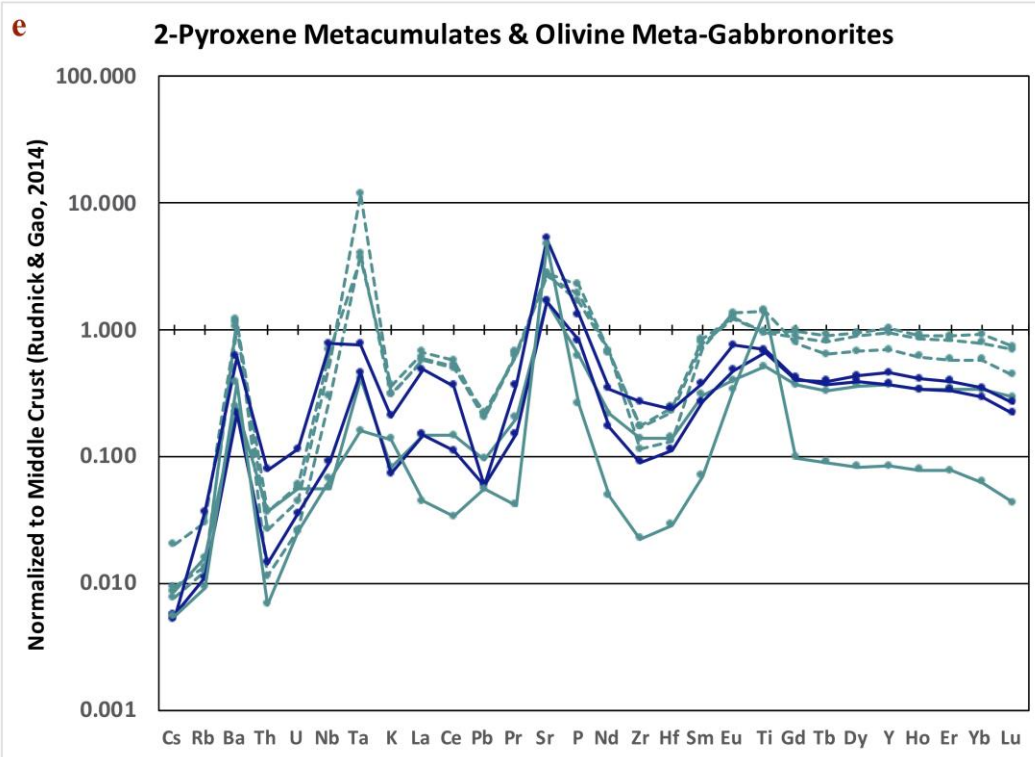
In contrast, the GVF metadiorites are more similar to middle crust than lower crust, i.e. the normalized values are closer to 1. However, they are significantly depleted in Cs, Th and U (Fig.31a). Quartzofeldspathic sample, pk-G-GN22-5 shows a trace element pattern similar to that of metadiorites, though with higher overall trace element concentrations and relative depletions for Ba, P, Eu and Ti. However, in contrast to all other GVF lower crustal xenoliths, this sample does not show the strong depletions in Th and U. The three other quartzofeldspathic xenoliths have very different patterns from pk-G-GN22-5, with lower concentrations of most incompatible trace elements and strong positive enrichments in elements that are hosted in feldspar, particularly K-feldspar, i.e. Rb, Ba, K, Pb and Sr, with two samples (MR-GN21-16 and MR-GN21-39) showing an unusual enrichment in HREE relative to MREE. Compositional differences for MR-GN21-16 and MR-GN21-39 indicate a very different petrogenetic history for these quartzofeldspathic lithologies. Although beyond the scope of this thesis to model, we believe these samples represent restite compositions, produced during dehydration melting during breakdown of a hydrous phase, possibly amphibole. Amphiboles are known to have higher partition coefficients for MREE relative to HREE, such that extraction of this phase by partial melting could leave behind a residue with the inverse pattern. Such a melt extraction event could explain the significant difference in the zircon geochronology for the different quartzofeldspathic xenoliths (see Discussion on geochronology, Section 3.5.3).

The greater similarity of metadiorites to middle crustal estimates and quartzofeldspathic granulite pk-G-GN22-5 to upper crustal estimates (Fig. 3.32) is consistent with a crustal history in which an earlier lower crust root has been removed by delamination or tectonic erosion, exposing

what was previously middle crust, converting the middle crust (i.e. the metadiorites) into the de facto lower crust and the upper crust (i.e. quartzofeldspathic granulites) into middle crust.







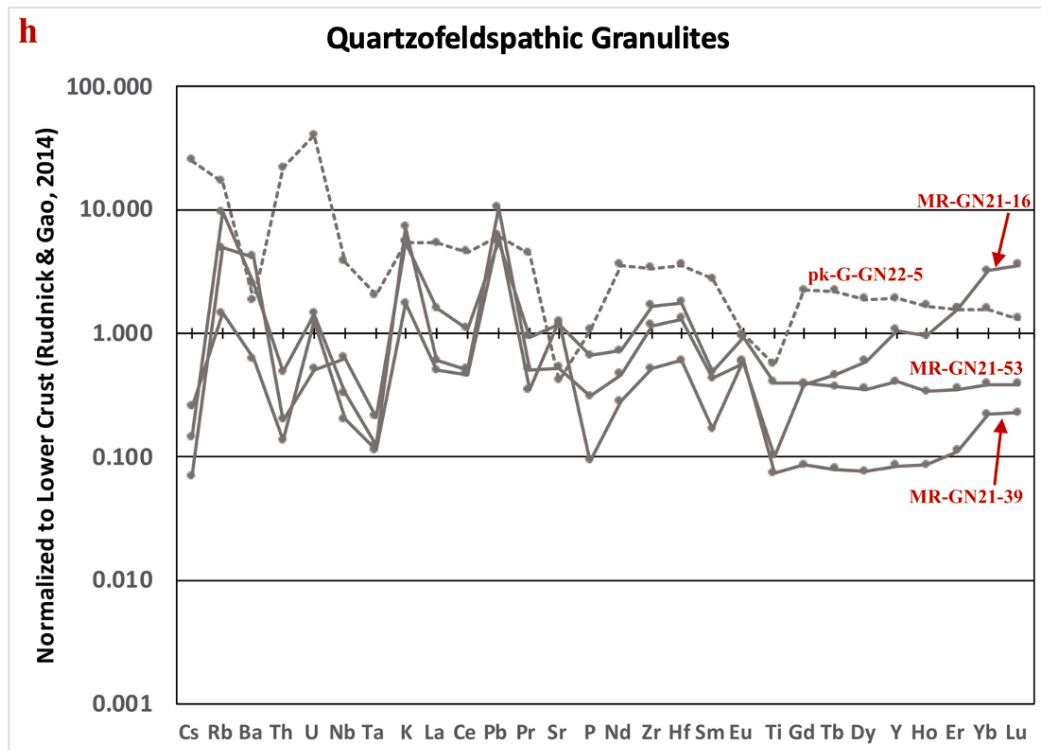
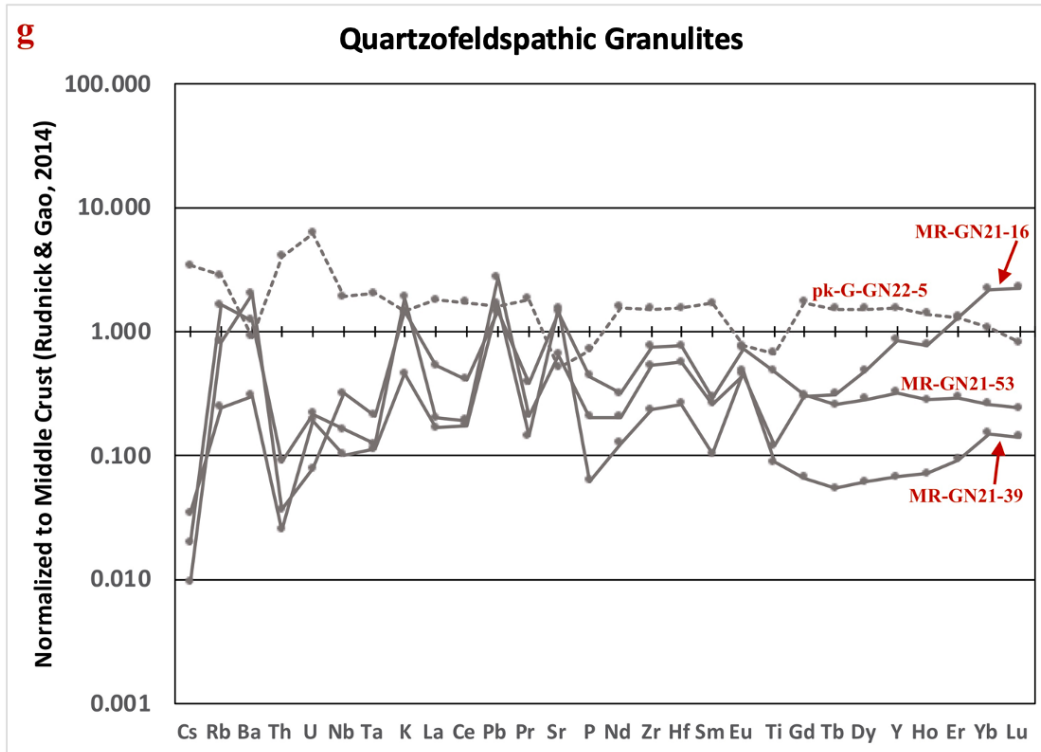


**Figure 3.31. Spider diagrams for whole rock trace element analyses normalized to middle and lower crust.**

Spider diagrams for whole rock trace element analyses, **normalized to middle (a, c, e, g) and lower crust (b, d, f, h)**. Decreasing incompatibility from left to right. The solid line in a-d represent new data and the dashed lines are reanalyzed from the original sample set. **a-b)** Metadiorites are shown in green while metadiorite-type xenoliths with biotite are shown in brown. **c-d)** One-pyroxene metacumulates shown in orange. **e-f)** Two-pyroxene metacumulates shown in teal and olivine meta-gabbronorites in dark blue. **g-h)** Quartzofeldspathic granulites shown in grey.

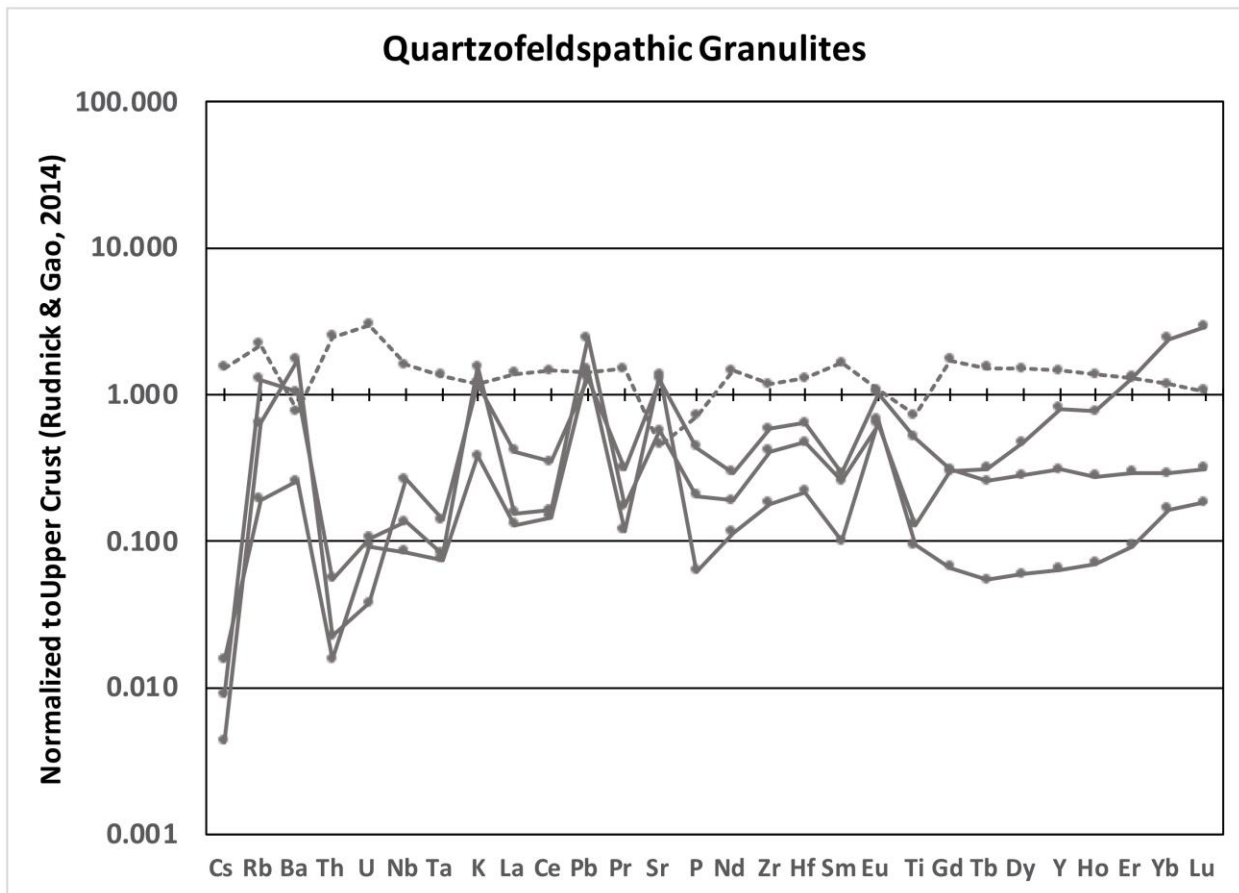


**Figure 3.32. Spider diagram for whole rock trace element analyses of quartzofeldspathic granulites normalized to upper crust.**

Decreasing incompatibility from left to right. The solid lines represent new data, and the dashed line is reanalyzed from the original sample set.

### 3.5.3. Geologic History of SE Arizona as Evidenced by U-Pb and Hf Geochronology

GVF xenoliths present three distinct zircon age populations at ~1.64-1.65 Ga, ~1.48-1.42 Ga, and ~76-2 Ma, with the majority of young ages concentrated around 35-25 Ma. Quartzofeldspathic xenoliths, pk-G-GN22-5 and pk-G-GN22-10, present evidence for the oldest geologic events at ~1.64 Ga, consistent with the timing of Mazatzal terrane formation (e.g. Whitmeyer and Karlstrom, 2007). One zircon core in pk-G-GN22-5 was dated at  $2.43 \pm 0.03$  Ga, and the whole rock Nd-model age is ~2.2 Ga (Kempton et al., 1990), which provides tantalizing evidence for an older history in this crustal block.

Hf-isotope data from two quartzofeldspathic xenoliths (MR-GN21-39 and MR-GN21-53) provide additional support for existence of an older, Paleoproterozoic, crustal component. No crustal evolution lines that separate from depleted mantle at 1.65 Ga can explain the old Paleoproterozoic zircon (Fig. 3.27). Additionally, the more intermediate to mafic evolution lines ( $^{176}\text{Lu}/^{177}\text{Hf} = 0.015\text{-}0.022$ ) cannot explain a large portion of the Hf data for the Cenozoic zircons (Fig. 3.28). An earlier separation from depleted mantle at ~2.4 Ga, following an intermediate evolution line, encompasses all the data available. However, with separation from depleted mantle in the early Paleoproterozoic, Mesoproterozoic zircon  $\epsilon\text{Hf}(t)$  should cluster around -5 (Fig. 3.33). Instead, Mesoproterozoic zircon have a smear of  $\epsilon\text{Hf}(t)$  values from +1 to +7, suggesting a later Proterozoic contribution of depleted mantle, likely at the time of Mazatzal formation, ca. 1.65 Ga (Fig. 3.35). The  $\epsilon\text{Hf}(t)$  values of the 1.65 Ga zircons are therefore best explained by a mixing or Hf isotope homogenization event during crust formation.

U-Pb geochronology for zircon cores from the quartzofeldspathic xenoliths (MR-GN21-39 and MR-GN21-53) yielded discordant U-Pb ages that trend toward ~1.64 Ga and ~1.48-1.42 Ga upper intercepts, further supporting lower crustal modification beginning in the Mazatzal and later

alteration at ~1.48 Ga, at onset of the Picuris orogeny (Daniel et al., 2013, Holland et al., 2020) and the 1.48-1.35 Ga A-type magmatism in the southwestern US (Whitmeyer and Karlstrom, 2007). Igneous cores of MR-GN21-39 and MR-GN21-53, have igneous and metamorphic overgrowths with young ages from ~50-15 Ma, suggesting lower crustal heating and partial melting during Cenozoic magmatism. Hf isotope data support this interpretation; following an intermediate crustal evolution ( $^{176}\text{Lu}/^{177}\text{Hf} = 0.018$ ; Roberts and Spencer, 2015) beginning at 2.4 Ga, data for Cenozoic zircon in the quartzofeldspathic samples should cluster just above  $-20 \epsilon\text{Hf}(t)$  (Fig. 3.33 & 3.34). The large range of  $\epsilon\text{Hf}(t)$  values in the young overgrowths for these two samples, ranging from -16 to 0, is consistent with contamination by a young radiogenic source, likely during Farallon slab subduction ~70-60 Ma and subsequent asthenospheric upwelling associated with slab foundering and/or rollback (Fig. 3.35).

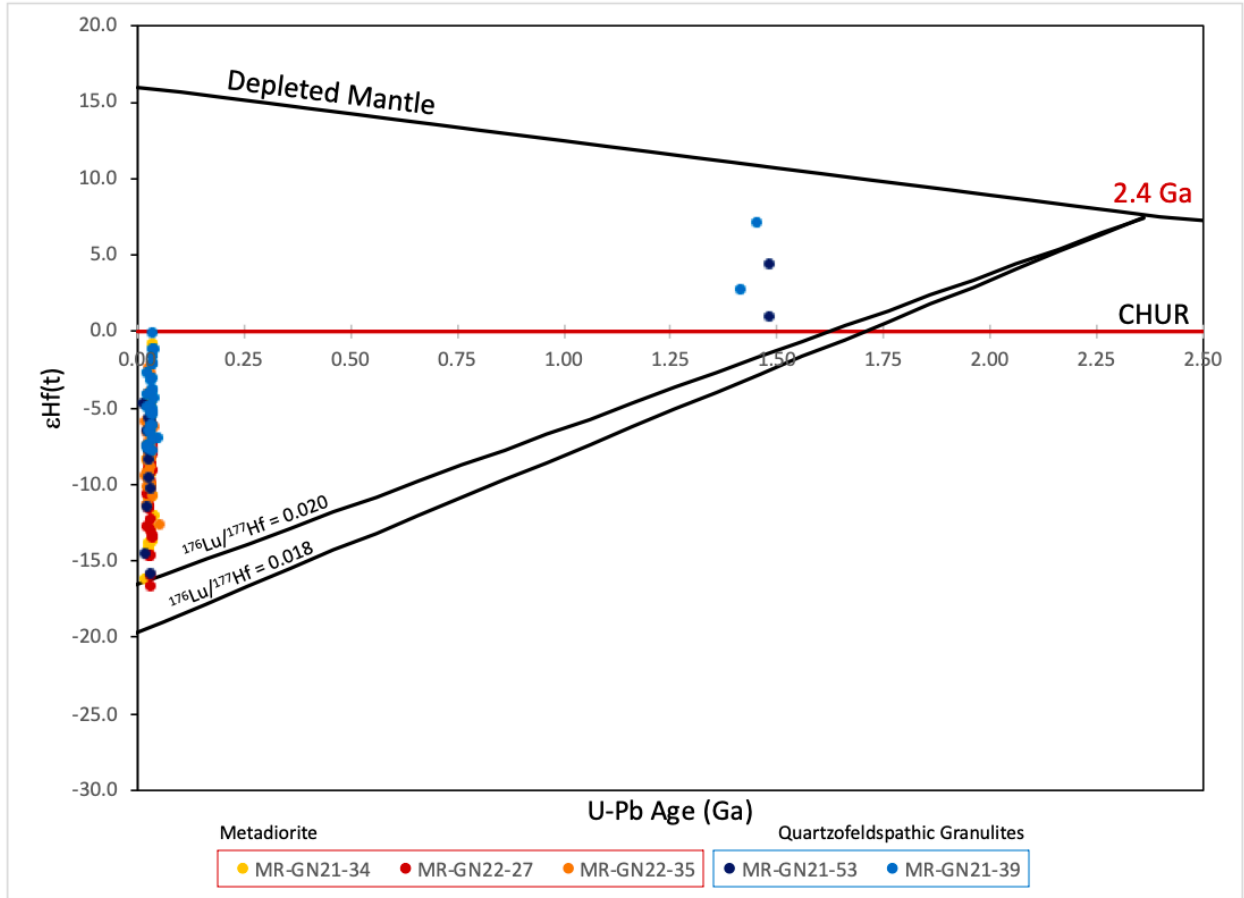


**Figure 3.33. Hf isotope analyses, with crustal evolution lines from 2.4 Ga.**

Hf isotope analysis for three metadiorites and two quartzofeldspathic samples. Evolution lines for intermediate ( $^{176}\text{Lu}/^{177}\text{Hf} = 0.018$ ) to mafic lithologies ( $^{176}\text{Lu}/^{177}\text{Hf} = 0.020$ ) are plotted from ~2.4 Ga.

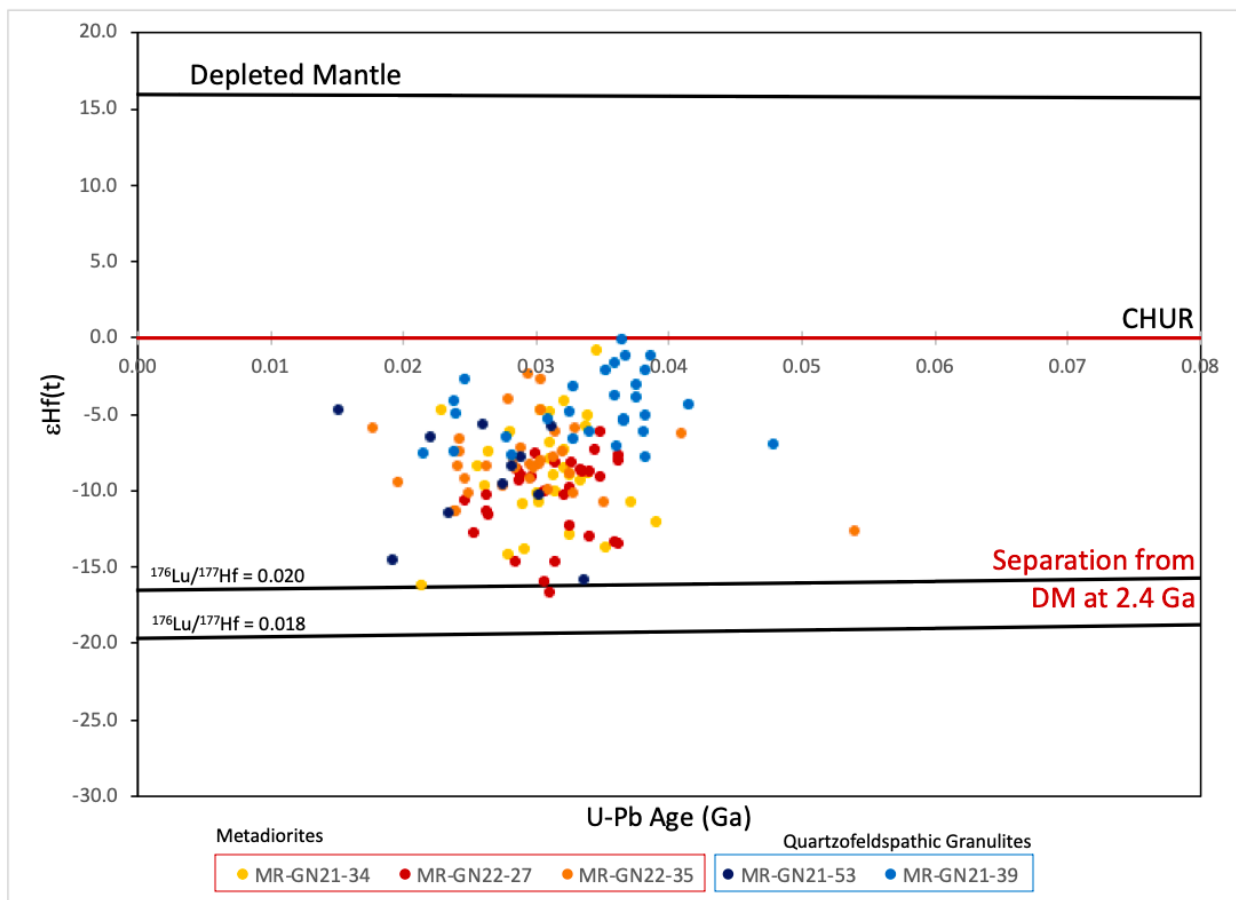


**Figure 3.34.** Hf isotope analyses, with crustal evolution lines from 2.4 Ga. Expanded to view the last 80 m.y.

Trace element patterns further support a model of Proterozoic terrane formation with late Cretaceous to Cenozoic modification (i.e. metasomatism and mixing) and partial melting. While pk-G-GN22-5 did not experience partial melting, creating a fairly smooth middle crustal REE composition and preserving Paleoproterozoic zircon ages, the other two quartzofeldspathic samples experienced partial melting, creating whole rock restite-like trace element patterns (Fig. 3.32). Simultaneously, a homogenization or mixing event with juvenile melt caused zircon recrystallization and dissolution/precipitation modifying zircon ages. From these data we suggest that quartzofeldspathic lithologies are what remains of the Proterozoic Mazatzal terrane, and this

terrane may contain a component of early Paleoproterozoic reworked crust. Furthermore, the Mazatzal terrane has undergone later modification by young magmatism during Farallon slab subduction and post-subduction slab roll-back and extension.

Metadiorite xenoliths contain only zircon with young U-Pb ages from ~76-2 Ma, but old (~1.4 Ga) whole rock Nd model ages (Kempton et al. 1990). No old zircon cores were observed, and zircon zones preserve very little age differentiation with zircon cores and rims covering the wide range of ages observed, as noted in the CL images (Fig. 3.16-3.19).  $\epsilon\text{Hf}(t)$  values for these zircons cover a large range from -17 to 0. Metadiorite geochronology can be interpreted two ways. In one scenario, the metadiorites represent Proterozoic Mazatzal crust that interacted with magmas during Farallon slab subduction. Lower crustal contamination began after subduction of the Shatsky oceanic plateau correlative, when a slab window opened allowing hot asthenospheric mantle to upwell and interact with the Mazatzal crust (Dickinson, 1997; Saleeby, 2003; Liu et al., 2010; Sun et al., 2017). Modification of this lower crust continued throughout the Mid-Cenozoic ignimbrite flare up from ~40-20 Ma, with the strongest modification (i.e. mixing and homogenization) taking place from 34-23 Ma when rhyolite volcanism was ongoing in the nearby Chiricahua mountains (du Bray et al., 2004; Best et al, 2013). Lower crust in this region was further affected by alkaline magmatism associated with Basin and Range spreading and GVF volcanism from 8-9.2 Ma to 260 thousand years (Kempton et al., 1990). This long history of lower crustal heating and metasomatism would allow for dissolution and reprecipitation or recrystallization of zircon to represent a young magmatic history beginning at 76 Ma stretching to 1.6 Ma at the time of the most recent GVF activity. Mesoproterozoic Nd-model ages suggest a history of contamination of a Paleoproterozoic terrane by young magmas. Hf-isotopes further support this argument and the model presented for quartzofeldspathic lithologies, where Mazatzal age crust

contains an older reworked component that separated from depleted mantle ~2.4 Ga. Metadiorites followed an intermediate crustal evolution ( $^{176}\text{Lu}/^{177}\text{Hf} = 0.018$ ), until Mazatzal and later Mesozoic and Cenozoic magmas contaminated this crust shifting  $\epsilon\text{Hf}(t)$  values towards zero and creating the large range in values observed (Fig. 3.35).

The second model for formation of metadiorites involves basaltic underplating beneath Mazatzal age crust, beginning at 76 Ma, when a slab tear allowed asthenospheric upwelling and decompression melting (Dickinson, 1997; Saleeby, 2003; Liu et al., 2010; Sun et al., 2017). This underplated crust would have undergone constant heating and interaction with new magmatic inputs throughout the last 76 m.y. These magmas would have interacted with and possibly incorporated fragments of the Mazatzal age crust. This model is supported by the absence of Proterozoic U-Pb ages; however, mass balance issues are encountered when trying to justify whole rock Nd-model ages and zircon  $\epsilon\text{Hf}(t)$  values. In order to create Mesoproterozoic Nd-model ages, underplated magmas would have had to assimilate large quantities of Mazatzal crust, which thermodynamically does not seem possible. Temperatures in excess of 1000°C would be needed to melt large portions of the lower crust, but lower crustal temperatures in this region as calculated by two-pyroxene geothermometry do not exceed 987°C. Additionally, zircon  $\epsilon\text{Hf}(t)$  values in this model would be strongly positive, reflecting their recent separation from depleted mantle. Reported  $\epsilon\text{Hf}(t)$  values for zircons in metadiorite samples, however, are all less than zero, suggesting a major contribution from recycled crust rather than a late Cretaceous addition of juvenile material.

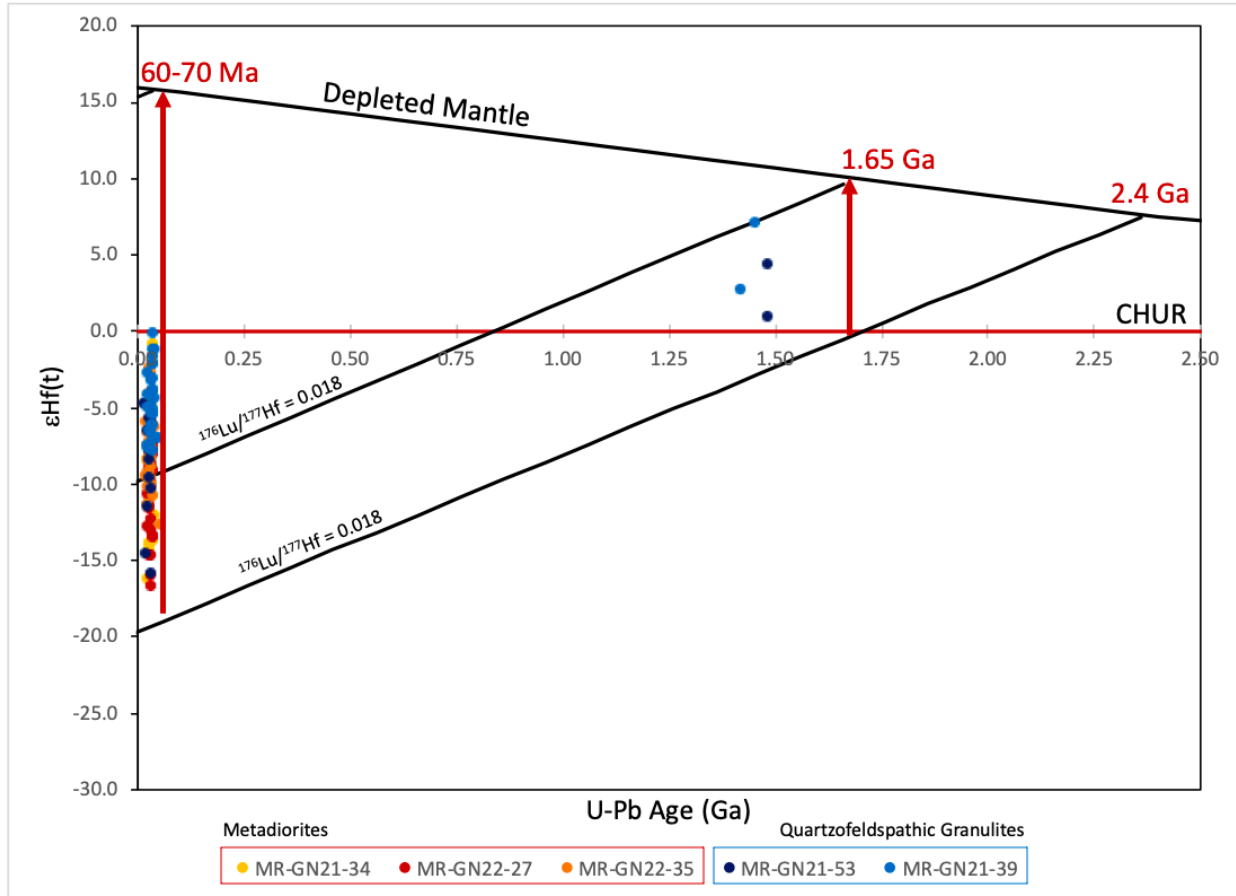


**Figure 3.35. Hf isotope model.**

Hf isotope analysis for three metadiorites and two quartzofeldspathic granulite samples. Isotope evolution lines for intermediate rock types ( $^{176}\text{Lu}/^{177}\text{Hf} = 0.018$ ) plotted for separation from depleted mantle at 2.4 Ga, 1.65 Ga, and ~60-70 Ma. Red arrows suggest a mixing or homogenization event occurring at 1.65 Ga and beginning at 70-60 Ma, creating a smear of  $\epsilon_{\text{Hf}}(t)$  towards more positive values.

A third model to account for the wide spread in  $\epsilon_{\text{Hf}}(t)$  values reported for both the quartzofeldspathic and metadiorite zircons considers the consequences of a hypothesized juvenile input into the crust at ~1.4 Ga, i.e. potentially associated with either the Picuris orogeny and/or the 1.4 Ga A-type granite event. The model presented in Fig. 3.35, with intermediated evolution lines from 2.4 Ga and 1.65 Ga, can only explain about 30% of the Cenozoic  $\epsilon_{\text{Hf}}(t)$  spread, relying then

on a large (>30%) contribution from young Farallon magmas to create the remainder of the upward spread in  $\epsilon\text{Hf}(t)$  values. However, based on the smooth incompatible element plots (Fig. 3.31a) and old Nd-model ages presented by the metadiorites, it seems unlikely, from a mass balance perspective, that a juvenile contribution at the time of Farallon slab subduction could have completely homogenized the Mazatazal age metadiorite lower crust while preserving smooth incompatible element patterns and 1.4 Ga Nd model ages. Therefore, in addition to 2.4 and 1.65 Ga juvenile contributions, we evaluate an additional juvenile contribution at the time of the widespread 1.4 Ga A-type granite event (Fig. 3.36). With this added Mesoproterozoic contribution from the mantle, we can then account ~75% of the  $\epsilon\text{Hf}(t)$  values observed in the Cenozoic. This model then requires a much smaller contribution from young Farallon magmas to create the upward spread in  $\epsilon\text{Hf}(t)$ .

Within the confines of these models, we propose that evidence presented here better supports a model in which juvenile Mid-Proterozoic magmas and a Paleoproterozoic reworked crustal component created the Mazatazal terrane. This crust was later modified due to Farallon slab subduction and magmatism. The nature of that modification remains unclear, and further work is required to reconcile the mass balance constraints imposed by the homogeneous whole rock major element, trace element and Nd isotope compositions relative to the heterogeneity in zircon Hf-isotope compositions.

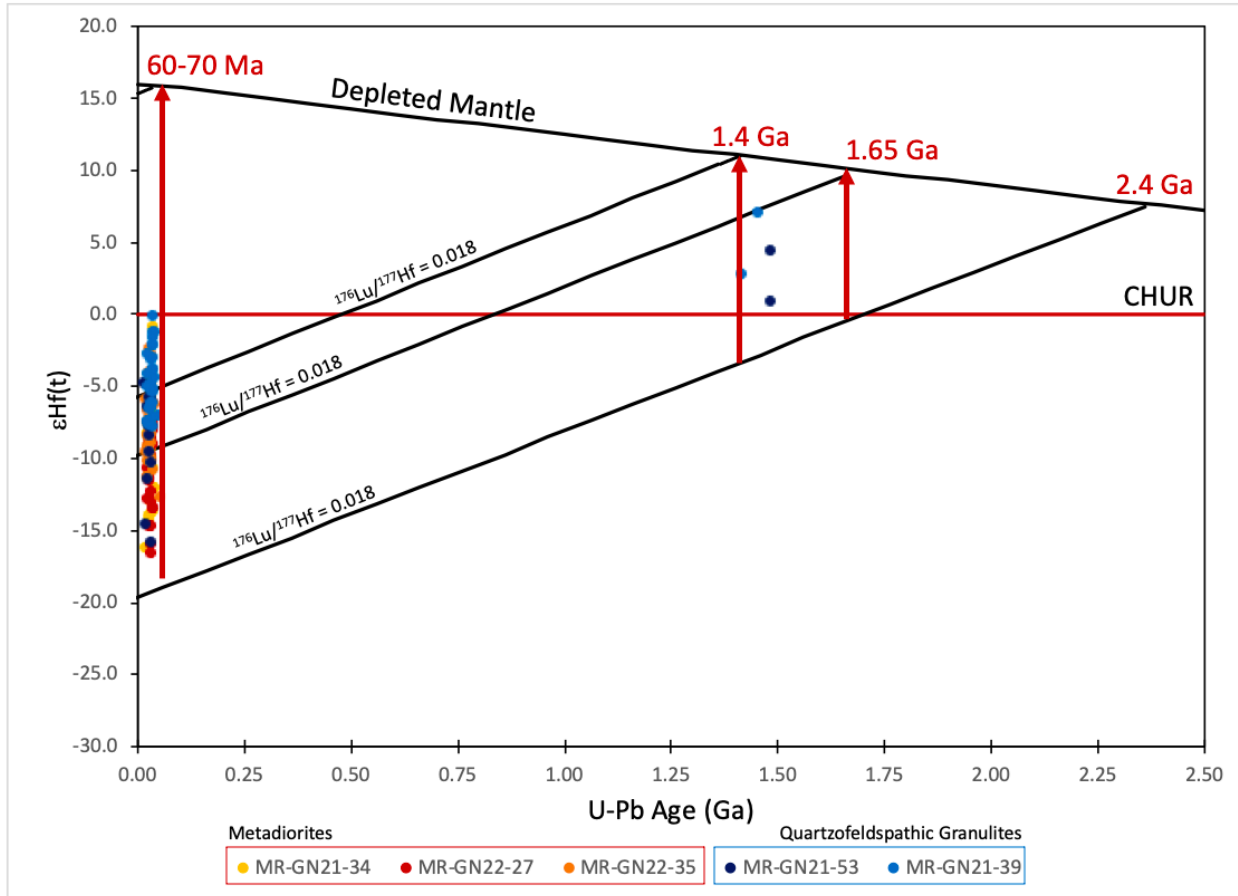


**Figure 3.36. Additional Hf isotope model**

Hf isotope analysis for three metadiorites and two quartzofeldspathic granulite samples. Isotope evolution lines for intermediate rock types ( $^{176}\text{Lu}/^{177}\text{Hf} = 0.018$ ) plotted for separation from depleted mantle at 2.4 Ga, 1.65 Ga, 1.4 Ga, and ~60-70 Ma. Red arrows suggest a mixing or homogenization event occurring at 1.65 Ga, 1.4 Ga, and beginning at 70-60 Ma, creating a smear of  $\epsilon\text{Hf}(t)$  towards more positive values.

Little new evidence is present for the origin of the mafic metacumulates; however, based on Sr-Nd data from Kempton et al. (1990) and the first model outlined above, a mixing model between older Proterozoic metadiorite crust and young Farallon basalts (i.e. late Cretaceous to Tertiary magmas associated with Farallon slab subduction), proposed by Kempton et al. (1990) is still viable (Fig. 3.3). The one zircon age from two-pyroxene metacumulate MR-GN21-59

measured at  $1799 \pm 22$  Ma may further support this model by suggesting interaction with and recycling of Mazatzal or Yavapai crust to create the metacumulate array.

### **3.6. Conclusions**

This study presents new U-Pb and Hf geochronology of the lower crust of the GVF, southeastern Arizona. While the lower crust in the region may be predominantly juvenile, zircon geochronology provides evidence for older crust components. These data align well with the model present by Holland et al. (2020), where the Mazatzal terrane formed on the margin of the previously accreted Yavapai province and received sediment input from cratonic Laurentia. Moreover, we see evidence for a 1.4-1.5 Ga event, possibly associated with the Picuris orogeny or the 1.4 Ga A-type granite event.

Zircon geochronology data are also consistent with a thermal event between 30-40 Ma, consistent with the timing of slab rollback initiating at 40 Ma. However, data also suggest a thermal event that preceded the ignimbrite eruptions in the region (i.e. in the Chiricahuas) by at least 10 m.y. and possibly longer, if the older ages (~76-55 Ma) in metadiorite GN22-3 are meaningful (which we suggest that they are due to their concordance and no indication of mixed ages). The large spread of ages indicates a protracted event continuing from the time of flat slab subduction, to rollback, and to Basin and Range extension.

Our data suggests that instead of the bulldozer effect seen further north, the lowermost crust beneath GVF must have been delaminated and replaced by mafic/ultramafic cumulates of Farallon origin. As a result, we suggest that the lower crustal history of southeastern Arizona is different than that further north in the Colorado Plateau Transition zone (central Arizona).

## Chapter 4 - Further Research

This thesis brings about numerous questions that may be answered through future research.

Some suggested analyses and research questions include:

- Petrography of these samples revealed large melt inclusions. Further research could analyze the phases (gas bubbles, mineral phases, etc.) present in these inclusions (Kempton et al. 1990).
- It would be wonderful to have geochronology of the mafic metacumulates, to place them in a temporal context with the other lithologies and better understand their geologic history.
- Additionally, it would be beneficial to collect additional data on more quartzofeldspathic xenoliths, particularly those like pk-GN22-5. What do the O-isotopes on these zircons look like? Can we prove that some of the quartzofeldspathic granulites are restites? Are they linked (geochemically) to the rhyolites in the Chiricahuas?

## References

- Armstrong, J. T. (1988). Quantitative analysis of silicate and oxide materials: comparison of Monte Carlo, ZAF, and phi-rho-z procedures. *Microbeam Analysis*, 239-246
- Artemieva, I. M. (2003). Lithospheric structure, composition, and thermal regime of the East European Craton: Implications for the subsidence of the Russian platform. *Earth and Planetary Science Letters*, 213(3-4), 431-446.
- Axen, G. J., Van Wijk, J. W., & Currie, C. A. (2018). Basal continental mantle lithosphere displaced by flat-slab subduction. *Nature Geoscience*, 11(12), 961-964.
- Best, M. G., Christiansen, E. H., & Gromme, S. (2013). Introduction: The 36-18 Ma southern Great Basin, USA, ignimbrite province and flareup: Swarms of subduction-related supervolcanoes. *Geosphere*, 9(2), 260-274.
- Bird, P. (1998). Kinematic history of the Laramide orogeny in latitudes 35°-49°N, western United States. *Tectonics*, 17(5), 780-801.
- Bolhar, R., Kamber, B. S., & Collerson, K. D. (2007). U-Th-Pb fractionation in Archaean lower continental crust: Implications for terrestrial Pb isotope systematics. *Earth and Planetary Science Letters*, 254(1-2), 127-145.
- Butcher, L., Mahan, K., & Allaz, J. (2017). Late Cretaceous crustal hydration in the Colorado Plateau, USA, from xenolith petrology and monazite geochronology. *Lithosphere*, 9(4), 561-578.
- Chantler, C.T., Olsen, K., Dragoset, R.A., Chang, J., Kishore, A.R., Kotochigova, S.A., & Zucker, D.S. (2005), X-Ray Form Factor, Attenuation and Scattering Tables (version 2.1). [Online] Available: <http://physics.nist.gov/ffast> [2020, Sept.]. National Institute of Standards and Technology, Gaithersburg, MD.
- Chapman\*, A. D., Riggs, N., Ducea, M. N., Saleeby, J. B., Rautela, O., & Shields, J. (2019). Tectonic development of the Colorado Plateau Transition ZONE, CENTRAL arizona: Insights from Lower lithosphere Xenoliths and volcanic host rocks. *Geologic Excursions in Southwestern North America*. doi:10.1130/2019.0055(09)
- Chapman, A., Shields, J., Ducea, M., & Saleeby, J. (2020). Fate of the Lower Lithosphere during shallow-angle subduction: the Laramide example. *GSA Today*, 30(1), 4-10.
- Conrey, R. M., Bailey, D. G., Singer, J. W., Wagoner, L., Parfitt, B., Hay, J., & Keh, O. (2019). Optimization of internal standards in LA-ICPMS analysis of geologic samples using lithium borate fused glass. *Conference: Northeastern Section Meeting, Geological Society of America, Abstracts with Programs*. 51(1), ISSN 0016-7592.

- Coogan, L., Saunders, A., & Wilson, R. (2014). Aluminum-in-olivine thermometry of primitive basalts: Evidence of an anomalously hot mantle source for large igneous provinces. *Chemical Geology*, 368, 1-10.
- Crowley, J. L., Schmitz, M. D., Bowring, S. A., Williams, M. L., & Karlstrom, K. E. (2006). U–Pb and Hf isotopic analysis of zircon in lower crustal xenoliths from the Navajo volcanic field: 1.4 Ga mafic magmatism and metamorphism beneath the Colorado Plateau. *Contributions to Mineralogy and Petrology*, 151(3), 313–330.
- Daniel, C. G., Pfeifer, L. S., Jones, J. V., & McFarlane, C. M. (2013). Detrital zircon evidence For non-laurentian provenance, Mesoproterozoic (CA. 1490-1450 MA) deposition and OROGENESIS in a reconstructed Orogenic belt, northern New MEXICO, USA: Defining the Picuris orogeny. *Geological Society of America Bulletin*, 125(9-10), 1423-1441.
- Dickinson, W. R. (1997). OVERVIEW: Tectonic implications of Cenozoic volcanism in coastal California. *Geological Society of America Bulletin*, 109(8), 936–954.
- Dickinson, William R. (2002). "The Basin and Range Province as a Composite Extensional Domain". *International Geology Review*, 44:1, 1-38.
- Du Bray, E. A., Pallister, J. S., & Snee, L. W. (2004). Geochemistry and Geochronology of Middle Tertiary volcanic rocks of the Central Chiricahua mountains, Southeast Arizona. *USGS Professional Paper*, 1684, 1-57.
- Ferry, J. M., & Watson, E. B. (2007). New thermodynamic models and revised calibrations for the Ti-in-zircon and Zr-in-rutile thermometers. *Contributions to Mineralogy and Petrology*, 154(4), 429-437.
- Harley, S. L., Kelly, N. M., & Möller, A. (2007). Zircon Behavior and the Thermal Histories of Mountain Chains. *Elements*, 3, 25-30.
- Holland, M. E., Grambling, T. A., Karlstrom, K. E., Jones, J. V., Nagotko, K. N., & Daniel, C. G. (2020). Geochronologic and Hf-isotope framework of Proterozoic rocks from central New Mexico, USA: Formation of the Mazatzal crustal province in an extended continental margin arc. *Precambrian Research*, 347, 105820, 1-19.
- Humphreys, E., Hessler, E., Dueker, K., Farmer, G. L., Erslev, E., & Atwater, T. (2003). How laramide-age hydration of North American Lithosphere by the Farallon Slab Controlled subsequent activity in the Western United States. *International Geology Review*, 45(7), 575-595.
- Jackson, S.E., Pearson, N.J., Griffin, W.L., & Belousova, E.A. (2004). The application of laser ablation-inductively coupled plasma-mass spectrometry to in situ U–Pb zircon geochronology. *Chemical Geology*, 211, 47–69.

- Johnson, D.M., Hooper, P.R., & Conrey, R.M. (1999). XRF Analysis of Rocks and Minerals for Major and Trace Elements on a Single Low Dilution Li-tetraborate Fused Bead. *JCPDS-International Centre for Diffraction Data 1999*, 843-867.
- Kay, R. W., & Kay, S. M. (1981). The nature of the lower continental crust: Inferences from geophysics, surface geology, and crustal xenoliths. *Reviews of Geophysics*, 19(2), 271.
- Kempton, P. (1984). Alkalic basalts from the Geronimo Volcanic Field: petrologic and geochemical data bearing on their petrogenesis. II. Petrography, petrology and geochemistry of xenoliths and megacrysts from the Geronimo Volcanic Field, Southeastern Arizona. III. An interpretation of contrasting nucleation and growth histories from the petrographic analysis of pillow and dike chilled margins, Hole 504B, DSDP Leg 83. Dallas, Texas, Southern Methodist University, Ph.D. dissertation, 275 p.
- Kempton, P. D., Dungan, M. A., & Blanchard, D. P. (1987). Petrology and geochemistry of xenolith-bearing alkalic basalts from the Geronimo Volcanic Field, southeast Arizona; Evidence for polybaric fractionation and implications for mantle heterogeneity. *Geological Society of America Special Papers, Mantle Metasomatism and Alkaline Magmatism*, 347–370.
- Kempton, P., Harmon, R., Hawkesworth, C., & Moorbath, S. (1990). Petrology and geochemistry of lower crustal granulites from the Geronimo Volcanic Field, southeastern Arizona. *Geochimica et Cosmochimica Acta*, 54(12), 3401–3426.
- Kempton, P. D., & Harmon, R. S. (1992). Oxygen isotope evidence for large-scale hybridization of the lower crust during magmatic underplating. *Geochimica et Cosmochimica Acta*, 56(3), 971-986.
- Klemperer S. L., Hauge T. A., Hauser E. C., Oliver J. E., & Potter C. J. (1986). The MOHO in the northern Basin and Range Province, Nevada, along the COCORP 40°N seismic-reflection transect. *Geological Society of America Bulletin*, 97, 603-618.
- Koreshkova, M., Downes, H., Millar, I., Levsky, L., Larionov, A., & Sergeev, S. (2017). Geochronology of Metamorphic events in the lower crust beneath NW Russia: A Xenolith HF Isotope study. *Journal of Petrology*, 58(8), 1567-1589.
- Liu, L., Gurnis, M., Seton, M., Saleeby, J., Müller, R. D., & Jackson, J. M. (2010). The role of oceanic plateau subduction in the Laramide orogeny. *Nature Geoscience*, 3(5), 353–357.
- Liu, S., & Currie, C. A. (2016). Farallon plate dynamics prior to the Laramide orogeny: Numerical models of flat subduction. *Tectonophysics*, 666, 33–47.
- Menzies, M., Kempton, P., & Dungan, M. (1985). Interaction of Continental Lithosphere and Asthenosphere Melts below the Geronimo Volcanic Field, Arizona, U.S.A. *Journal of Petrology*, 26(3), 663-693.

- Mueller, P.A., Kamenov, G.D., Heatherington, A.L., & Richards, J. (2008). Crustal evolution in the Southern Appalachian Orogen: Evidence from Hf isotopes in detrital zircons. *Journal of Geology*, 116, 414-422.
- Paces, J.B., Miller, J.D. (1993). Precise U–Pb ages of Duluth Complex and related mafic intrusions, northeastern Minnesota: geochronological insights into physical, petrogenetic, paleomagnetic and tectonomagmatic processes associated with the 1.1 Ga midcontinent rift system. *Journal of Geophysical Research*, 98, 13997-14013.
- Padovani E. and Carter J. (1977). Aspects of the deep crustal evolution beneath southcentral New Mexico. In *The Earth's Crust* (ed. J. G. Heacock); *AGU Monograph 20*, 19-55.
- Paton, C., Woodhead, J.D., Hellstrom, J.C., Hergt, J.M., Greig, A., & Maas, R. (2010). Improved laser ablation U-Pb zircon geochronology through robust down hole fractionation correction. *Geochemistry, Geophysics, Geosystems*, 11(3), 1-36.
- Paton, C., Hellstrom, J., Paul, B., Woodhead, J., & Hergt, J. (2011). Iolite: Freeware for the visualization and processing of mass spectrometry data. *Journal of Analytical Atomic Spectrometry*, 26, 2508-2518.
- Petrus, J.A., & Kamber, B.S. (2012). Vizual Age: A novel approach to laser ablation ICP-MS U-Pb geochronology data reduction. *Geostandards and Geoanalytical Research*, 36, 247-270.
- Plank, T., & Forsyth, D. W. (2016). Thermal structure and melting conditions in the mantle beneath the Basin and Range province from seismology and Petrology. *Geochemistry, Geophysics, Geosystems*, 17(4), 1312-1338.
- Putirka, K. (2008) Thermometers and Barometers for Volcanic Systems. In: Putirka, K., Tepley, F. (Eds.), *Minerals, Inclusions and Volcanic Processes. Reviews in Mineralogy and Geochemistry, Mineralogical Soc. Am.*, 69, 61-120.
- Rader, M., Kempton, P., & Möller, A. (2017). Evidence for the timing of post-Laramide magmatic underplating in the southern Basin and Range: new zircon geochronology of granulite xenoliths from the Geronimo Volcanic Field, SE Arizona. *2017 GSA Abstracts with Programs*. 49(6).
- Rader, M. A., Kempton, P. D., & Möller, A. (2019). In situ U-Pb zircon geochronology of xenoliths from the Geronimo Volcanic Field, SE Arizona: implications for lower crustal development of the southern Basin and Range. *2019 GSA Abstracts with Programs*. 51(5).
- Roberts, N. M., & Spencer, C. J. (2014). The zircon archive of continent formation through time. *Geological Society, London, Special Publications*, 389(1), 197-225.
- Rudnick, R., & Gao, S. (2014). Composition of the continental crust. *Treatise on Geochemistry*, 3.01-64, 1-51.

- Saleeby, J. (2003). Segmentation of the Laramide Slab—evidence from the southern Sierra Nevada region. *Geological Society of America Bulletin*, 115, 655–668.
- Selverstone, J. (1982). Fluid inclusions as petrogenetic indicators in Granulite xenoliths, PALI-AIKE Volcanic field, Chile. *Contributions to Mineralogy and Petrology*, 79(1), 28–36.
- Siebel, W., & Van den Haute, P. (2007). Radiometric Dating and Tracing. *In Radio Chemistry and Nuclear Chemistry*, 1, doi: 10.1017/9781108186551.006.
- Sláma, J., Košler, J., Condon, D.J., Crowley, J.L., Gerdes, A., Hanchar, J.M., Horstwood, S.A., Morris, G.A., Nasdala, L., Norberg, N., Schaltegger, U., Schoene, B., Tubrett, M.N., & Whitehouse, M.J. (2008). Plešovice zircon—A new natural reference material for U-Pb and Hf isotopic microanalysis. *Chemical Geology*, 249, 1–35.
- Sláma, J., Košler, J., & Pedersen, R. B. (2007). Behaviour of zircon in high-grade metamorphic rocks: Evidence from Hf isotopes, trace elements and textural studies. *Contributions to Mineralogy and Petrology*, 154(3), 335–356.
- Spencer, C., Kirkland, C., Roberts, N., Evans, N., & Liebmann, J. (2020). Strategies towards robust interpretations of in situ zircon Lu–Hf isotope analyses. *Geoscience Frontiers*, 11(3), 843–853.
- Speed, R. C., & Sleep, N. H. (1982). Antler orogeny and foreland basin: A model. *Geological Society of America Bulletin*, 93(9), 815.
- Sun, S.S., & McDonough, W.F. (1989). Chemical and isotopic systematics of oceanic basalts; implications for mantle composition and processes. *Special Publication - Geological Society of London*, 42, 313–345.
- Sun, D., Gurnis, M., Saleeby, J., & Helmberger, D. (2017). A dipping, thick segment of the Farallon Slab beneath central U.S. *Journal of Geophysical Research: Solid Earth*, 122(4), 2911–2928.
- Thakurdin, Y., Bolhar, R., Horváth, P., Wiedenbeck, M., & Rocholl, A. (2019). Formation of lower to middle crust of the Wyoming Craton, Montana (USA), using evidence from zircon Hf-O isotopic and trace element compositions. *Chemical Geology*, 525, 218–244.
- Thomas, J., Bodnar, R., Shimizu, N., & Sinha, A. (2002). Determination of zircon/melt trace element partition coefficients from SIMS analysis of melt inclusions in zircon. *Geochimica Et Cosmochimica Acta*, 66(16), 2887–2901.
- Thorman, C. H., & Drewes, H. (1978). Cretaceous-early Tertiary history of the northern Pyramid Mountains, southwestern New Mexico. Land of Cochise (Southeastern Arizona), New Mexico Geological Society 29th Annual Fall Field Conference Guidebook, 215–218.

- Turlin, F., Vanderhaeghe, O., Gervais, F., André-Mayer, A., Moukhsil, A., Zeh, A., . . . I.P.T.N. (2019). Petrogenesis of Lree-rich pegmatic Granite dykes in the central Grenville province by partial melting of Paleoproterozoic-Archean metasedimentary rocks: Evidence from zircon U-Pb-Hf-O isotope and trace Element analyses. *Precambrian Research*, 327, 327-360.
- Watson, E. B., Wark, D. A. & Thomas, J. B. (2006) Crystallization thermometers for zircon and rutile. *Contributions to Mineralogy and Petrology*, 151(4), 413.
- Whitmeyer, S., & Karlstrom, K. (2007). Tectonic model for the Proterozoic growth of North America. *Geosphere*, 3(4), 220-259.
- Wotzlaw JF, Schaltegger U, Frick DA, Dungan MA, Gerdes A, & Günther D. (2013). Tracking the evolution of large-volume silicic magma reservoirs from assembly to super eruption. *Geology*, 41, 867-70.
- Zweifelhofer, G., Kempton, P.D., Mathur, R., & Brueseke, M. (2018) Cu-isotope heterogeneity in mantle peridotite xenoliths from the Geronimo Volcanic Field, SE Arizona: Is metasomatism a possible mechanism for fractionating stable Cu isotopes in the lithospheric mantle? *Geological Society of America North-Central Section, Ames, Iowa*, April 16-17, 2018.

## Appendix A - Mineral Abbreviations

Symbol	Mineral Name
bt	biotite
cpx	clinopyroxene
kspar	K-feldspar
ol	olivine
opx	orthopyroxene
ox	oxide
plg	plagioclase
qtz	quartz
sp	spinel

Appendix Table A.1. List of mineral abbreviations.

## Appendix B - Petrographic Descriptions

**Sample ID:** MR-GN21-7

**Rock Type:** Two-pyroxene metacumulate

**Analysis:** Whole rock ICP-MS and XRF

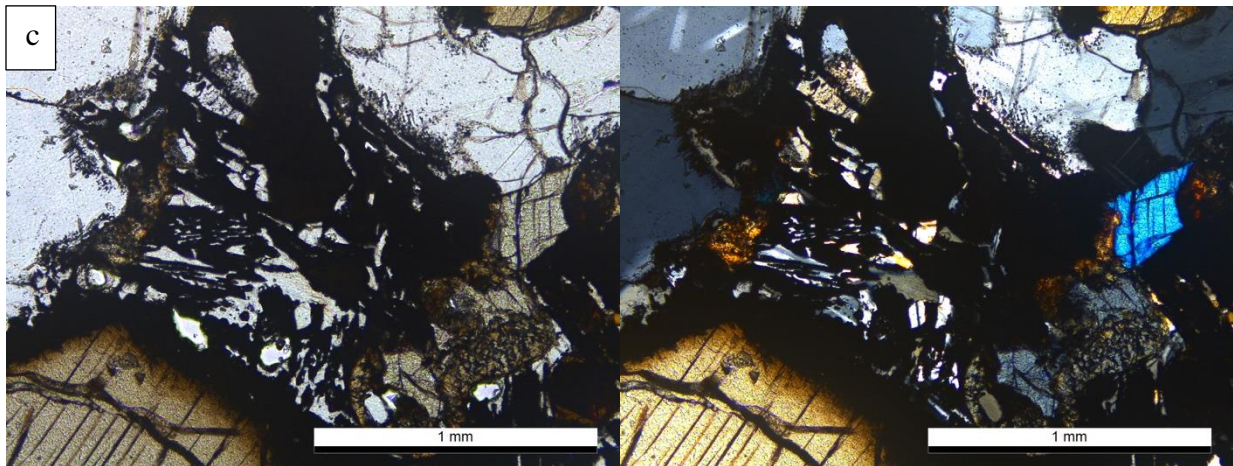
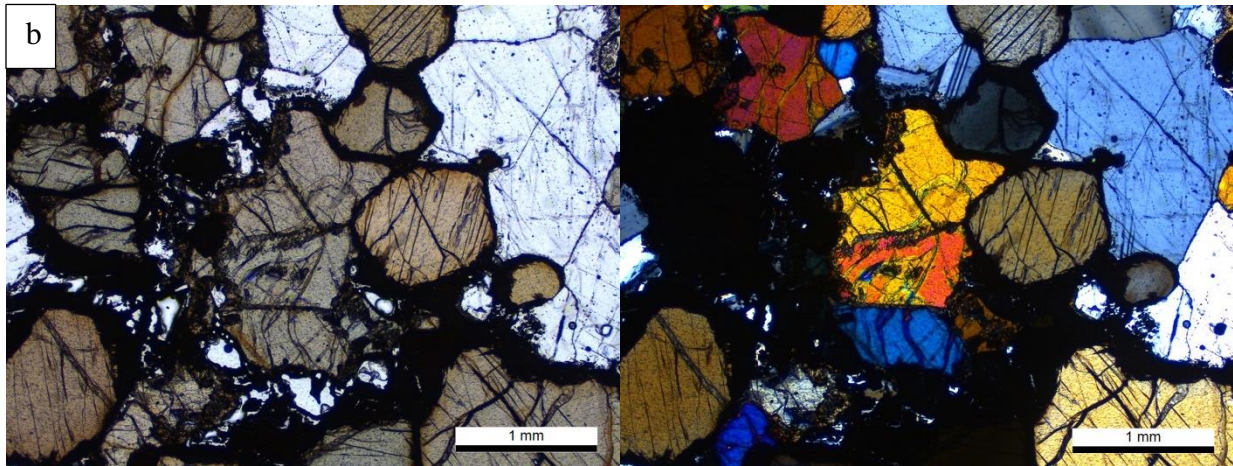
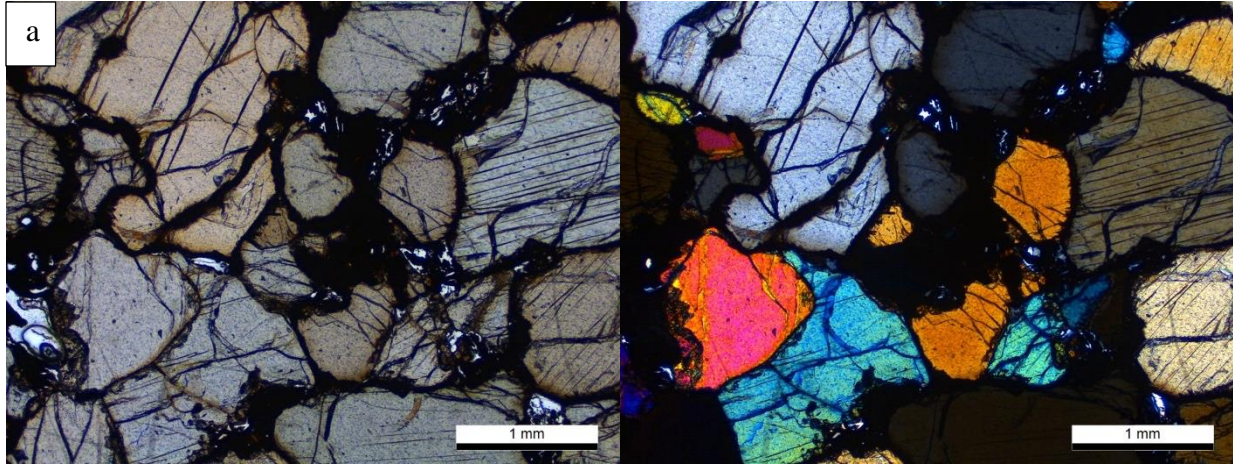
**Hand Sample:** Medium grain, equigranular rock with strong foliation defined by pyroxenes, 25% felsic minerals, 75% mafic minerals. Fresh (<2% low temperature alteration).



**Thin Section:** Medium to coarse-grained, granoblastic, two-pyroxene rock. Plagioclase (15%) grains are anhedral, equant in shape, display polysynthetic twinning and range in size from 0.5-2 mm. Plagioclase tend to occur in clusters, with 120-degree triple junctions in relationship to each other, and reaction rims where they contact other mineral phases. Orthopyroxene (55%) is anhedral, pleochroic shades of tan, ranging in size from 1-3 mm. Clinopyroxene (30%) is pleochroic tan to light green, sub to anhedral, ranging in size from 1-3 mm. Foliation is not well defined in thin section.

Partial melting affects ~15% of the sample, with patches of glass and secondary acicular plagioclase, cryptocrystalline quench, oxides, and a reddish-brown to honey colored mystery mineral with 60/120° cross hatching pattern (Fig. A.1d). Primary mineral phases exhibit zoning adjacent to melt patches and spongy textures.

**Suggested Future Analyses:** Microprobe of mystery mineral and thermometry



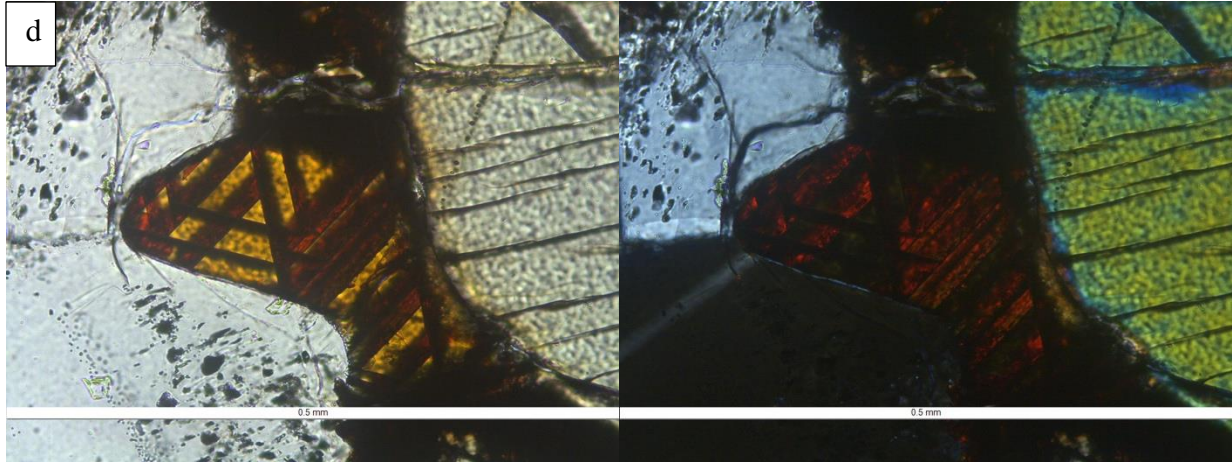


**Figure B.1** a) Orthopyroxene and clinopyroxene with 120-degree triple junctions; b) Regions of melt with opaques and cryptocrystalline quench; c) Close up of secondary, acicular plagioclase, spongy textures of adjacent regions and zoning of pyroxenes. d) Mystery mineral.

\*\*For this figure and all that follow, images on the left are in plane-polarized light, and images on the right are cross-polarized light.

\*\*\*Abbreviations used:

plag = plagioclase  
 cpx = clinopyroxene  
 opx = orthopyroxene

**Sample ID:** MR-GN21-9

**Rock Type:** Olivine Meta-Gabbro

**Analysis:** Whole rock ICP-MS and XRF

**Hand Sample:** Medium grain, equigranular rock, weakly foliated. 60% felsic minerals, 40% mafic minerals. Fresh (<2% low temperature alteration).



**Thin Section:** Medium to coarse-grained, foliated, two-pyroxene rock. Plagioclase (60%) grains are sub to anhedral, equant to tabular, ranging in size from 0.1-1.5 mm, with deformed polysynthetic twins. Clinopyroxene (20%) is anhedral, colorless, 0.1-1 mm in size. Orthopyroxene (10%) is sub to anhedral, pleochroic tan to colorless. Pyroxene grains are highly altered and significantly resorbed with a spongy texture. Iddingsitized primary olivine (10%) is anhedral, 0.5-2 mm. Aligned pyroxenes and plagioclase help to define foliation.

Areas of partial melting <10%, with melting restricted to glass along grain boundaries and minimal involvement of primary pyroxenes and olivine.

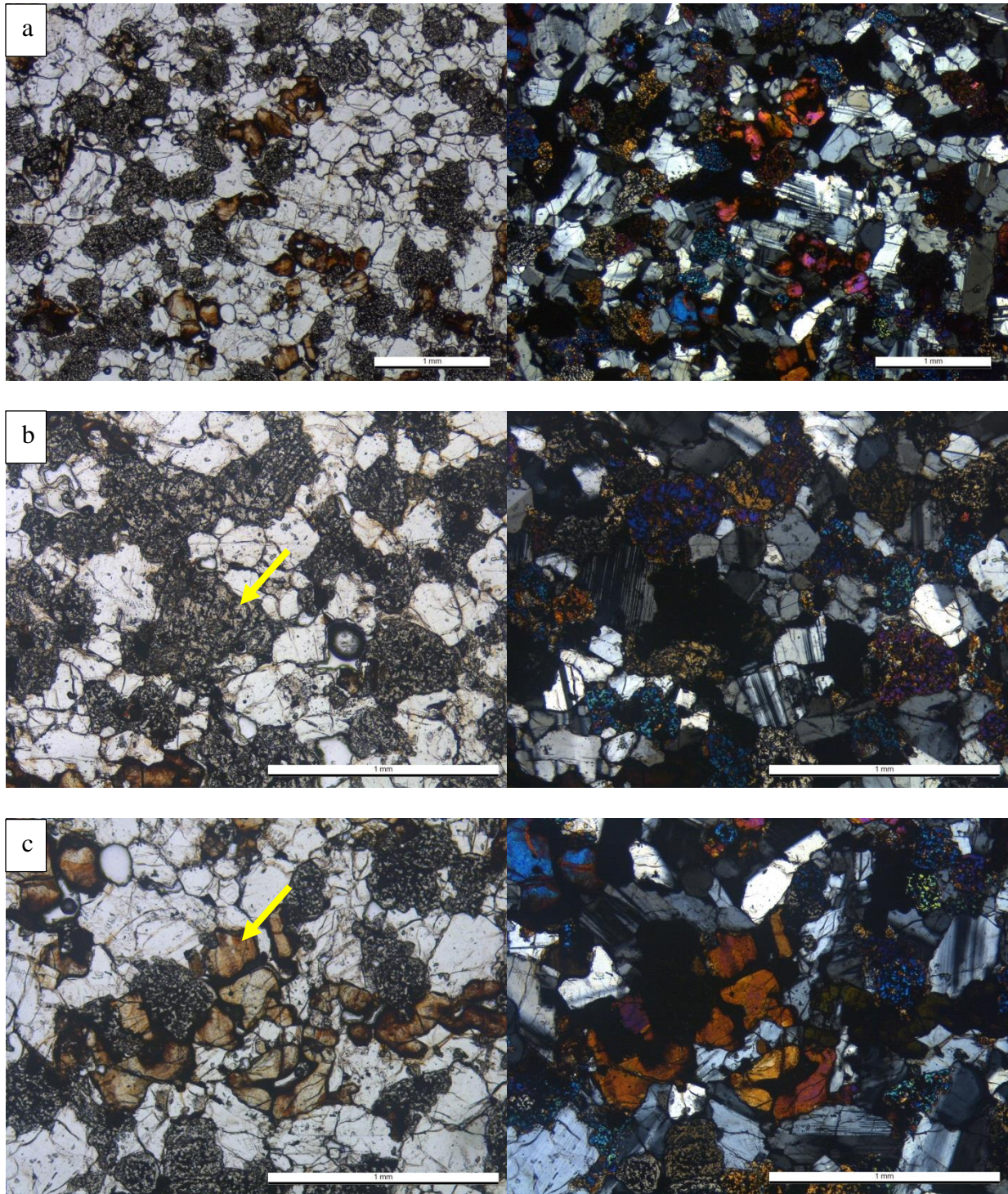


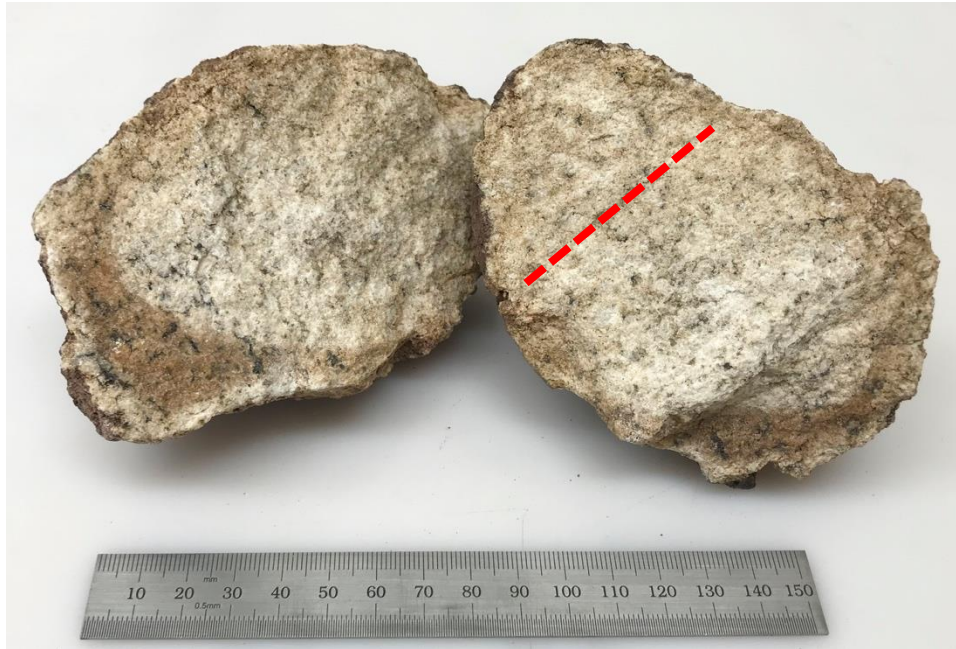
**Figure B.2** a) Plagioclase, pyroxene, and olivine textures; b) Close up of plagioclase and spongy pyroxene textures; c) Primary iddingsitized olivine.

**Sample ID:** MR-GN21-16

**Rock Type:** Quartzofeldspathic

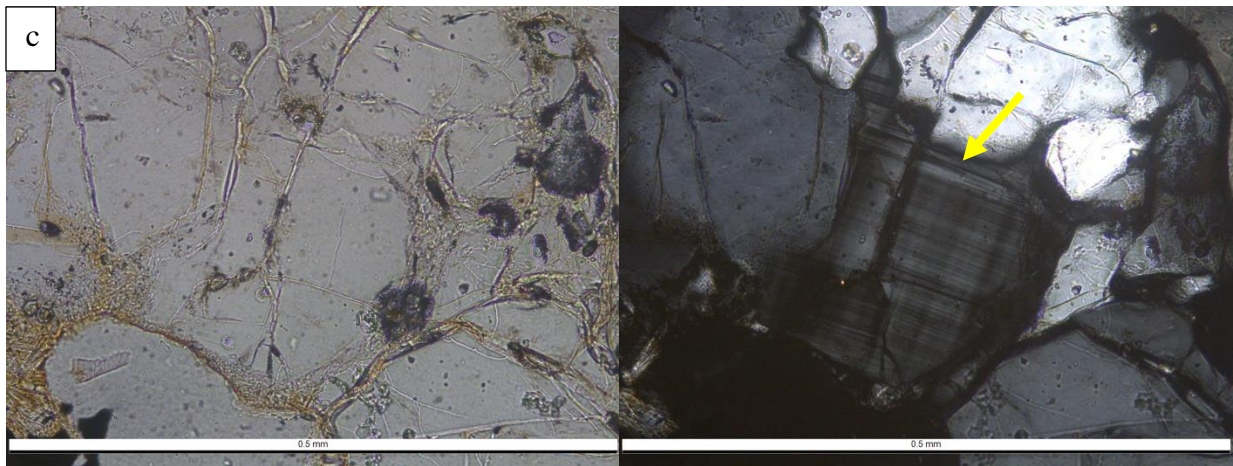
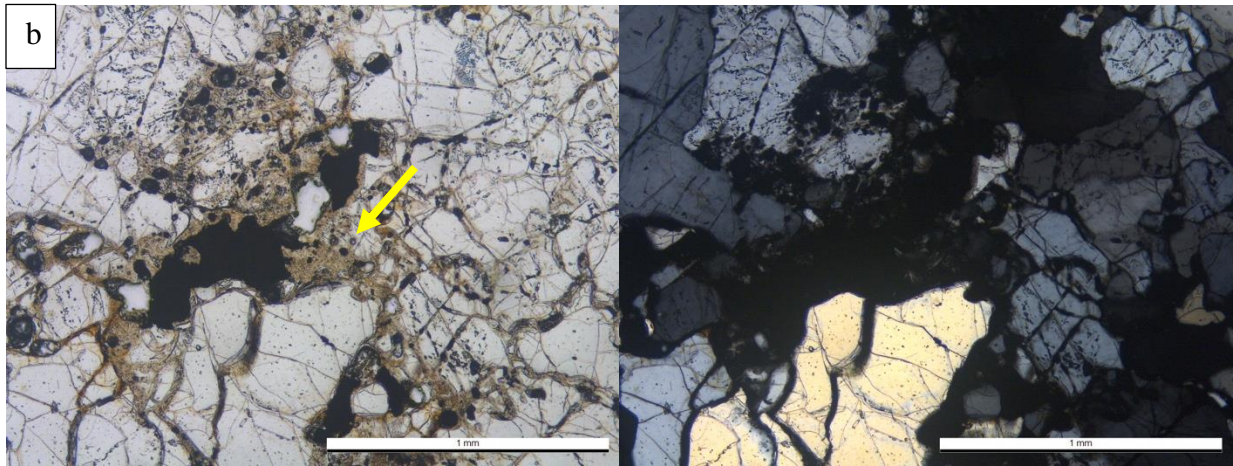
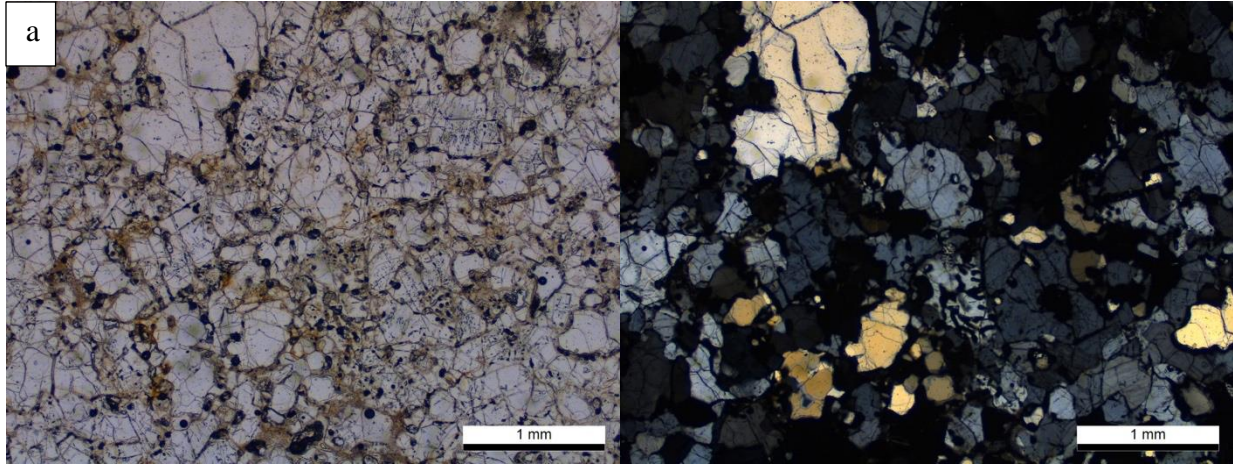
**Analysis:** Whole rock ICP-MS and XRF

**Hand Sample:** Fine to medium grain, equigranular rock, weakly foliated, 100% felsic minerals, <1% mafic minerals. Fresh (<2% low temperature alteration).



**Thin Section:** Medium to coarse-grained, porphyroblastic rock. Quartz (30%) grains are anhedral, with significant embayment, undulose extinction, and subgrain boundaries. Quartz grains are seriate, ranging from 0.1 to 3 mm porphyroblasts. Potassium feldspar (40%) is abundant, but difficult to differentiate from quartz due to lack of zoning in most grains. Textures are similar, with subgrain boundaries and embayment, ranging from 0.1-4 mm in size. Microcline (10%) can be differentiated by tartan twinning. Plagioclase (20%) is anhedral with deformed polysynthetic twins. Myrmekitic intergrowths present throughout. Orthopyroxene (<1%) is anhedral, pleochroic shades of tan, ranging in size from 0.25-0.5 mm. Opaques <1%. Zircons are abundant, occurring in clusters as inclusions in quartz and K-feldspar, rarely found interstitially. Zircons are euhedral, <50  $\mu\text{m}$ .

Areas of partial melting <10%, with melting restricted to glass or cryptocrystalline quench products common along grain boundaries.



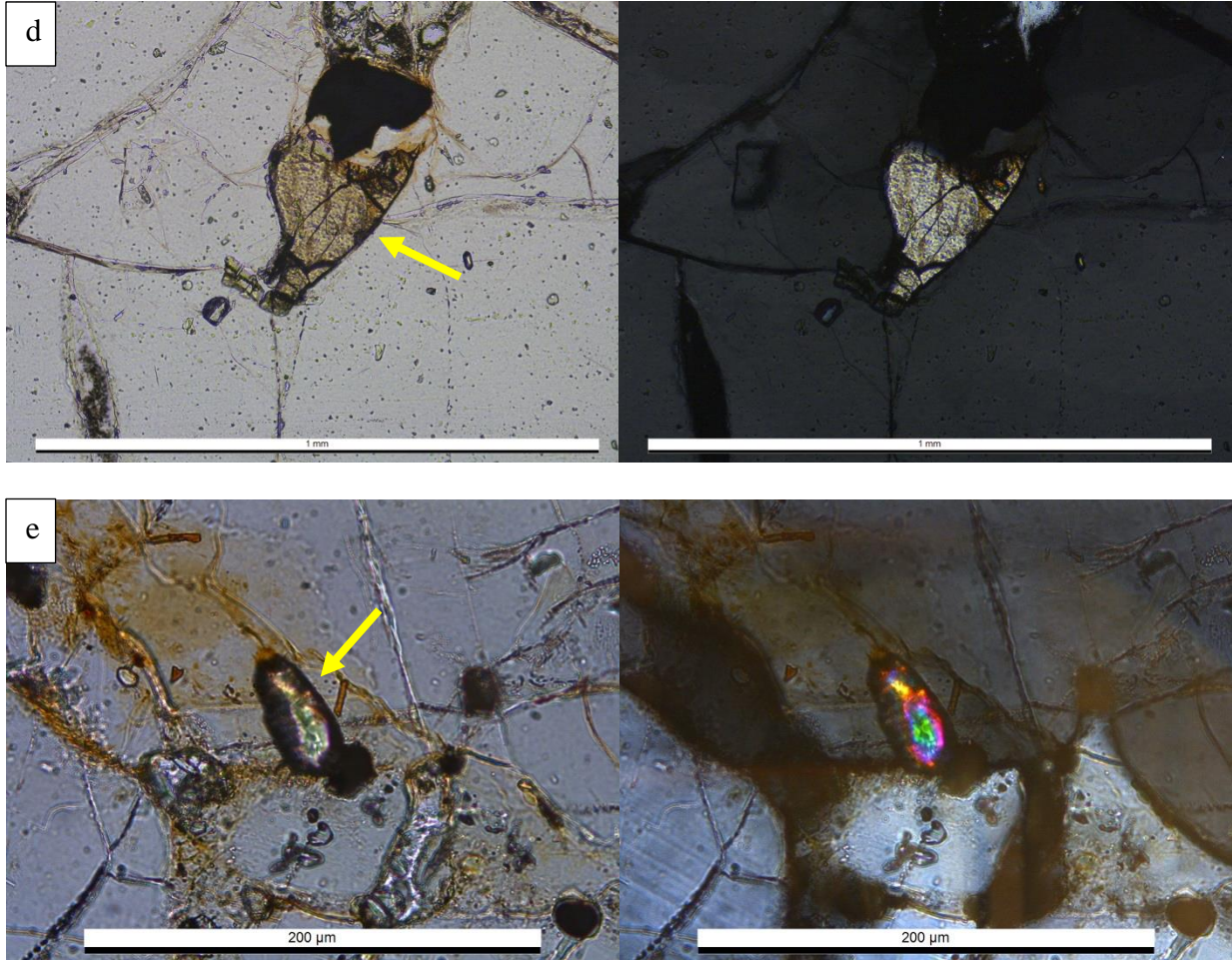


**Figure B.3** a) Quartz and feldspar textural relationship. Myrmekite also visible; b) Melt regions with cryptocrystalline quench and opaques; c) Microcline; d) Primary orthopyroxene found in minor amounts; e) Subhedral zircon inclusion in quartz.

**Sample ID:** MR-GN21-33

**Rock Type:** One-pyroxene metacumulate

**Analysis:** Whole rock ICP-MS and XRF

**Hand Sample:** Medium to coarse grain, equigranular, weakly foliated, 80% felsic minerals, 20% mafic minerals. Fresh (<2% low temperature alteration).



**Thin Section:** Medium to coarse-grained, granoblastic rock. Plagioclase (80%) grains are anhedral, equant to elongate, with deformed polysynthetic twins and 120-degree triple junctions, ranging in size from 0.5-5 mm. Clinopyroxene (20%) is pleochroic tan to light green, anhedral, ranging in size from 0.25-1.5 mm. Weak foliation defined by pyroxenes.

Partial melting affects ~35% of the sample, with patches of dark cryptocrystalline quench and secondary microcrystalline, euhedral, tabular plagioclase and opaques. Primary mineral phases exhibit zoning adjacent to melt patches and spongy textures.

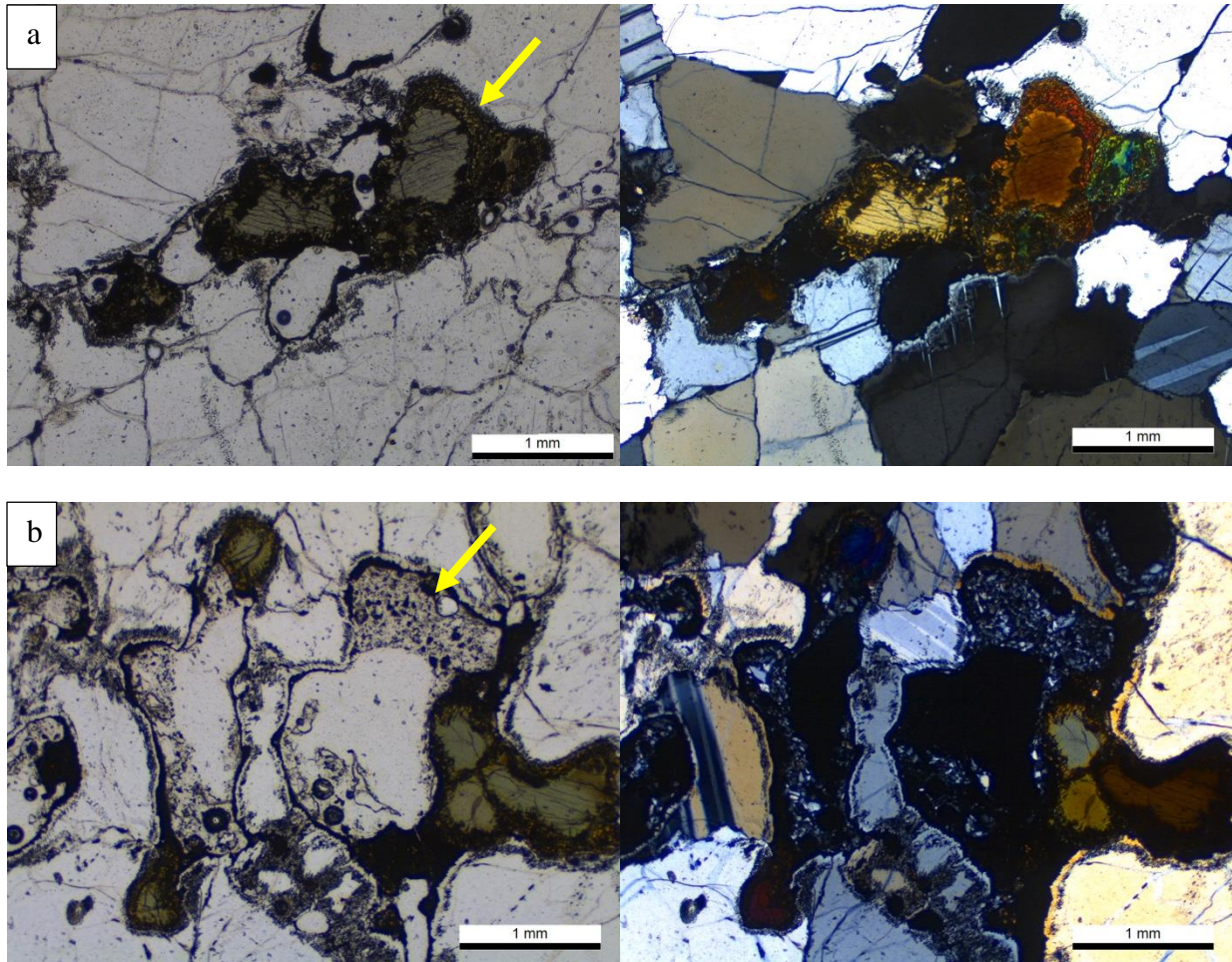


**Figure B.4** a) Plagioclase and clinopyroxene with spongy reaction rims; b) Partial melting with secondary microcrystalline plagioclase, reaction rims on clinopyroxene and plagioclase, and zoning on plagioclase.

**Sample ID:** MR-GN21-34

**Rock Type:** Metadiorite

**Analysis:** Whole rock ICP-MS and XRF, U-Pb and Hf LA-ICP-MS, Geothermometry

**Hand Sample:** Fine to medium grain, equigranular rock, weakly foliated, 80% felsic minerals, 20% mafic minerals. Fresh (<2% low temperature alteration).



**Thin Section:** Fine to medium grained, granoblastic rock. Plagioclase (40%) grains are anhedral, equant to elongate, with deformed polysynthetic twins and range in size from 0.5-1.5 mm. Potassium feldspar (25%) and quartz (10%) are both present but difficult to differentiate due to lack of twinning in feldspars. Both are equant, anhedral, with subgrain boundaries, ranging in size from 0.1-2 mm. Myrmekitic textures and perthite present. Clinopyroxene (10%) is pleochroic tan to light green, anhedral, ranging in size from 0.25-1.5 mm. Orthopyroxene (10%) is pleochroic shades of tan, same textures and sizes as cpx. Weak foliation defined by pyroxenes. Zircon and apatite present throughout in trace amounts. Apatite found as inclusions in feldspars and pyroxene. Zircon present as inclusions in feldspars and interstitially.

Areas of partial melting ~15%, with melting restricted to brown glass along grain boundaries and secondary opaques, minimal involvement of primary pyroxenes/feldspars. Melting occurs in close association with pyroxenes.

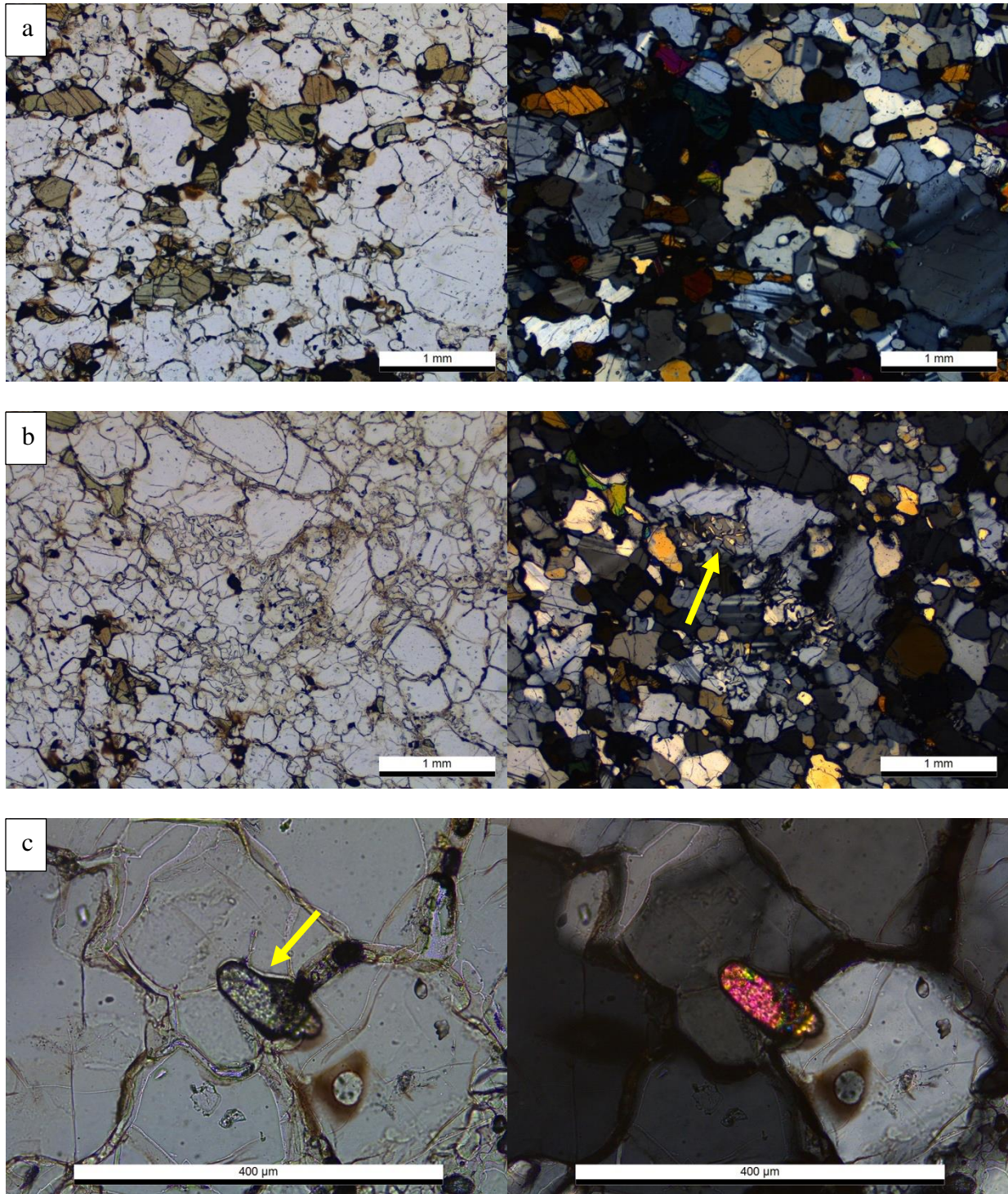


**Figure B.5** a) Plagioclase and pyroxenes. Alignment of pyroxenes visible, as well as melt regions with brown glass and opaques; b) Myrmekitic textures and perthite; c) Interstitial zircon.

**Sample ID:** MR-GN21-35

**Rock Type:** Metadiorite

**Analysis:** Whole rock ICP-MS and XRF

**Hand Sample:** Fine to medium grain, equigranular rock, weakly foliated, 80% felsic minerals, 20% mafic minerals. Slightly altered (5% secondary minerals)



**Thin Section:** Fine to medium-grained, granoblastic rock. Plagioclase (50%) grains are anhedral, equant to elongate, with deformed polysynthetic twins and range in size from 0.1-1.5 mm. Potassium feldspar (20%) and quartz (5%) are both present but difficult to differentiate due to lack of twinning in feldspars. Both are equant, anhedral, with subgrain boundaries, ranging in size from 0.1-2 mm. Antiperthite present. Clinopyroxene (15%) is pleochroic tan to light green, anhedral, ranging in size from 0.25-1.5 mm. Orthopyroxene (10%) is pleochroic shades of tan, same textures and sizes as cpx. Alignment and elongation of pyroxenes define a weak foliation. Zircon and apatite throughout. Zircons are sub to euhedral with rounded ends, 100-150  $\mu\text{m}$ , present as inclusions in feldspars and interstitially. Apatite found as inclusions in plagioclase and pyroxenes.

Areas of partial melting ~20%, with melting restricted to brown glass along grain boundaries and secondary opaques, minimal involvement of primary pyroxenes/feldspars. Primary mineral phases exhibit spongy textures adjacent to melt patches. Melting occurs in close association with pyroxenes.

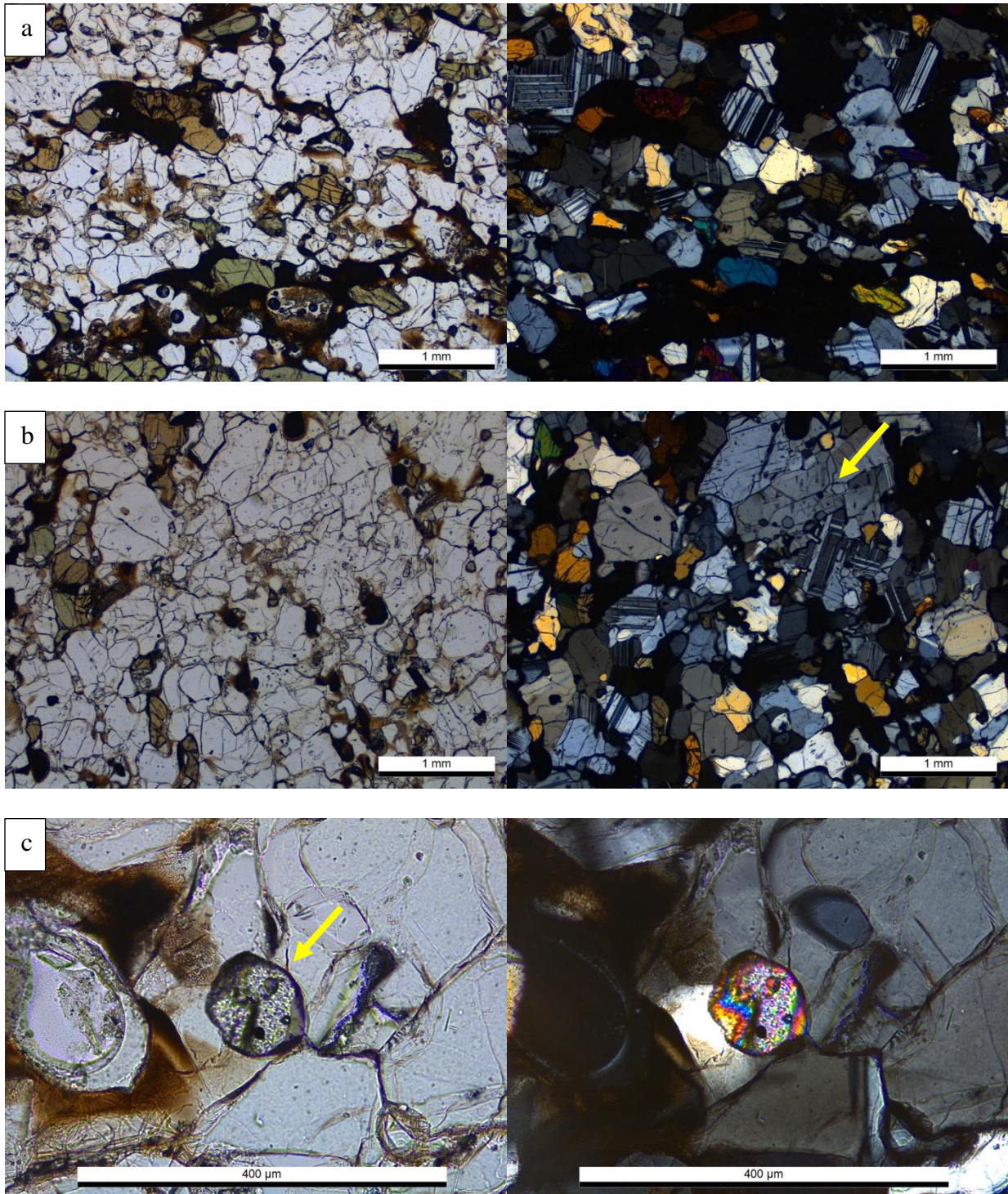


**Figure B.6** a) Plagioclase and pyroxenes. Alignment of pyroxenes visible, as well as melt regions with brown glass and opaques. Secondary minerals from low temperature alteration also visible; b) Myrmekitic textures and perthite; c) Zircon inclusion in feldspar.

**Sample ID:** MR-GN21-37

**Rock Type:** One-pyroxene metacumulate

**Analysis:** Whole rock ICP-MS and XRF

**Hand Sample:** Medium grain, equigranular, weakly foliated. 50% felsic minerals, 50% mafic minerals. Fresh (<2% low temperature alteration).



**Thin Section:** Medium to coarse-grained, granoblastic rock. Plagioclase (50%) grains are anhedral, equant to elongate, ranging in size from 0.25 mm-4 mm, with 120-degree triple junctions, and deformed polysynthetic twins. Clinopyroxene (43%) is pleochroic tan to green, anhedral, ranging in size from 0.25-2.5 mm, with sieve textures. Pyroxenes and opaques define a weak foliation. Olive green, aluminous, anhedral spinel present in trace amounts.

Partial melting affects ~35% of the sample, with patches of glass and secondary fine grained euhedral, tabular to acicular plagioclase, skeletal olivine (7%), and opaques. Primary mineral phases exhibit zoning adjacent to melt patches and sieve textures.

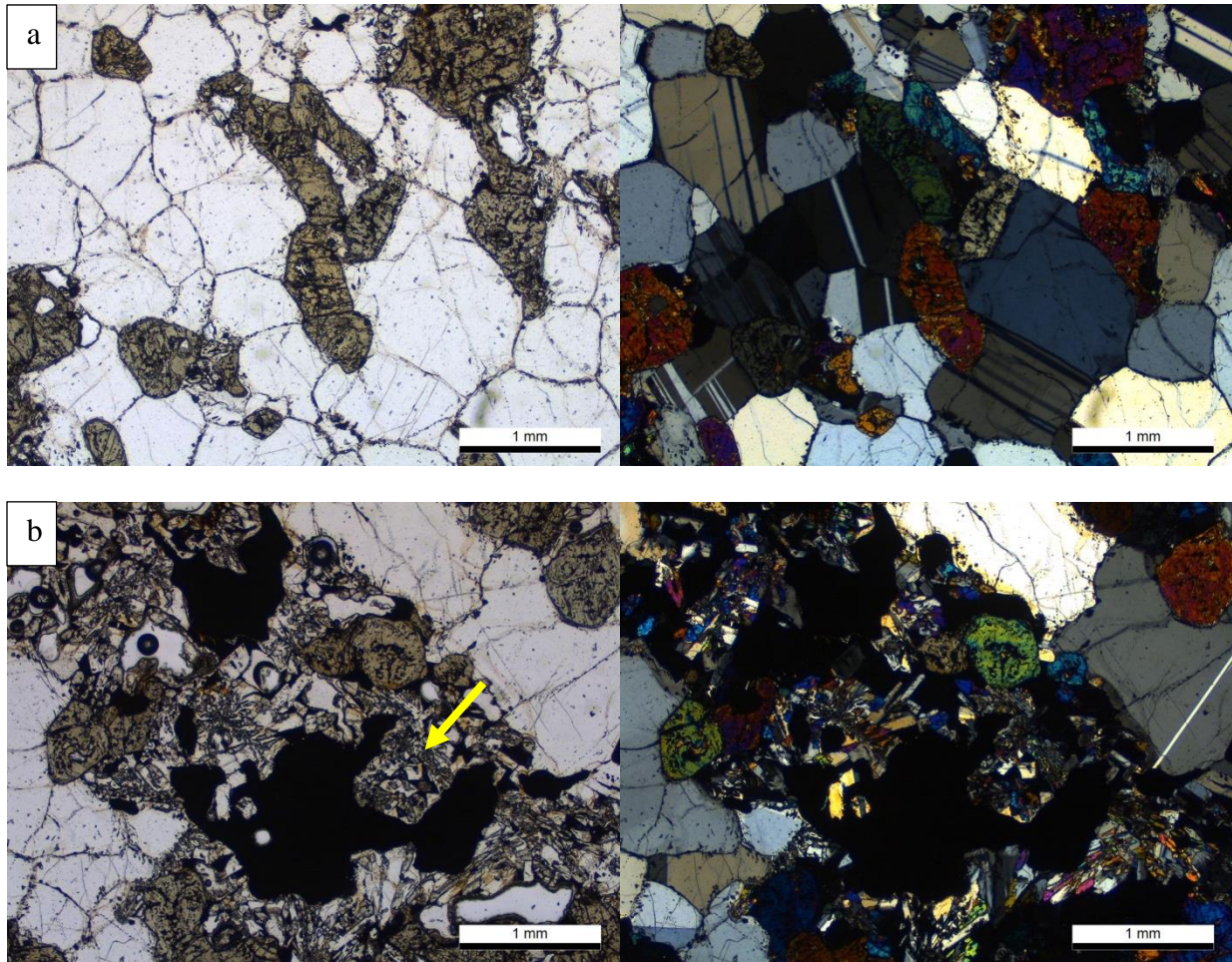


**Figure B.7** a) Plagioclase and pyroxenes. Spongy textures visible in pyroxenes, as well as a slight alignment; b) Partial melting with patches of glass and secondary fine grained euhedral, tabular to acicular plagioclase, skeletal olivine, and opaques.

**Sample ID:** MR-GN21-39

**Rock Type:** Quartzofeldspathic

**Analysis:** Whole rock ICP-MS and XRF, U-Pb and Hf LA-ICP-MS, Geothermometry

**Hand Sample:** Fine to medium grain, equigranular rock, weakly foliated. 98% felsic minerals, 2% mafic minerals. Slightly altered (10% secondary minerals, i.e. caliche and clays along grain boundaries).



**Thin Section:** Fine to coarse-grained, porphyroblastic rock. Quartz (40%) grains are anhedral, with significant embayment, undulose extinction and subgrain boundaries. Quartz grains are seriate, ranging from 0.2mm to large poikiloblastic 1.5cm grains, partially to fully enclosing K-spar and plagioclase. Potassium feldspar (25%) is abundant, but difficult to differentiate from quartz due to lack of zoning (differentiated through optic figures). Textures are similar, with subgrain boundaries and embayment, ranging from 0.1-5 mm in size. Plagioclase (30%) is anhedral with deformed polysynthetic twins, ranging in size from 0.25-3mm. Myrmekitic intergrowths also present. Orthopyroxene (<2%) is pleochroic shades of tan, anhedral, ranging in size from 0.25-0.5 mm with spongy textures. Zircons are elongate, euhedral, 50-200 micron, present as inclusions in quartz and interstitially.

Areas of partial melting <10%, with melting restricted to brown and colorless glass along grain boundaries and opaques, minimal involvement of primary pyroxenes/feldspars. Primary pyroxenes and feldspars exhibit spongy textures and reaction rims adjacent melt regions. Caliche and the grain boundary clay minerals both present, indicating of low-T surface alteration, which may affect WR analysis.

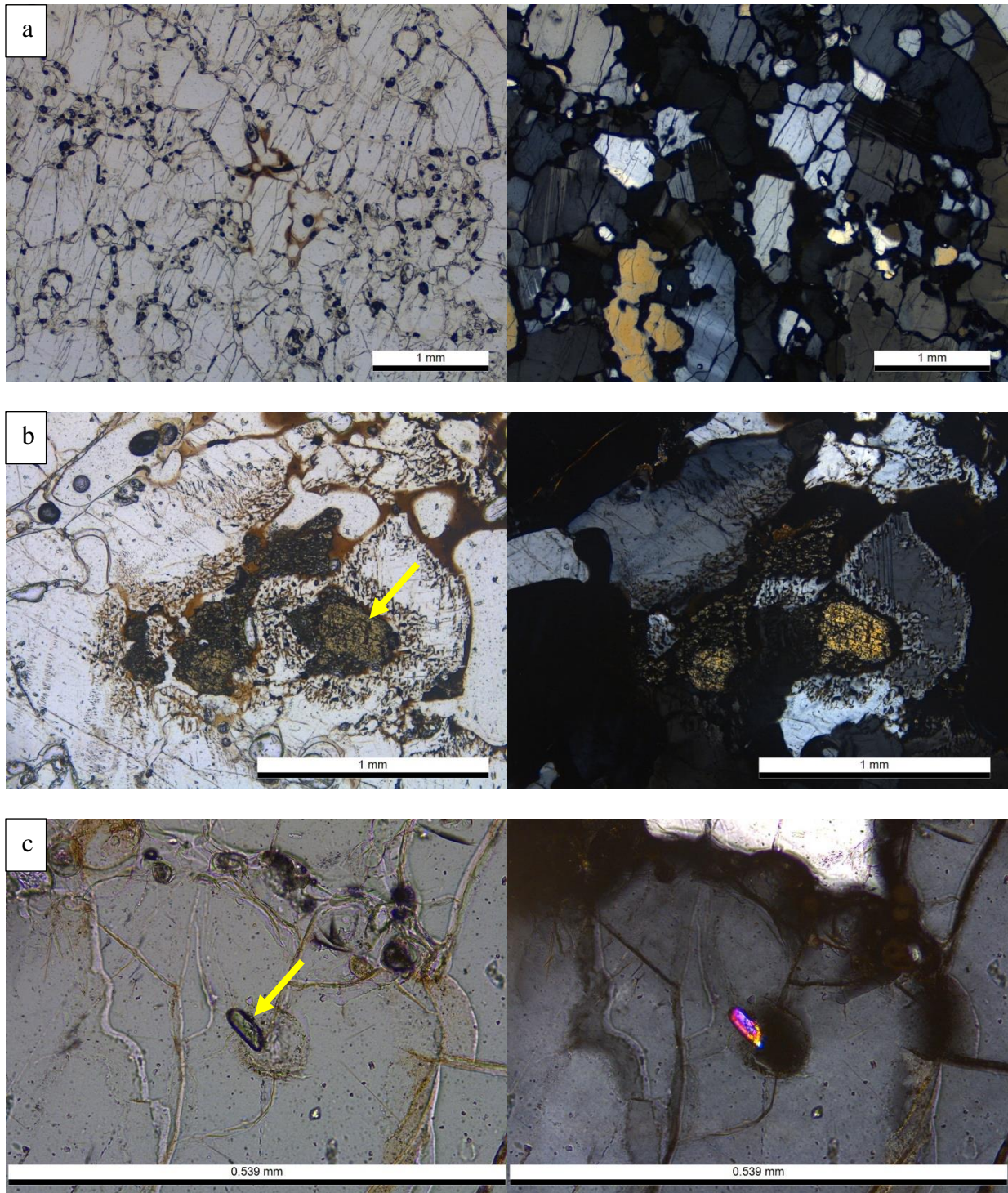


**Figure B.8** a) Quartz and feldspars with colorless to brown glass along grain boundaries; b) Spongy orthopyroxene, and brown glass. Reaction rims visible on feldspars; c) Zircon inclusion in quartz.

**Sample ID:** MR-GN21-53

**Rock Type:** Quartzofeldspathic

**Analysis:** Whole rock ICP-MS and XRF, U-Pb and Hf LA-ICP-MS, Geothermometry

**Hand Sample:** Fine to medium grain, equigranular, strongly foliated rock. 95% felsic minerals, 5% mafic minerals. Slightly altered (10% secondary minerals, i.e. caliche and clays along grain boundaries).



**Thin Section:** Fine to medium-grained, porphyroblastic rock. Quartz (35%) grains are anhedral and elongate with significant embayment, and subgrain boundaries. Quartz grains are bimodal, ranging from 0.2-0.5mm to 3-5mm porphyroblasts. Potassium feldspar (25%) is abundant, but difficult to differentiate from quartz due to lack of twinning. Textures are similar, with subgrain boundaries and embayment, and bimodal grain sizes from 0.25-1 mm to a large 1.5 cm, perthitic porphyroblast. Plagioclase (35%) is anhedral, equant, 0.1-0.5 mm, with polysynthetic twinning. Myrmekitic intergrowths and perthite also present throughout. Orthopyroxene (5%) is anhedral, equant to elongate, pleochroic tan, ranging in size from 0.5-1.5 mm. Foliation indicated by alignment of pyroxenes and quartz. Apatite present as inclusions in quartz and plagioclase. Opaques (1%) throughout, helping to define the foliation. Zircons are subhedral, rounded, 50-100  $\mu\text{m}$ , found interstitially to feldspars and as inclusions in quartz.

Areas of partial melting <10%, with melting restricted to brown and colorless glass along grain boundaries and opaques, minimal involvement of primary pyroxenes/feldspars. Primary pyroxenes and feldspars exhibit reaction rims adjacent the brown glass. Caliche and the grain boundary clay minerals both present, indicating of low-T surface alteration, which may affect WR analysis.

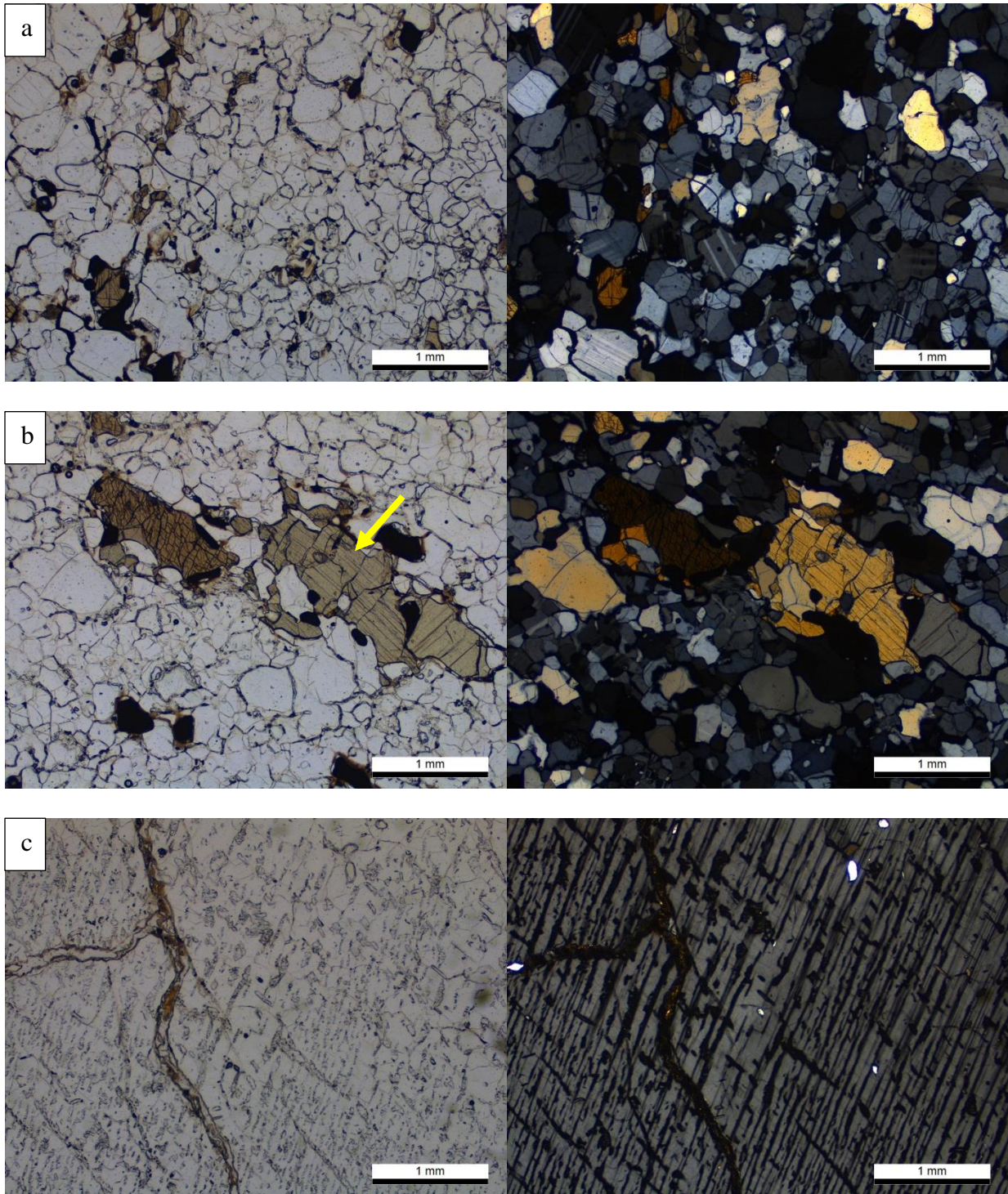


**Figure B.9** a) Quartz and feldspars with colorless to brown glass along grain boundaries; b) Alignment of orthopyroxene and opaques. Reaction rims visible on feldspars; c) Large perthitic porphyroblast.

**Sample ID:** MR-GN21-56

**Rock Type:** Olivine Meta-Gabbro

**Analysis:** Whole rock ICP-MS and XRF

**Hand Sample:** Coarse-grain rock, highly altered, lacks foliation. 50% felsic minerals, 50% mafic minerals. Fresh (<2% low temperature alteration).



**Thin Section:** Coarse-grained, granoblastic rock. Plagioclase (50%) is bimodal with grains from <1-2 mm to >8 mm. Grains are anhedral, equant to tabular, with highly deformed polysynthetic twins and reaction rims where the grains contact other mineral phases. Where plagioclase grains are in contact with each other, they show subgrain boundaries and 120-degree triple junctions. Clinopyroxene (25%), orthopyroxene (10%?), and primary olivine (15%) present in close association with regions of melt. Pyroxene grains are anhedral ranging in size from 0.5 mm to large poikiloblastic 1 cm grains. It appears that pyroxene grains were originally large, but partially melted with a spongy appearance. Primary olivine is anhedral and heavily iddingsitized, ranging in size from 0.5-3 mm. Dark green spinel present in small quantities in association with iddingsitized olivine.

Partial melting affects more than 50% of the sample, with patches of glass and secondary euhedral, tabular plagioclase, skeletal olivine, and opaques. Melting occurs within and around primary coarse-grained plagioclase and pyroxenes. Primary mineral phases exhibit zoning adjacent to melt patches and spongy textures.

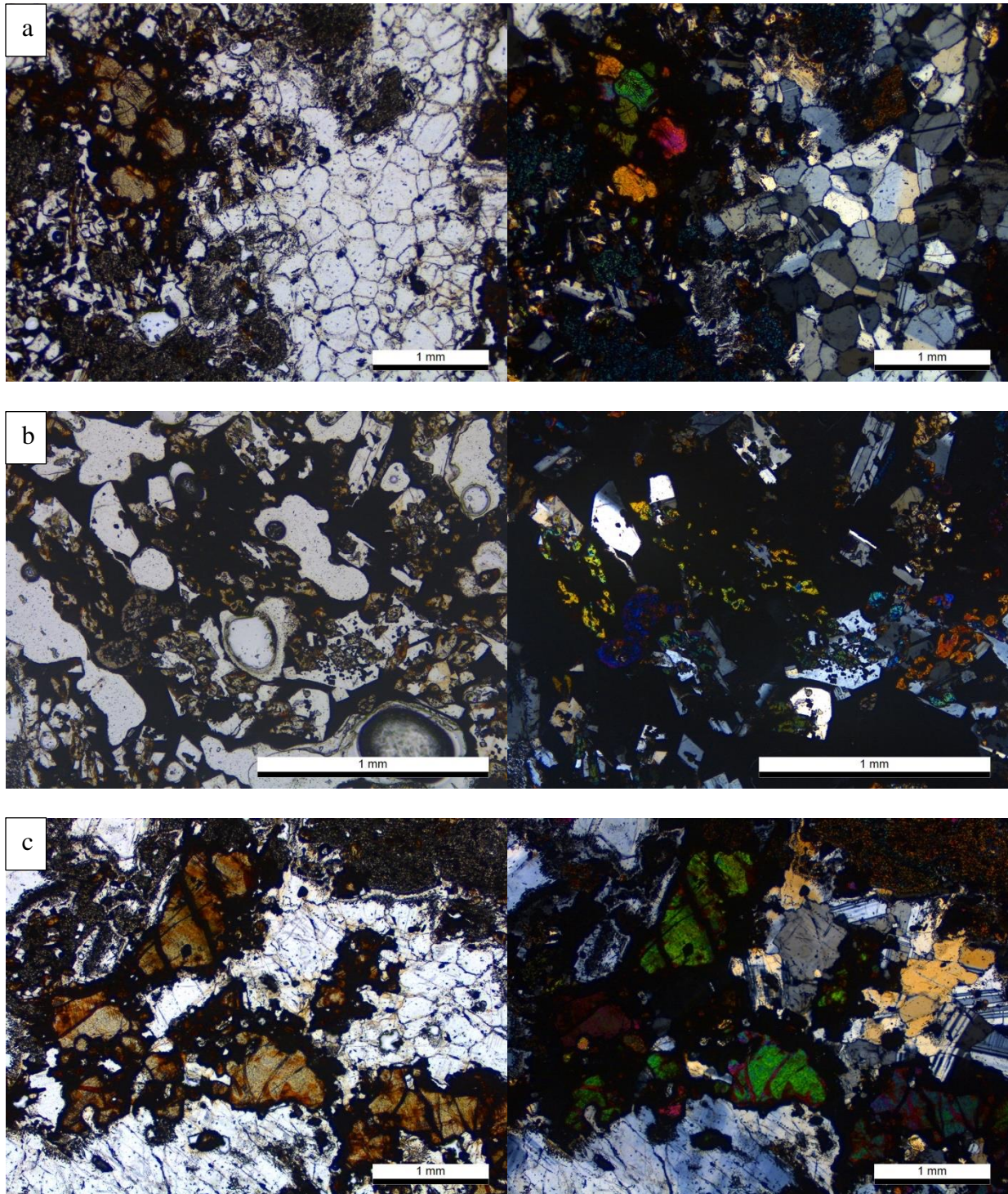


**Figure B.10** a) Fine-grained plagioclase, primary iddingsitized olivine, and spongy pyroxene (lower left corner); b) Partial melting with patches of glass and secondary euhedral, tabular plagioclase, skeletal olivine, and opaques; c) Large plagioclase porphyroblast (lower left), iddingsitized primary olivine (center), and spongy pyroxene (upper right).

**Sample ID:** MR-GN21-59

**Rock Type:** Two-pyroxene metacumulate

**Analysis:** Whole rock ICP-MS and XRF

**Hand Sample:** Medium grain, equigranular rock, lacks foliation. 80% felsic minerals, 20% mafic minerals. Fresh (<2% low temperature alteration).



**Thin Section:** Fine to coarse-grained, granoblastic rock. Plagioclase (80%) grains are anhedral, equant to elongate, with deformed polysynthetic twins and reaction rims, ranging in size from 0.5-5 mm. Clinopyroxene (15%) is pleochroic tan to light green, anhedral, ranging in size from 0.25-1.5 mm, with significant sieve textures. Orthopyroxene (5%) is pleochroic shades of tan, same textures and sizes as clinopyroxene.

Partial melting affects ~25% of the sample, with patches of dark mesostasis and secondary euhedral iddingsitized olivine, fine to medium grain, euhedral, tabular plagioclase, and opaques. Primary mineral phases exhibit zoning adjacent to melt patches, reaction rims, and spongy textures.

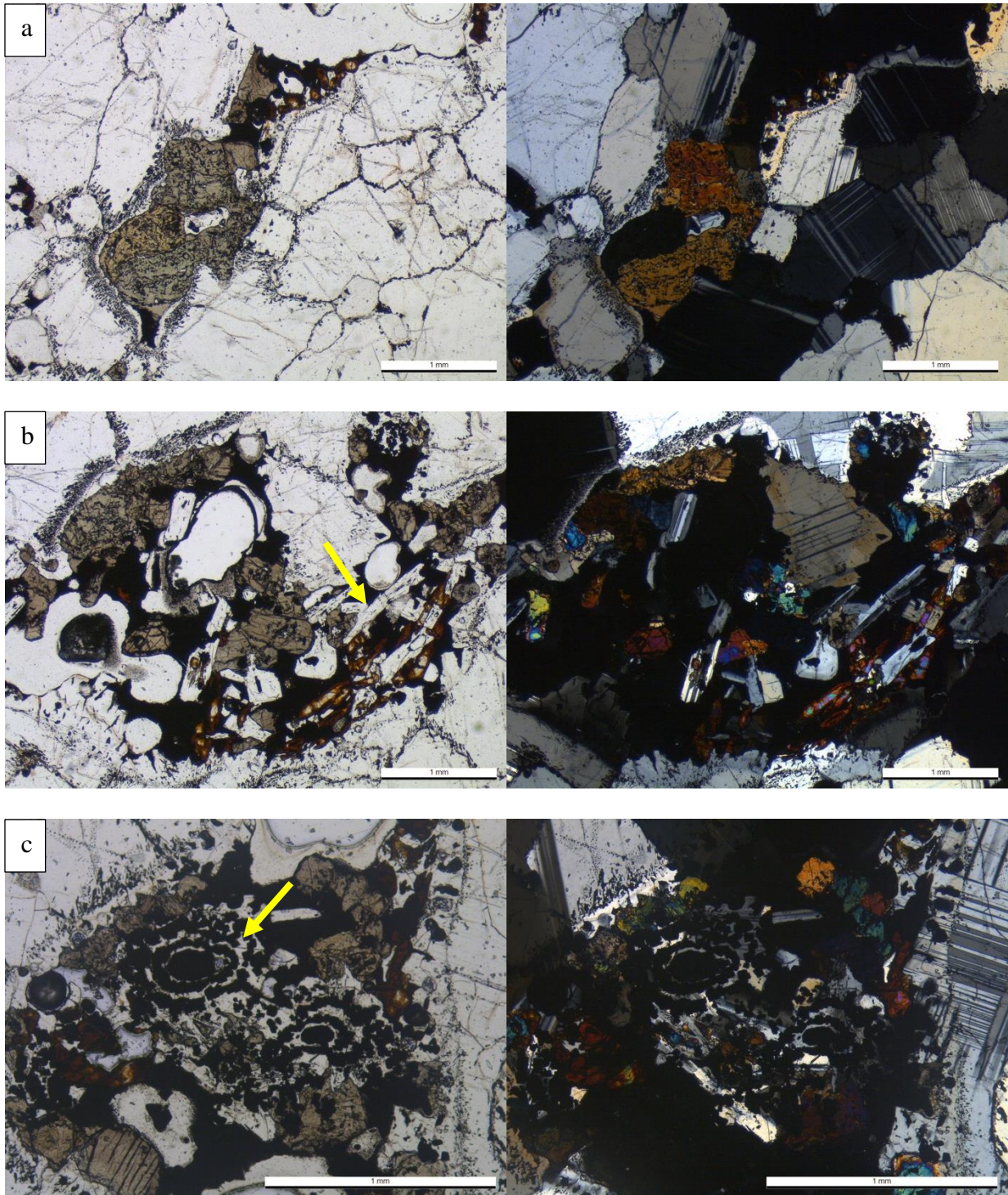


**Figure B.11** a) Plagioclase with  $120^\circ$  triple junctions, and spongy, zoned reaction rims. Pyroxenes with sieve textures; b) Partial melting with patches of glass and secondary euhedral, tabular plagioclase, skeletal iddingsitized olivine, and opaques; c) Opaque necklaces.

**Sample ID:** MR-GN21-62

**Rock Type:** One-pyroxene metacumulate

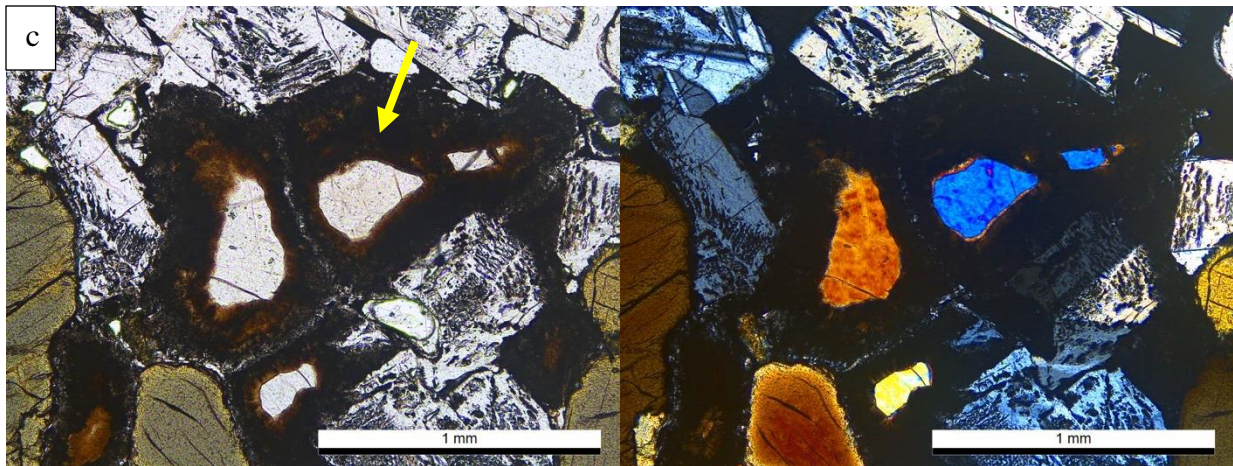
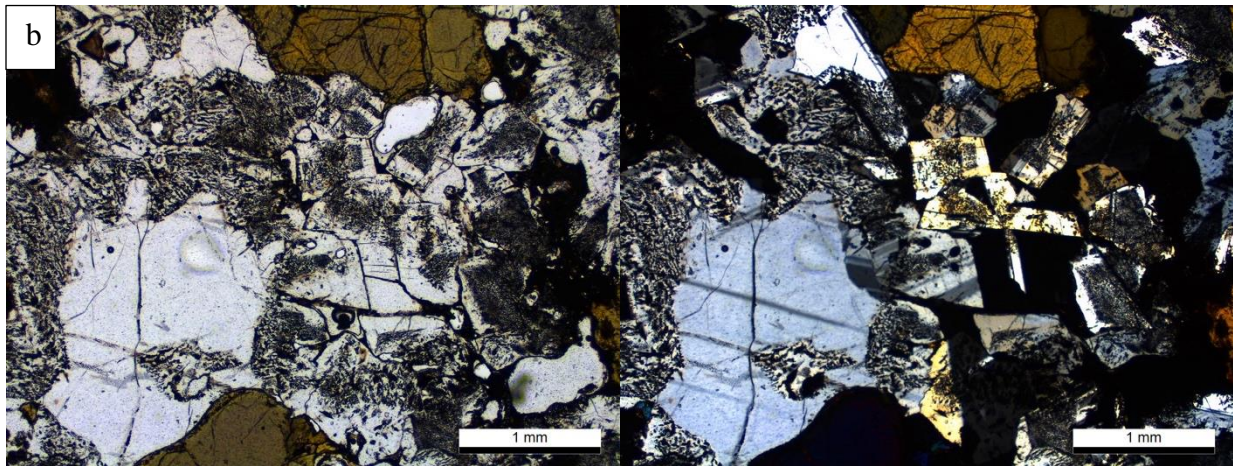
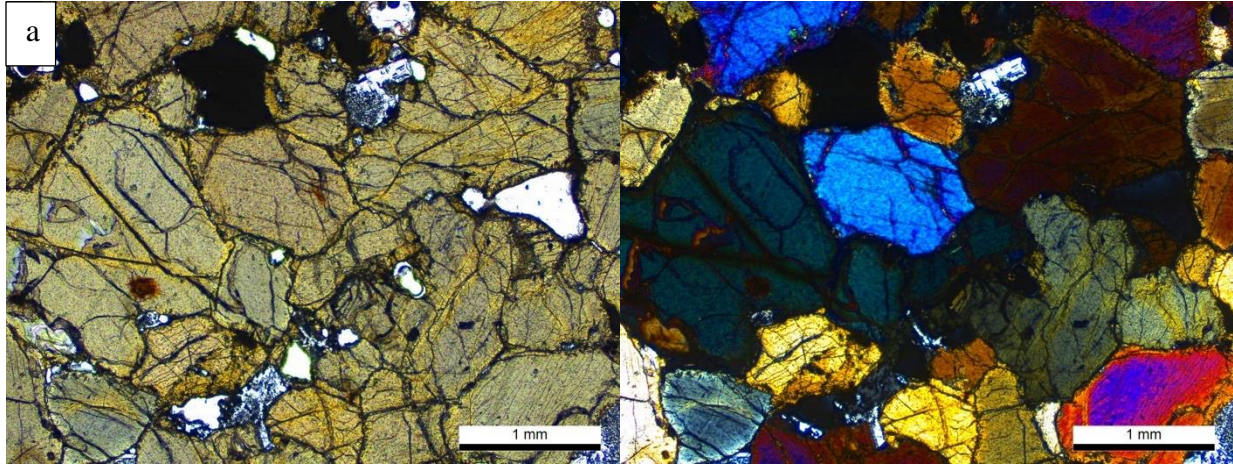
**Analysis:** Whole rock ICP-MS and XRF

**Hand Sample:** Medium grain, equigranular, strongly foliated rock, 40% felsic minerals, 60% mafic minerals. Fresh (<2% low temperature alteration).



**Thin Section:** Medium-grained, strongly foliated rock. Plagioclase (40%) grains are sub to euhedral, tabular, range in size from 0.5-2.5 mm, with polysynthetic twins, reaction rims, and spongy textures. Clinopyroxene (60%) is pleochroic tan to green, anhedral, ranging in size from 0.25-2.5 mm. Zoning of cpx evident on crystal boundaries and along grain fractures. Pyroxenes define the foliation. Apatite present as inclusions in clinopyroxene.

Partial melting affects ~25% of the sample, with patches of dark mesostasis and secondary anhedral olivine, and opaques. Olivine rims are significantly altered, with a dark brown fuzzy cryptocrystalline quench. Primary mineral phases exhibit zoning adjacent to melt patches, reaction rims, and spongy textures. Plagioclase textures and mineral relationship suggest localized in situ partial melting and crystallization, while pyroxene textures are more typical of metamorphic equilibration.



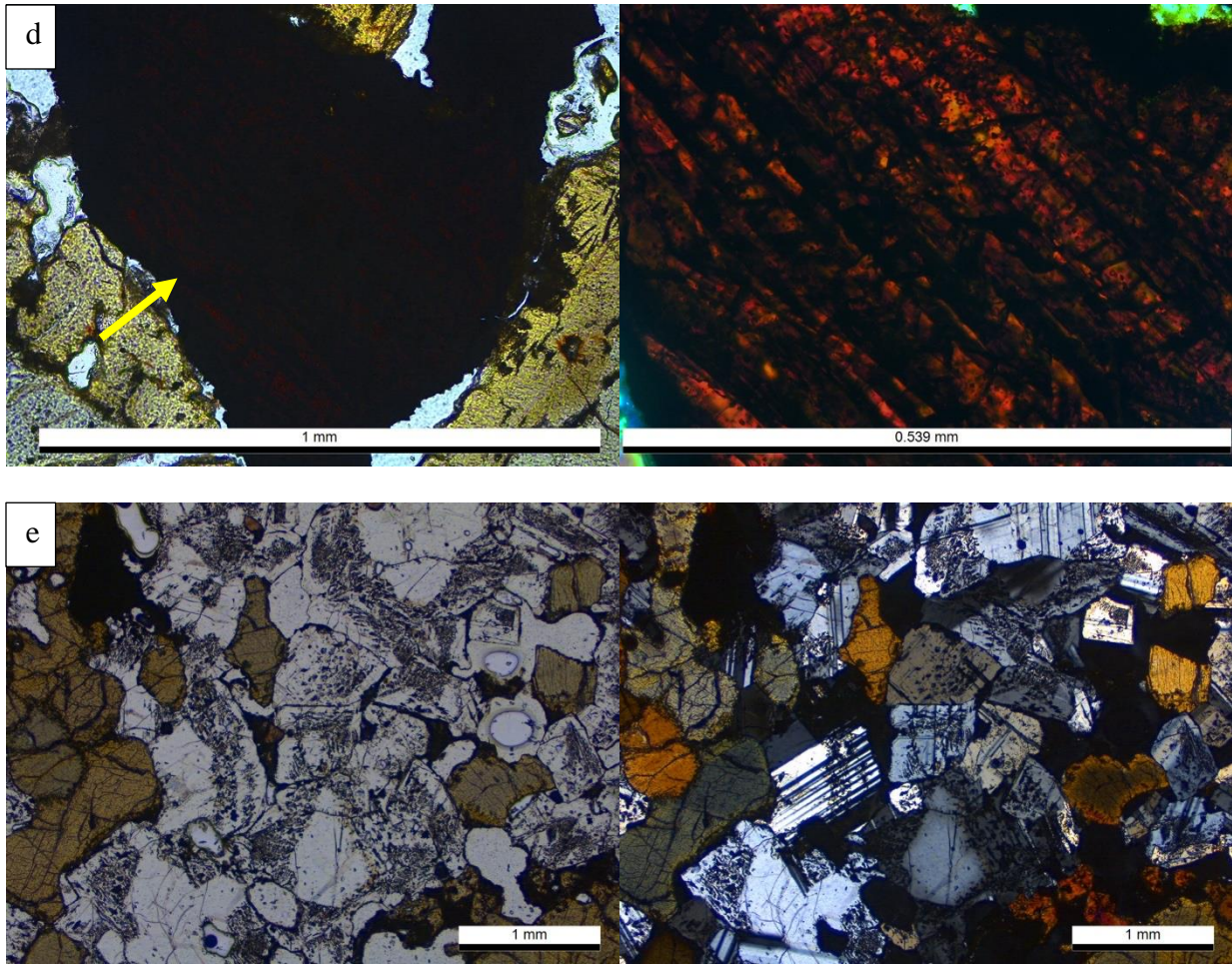


**Figure B.12** a) Clinopyroxene with zoning on crystal boundaries; b) Plagioclase with spongy textures and reaction rims; c) Secondary olivine with dark cryptocrystalline rims; d) Mystery mineral; e) Primary clinopyroxene and plagioclase textures.

**Sample ID:** MR-GN22-25

**Rock Type:** Biotite-bearing Metadiorite

**Analysis:** Whole rock ICP-MS and XRF

**Hand Sample:** Fine to medium grain, equigranular rock, weakly foliated. 65% felsic minerals, 35% mafic minerals. Fresh (<2% low temperature alteration).



**Thin Section:** Phaneritic, granoblastic, two-pyroxene rock. Plagioclase (55%) grains are anhedral, equant in shape, display polysynthetic twinning, 120-degree triple junctions, and range in size from 0.5-1.5 mm. Potassium feldspar (10%) present with the same textures and sizes as plag. Clinopyroxene (20%) is anhedral, pleochroic tan to light green, ranging in size from 0.25-1.5 mm. Orthopyroxene (10%) is pleochroic shades of tan, with the same textures and sizes as cpx. Some pyroxenes present as inclusions in plagioclase. Biotite (5%) is pleochroic tan to brown, aligned subparallel to foliation, ranges in size from 0.25-1mm, and slightly altered. Pyroxenes and biotite define a weak foliation. Apatite present as inclusions in plag and pyroxene. Zircon found as inclusions in plagioclase. Opaques in close association with pyroxenes.

Partial melting affects ~10% of the sample, with patches of brown cryptocrystalline quench and secondary opaques found near biotite, likely a result of dehydration melting. Primary mineral phases exhibit reaction rims adjacent to melt patches.

**Suggested Future Analyses:** U-Pb geochronology, microprobe of mica, and 2-pyroxene thermometry

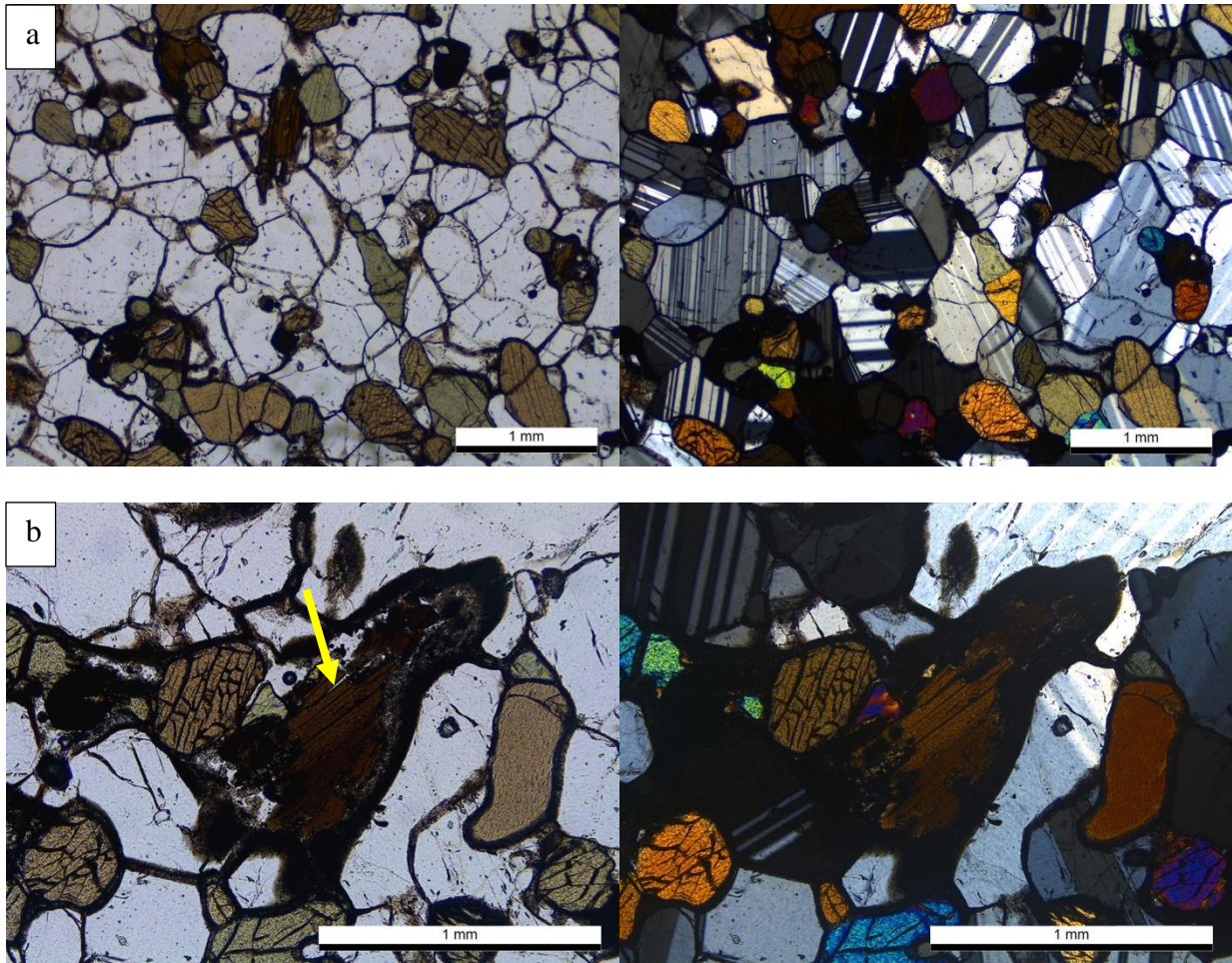


**Figure B.13** a) Pyroxenes and plagioclase textures throughout. Subparallel alignment of pyroxenes; b) Biotite and partial melt with cryptocrystalline quench and opaques.

**Sample ID:** MR-GN22-27

**Rock Type:** Metadiorite

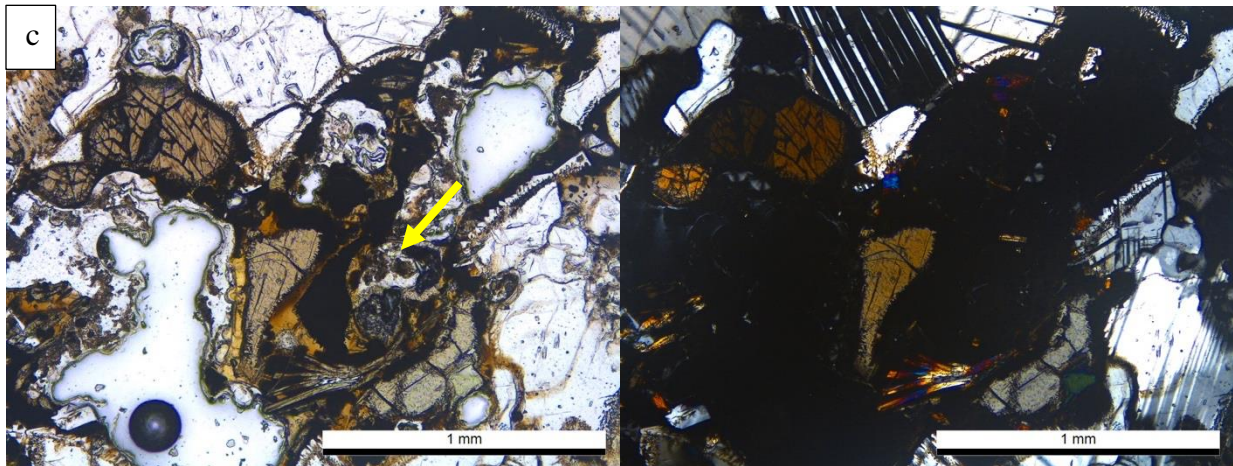
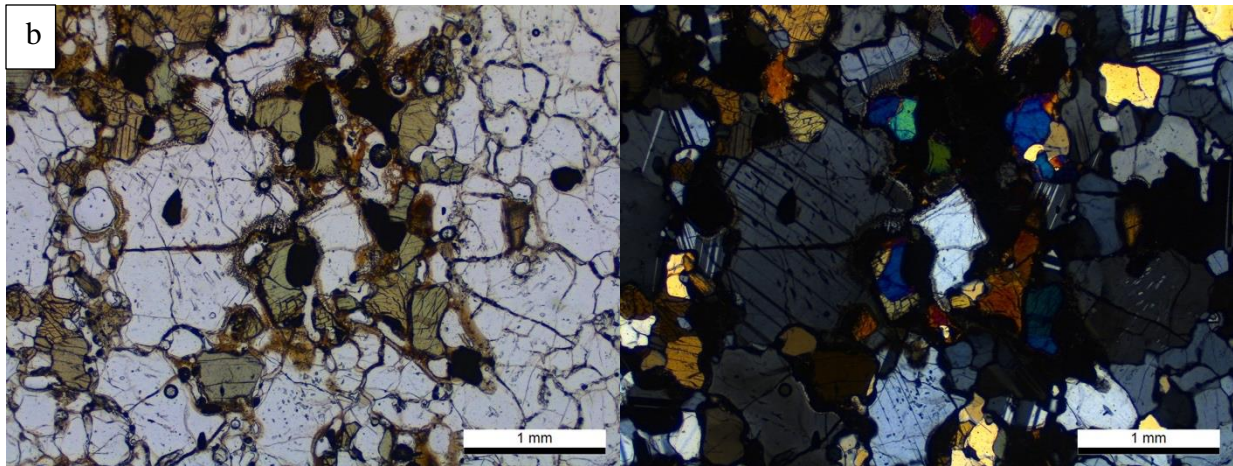
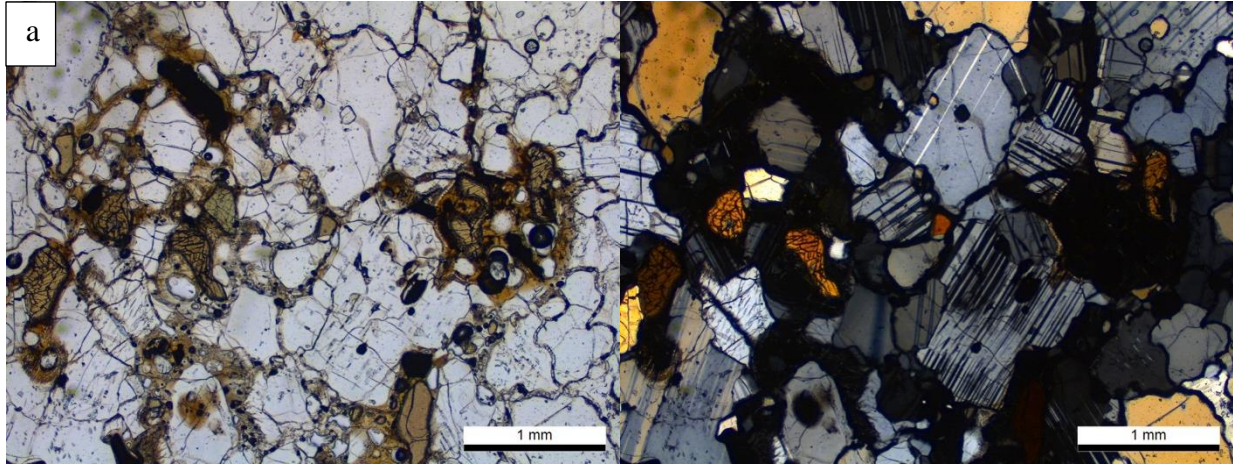
**Analysis:** Whole rock ICP-MS and XRF, U-Pb and Hf LA-ICP-MS, Geothermometry

**Hand Sample:** Fine to medium grain, equigranular rock, weakly foliated. 75% felsic minerals, 25% mafic minerals. Fresh (<2% low temperature alteration).



**Thin Section:** Fine to medium-grained, granoblastic rock. Plagioclase (50%) grains are anhedral, equant to elongate, with deformed polysynthetic twins and range in size from 0.1-2.5 mm. Antiperthite abundant throughout. Potassium feldspar (orthoclase-15%) and quartz (10%) are both present but difficult to differentiate due to lack of twinning in feldspars. Both are equant, anhedral, with subgrain boundaries, ranging in size from 0.1-2 mm. Myrmekitic intergrowths present. Clinopyroxene (15%) is anhedral, pleochroic tan to light green, ranging in size from 0.25-1.5 mm. Orthopyroxene (10%) is pleochroic shades of tan, with the same textures and sizes as cpx. Pyroxenes help to define a weak foliation. Apatite present as inclusions in plag. Zircons are anhedral and rounded, 100-150  $\mu\text{m}$ , as inclusions in feldspars and interstitially.

Partial melting affects 50% of the sample, with patches of dark cryptocrystalline quench and secondary acicular pyroxene, fine grained, euhedral, tabular plagioclase, and opaques. Primary mineral phases exhibit zoning and spongy textures adjacent to melt patches. Some strange spherulitic structures, could be zeolites.



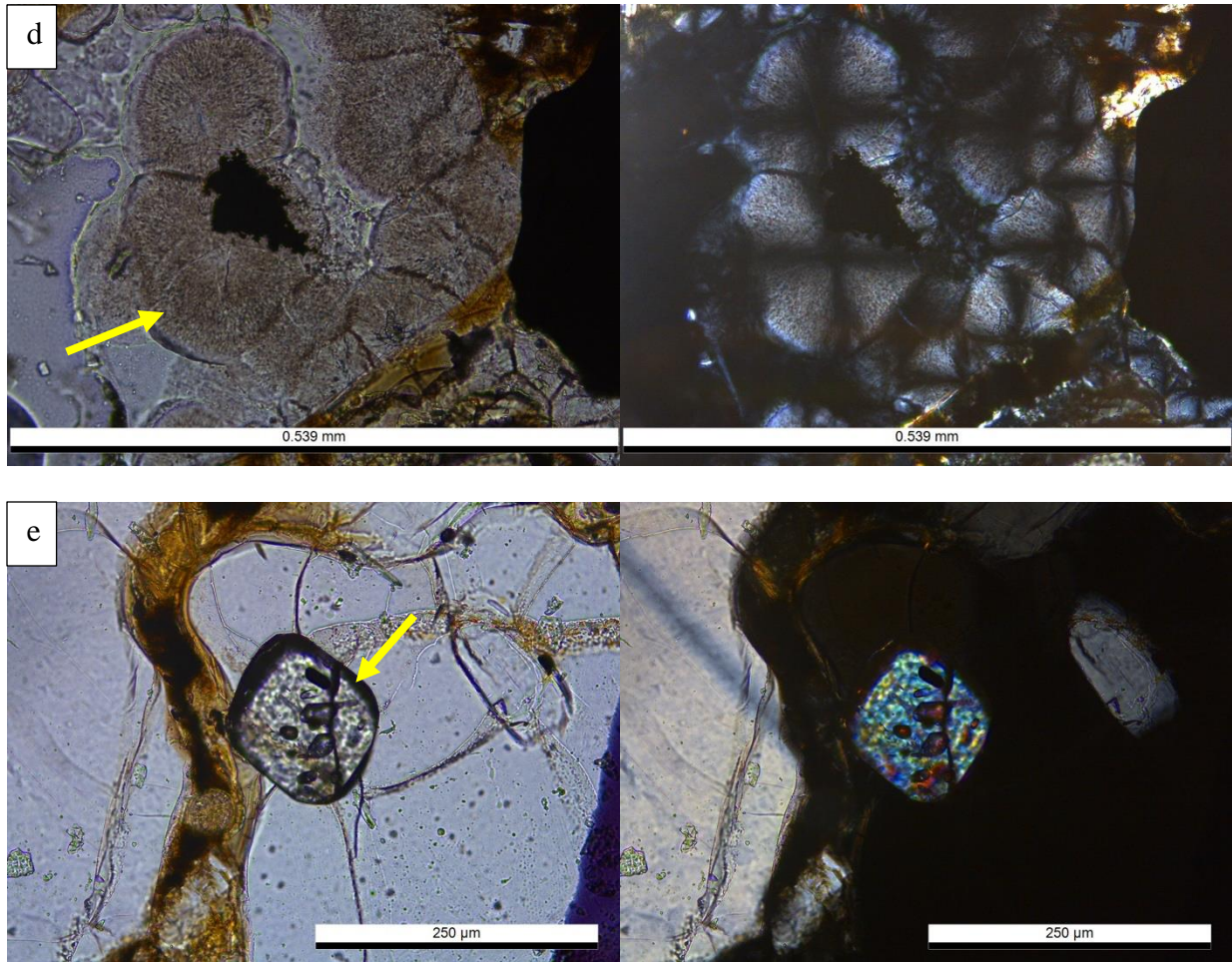


**Figure B.14** a & b) Plagioclase and pyroxene textures throughout, with grain boundary brown glass, and opaques in association with pyroxenes; c) Partial melt with patches of dark cryptocrystalline quench and secondary acicular pyroxene, fine grained, euhedral, tabular plagioclase, and opaques; d) Spherulitic structures; e) Anhedronal zircon inclusion in plagioclase.

**Sample ID:** MR-GN22-35

**Rock Type:** Metadiorite

**Analysis:** Whole rock ICP-MS and XRF, U-Pb and Hf LA-ICP-MS, Geothermometry

**Hand Sample:** Fine to medium grain, equigranular rock, lacking foliation. 75% felsic minerals, 25% mafic minerals. Slightly altered (5% secondary minerals – calcite).



**Thin Section:** Fine to coarse-grained, granoblastic rock. Plagioclase (70%) grains are anhedral, equant to elongate, with deformed polysynthetic twins and range in size from 0.5-3.5 mm. Antiperthite abundant throughout. Potassium feldspar (5%) is equant, anhedral, ranging in size from 0.1-2 mm. Feldspars share 120-degree triple junctions. Clinopyroxene (15%) is anhedral, pleochroic tan to light green, ranging in size from 0.1-1.5 mm. Orthopyroxene (10%) is pleochroic shades of tan, with the same textures and sizes as cpx. Pyroxenes are highly fractured and provide a sense of foliation. Small amounts of opaques (2%) associated with pyroxenes. Zircon and apatite throughout. Zircons are subhedral with rounded ends, 100-150  $\mu\text{m}$ , present as inclusions in feldspars and interstitially. Some interstitial carbonate, likely a result of low-temperature alteration.

Areas of partial melting <10%, with melting restricted to glass and cryptocrystalline quench along grain boundaries and minimal involvement of primary pyroxenes/feldspars.

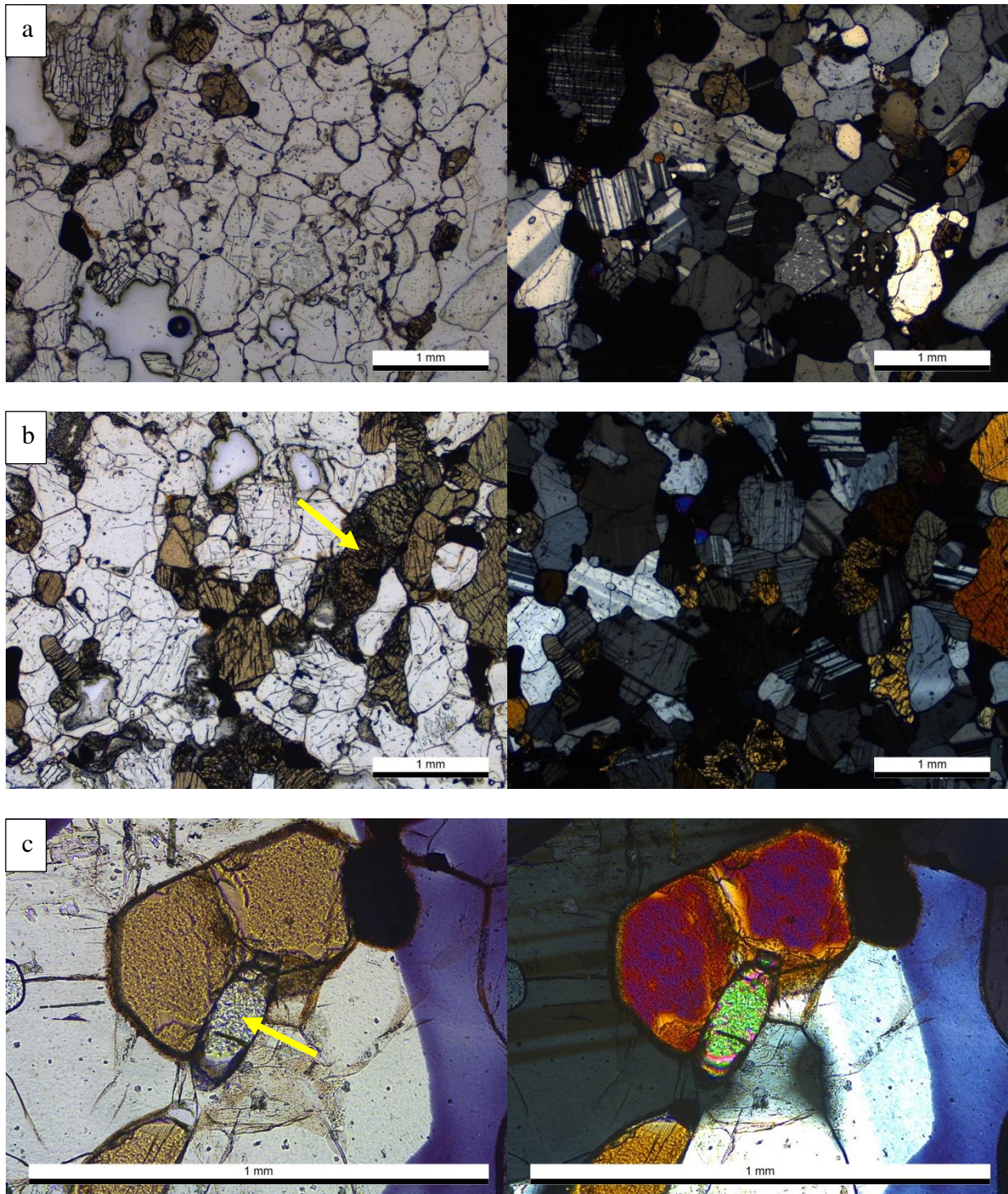


**Figure B.15** a) Feldspars with 120° triple junctions and antiperthite; b) Highly fractured and aligned pyroxenes; c) Interstitial, subhedral zircon.

**Sample ID:** MR-GN22-36

**Rock Type:** Biotite-bearing Metadiorite

**Analysis:** Whole rock ICP-MS and XRF

**Hand Sample:** Medium grain, equigranular, strongly foliated rock, 60% felsic minerals, 40% mafic minerals. Fresh (<2% low temperature alteration).



**Thin Section:** Fine to coarse-grained, granoblastic, two-pyroxene rock. Plagioclase (40%) grains are anhedral, equant in shape, display polysynthetic twinning and range in size from 0.5-3 mm. Potassium feldspar (20%) is anhedral, equant to elongate, lacks twinning, and ranges in size from 0.5-3mm. Clinopyroxene (20%) is anhedral, pleochroic tan to light green, ranging in size from 0.25-2.5 mm. Orthopyroxene (15%) is pleochroic shades of tan, with the same textures and sizes as cpx. Some pyroxenes present as inclusions in plagioclase. Most grains (plag and pyx) share 120-degree triple junctions. Biotite (5%) is pleochroic tan to brown, aligned subparallel, and ranges in size from 0.25-1.5mm. Pyroxenes and biotite form the foliation in this rock. Opaques (1%) present in association with pyroxenes and biotite.

Partial melting affects ~40% of the sample, with patches of brown cryptocrystalline quench, secondary acicular pyroxenes, and opaques found near biotite. Biotite records partial breakdown reaction to opaques + melt/fluids. Grains surrounding altered biotite have spongy and zoned reaction rims.

**Suggested Future Analyses:** Microprobe of mica and 2-pyroxene thermometry

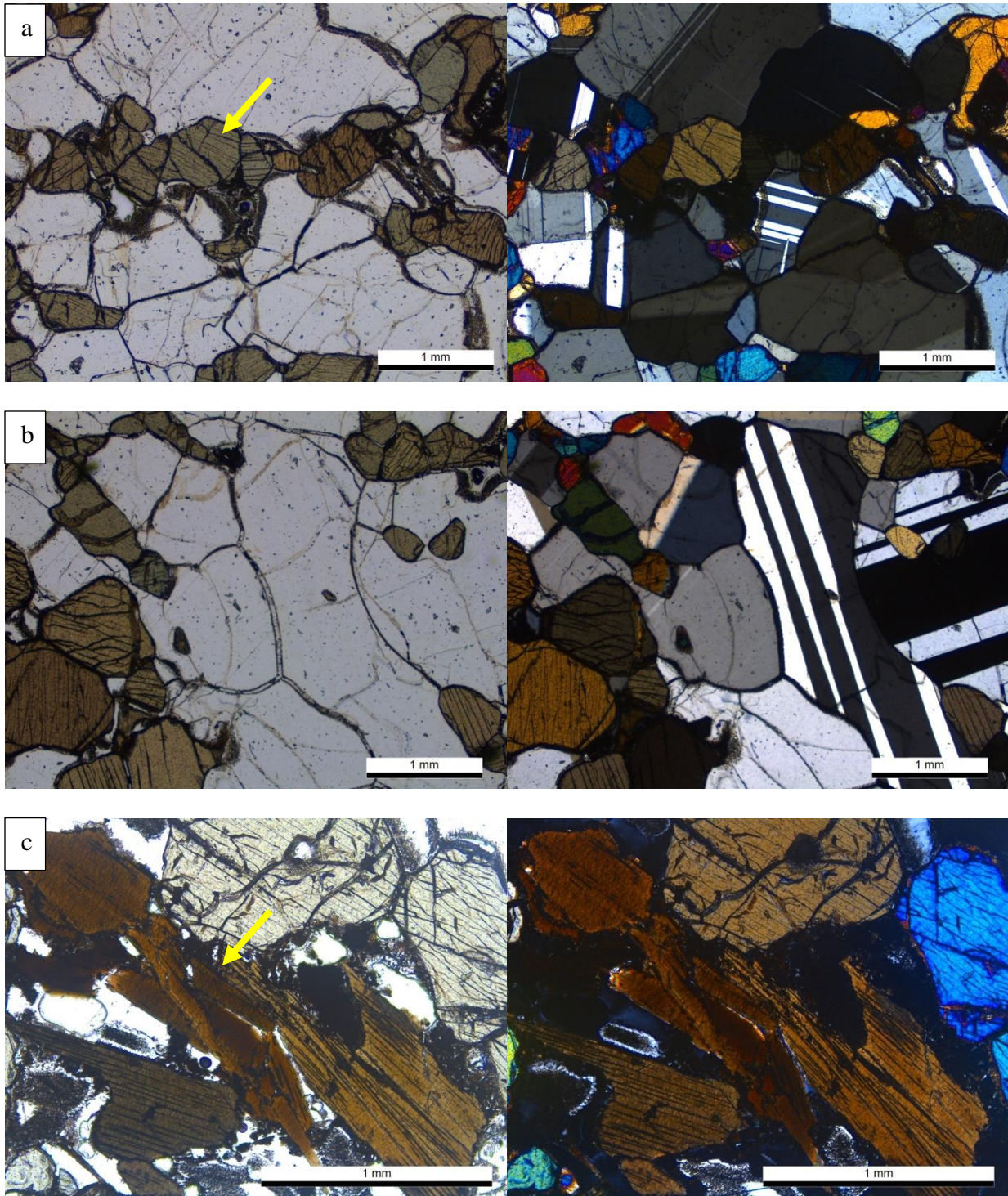


**Figure B.16** a & b) Pyroxenes and plagioclase textures throughout. Subparallel alignment of pyroxenes; c) Biotite and partial melt with cryptocrystalline quench and opaques.

## Appendix C - Whole Rock Geochemistry

Sample ID	MR-GN21-33	MR-GN21-37	MR-GN21-62	pk-G-GN21-1	pk-G-GN21-6	pk-G-GN21-8	pk-G-GN21-9
Rock Type	One-pyx metacumulate						
Major Elements (wt%)							
SiO <sub>2</sub>	53.08	49.40	42.30	46.23	51.91	48.67	48.64
TiO <sub>2</sub>	0.39	0.64	1.89	1.32	0.26	0.57	0.55
Al <sub>2</sub> O <sub>3</sub>	25.24	19.67	16.37	24.63	22.30	23.12	22.06
Fe <sub>2</sub> O <sub>3</sub>	--	--	--	--	--	--	--
FeO*	2.75	4.86	9.73	6.85	3.86	4.27	4.49
MnO	0.04	0.10	0.14	0.08	0.07	0.07	0.08
MgO	1.32	7.24	6.01	2.50	5.28	5.04	6.10
CaO	10.72	14.41	19.92	13.17	11.32	13.33	13.30
Na <sub>2</sub> O	4.76	2.65	1.24	2.93	3.69	3.31	3.09
K <sub>2</sub> O	0.46	0.12	0.08	0.23	0.28	0.13	0.27
P <sub>2</sub> O <sub>5</sub>	0.11	0.09	0.68	0.10	0.03	0.02	0.08
Total	98.87	99.18	98.37	98.04	99.00	98.53	98.66
LOI	0.76	0.48	0.67	--	--	--	--
Mg#	50.10	75.75	56.43	43.35	74.14	71.22	74.01
REE and Trace Elements (ppm)							
Rb	2.0	0.4	0.6	1.4	1.1	0.7	2.5
Sr	1366	882	766	755	1052	976	801
Y	5	11	24	11	5	8	9
Zr	16	21	96	62	17	21	40
V	43	178	182	231	50	143	152
Ni	16	53	52	33	63	57	72
Cr	8	104	24	13	66	54	30
Nb	1.3	0.2	1.9	8.1	1.9	2.6	4.1
Ga	20.0	16.0	17.6	22.2	16.2	17.7	18.2
Cu	20	5	35	25	10	11	20
Zn	63	81	73	53	36	50	58
Co	--	--	--	--	--	--	--
Ba	369	102	129	264	227	143	135
U	0.0	0.0	0.1	0.1	0.1	0.0	0.1
Th	0.2	0.0	0.2	0.3	0.2	0.2	0.4
Sc	6.2	28.6	21.3	15.9	14.6	20.5	24.3
Pb	3.1	0.3	0.9	4.5	1.4	0.6	0.6
Hf	0.48	0.92	2.89	1.68	0.50	0.76	1.26
Ta	0.15	0.07	0.41	4.24	1.70	3.11	2.10
Cs	0.02	0.01	0.01	0.02	0.01	0.02	0.02
La	6.05	2.11	14.77	10.35	4.43	2.66	5.64
Ce	10.18	5.30	40.14	21.39	8.48	5.78	10.30
Pr	1.11	0.90	6.08	2.56	1.03	0.86	1.25
Nd	4.59	5.19	28.71	10.63	4.52	4.67	5.49
Sm	1.01	1.77	6.43	2.34	1.11	1.37	1.68
Eu	0.87	0.80	1.83	0.85	0.79	0.73	0.79
Gd	0.92	2.18	5.81	2.16	1.07	1.64	1.88
Tb	0.16	0.36	0.86	0.37	0.19	0.27	0.31
Dy	0.92	2.11	4.64	2.13	1.01	1.63	1.82
Ho	0.18	0.39	0.87	0.40	0.19	0.30	0.36
Er	0.51	1.10	2.32	1.15	0.56	0.79	0.90
Tm	0.07	0.14	0.33	0.17	0.08	0.11	0.13
Yb	0.44	0.85	1.95	1.01	0.54	0.67	0.81
Lu	0.07	0.12	0.28	0.15	0.07	0.09	0.11

Sample ID	MR-GN21-9	MR-GN21-56	MR-GN21-7	MR-GN21-59	pk-G-GN21-3	pk-G-GN21-4	pk-G-GN21-5
Rock Type	Meta-Gabbro		Two-pyx metacumulate				
Major Elements (wt%)							
SiO <sub>2</sub>	50.22	51.02	47.52	51.16	52.30	53.99	54.21
TiO <sub>2</sub>	0.45	0.48	0.35	0.98	0.64	0.96	0.66
Al <sub>2</sub> O <sub>3</sub>	17.81	21.62	13.09	25.27	18.49	20.13	17.94
Fe <sub>2</sub> O <sub>3</sub>	--	--	--	--	--	3.57	--
FeO*	5.85	5.46	11.74	3.95	7.16	3.65	7.08
MnO	0.12	0.09	0.18	0.03	0.17	0.08	0.17
MgO	9.61	5.57	16.63	1.83	4.97	3.93	4.87
CaO	11.72	10.62	7.61	11.38	8.17	7.40	8.21
Na <sub>2</sub> O	2.72	3.73	1.38	4.29	4.57	4.68	4.53
K <sub>2</sub> O	0.17	0.48	0.18	0.31	0.70	0.83	0.69
P <sub>2</sub> O <sub>5</sub>	0.12	0.20	0.09	0.04	0.25	0.30	0.28
Total	98.79	99.27	98.77	99.24	99.73	99.52	99.35
LOI	0.86	0.59	0.26	0.29	2.30	--	0.71
Mg#	77.50	68.15	74.82	49.28	59.27	54.56	59.06
REE and Trace Elements (ppm)							
Rb	0.7	2.4	1.0	0.6	0.9	2.0	0.8
Sr	470	1456	471	1322	777	784	753
Y	9	7	7	2	19	14	21
Zr	13	40	21	3	25	17	26
V	148	88	70	112	144	116	143
Ni	242	82	347	22	45	26	44
Cr	100	22	25	11	77	44	71
Nb	0.9	7.8	0.6	0.7	5.5	6.9	3.0
Ga	12.3	14.5	12.4	19.9	17.6	18.4	17.6
Cu	42	29	21	18	10	10	8
Zn	41	79	128	59	85	68	75
Co	--	--	--	--	--	--	--
Ba	117	327	131	203	551	609	642
U	0.0	0.1	0.1	0.0	0.1	0.1	0.0
Th	0.1	0.5	0.2	0.0	0.2	0.2	0.1
Sc	26.5	12.8	15.7	6.6	18.6	12.5	20.1
Pb	0.9	0.9	1.4	0.8	3.4	3.2	3.1
Hf	0.49	1.05	0.62	0.13	0.99	0.58	1.07
Ta	0.28	0.46	0.25	0.10	7.07	2.18	2.38
Cs	0.01	0.01	0.02	0.01	0.02	0.04	0.02
La	3.58	11.54	3.54	1.07	13.81	16.07	14.26
Ce	5.89	19.24	7.73	1.79	26.46	30.30	27.44
Pr	0.87	2.12	1.16	0.24	3.59	3.87	3.74
Nd	4.30	8.52	5.42	1.23	16.53	16.57	16.62
Sm	1.24	1.72	1.40	0.32	3.64	3.28	3.90
Eu	0.67	1.06	0.55	0.46	1.71	1.88	1.78
Gd	1.61	1.67	1.46	0.39	3.49	3.14	3.91
Tb	0.27	0.26	0.23	0.06	0.56	0.45	0.63
Dy	1.65	1.49	1.38	0.32	3.42	2.57	3.59
Ho	0.33	0.28	0.28	0.06	0.70	0.50	0.74
Er	0.91	0.77	0.79	0.18	1.91	1.33	2.06
Tm	0.12	0.10	0.11	0.02	0.28	0.19	0.31
Yb	0.76	0.65	0.74	0.14	1.73	1.27	2.00
Lu	0.11	0.09	0.12	0.02	0.28	0.18	0.29

Sample ID	MR-GN22-25	MR-GN22-36	MR-GN21-34	MR-GN21-35	MR-GN22-27	MR-GN22-35	pk-G-GN21-2	pk-G-GN21-10	pk-G-GN22-2	pk-G-GN22-3
Rock Type	Metadiorite + biotite		Metadiorite							
Major Elements (wt%)										
SiO <sub>2</sub>	54.39	52.41	59.96	57.34	57.84	56.03	56.84	57.34	58.75	59.67
TiO <sub>2</sub>	0.92	0.63	0.85	0.96	0.91	0.91	0.90	0.75	0.89	0.66
Al <sub>2</sub> O <sub>3</sub>	18.06	16.35	17.49	17.83	17.86	17.47	18.81	17.41	16.74	17.09
Fe <sub>2</sub> O <sub>3</sub>	--	--	--	--	--	--	2.44	7.17	--	--
FeO*	7.08	7.65	5.77	6.64	6.42	6.80	4.42	--	5.98	5.55
MnO	0.12	0.14	0.12	0.13	0.12	0.11	0.08	0.08	0.08	0.08
MgO	4.76	7.92	2.36	3.06	2.95	4.35	3.11	3.39	3.69	3.03
CaO	7.96	10.47	5.60	6.38	6.03	7.11	7.12	6.36	6.27	5.74
Na <sub>2</sub> O	4.36	2.98	3.78	3.90	3.77	3.93	3.82	3.75	3.95	3.71
K <sub>2</sub> O	1.28	0.79	2.49	1.95	2.00	2.03	1.60	2.08	2.43	2.59
P <sub>2</sub> O <sub>5</sub>	0.24	0.10	0.26	0.24	0.20	0.23	0.26	0.28	0.26	0.17
Total	99.17	99.42	98.67	98.43	98.09	98.98	99.40	98.61	99.04	98.29
LOI	0.28	0.02	0.53	0.63	0.96	0.41	--	--	--	--
Mg#	58.51	68.47	46.21	49.12	49.07	57.28	49.64	52.42	56.40	53.37
REE and Trace Elements (ppm)										
Rb	6.7	3.8	42.7	33.4	33.2	22.7	22.5	39.4	45.7	53.7
Sr	627	873	507	537	533	572	577	548	551	512
Y	21	17	22	30	25	23	24	23	25	23
Zr	85	68	171	177	197	156	125	166	224	151
V	153	151	117	156	124	147	141	138	134	122
Ni	52	152	7	10	10	46	11	35	42	23
Cr	73	149	4	3	5	95	18	40	67	35
Nb	6.3	2.5	7.7	9.6	8.5	7.0	9.8	7.5	9.9	10.3
Ga	20.5	16.9	18.8	20.1	19.1	22.4	20.0	18.5	19.0	17.5
Cu	9	17	7	6	12	7	0	0	0	0
Zn	83	74	114	121	80	91	88	78	81	70
Co	--	--	--	--	--	--	--	--	--	--
Ba	516	341	1204	713	916	636	716	754	788	705
U	0.1	0.2	0.2	0.1	0.1	0.1	0.1	0.1	0.1	0.2
Th	0.1	0.5	0.6	0.2	0.1	0.1	0.1	0.2	0.1	0.7
Sc	17.8	27.0	12.5	17.4	14.6	16.8	15.7	17.5	15.8	15.4
Pb	7.9	3.8	11.7	10.7	10.3	9.6	10.4	10.8	10.8	12.6
Hf	2.26	2.15	4.07	4.57	4.86	4.01	3.00	4.37	5.82	3.98
Ta	0.59	0.37	0.51	0.65	0.53	0.55	2.87	0.75	3.01	2.98
Cs	0.04	0.05	0.09	0.03	0.02	0.02	0.02	0.03	0.01	0.04
La	19.16	11.22	20.39	23.92	19.08	21.41	22.29	22.15	23.42	23.17
Ce	40.21	25.87	40.39	49.75	40.66	46.10	45.55	43.63	50.02	45.19
Pr	5.02	3.65	4.94	6.30	5.16	5.98	5.52	5.28	6.38	5.34
Nd	20.94	16.67	20.43	25.92	21.99	24.89	22.90	21.48	26.79	20.55
Sm	4.60	3.91	4.37	5.71	4.77	5.35	4.74	4.35	5.57	4.31
Eu	1.34	1.10	1.56	1.57	1.50	1.39	1.57	1.30	1.41	1.26
Gd	4.10	3.76	4.35	5.55	4.68	4.85	4.53	4.14	5.25	3.68
Tb	0.63	0.56	0.64	0.87	0.73	0.71	0.72	0.63	0.79	0.63
Dy	3.77	3.21	3.78	5.31	4.53	4.20	4.26	3.90	4.52	3.86
Ho	0.74	0.65	0.75	1.06	0.90	0.82	0.82	0.82	0.89	0.80
Er	2.05	1.73	2.14	3.03	2.51	2.31	2.25	2.34	2.42	2.32
Tm	0.32	0.24	0.32	0.44	0.38	0.35	0.35	0.36	0.36	0.37
Yb	2.00	1.60	2.00	2.82	2.44	2.17	2.30	2.38	2.31	2.44
Lu	0.31	0.24	0.30	0.41	0.36	0.33	0.32	0.35	0.34	0.38

Sample ID	MR-GN21-16	MR-GN21-39	MR-GN21-53	pk-G-GN22-5
Rock Type	Quartzo-feldspathic			
Major Elements (wt%)				
SiO <sub>2</sub>	72.21	74.61	72.01	73.15
TiO <sub>2</sub>	0.08	0.06	0.32	0.46
Al <sub>2</sub> O <sub>3</sub>	14.95	14.68	14.12	12.77
Fe <sub>2</sub> O <sub>3</sub>	--	--	--	2.92
FeO*	0.89	0.58	2.24	--
MnO	0.07	0.02	0.03	0.08
MgO	0.13	0.12	0.73	0.76
CaO	1.46	3.12	2.48	1.95
Na <sub>2</sub> O	3.96	4.65	3.43	2.77
K <sub>2</sub> O	4.26	1.05	3.30	3.38
P <sub>2</sub> O <sub>5</sub>	0.03	0.01	0.06	0.10
Total	98.05	98.88	98.73	98.34
LOI	1.10	0.51	0.50	--
Mg#	23.67	29.61	40.74	37.75
REE and Trace Elements (ppm)				
Rb	<i>106.1</i>	<i>16.0</i>	<i>54.0</i>	<i>185.3</i>
Sr	<i>182</i>	<i>436</i>	<i>406</i>	<i>4</i>
Y	<i>17</i>	<i>1</i>	<i>6</i>	<i>31</i>
Zr	<i>79</i>	<i>35</i>	<i>113</i>	<i>227</i>
V	<i>5</i>	<i>8</i>	<i>32</i>	<i>34</i>
Ni	<i>10</i>	<i>4</i>	<i>10</i>	<i>18</i>
Cr	<i>2</i>	<i>3</i>	<i>13</i>	<i>89</i>
Nb	<i>1.6</i>	<i>1.0</i>	<i>3.2</i>	<i>19.0</i>
Ga	<i>16.8</i>	<i>17.2</i>	<i>15.2</i>	<i>15.8</i>
Cu	<i>6</i>	<i>5</i>	<i>10</i>	<i>11</i>
Zn	<i>69</i>	<i>69</i>	<i>80</i>	<i>54</i>
Co	--	--	--	--
Ba	<i>653</i>	<i>160</i>	<i>1074</i>	<i>480</i>
U	<i>0.3</i>	<i>0.2</i>	<i>0.1</i>	<i>8.0</i>
Th	<i>0.6</i>	<i>0.2</i>	<i>0.2</i>	<i>26.2</i>
Sc	<i>3.3</i>	<i>0.8</i>	<i>4.3</i>	<i>9.6</i>
Pb	<i>41.4</i>	<i>25.1</i>	<i>22.2</i>	<i>24.2</i>
Hf	<i>2.48</i>	<i>1.14</i>	<i>3.37</i>	<i>6.80</i>
Ta	<i>0.07</i>	<i>0.07</i>	<i>0.13</i>	<i>1.21</i>
Cs	<i>0.04</i>	<i>0.08</i>	<i>0.02</i>	<i>7.50</i>
La	<i>4.84</i>	<i>4.02</i>	<i>12.71</i>	<i>42.83</i>
Ce	<i>10.19</i>	<i>9.25</i>	<i>21.81</i>	<i>91.62</i>
Pr	<i>1.23</i>	<i>0.84</i>	<i>2.23</i>	<i>10.66</i>
Nd	<i>5.08</i>	<i>3.11</i>	<i>7.92</i>	<i>39.38</i>
Sm	<i>1.20</i>	<i>0.47</i>	<i>1.35</i>	<i>7.75</i>
Eu	<i>0.63</i>	<i>0.67</i>	<i>1.03</i>	<i>1.07</i>
Gd	<i>1.18</i>	<i>0.26</i>	<i>1.22</i>	<i>6.85</i>
Tb	<i>0.22</i>	<i>0.04</i>	<i>0.18</i>	<i>1.06</i>
Dy	<i>1.84</i>	<i>0.23</i>	<i>1.09</i>	<i>5.81</i>
Ho	<i>0.64</i>	<i>0.06</i>	<i>0.23</i>	<i>1.13</i>
Er	<i>2.96</i>	<i>0.21</i>	<i>0.67</i>	<i>2.98</i>
Tm	<i>0.59</i>	<i>0.04</i>	<i>0.09</i>	<i>0.39</i>
Yb	<i>4.79</i>	<i>0.33</i>	<i>0.58</i>	<i>2.36</i>
Lu	<i>0.90</i>	<i>0.06</i>	<i>0.10</i>	<i>0.33</i>

**Appendix Table C.1. Whole rock geochemistry organized by lithology.**

Centered data were collected as part of the original data set by Kempton et al. (1990). Right aligned data are part of the new data set or reanalyzed from samples collected by Kempton et al. (1990). Non-italicized data was collected by XRF. Italicized data was collected via LA-ICP-MS.

Sample Name	MR-GN21-33	MR-GN21-37	MR-GN21-62	MR-GN21-9	MR-GN21-56	MR-GN21-7	MR-GN21-59
<b>Lithology</b>	<b>1-Pyroxene Metacumulates</b>			<b>Olivine Meta-Gabbro-norites</b>		<b>2-Pyroxene Metacumulates</b>	
q	0.00	0.00	0.00	0.00	0.00	0.00	0.00
or	2.78	0.72	-13.08	0.99	2.84	1.11	1.86
ab	39.96	20.03	0.00	23.24	31.80	11.81	34.11
an	46.68	41.60	36.89	36.21	41.08	29.32	49.13
lc	0.00	0.00	10.60	0.00	0.00	0.00	0.00
ne	0.40	1.33	5.41	0.00	0.00	0.00	1.34
di	5.33	24.27	50.19	17.76	8.80	6.78	6.25
hy	0.00	0.00	0.00	6.59	0.43	23.41	0.00
ol	3.85	10.61	5.07	14.05	13.68	26.69	5.35
mt	0.00	0.00	0.00	0.00	0.00	0.00	0.00
il	0.75	1.21	3.39	0.86	0.91	0.67	1.87
ap	0.26	0.22	1.53	0.29	0.47	0.22	0.09
<b>Normative Composition</b>	Normative nephline and olivine			Normative hypersthene and olivine		Normative hypersthene and olivine	Normative nephline and olivine

Sample Name	MR-GN21-34	MR-GN21-35	MR-GN22-27	MR-GN22-35	MR-GN22-25	MR-GN22-36	MR-GN21-16	MR-GN21-39	MR-GN21-53
<b>Lithology</b>	<b>Metadiorites</b>				<b>Metadiorites + Biotite</b>		<b>Quartzofeldspathic Granulites</b>		
q	10.09	5.82	7.45	1.33	0.00	0.00	28.66	36.53	31.61
or	14.89	11.68	12.03	12.10	7.61	4.69	25.68	6.26	19.73
ab	32.41	33.54	32.50	33.60	37.17	25.29	34.21	39.77	29.40
an	23.74	25.79	26.43	24.28	26.15	29.03	10.60	16.27	13.56
lc	0.00	0.00	0.00	0.00	0.00	0.00	0.00	0.00	0.00
ne	0.00	0.00	0.00	0.00	0.00	0.00	0.00	0.00	0.00
di	2.26	3.96	2.29	8.19	10.03	18.54	-2.91	-0.56	-1.27
hy	14.36	16.78	17.06	18.22	10.86	12.63	3.54	1.59	6.19
ol	0.00	0.00	0.00	0.00	5.86	8.39	0.00	0.00	0.00
mt	0.00	0.00	0.00	0.00	0.00	0.00	0.00	0.00	0.00
il	1.63	1.86	1.75	1.74	1.76	1.21	0.16	0.11	0.62
ap	0.61	0.58	0.48	0.54	0.56	0.23	0.07	0.02	0.15
<b>Normative Composition</b>	Normative quartz and hypersthene				Normative hypersthene and olivine		Normative quartz and hypersthene		

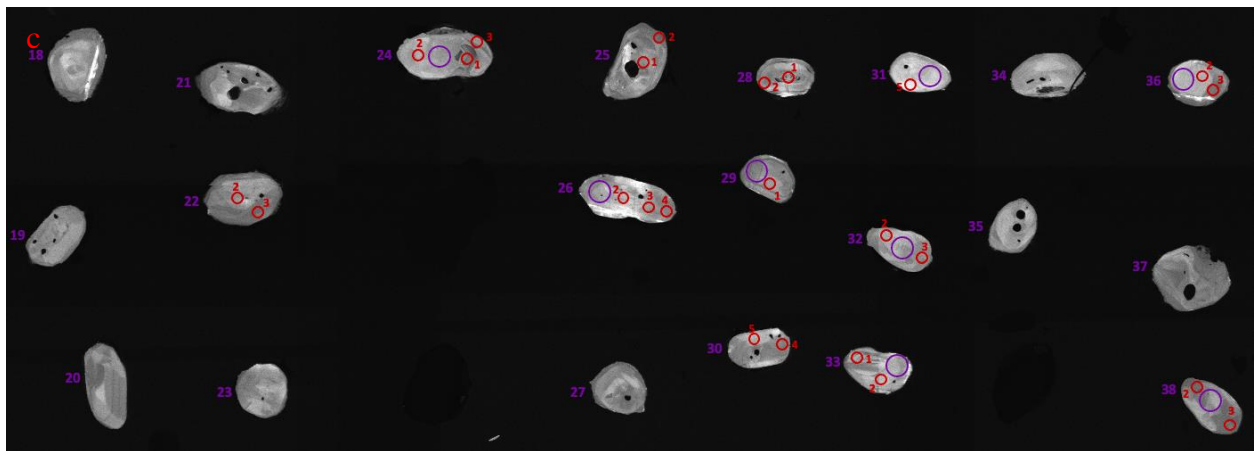
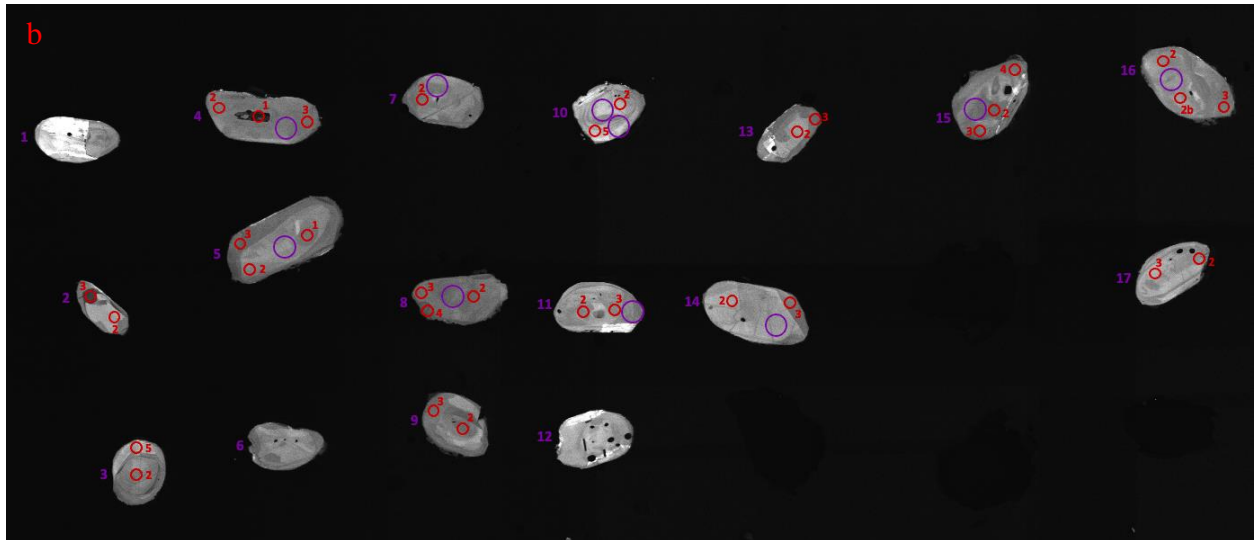
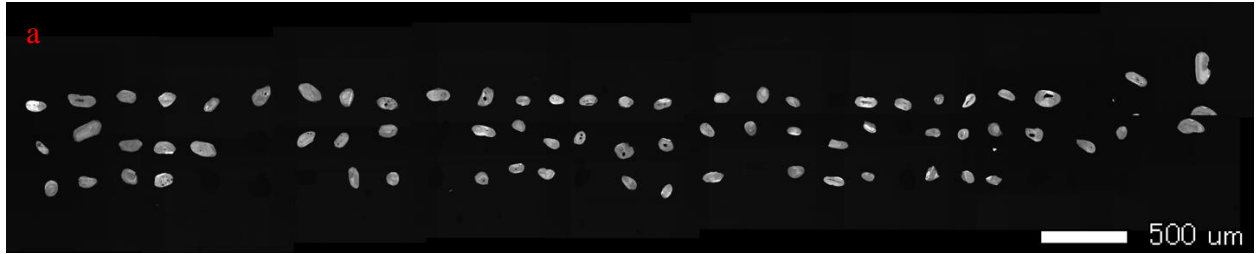
**Appendix Table C.2. Normative compositions.**

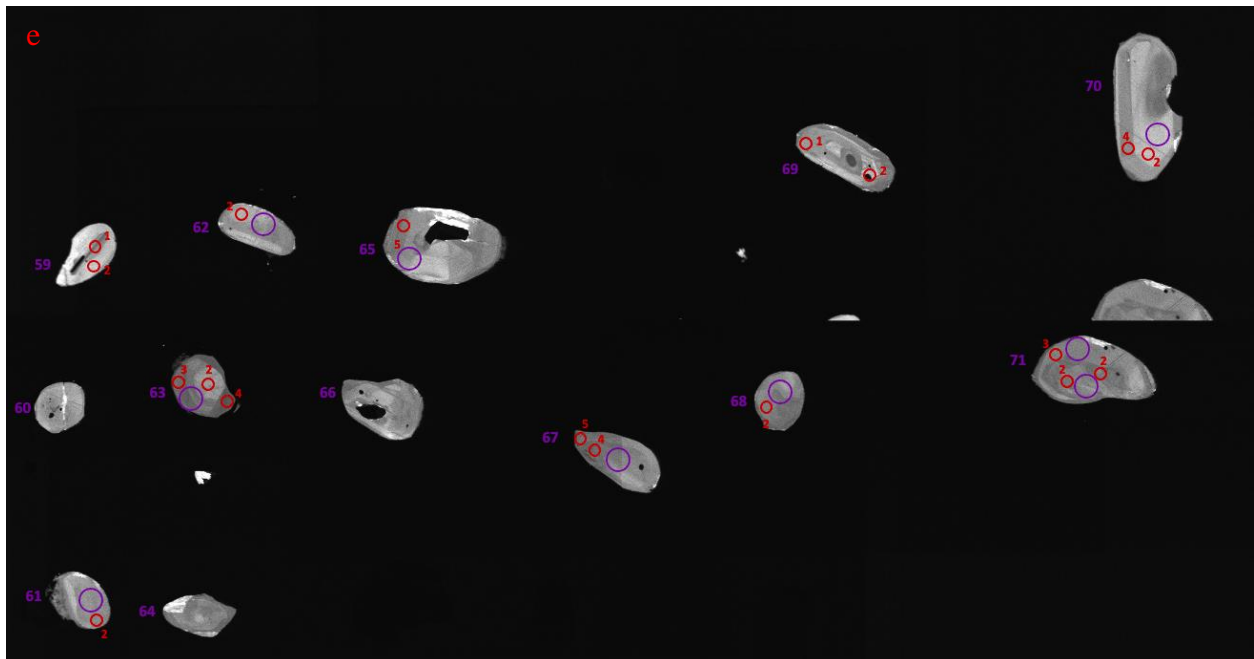
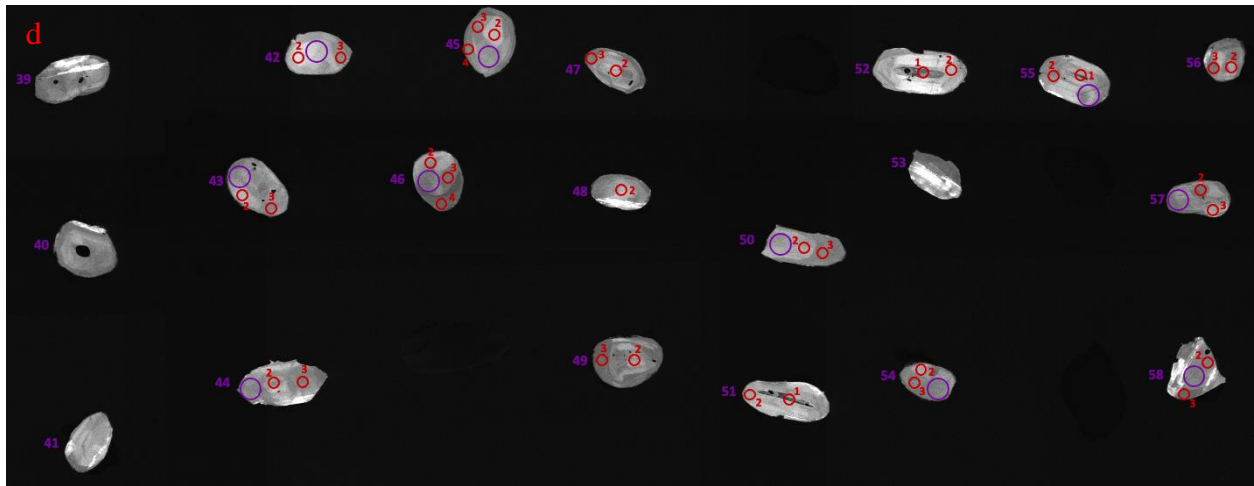
## **Appendix D - Geothermometry**

For the complete data set of two-pyroxene and two-feldspar analyses used for geothermometry calculations, see supplemental file “MikaelaRader2021\_GeothermometryData”.

# Appendix E - Cathodoluminescence Imaging

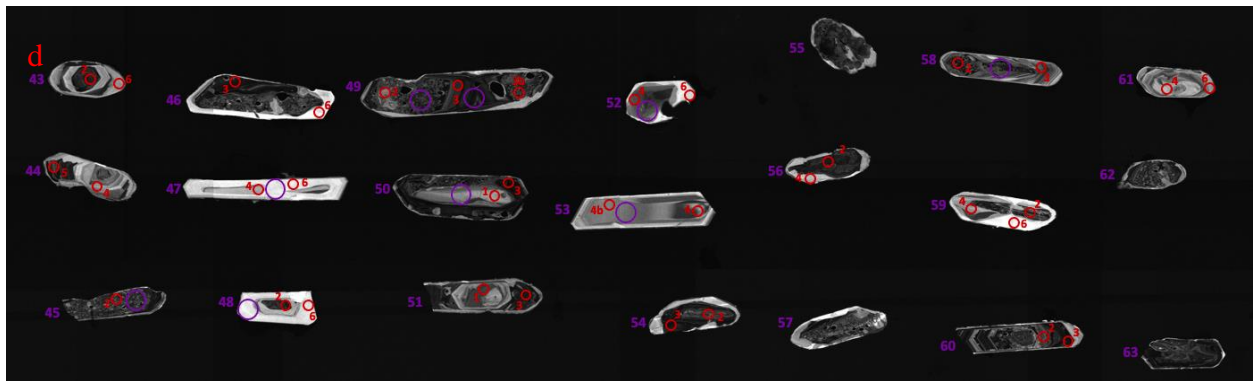
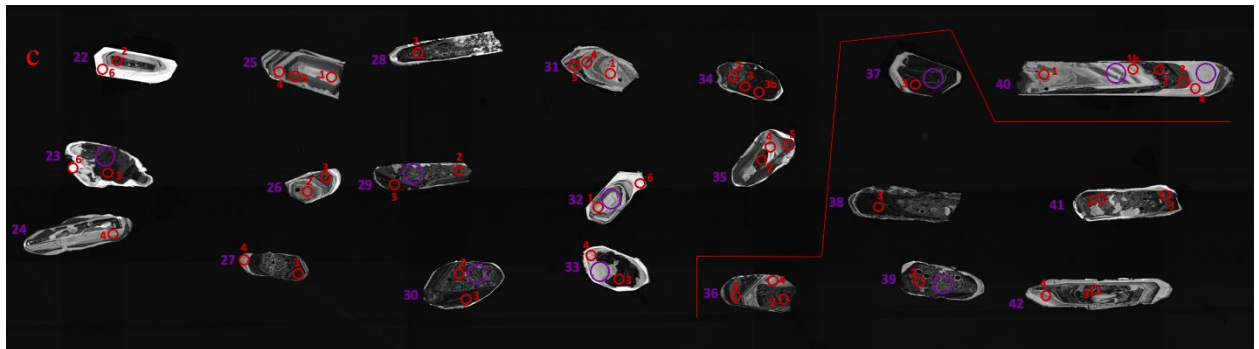
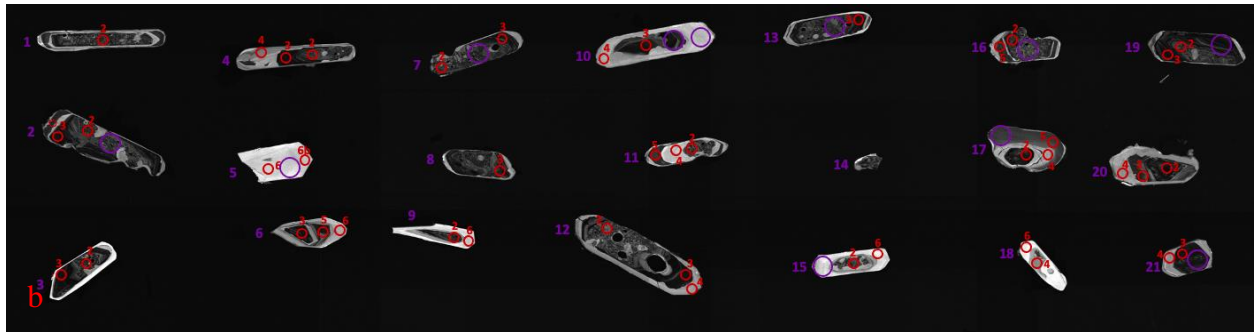
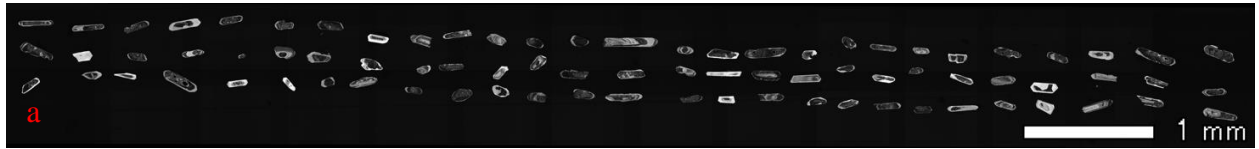
MR-GN21-34

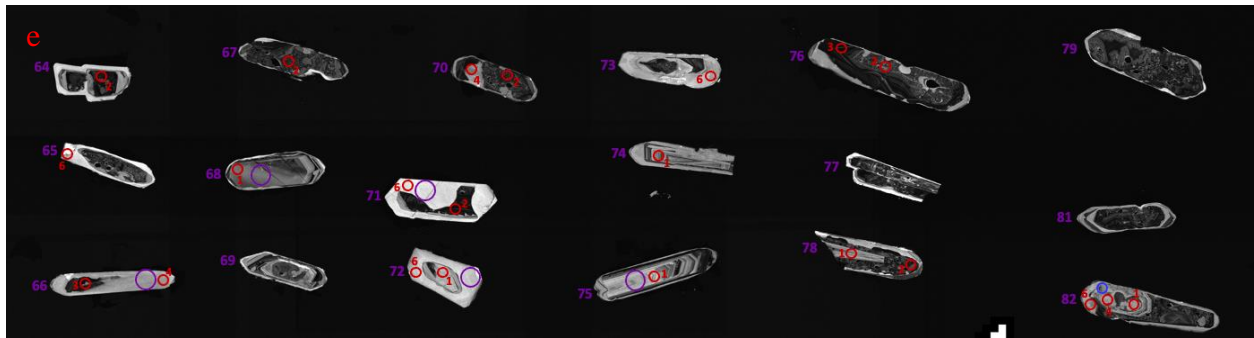




**Figure E.1 a)** CL map of all grains for sample **MR-GN21-34**. **b-e)** Close up of subsets of grains with grain numbers. Red circles indicate U-Pb analyses and purple circles indicate Hf analyses. Spots are labeled with zone being analyzed. **b-c)** Red spots analyzed by U-Pb geochronology only. **d-e)** Red spots analyzed for both U-Pb and trace elements.

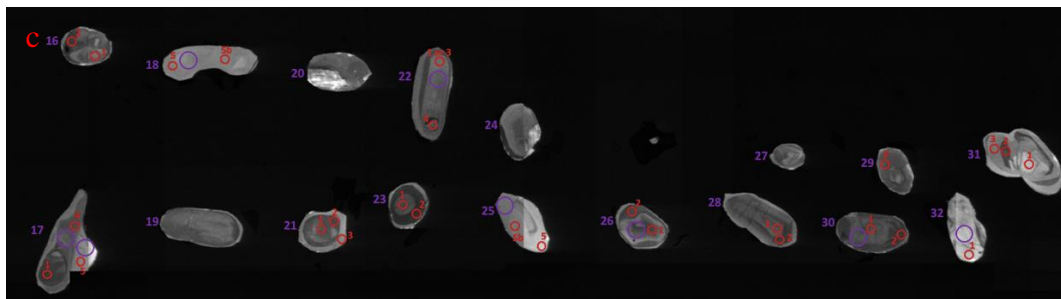
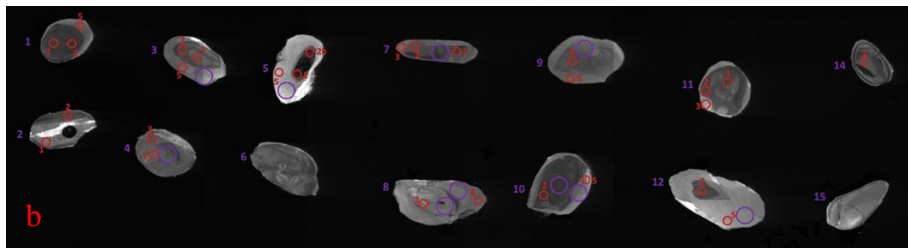
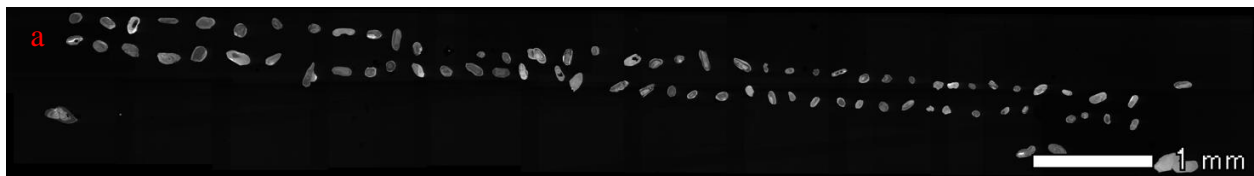
MR-GN21-39

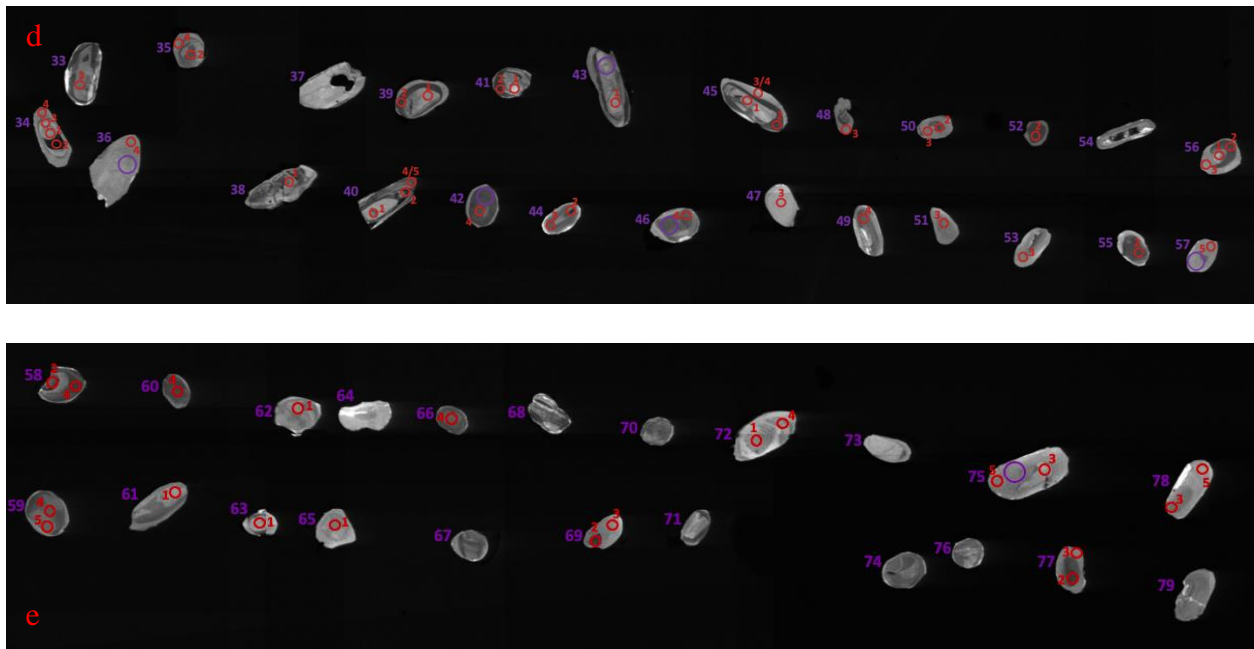




**Figure E.2** a) CL map of all grains for sample MR-GN21-39. b-e) Close up of subsets of grains with grain numbers. Red circles indicate U-Pb analyses and purple circles indicate Hf analyses. Spots are labeled with zone being analyzed. b-c) Grains 1-35 and 40, red spots analyzed by U-Pb geochronology only. d-e) Grains 36-82 excluding 40, red spots analyzed for both U-Pb and trace elements.

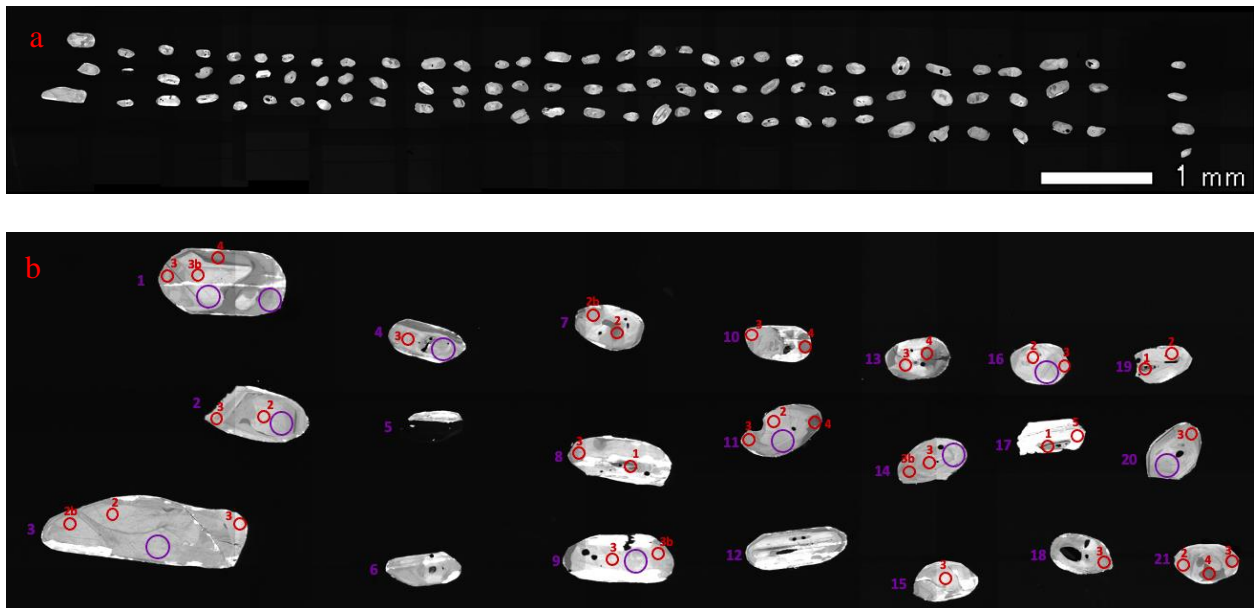
### MR-GN21-53

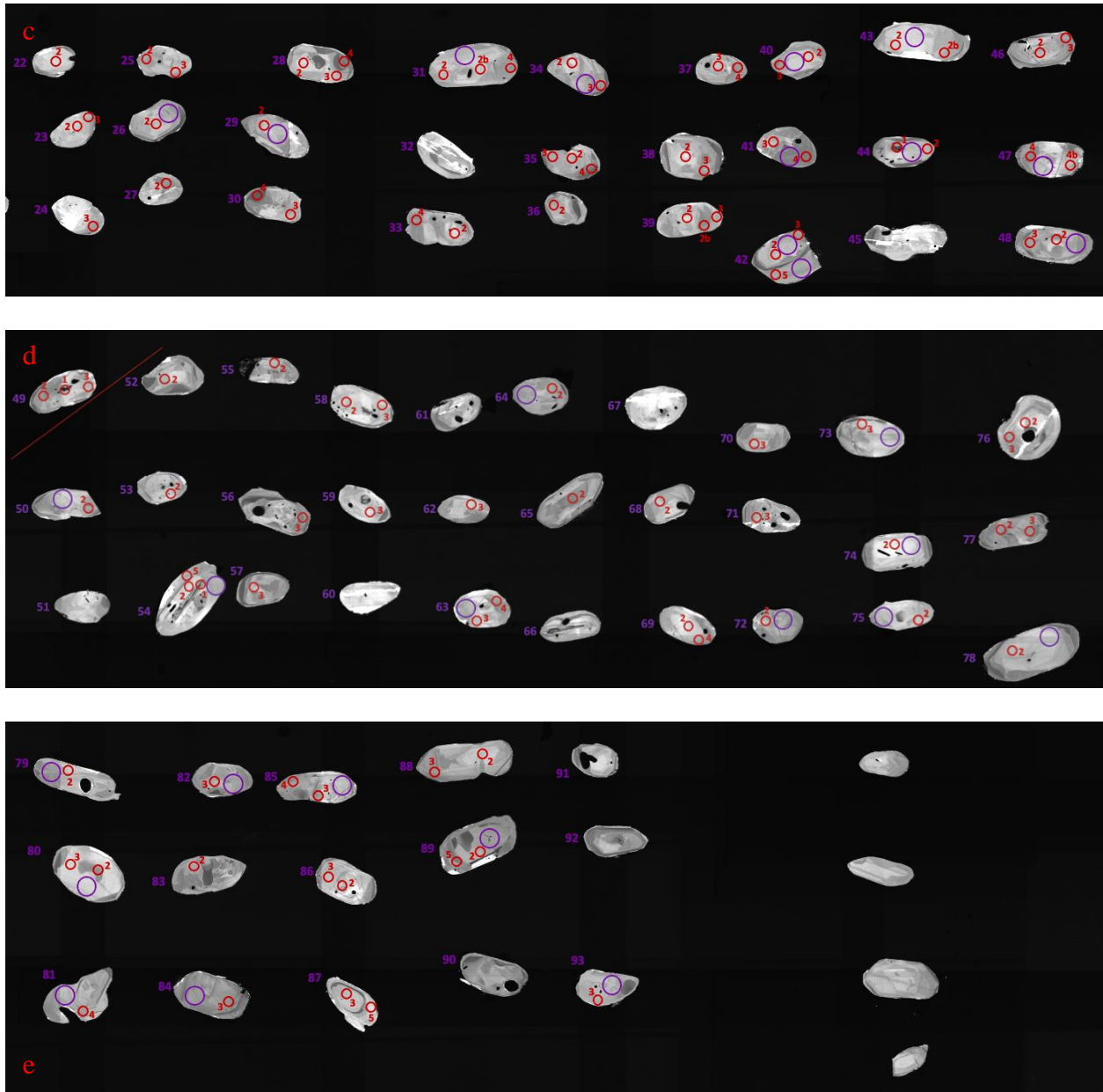




**Figure E.3** a) CL map of all grains for sample **MR-GN21-53**. **b-e)** Close up of subsets of grains with grain numbers. Red circles indicate U-Pb analyses and purple circles indicate Hf analyses. Spots are labeled with zone being analyzed. **b-c)** Red spots analyzed by U-Pb geochronology only. **d-e)** Red spots analyzed for both U-Pb and trace elements.

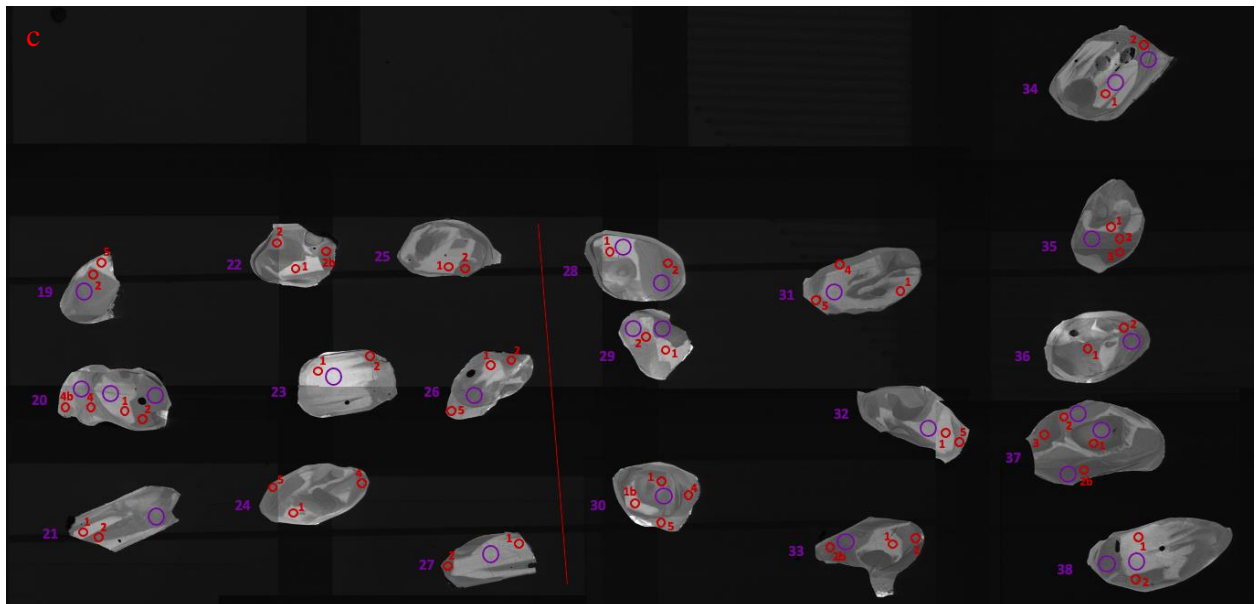
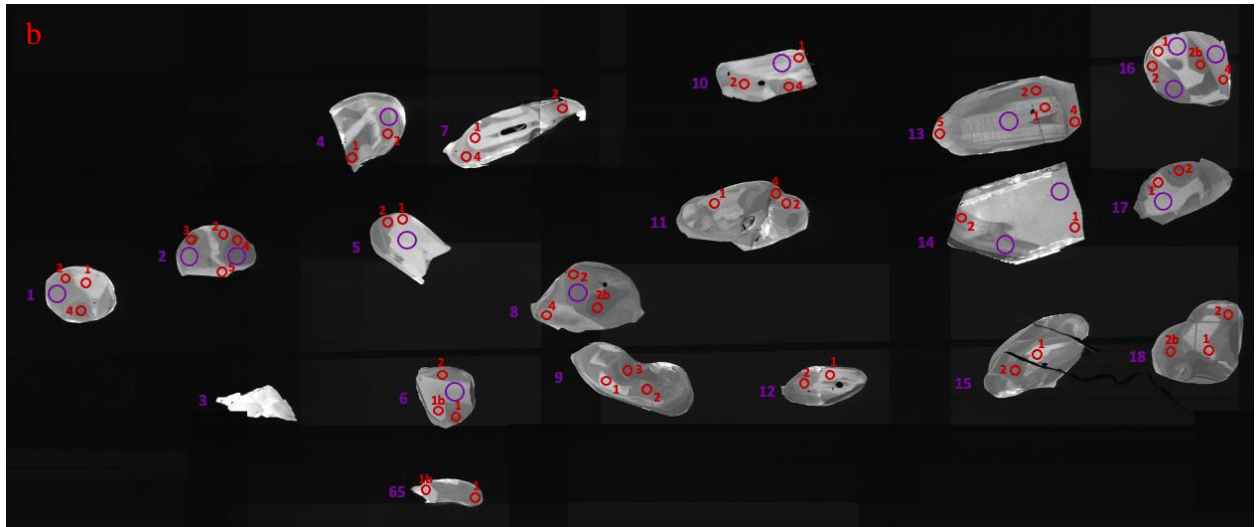
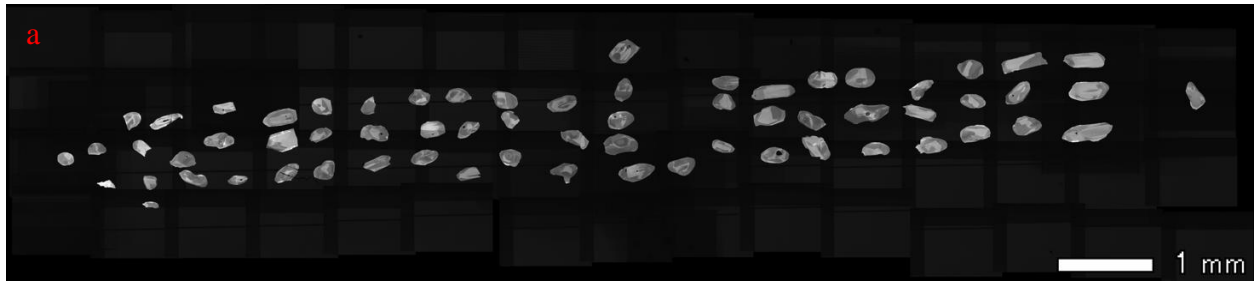
**MR-GN22-27**

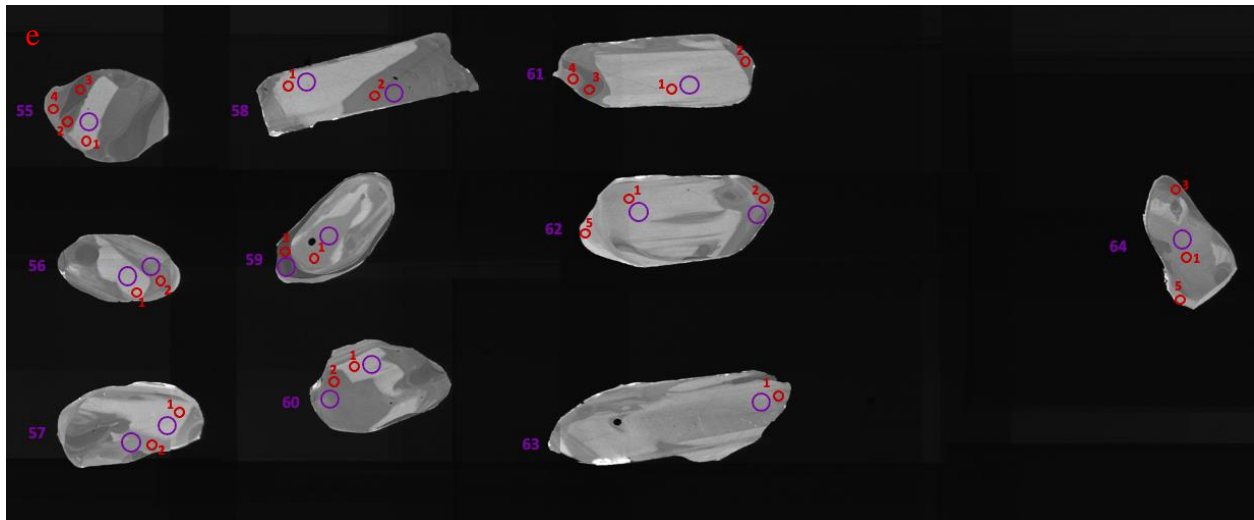
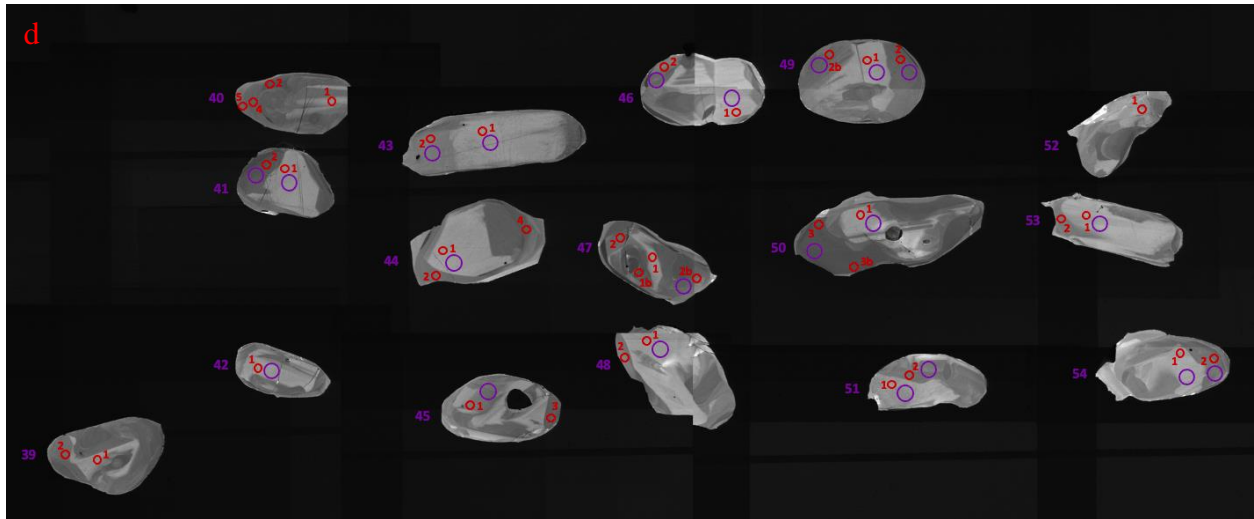




**Figure E.4** a) CL map of all grains for sample **MR-GN22-27**. **b-e)** Close up of subsets of grains with grain numbers. Red circles indicate U-Pb analyses and purple circles indicate Hf analyses. Spots are labeled with zone being analyzed. **b-d)** Grains 1-49, red spots analyzed by U-Pb geochronology only. **d-e)** Grains 50-93, red spots analyzed for both U-Pb and trace elements.

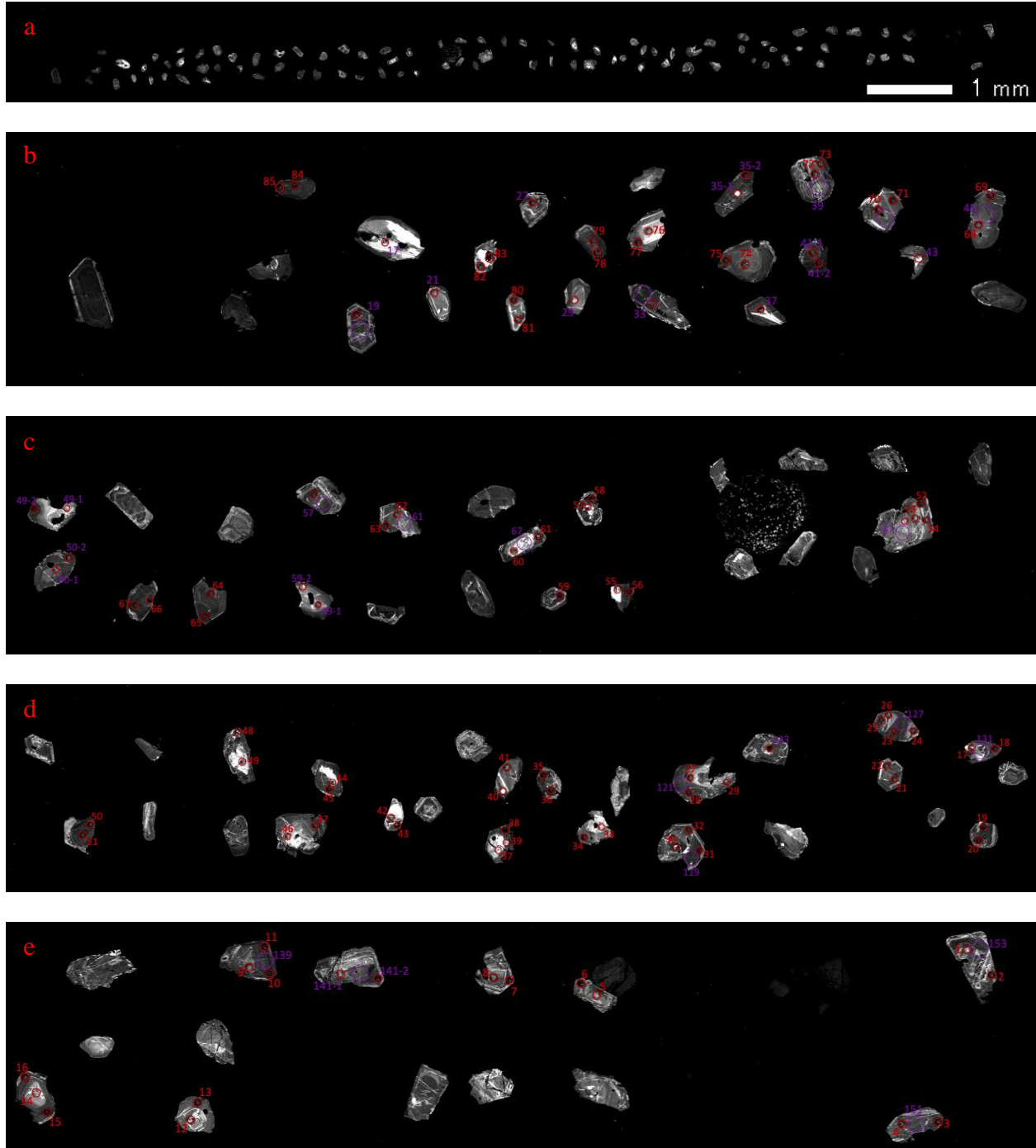
MR-GN22-35





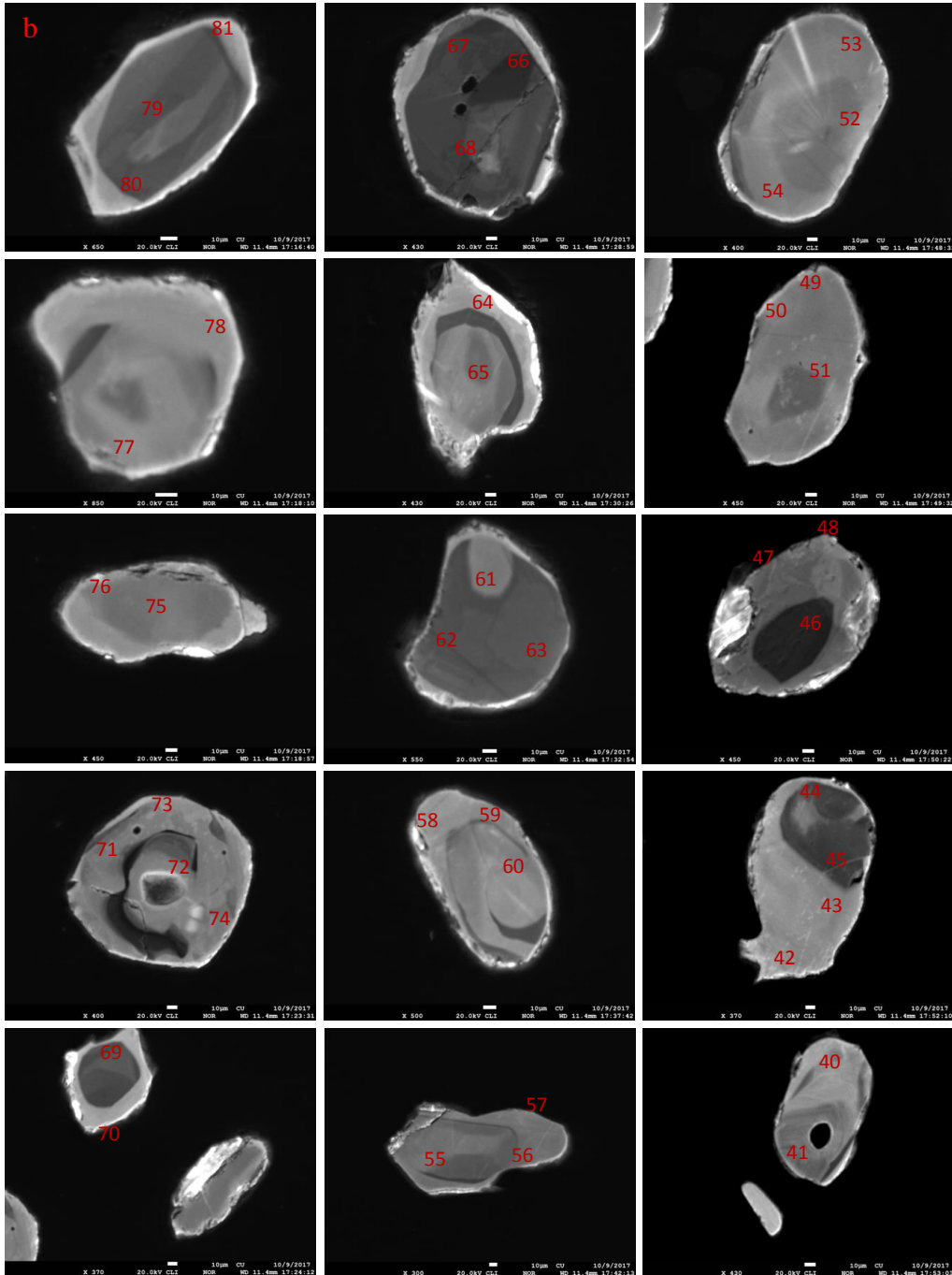
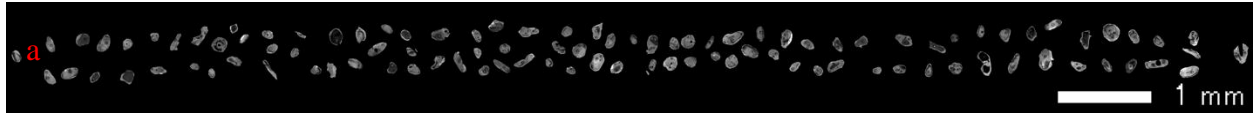
**Figure E.5** a) CL map of all grains for sample **MR-GN22-35**. **b-e)** Close up of subsets of grains with grain numbers. Red circles indicate U-Pb analyses and purple circles indicate Hf analyses. Spots are labeled with zone being analyzed. **b-c, e)** Grains 1-27 and 55-64, red spots analyzed by U-Pb geochronology only. **c-d)** Grains 28-54, red spots analyzed for both U-Pb and trace elements.

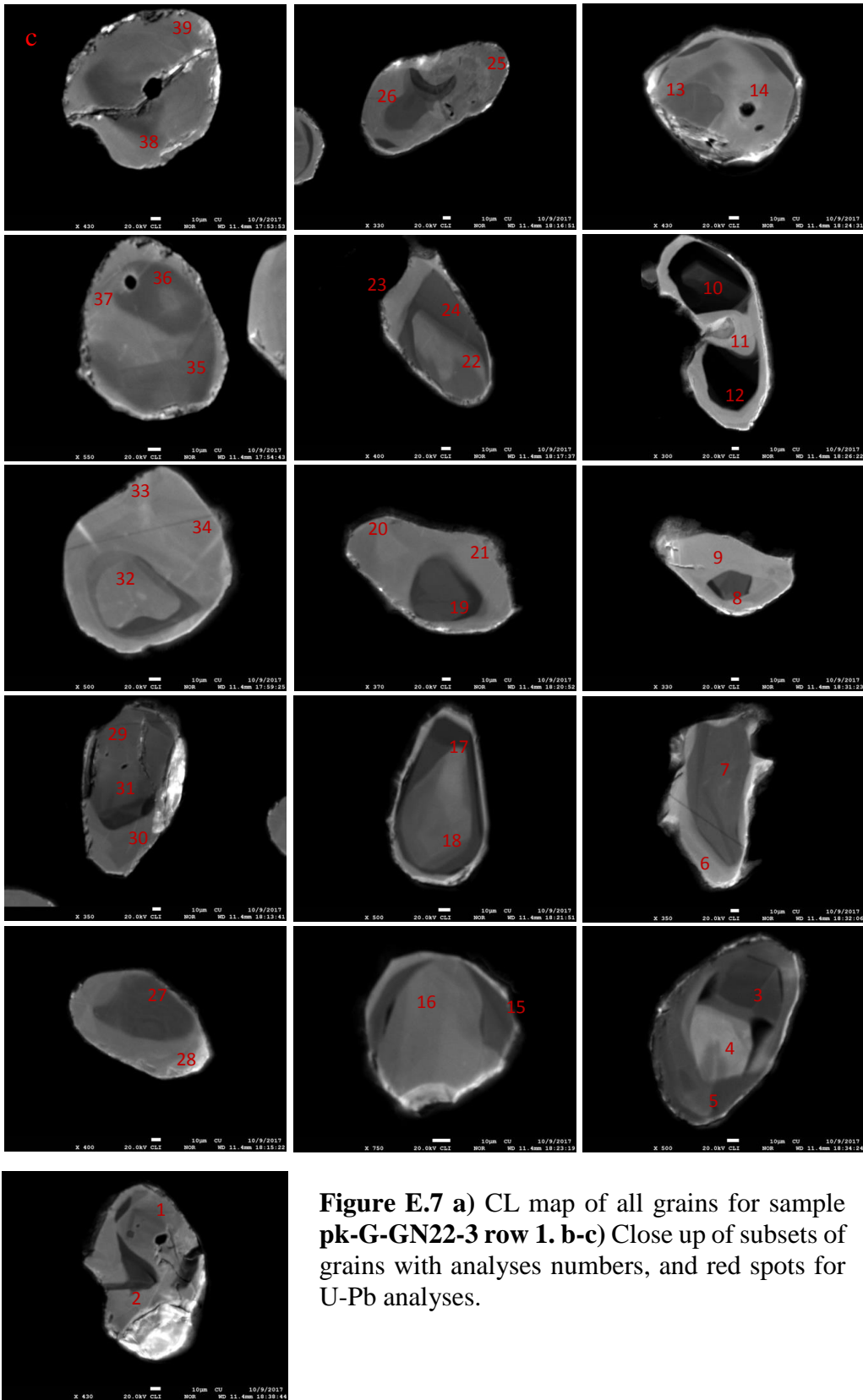
pk-G-GN22-5



**Figure E.6** a) CL map of all grains for sample **pk-G-GN22-5**. b-e) Close up of subsets of grains with grain numbers. Red circles indicate U-Pb analyses and purple circles indicate Hf analyses. Red numbers indicate original U-Pb analyses conducted on 02.19.19 and purple numbers indicate new U-Pb analyses conducted on 11.09.20.

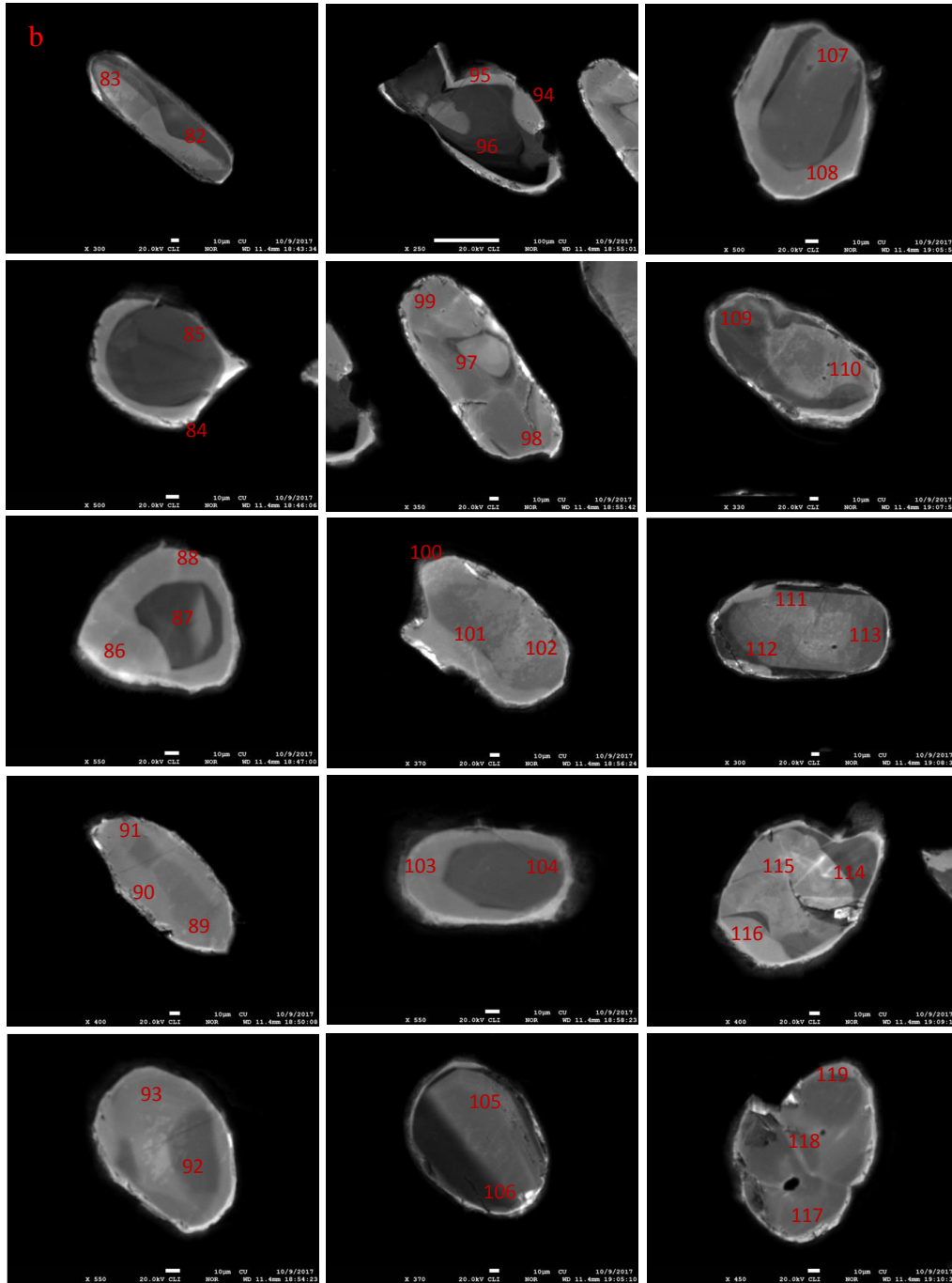
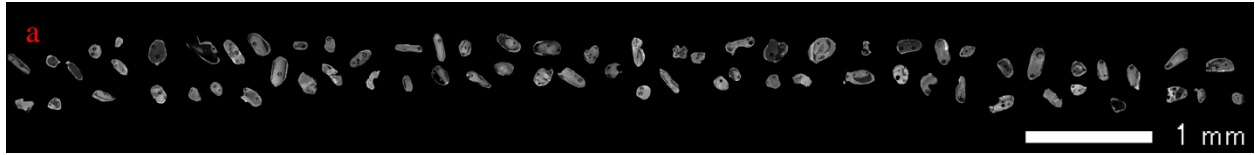
pk-G-GN22-3 Row 1

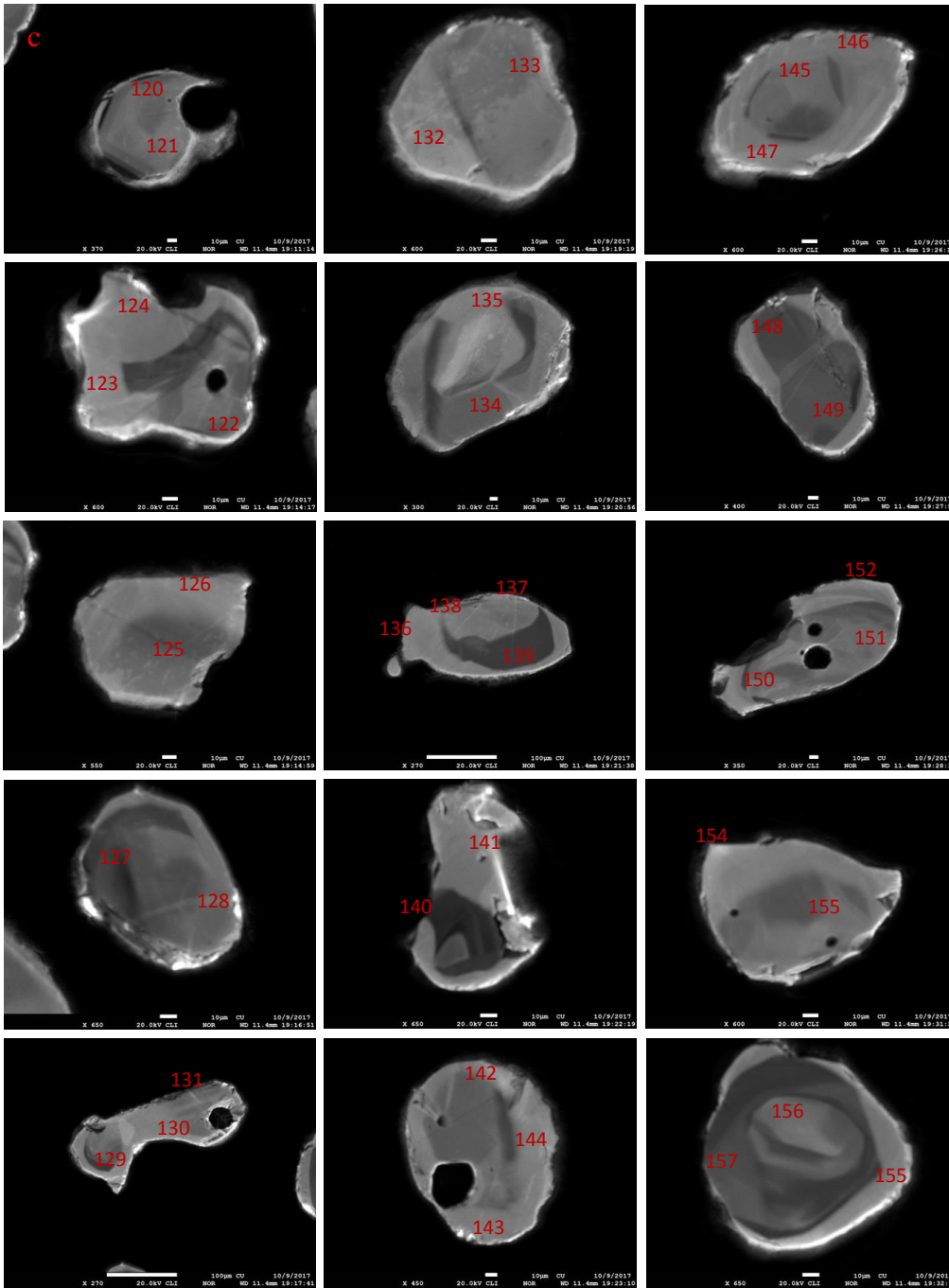




**Figure E.7 a)** CL map of all grains for sample **pk-G-GN22-3 row 1.** **b-c)** Close up of subsets of grains with analyses numbers, and red spots for U-Pb analyses.

pk-G-GN22-3 Row 2





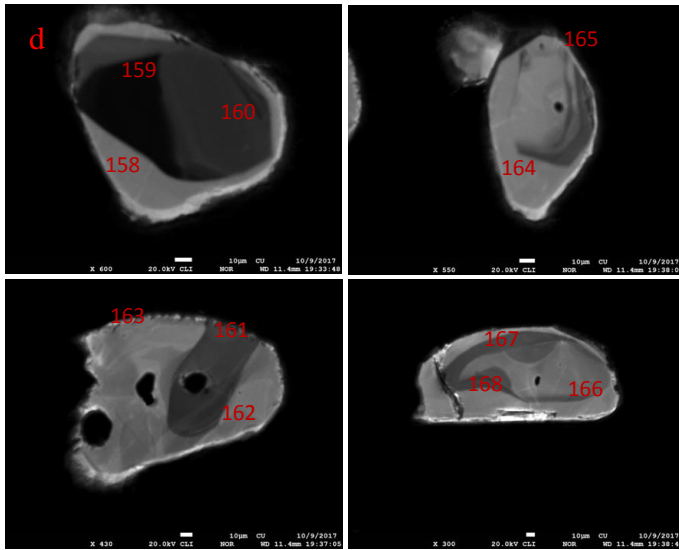


**Figure E.8** a) CL map of all grains for sample **pk-G-GN22-3 row 2**. **b-d)** Close up of subsets of grains with analyses numbers, and red spots for U-Pb analyses.

## Appendix F - U-Pb LA-ICP-MS Laser Methods and Geochronology

### Data

Publication	Rader et al. 2021
<b>Laboratory &amp; Sample Preparation</b>	
Laboratory name	The University of Kansas, Isotope Geochemistry Laboratories
Sample type/mineral	zircon
Sample preparation	polished grain mounts, thin sections, tape mounts
Imaging	CL
<b>Laser ablation system</b>	
Make, Model & type	Arf excimer 193 nm, Photon Machines Analyte G2, Atlex300
Ablation cell & volume	Helix 2, two-volume cell
Laser wavelength (nm)	193
Pulse width (ns)	5
Fluence ( $J.cm^{-2}$ )	1.2
Repetition rate (Hz)	10
Spot size ( $\mu m$ )	20
Carrier gas	He, 1.01 l/min, Ar, 1.1 l/min
Ablation duration (secs)	25 U-Pb / 25 trace element
<b>ICP-MS Instrument</b>	
Make, Model & type	Thermo Element2 magnetic sector field ICP-MS
RF power (W)	1100-1220
Make-up gas flow (l/min)	Ar, 1.1 l/min
sampling depth (z position of torch)	-3.8
Detection system	single detector, counting & analog
Masses measured (ms per peak) U-Pb method	Pb206 (2), Pb207 (5), Pb208 (1), Th232 (1), U238 (2)
Masses measured (ms per peak) U-Pb young method	Pb206 (10), Pb207 (12), Pb208 (2), Th232 (2), U238 (4)
Masses measured (ms per peak) U-Pb trace method	Si29 (3), Ti49 (12), Y89 (2), La139 (15), Ce140 (10), Pr141 (15), Nd146 (15), Sm147 (15), Eu153 (15), Gd157 (5), Dy163 (5), Er166 (5), Yb172 (5), Hf178 (2), Pb206 (8), Pb 207 (12), Pb208 (2), Th232 (2), U238 (3)
Integration time per peak (ms)	Pb206, Pb207, Pb208, Th232, U238
Total method time	45 (U-Pb), 45 (trace elements)
Gas blank (s)	18
IC Dead time (ns)	6
UO+/U+ (%)	0.2-0.25
238U+/232Th+	0.7
<b>Data Processing</b>	
Reference Material info: U-Pb / U-Pb trace	GJ1 red (Jackson et al. 2004) / NIST 612 (GEOREM Dec2009)
238U/238U	137.818
Data processing package used / Correction for LIEF	IGOR PRO, Iolite 2.5, Vizual Age
Common-Pb correction, composition and uncertainty	none
Uncertainty level & propagation	2s, quadratic addition (VisualAge)
Reproducibility (%) propagated 2s error 2s / spot	206Pb/238U GJ1 (1-2%)
Quality control / Validation	Plesovice (Slama et al. 2008, Kosler et al. 2013) FCSZ (Paces & Miller, 1993) Fish Canyon Tuff (e.g. Wotzlav et al. 2013)

For the complete data set of U-Pb geochronology analyses, see supplemental file “MikaelaRader2021\_UPbGeochronology”.

## **Appendix G - Hf Isotope Data**

For the complete data set of Hf isotope analyses, see supplemental file “MikaelaRader2021\_HfData”.